Direct Simulation of Quantum Dynamics in Complex Systems

Thesis by

Artur R. Menzeleev

In Partial Fulfillment of the Requirements

for the Degree of

Doctor of Philosophy

California Institute of Technology

Pasadena, California

2014

(Defended April 30, 2014)

To my parents

Acknowledgments

First, I would like to thank Dr. Thomas F. Miller, my advisor. Over the course of my graduate work, he has taught me much about being a scientist, as well as the value of imagination, tenacity, rigor, and hard work.

I would also like to thank the faculty of the Division of Chemistry and Chemical Engineering. In particularly, I would like to thank my thesis committee, Dr. Rudy Marcus, Dr. Harry Gray, and Dr. Mitchio Okumura for continuing support and valuable scientific discussions. Also, I remember Dr. Aron Kuppermann, his inspirational presentation of the intricacies of quantum mechanics, and his friendly conversations.

I appreciate the support of division administrative and technical staff, in particular Priscilla Boon, who is instrumental to the smooth running of the chemical physics subdivision and the Miller Group. Also, I thank Agnes Tong, Anne Penney, and Tom Dunn for their technical and administrative expertise. Finally, I am thankful for the technical aid of the Caltech High-Performance Computing staff, in particular Zailo Leite and Naveed Near-Ansari.

I greatly appreciate the friendly and supportive demeanor of the Miller Group. Bin, Nick, Nandini, Jason, Josh, Connie, Taylor, Mike, Fran, Kuba, Frank, Romelia, Michiel, Joonho, and Matt—thank you all for the scientific discussion over the years, the feedback on my ideas, and the great company. Thank you also to my friends both outside the lab and outside of Caltech.

Finally, I would like to thank my parents, Dr. Ramil Menzeleev and Gulzhan Menzeleeva, for the inspiration and support.

Abstract

Accurate simulation of quantum dynamics in complex systems poses a fundamental theoretical challenge with immediate application to problems in biological catalysis, charge transfer, and solar-energy conversion. The varied length- and timescales that characterize these kinds of processes necessitate development of novel simulation methodology that can both accurately evolve the coupled quantum and classical degrees of freedom and also be easily applicable to large, complex systems. In the following dissertation, the problems of quantum dynamics in complex systems are explored through direct simulation using path-integral methods as well as application of state-of-the-art analytical rate theories.

Chapter 1 describes the investigation of the distance dependence of rates of long-range proton-coupled electron transfer (PCET) reactions. In concert with experimental observations, we employ molecular dynamics and electronic structure methods, applied within the framework of analytical rate theories, to determine, for the first time, the redox donor-acceptor distance decay constant, β, associated with a concerted proton-coupled electron transfer (CPET) reaction. We show that, although the calculation of β is sensitive to specific details of the theoretical assumptions, values of β obtained from studies of electron transfer (ET) reactions can be directly applied to vibronically nonadiabatic CPET reactions. The collaborative study is published as Warren, J. J., Menzeleev, A. R., et al., "Long-range proton-coupled electron-transfer reactions of bis(imidazole) iron tetraphenylporphyrins linked to benzoates," *Journal of Physical Chemistry Letters*, **4**, 519 (2013).

Chapter 2 describes the use of ring polymer molecular dynamics (RPMD), a path-integral based method, to directly simulate the non-equilibrium process of electron localization following photoinjection into supercritical helium and ambient liquid water. We study the injection of both low- and high-energy excess electrons and consider the coupled electronic and nuclear dynamics associated with the relaxation of the excess electron into its equilibrium configuration. The results obtained are generally consistent with previous experimental and theoretical investigations of the electron injection process, with regard to the observed mechanisms and relaxation timescales, which marks RPMD as a robust method for directly simulating electronic dynamics far from equilibrium. This work has been published as Menzeleev, A. R. and Miller, T. F., "Ring polymer molecular dynamics

beyond the linear response regime: excess electron injection and trapping in liquids," *Journal of Chemical Physics*, **132**, 034106 (2010).

Chapter 3 explores the use of RPMD to directly simulate ET reactions between mixed-valence transition metal ions in water. We compare the RPMD approach against benchmark semiclassical and quantum dynamics methods in both atomistic and system-bath representations for ET in a polar solvent. Without invoking any prior mechanistic or transition state assumptions, RPMD correctly predicts the ET reaction mechanism and quantitatively describes the ET reaction rate over twelve orders of magnitude in the normal and activationless regimes of ET. Detailed analysis of the dynamical trajectories reveals that the accuracy of the method lies in its exact description of statistical fluctuations, with regard to both reorganization of classical nuclear degrees of freedom and the electron tunneling event. The vast majority of the ET reactions in biological and synthetic systems occur in the normal and activationless regimes, and this work provides the foundation for future studies of ET and PCET reactions in condensed-phase systems. Additionally, this study discovers a shortcoming of the method in the inverted regime of the ET, which arises from the inadequate description of the quantization of the real-time electronic-state dynamics, and directly motivates further methodological refinement. This work has been published as Menzeleev, A. R., Ananth, N. and Miller, T. F., "Direct simulation of electron transfer using ring polymer molecular dynamics: Comparison with semiclassical instanton theory and exact quantum methods," *Journal of Chemical Physics*, **135**, 074106 (2011).

Chapter 4 describes an extension of RPMD to allow accurate description of non-adiabatic, multi-electron processes in large systems. Starting from a path-integral discretization in both position and electronic state representation, we employ a coarse-graining procedure to map the fluctuations of the electronic state variables to values of a single continuous coordinate and introduce a kinetic constraint(KC) to address the known failures of position-representation RPMD. The resulting approximate quantum-mechanical Boltzmann distribution is exactly preserved with continuous equations of motion, yielding dynamics that exhibit the formal robustness and favorable scalability of the position-representation RPMD. We show that KC-RPMD accurately describes nonadiabatic dynamics in a range of model systems, and we expect it to be useful for direct simulation of charge-transfer and non-adiabatic chemistries in a range of future applications. This work has been published as Menzeleev, A. R., Bell, F., and Miller, T. F., "Kinetically constrained ring-polymer molecular dynamics for non-adiabatic chemical reactions," *Journal of Chemical Physics*, **140**, 064103 (2014). Appendix A contains an expanded version of several derivations presented in Chapter 4.

Contents

Acknowledgments **iv**

Abstract **v**

1 Theoretical aspects of investigating distance dependence of CPET reactions of bis(imidazole) iron tetraphenylporphyrins **1**

1.1 Introduction 1

1.2 Summary of thermochemical and kinetic properties of the model PCET reactions . . 2

1.3 Theoretical analysis 3

1.3.1 A simplified bimolecular CPET rate expression 3

1.3.2 Derivation of the CPET rate ratio 7

1.4 Calculation of the components of the decay constant β 7

1.4.1 Description of the MD simulations 8

1.4.2 Calculation of $w_{\mathrm{r}}^{(n)}(R)$ and $w_{\mathrm{p}}^{(n)}(R)$ 9

1.4.3 Calculation of the CPET reorganization energies 15

1.4.3.1 Calculation of λ_{i} 15

1.4.3.2 Calculation of $\lambda_{\mathrm{o}}(R)$ using all-atom MD simulations 16

1.4.3.3 Calculation of $\lambda_{\mathrm{o}}(R)$ using the frequency-resolved cavity model . . . 18

1.4.4 Calculation of $\Delta G^{o(n)}$ and $\Delta\Delta G^{o}$. 20

1.4.5 Decorrelation of the proton and electron donor-acceptor distances, and insensitivity of the proton donor-acceptor distance distribution to phenylene linker length. 20

1.5 Determination of the electron transfer decay constant β 22

1.6 Conclusions 24

Appendix A Parameters of the force field used in the MD simulations 25

Appendix B Optimized molecular geometries of PCET reactant and product species . . 32

2 Ring polymer molecular dynamics beyond the linear response regime: Excess electron injection and trapping in liquids 57

2.1 Introduction . . . 57

2.2 Methods . . . 58

2.2.1 Ring polymer molecular dynamics . . . 58

2.2.2 RPMD model for electron injection . . . 59

2.2.3 One-electron energy eigenvalue calculations . . . 60

2.2.4 Simulation details . . . 61

2.3 Results and discussion . . . 63

2.3.1 Injection of an excess electron into supercritical helium . . . 63

2.3.1.1 From the perspective of the electron . . . 63

2.3.1.2 From the perspective of the solvent . . . 67

2.3.1.3 Adiabatic versus non-adiabatic dynamics . . . 71

2.3.1.4 Energy dissipation and slow equilibration timescales . . . 72

2.3.2 Injection of an excess electron into liquid water . . . 74

2.4 Conclusions . . . 80

Appendix A Alternative justification for the electron injection protocol . . . 82

3 Direct simulation of electron transfer using ring polymer molecular dynamics: Comparison with semiclassical instanton theory and exact quantum methods 89

3.1 Introduction . . . 89

3.2 Methods . . . 90

3.2.1 Ring polymer molecular dynamics . . . 90

3.2.2 Semiclassical instanton theory . . . 92

3.2.3 Exact quantum dynamics . . . 94

3.2.4 Marcus theory for ET in a classical solvent . . . 97

3.3 Systems . . . 98

3.3.1 Atomistic representation for ET . . . 99

3.3.2 System-bath representations for ET . . . 101

3.4 Calculation details . . . 103

3.4.1 Atomistic representation . . . 103

3.4.1.1 RPMD . . . 104

3.4.1.2 Marcus theory . . . 106

3.4.2 System-bath representation . . . 106
3.4.2.1 RPMD . . . 106
3.4.2.2 Marcus Theory . . . 107
3.4.2.3 Semiclassical instanton theory . . . 108
3.4.2.4 QUAPI . . . 108
3.5 Results . . . 110
3.5.1 Atomistic simulations . . . 110
3.5.2 System-Bath Simulations . . . 114
3.6 Conclusions . . . 120
Appendix A System-Bath Potential Energy Parameters . . . 121
Appendix B Transformation to Diabatic Basis . . . 123

4 Kinetically constrained ring polymer molecular dynamics for non-adiabatic chemical reactions 131

4.1 Introduction . . . 131
4.2 Theory . . . 132
4.2.1 Path-integral discretization in a two-level system . . . 132
4.2.2 Mean-field (MF) non-adiabatic RPMD . . . 134
4.2.3 Kinetically constrained (KC) RPMD . . . 135
4.2.3.1 A collective variable that reports on kinks . . . 135
4.2.3.2 A kinetic constraint on the quantum Boltzmann distribution . . . 138
4.2.3.3 The mass of the auxiliary variable . . . 141
4.2.3.4 Summary of the KC-RPMD method . . . 142
4.3 Model Systems . . . 142
4.4 Calculation of reaction rates . . . 145
4.4.1 Calculation of KC-RPMD rates . . . 145
4.4.1.1 KC-RPMD rate calculation in System B . . . 146
4.4.1.2 KC-RPMD rate calculation in System A . . . 148
4.4.2 Calculation of reference TST rate expressions . . . 150
4.5 Results . . . 151
4.5.1 Simple avoided-crossing reaction . . . 151
4.5.2 Condensed-phase electron transfer . . . 152
4.6 Concluding Remarks . . . 156

Appendix A Derivation of the penalty function 157
4.A.1 1D redox system with constant K and classical nuclei 157
4.A.2 1D redox system with constant K and quantized nuclei 160
4.A.3 Multi-dimensional redox system with position-dependent $K(\mathbf{R})$ 161
Appendix B KC-RPMD forces and the Bell algorithm 163
4.B.4 The Bell algorithm 164
Appendix C Derivation of the mass of the auxiliary variable 165
4.C.5 1D redox system with constant K and classical nuclei 165
4.C.6 Multi-dimensional redox system with position-dependent $K(\mathbf{R})$ 166

A Deriving the mass of the continuous auxiliary variable in KC-RPMD 173
A.1 Deriving the KC-RPMD mass from 1D Landau-Zener transition state theory 173
A.2 Deriving a multidimensional LZ-TST 176

List of Figures

1.1 Thermochemical cycle for PCET reactions 2

1.2 RPCET Reaction of $\mathbf{Fe^{III}Ph_nCO_2^-}$ with TEMPOH 3

1.3 The system employed in MD calculation of $w_{\mathrm{r}}^{(n)}(R)$ 10

1.4 Free energy profiles $w_{\mathrm{r}}^{(n)}(R)$ and $w_{\mathrm{p}}^{(n)}(R)$ 14

1.5 Outer-sphere CPET reorganization energies computed using MD 18

1.6 Outer-sphere CPET reorganization energies computed using FRCM 19

1.7 Distributions of the proton donor-acceptor distances in iron-porphyrin-TEMPOH complexes 21

1.8 Atom types for the $n = 1$ iron-porphyrin complex. 25

1.9 Atom types for the $n = 2$ iron-porphyrin complex. 28

1.10 Atom types for the TEMPOH molecule. 31

2.1 Cold electron injection into supercritical helium 64

2.2 Ring polymer radius of gyration following injection 65

2.3 Hot electron injection into supercritical helium 66

2.4 Time-resolved radial distribution function $\langle g_{\mathrm{e-He}}(r,t)\rangle$ 68

2.5 Eigenstates of the excess electron following electron injection into supercritical helium 69

2.6 Time-resolved radial distribution function $\langle g_{\mathrm{e-He}}(r,t)\rangle$ for simulations with 4096 He atoms 70

2.7 Components of the system energy following cold electron injection into helium 71

2.8 Components of the system energy following hot electron injection into helium 72

2.9 Energy dissipation following electron injection into helium 73

2.10 Ring polymer radius of gyration following excess electron injection into liquid water . 75

2.11 Solvent dynamics following cold electron injection into water 76

2.12 Solvent dynamics following hot electron injection into water. 77

2.13 Excess electron eigenstates following electron injection into water 77

2.14 Transient electron absorption spectra for excess electron injection into water 78

3.1 Snapshots of the atomistic representation of the ET reaction 98
3.2 Free energy profiles for the ET reaction in the atomistic representation 111
3.3 ET reaction rates and representative trajectories in the atomistic representation – normal and activationless regimes 113
3.4 ET reaction rates and representative trajectories in the atomistic representation – inverted regime 115
3.5 ET reaction rates and FE profiles for Model SB1 116
3.6 Comparison of ET rates for Marcus-like and "direct" mechanisms 118
3.7 Normalized $C_{\mathrm{FF}}(t)$ for ET reaction in Model SB2 119

4.1 A schematic illustration of ring-polymer configurations that exhibit kink-pairs. . . . 136
4.2 Thermal reaction rate coefficients for System A 151
4.3 ET reaction rate coefficients for System B in classical and quantized solvent 153
4.4 Representative trajectories from the ensemble of reactive KC-RPMD trajectories in various regimes of ET 154
4.5 ET reaction rate coefficients for System B as a function of the diabatic coupling . . . 155

List of Tables

1.1 Values of electronic decay constant β. 23

1.2 Atom types and charges in the reactant and product states for the $n = 1$ iron porphyrin complex. 26

1.3 Atom types and charges in the reactant and product states for the $n = 2$ iron porphyrin complex. 29

1.4 TEMPOH atom types and charges in the reactant and product states. 31

1.5 Optimized Cartesian coordinates of the TEMPO molecule 32

1.6 Optimized Cartesian coordinates of the TEMPOH molecule 33

1.7 Optimized Cartesian coordinates of the $\mathbf{Fe^{III}PhCO_2^-}$ molecule 34

1.8 Optimized Cartesian Coordinates of the $\mathbf{Fe^{II}PhCO_2H}$ molecule 37

1.9 Optimized Cartesian Coordinates of the $\mathbf{Fe^{III}Ph_2CO_2^-}$ molecule 40

1.10 Optimized Cartesian Coordinates of the $\mathbf{Fe^{II}Ph_2CO_2H}$ molecule 43

1.11 Energies for the optimized geometries provided in Tables 1.7-1.10 45

1.12 Cartesian coordinates of the rigid portion of the iron-porphyrin species $\mathbf{Fe^{III}PhCO_2^-}$ employed in calculation of $w_{\mathrm{r}}^{(1)}(R)$ and $w_{\mathrm{r}}^{(2)}(R)$ 46

1.13 Cartesian coordinates of the rigid portion of the iron-porphyrin species $\mathbf{Fe^{III}Ph_2CO_2^-}$ employed in calculation of $w_{\mathrm{r}}^{(1)}(R)$ and $w_{\mathrm{r}}^{(2)}(R)$ 48

1.14 Cartesian coordinates of the rigid portion of the iron-porphyrin species $\mathbf{Fe^{II}PhCO_2H}$ employed in calculation of $w_{\mathrm{p}}^{(1)}(R)$ and $w_{\mathrm{p}}^{(2)}(R)$ 50

1.15 Cartesian coordinates of the rigid portion of the iron-porphyrin species $\mathbf{Fe^{II}Ph_2CO_2H}$ employed in calculation of $w_{\mathrm{p}}^{(1)}(R)$ and $w_{\mathrm{p}}^{(2)}(R)$ 52

3.1 Complex times t_k used to calculate the $\{B_{kk'}\}$. 97

3.2 Parameters for the atomistic representation of ET. 99

3.3 Values of the asymmetry parameter ϵ considered in the atomistic representation . . . 100

3.4 Values of the asymmetry parameter ϵ considered in the system-bath representation . . 102

3.5 Parameters for the system-bath representation of ET. 103

3.6 ET reaction rates for the atomistic representation, obtained using RPMD and Marcus theory. 110
3.7 ET reaction rates for Model SB1, obtained using RPMD, Marcus theory, and SCI theory 115
3.8 ET reaction rates for a 1D asymmetric double well, obtained using SCI theory. . . . 117
3.9 ET reaction rates for Model SB2, obtained using RPMD, Marcus theory, SCI theory, and exact quantum dynamics 119
3.10 Parameters for the left Coulombic well in Model SB1 121
3.11 Parameters for the right Coulombic well in Model SB1 121
3.12 Parameters for the left Coulombic well in Model SB2 122
3.13 Parameters for the right Coulombic well in Model SB2 122
3.14 The diagonal elements of the diabatic potential matrix for Model SB2. 124

4.1 Parameters for System A. 144
4.2 Values of m_y for the KC-RPMD simulations of System A. 144
4.3 Parameters for System B. 144

Chapter 1

Theoretical aspects of investigating distance dependence of CPET reactions of bis(imidazole) iron tetraphenylporphyrins

1.1 Introduction

Electron transfer (ET) reactions coupled to proton transfer(PT) reactions are common in chemistry in biology. This process can occur sequentially, with ET followed by PT, PT followed by ET, or in a concerted fashion, where the electron and proton transfer in a single chemical step. The latter process, CPET, is implicated in biological processes that involve spatial separation of the donor and acceptor sites.[1–3] The oxidation of tyrosine Z in photosystem II, for example, is a prototypical separated CPET reaction, with PT occurring between the tyrosine and a nearby histidine and ET occurring between tyrosine and oxidized chlorophyll $P680^+$ located nearly 10 Å away.[1]

In electron transfer reactions, the ET rate exponentially decreases with the redox donor-acceptor distance, and the exponential decay is described by the electronic coupling decay constant, β. Values of β strongly depend on the characteristics of the medium between donor and acceptor, and measurements of β thus shed light on specific ET pathways and mechanisms.[4–6] This chapter describes a collaborative experimental and theoretical investigation of PCET reactions in model iron tetraphenylporphyrin complexes, conducted with the aim to determine the electronic coupling decay constant β. The model complexes employ rigid phenylene spacers to systematically vary the ET donor-acceptor distance of a CPET reaction while keeping the other properties of the system unaffected. Here, the experimental findings of our collaborators are briefly summarized, and the subsequent discussion focuses on the theoretical and computational aspects of the analysis. The study is published as Warren, J. J., Menzeleev, A. R., et al., "Long-Range proton-coupled electron-transfer reactions of bis(imidazole) iron tetraphenylporphyrins linked to benzoates," *Journal of Physical Chemistry Letters*, **4**, 519 (2013).[7]

1.2 Summary of thermochemical and kinetic properties of the model PCET reactions

This study is concerned with PCET reactions of iron complexes of 5-(4-carboxyphenyl)-10,15-20-triphenyl-porphyrin ($\mathbf{Fe^{III}PhCO_2H}$) and 5-(1,1′-biphenyl-4-carboxylic acid)-10,15,20-triphenylporphyrin ($\mathbf{Fe^{III}Ph_2CO_2H}$), which differ by the number of phenylene spacers between the heme and the acid moiety. These compounds were synthesized and metalated according to published procedures.[8–10] Spectroscopic and electrochemical evidence indicate that the heme-iron and the benzoate moiety of these compounds are largely electronically uncoupled, and that the thermochemical properties of the iron systems are in general very similar.[7] The thermochemical properties of the PCET reactions are given in Figure 1.1.

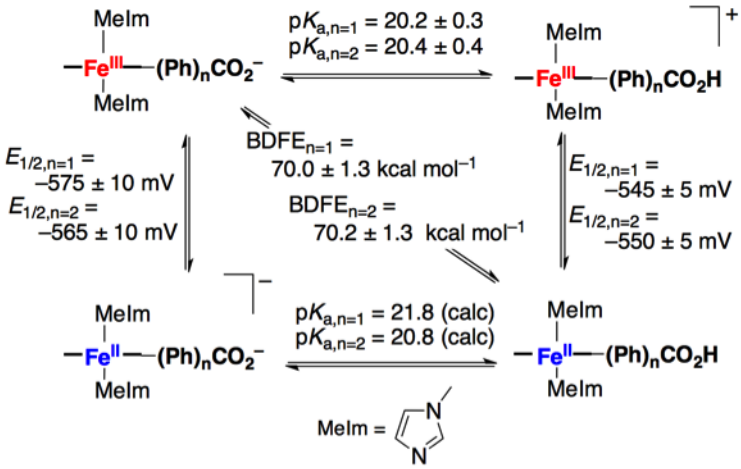

Figure 1.1: Thermochemical cycle relevant to PCET reactions of bis(imidazole) iron tetraphenylporphyrins linked to benzoates

The deprotonated ferric compounds $\mathbf{Fe^{III}PhCO_2^-}$ and $\mathbf{Fe^{III}Ph_2CO_2^-}$, reacted with 2,2′-4,4′-tetramethylpi-peridin-1-ol (TEMPOH) to yield the ferrous species $\mathbf{Fe^{II}PhCO_2H}$ and $\mathbf{Fe^{II}Ph_2CO_2H}$ (Figure 1.2). The reaction rates under pseudo-first-order condition of excess TEMPOH at 298K were determined to be: $k^{(1)} = 15.3 \pm 1.4\mathrm{M^{-1}s^{-1}}$ and $k^{(2)} = 6.5 \pm 0.8\mathrm{M^{-1}s^{-1}}$. The KIE was not determined due to a competing precipitation reaction, however, the initial rates were clearly slower for the transfer of deuterium.

In principle, these PCET reactions can occur by either the concerted or sequential mechanism. The iron-porphyrin complexes, $\mathbf{Fe^{III}PhCO_2H}$ and $\mathbf{Fe^{III}Ph_2CO_2H}$, do not favor one mechanism over the other, due to the thermodynamic uncoupling of the redox and acid-base sites. However,

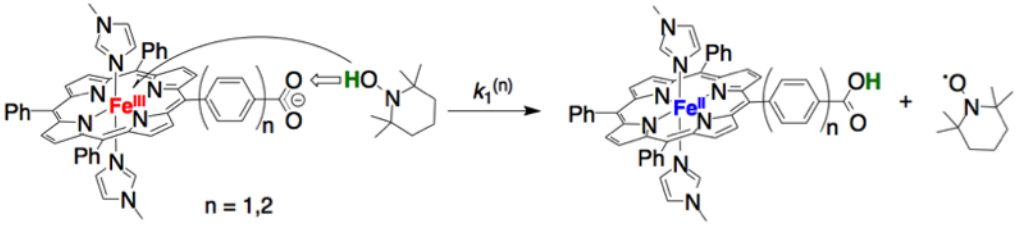

Figure 1.2: PCET Reaction of $\mathbf{Fe^{III}Ph_nCO_2^-}$ with TEMPOH

TEMPOH strongly favors CPET in order to avoid high-energy intermediates that would be generated by individual ET or PT reactions. Specifically, for the CPET from TEMPOH to $\mathbf{Fe^{III}PhCO_2^-}$, the driving force is $\Delta G^o_{\mathrm{CPET}} = -3.5 \pm 1.1$ kcal/mol, whereas the driving forces for the PT and ET reactions are $\Delta G^o_{\mathrm{PT}} = 28.5$ kcal/mol and $\Delta G^o_{\mathrm{ET}} = 29.6$ kcal/mol, respectively. The measured barrier $\Delta G^{\ddagger} = 15.8$ kcal/mol is below the ΔG^o_{PT} and ΔG^o_{ET}, which indicates that the reaction occurs by a CPET mechanism. The PCET reaction between $\mathbf{Fe^{III}Ph_2CO_2^-}$ and TEMPOH has $\Delta G^o_{\mathrm{CPET}} = -3.7 \pm 1.1$ kcal/mol, $\Delta G^o_{\mathrm{PT}} = 28.2$ kcal/mol, $\Delta G^o_{\mathrm{ET}} = 29.4$ kcal/mol, and $\Delta G^{\ddagger} = 16.3$ kcal/mol and therefore also occurs by CPET.

The observed twofold decrease in measured bimolecular PCET rate is consistent with previous unimolecular observations of ET through phenylene linkers.[4] However, the determination of the electronic coupling constant β from the measured reaction rates involves factors that are difficult to obtain experimentally. The following sections describe the theoretical formulation and calculations that were performed to obtain the value of β.

1.3 Theoretical analysis

1.3.1 A simplified bimolecular CPET rate expression

In this section, a simplified rate equation is derived for the CPET between $\mathbf{Fe^{III}Ph_nCO_2^-}$ and TEMPOH. The full equation for the bimolecular, vibronically non-adiabatic CPET is[11–13]

$$k = \int dR \int dr \sum_j \sum_k \frac{2\pi}{\hbar} P_j |V_{jk}|^2 (4\pi(\lambda + \Delta\lambda_{jk}) k_{\mathrm{B}} T)^{-\frac{1}{2}} \times \exp\left[-\frac{\beta(\Delta G^o + \lambda + \Delta\lambda_{jk} + \epsilon_k - \epsilon_j)^2}{4(\lambda + \Delta\lambda_{jk})} \right] \exp[-\beta w_{\mathrm{r}}]. \tag{1.1}$$

Eq. 1.1 explicitly includes the effect of conformational sampling in the electron and proton donor-acceptor distances, R and r, respectively. Here, j and k index the reactant and product vibrational

states, respectively, P_j is the Boltzmann probability of the reactant vibrational state, V_{jk} is the CPET vibronic coupling, λ is the CPET reorganization energy for the ground vibrational sates, $\Delta\lambda_{jk}$ is the difference between the ground and excited vibrational state reorganization energies, ΔG^o is the driving force for the CPET reaction, ϵ_j and ϵ_k are the respective energies of reactant and product vibrational states relative to their corresponding ground states, $w_{\rm r}$is the work of preorganization for the reactants, and in this subsection $\beta = 1/k_{\rm B}T$. In general, each of these terms (aside from β) depends on both R and r.

Eq. 1.1 can be rewritten as

$$k = \int dR \int dr \sum_j \sum_k \exp[-\beta w_{\rm r}] a_{jk} \times \exp\left[-\beta\left(\frac{\lambda^2}{4(\lambda+\Delta\lambda_{jk})} + \frac{2\lambda\phi_{jk}}{4(\lambda+\Delta\lambda_{jk})} + \frac{\phi_{jk}^2}{4(\lambda+\Delta\lambda_{jk})}\right)\right], \tag{1.2}$$

where

$$a_{jk} = \frac{2\pi}{\hbar} P_j |V_{jk}|^2 (4\pi(\lambda+\Delta\lambda_{jk})k_{\rm B}T)^{-\frac{1}{2}} \tag{1.3}$$

and

$$\phi_{jk} = \Delta G^o + \Delta\lambda_{jk} + \epsilon_k - \epsilon_j. \tag{1.4}$$

If $\lambda + \Delta\lambda_{jk} \approx \lambda$, which is the case for the systems considered in this study ($\lambda \approx 40 - 45$kcal/mol and $\Delta\lambda_{jk} \approx 1$ kcal/mol), this expression can be further simplified, yielding

$$a_{jk} = \frac{2\pi}{\hbar} P_j |V_{jk}|^2 \sqrt{\frac{\pi}{\lambda k_{\rm B} T \hbar^2}} \tag{1.5}$$

and

$$k = \int dR \int dr \sum_j \sum_k a_{jk} \exp\left[-\beta\left(\frac{\lambda}{4} + \frac{\phi_{jk}}{2} + \frac{\phi_{jk}^2}{4\lambda}\right)\right] \exp[-\beta w_{\rm r}]. \tag{1.6}$$

Further simplification of Eq. 1.6 can be performed if the $\frac{\phi_{jk}^2}{4\lambda}$ can be neglected. This is indeed true, as is now shown. Firstly, only the ground vibrational state of the reactant is thermally populated, and only terms associated with $j = 0$ in Eq. 1.6 need be considered. Furthermore, ϵ_k is positive and increasing with k, and therefore ϕ_{0k} starts with $\phi_{00} = \Delta G^o$ and increases in the positive direction with k. For reactions in which ΔG^o is small in comparison to λ (which is the case here), $\frac{\phi_{jk}^2}{4\lambda}$ is negligible for $j = k = 0$ case, and only becomes significant for values of k such that $\phi_{0k}/2 \approx \sqrt{\lambda}$. However, such large values of ϕ_{0k} do not occur in the sum over k in Eq. 1.6, as it is

effectively truncated by the $\phi_{jk}/2$ term in the exponand. Thus, the term $\frac{\phi_{jk}^2}{4\lambda}$ is negligible for all j and k. Eq. 1.6 thus simplifies to

$$\begin{aligned} k &= \int dR \int dr \sum_j \sum_k a_{jk} \exp\left[-\beta\left(\frac{\lambda}{4}+\frac{\phi_{jk}}{2}\right)\right] \exp[-\beta w_{\mathrm{r}}] \\ &= \int dR \int dr \left[P_j |V_{jk}|^2 \exp\left[-\beta\left(\frac{\Delta\lambda_{jk}+\epsilon_k-\epsilon_j}{2}\right)\right]\right] \\ &\quad \times \sqrt{\frac{\pi}{\lambda k_{\mathrm{B}} T \hbar^2}} \exp\left[-\beta\left(\frac{\lambda}{4}+\frac{\Delta G^o}{2}\right)\right] \exp[-\beta w_{\mathrm{r}}], \end{aligned} \tag{1.7}$$

where the last line was arrived by substituting the expressions for a_{jk} and ϕ_{jk}.

The final simplifications of the rate expression are derived by considering the dependence of the constituent terms on the electron and proton donor-acceptor distances, R and r. For values of R that are sufficiently small that the TEMPOH-complex hydrogen bond is formed, the probability distributions for r and R are statistically uncorrelated (as will be explicitly shown in Section 1.4.5). This lack of correlation, which will be invoked several times in the remainder of this subsection, follows from the fact that low-energy motions associated with changes in R, such as bending of the phenylene linker domain and rotations of the TEMPOH molecule about the hydrogen bond, can occur without changes in r. Contributions to the CPET rate from configurations associated with larger values of R, for which the inter-complex hydrogen bond is dissociated, are negligible because they are thermally inaccessible in the preorganized reactant complex (i.e., the $e^{-\beta w_{\mathrm{r}}}$ term becomes relatively small in Eq. 1.6) and because the vibronic coupling becomes vanishingly small.

The terms P_j, $\Delta\lambda_{jk}$, ϵ_k, and ϵ_j are dependent upon the vibrational state of the transferring proton and are thus sensitive to the features of the hydrogen-bonding interface between $\mathbf{Fe^{III}Ph_nCO_2^-}$ and TEMPOH. The r-dependence of these terms is therefore included in this analysis. However, since changes in R do not significantly impact the hydrogen-bonding interface, these terms are assumed to be independent of R.

As in previous studies, the dependence of λ on r is neglected.[14] This follows from the fact that fluctuations in r lead to relatively small changes in the charge distributions for either the reactant or product complexes. However, the dependence of λ on R is explicitly included.

The preorganization work, w_{r}, accounts for both the work (along R) to bring the reacting species from infinite separation to a hydrogen-bonded configuration and the work (along r) necessary to compress the hydrogen bond to configurations that facilitate proton transfer. We thus explicitly include the dependence of both r and R in this term. Again using that the probability distributions

for r and R are statistically uncorrelated for configurations that contribute to the CPET rate, it follows that the joint probability distribution factorizes,

$$\rho(r, R) = \rho(r)\rho(R), \tag{1.8}$$

such that the potential of mean force associated with these coordinates is additive,

$$w_{\mathrm{r}}(r, R) = w_{\mathrm{r}}(R) + w_{\mathrm{r}}(r). \tag{1.9}$$

A similar argument holds for the preorganization work for the products, $w_{\mathrm{p}}(r, R)$.

The driving force ,$\Delta G^o(r, R)$, for the CPET reaction at a particular value of r and R is given by[15–17]

$$\Delta G^o(r, R) = \Delta G^o_{\mathrm{CPET}} + w_{\mathrm{p}}(r, R) - w_{\mathrm{r}}(r, R), \tag{1.10}$$

where $\Delta G^o_{\mathrm{CPET}}$ is the driving force at infinite separation with respect to either r or R. The preceding analysis of $w_{\mathrm{r}}(r, R)$ and $w_{\mathrm{p}}(r, R)$ thus leads to an additive expression for the driving force,

$$\Delta G^o(r, R) = \Delta G^o(r) + \Delta G^o(R). \tag{1.11}$$

Lastly, note that in the regime of weak electronic coupling ($H_{\mathrm{AB}} \ll k_{\mathrm{B}}T$), the CPET vibronic coupling takes the form[4–6]

$$V_{jk}(r, R) = \langle j|H_{\mathrm{AB}}(r, R)|k\rangle, \tag{1.12}$$

where $H_{\mathrm{AB}}(r, R)$ is the electronic coupling matrix element, and $|j\rangle$ and $|k\rangle$ are the reactant and product vibrational wavefunctions, respectively. We then employ the standard Condon approximation that the electronic coupling is insensitive to changes in the proton position over the lengthscale of the proton vibrational wavefunctions, such that $H_{\mathrm{AB}}(r, R) = H_{\mathrm{AB}}(R)$, and[18–20]

$$V_{jk}(r, R) = H_{\mathrm{AB}}(R)\langle j|k\rangle(r). \tag{1.13}$$

Here, $\langle j|k\rangle(r)$ is the overlap between the reactant and product vibrational wavefunctions, which still strongly depends on r, and the electronic coupling preserves its dependence on R.

Including these results into Eq. 1.6 and separating the $r-$ and $R-$dependent terms yields

$$\begin{aligned} k &= \int dr \left[\sum_j \sum_k P_j(r) \, |\langle j|k\rangle(r)|^2 \, \exp\left[-\beta \left(\frac{\Delta\lambda_{jk}(r) + \epsilon_k(r) - \epsilon_j(r) + \Delta G^o(r)}{2} + w_{\mathrm{r}}(r) \right) \right] \right] \\ &\quad \times \int dR |H_{\mathrm{AB}}(R)|^2 \sqrt{\frac{\pi}{\lambda(R) k_{\mathrm{B}} T \hbar^2}} \exp\left[-\beta \left(\frac{\lambda(R)}{4} + \frac{\Delta G^o(R)}{2} \right) \right] \exp[-\beta w_{\mathrm{r}}(R)] \\ &= \gamma \int dR |H_{\mathrm{AB}}(R)|^2 \sqrt{\frac{\pi}{\lambda(R) k_{\mathrm{B}} T \hbar^2}} \exp\left[-\beta \left(\frac{\lambda(R)}{4} + \frac{\Delta G^o(R)}{2} \right) \right] \exp[-\beta w_{\mathrm{r}}(R)], \end{aligned} \tag{1.14}$$

where the γ term in the last line contains all the $r-$dependent terms.

The analysis presented in this subsection employs approximations that are standard in the characterization of the CPET reactions. The only novel aspect of this analysis is utilization of the fact that the r and R coordinates are statistically uncorrelated for configurations that contribute to the CPET rate, which is numerically demonstrated in Section 1.4.5.

1.3.2 Derivation of the CPET rate ratio

In the vibronically nonadiabatic regime, $H_{\mathrm{AB}}(R)$ varies exponentially with the electron donor-acceptor distance[15–17]

$$H_{\mathrm{AB}}(R) = H^o_{\mathrm{AB}} \left(-\frac{1}{2} \beta (R - R^o) \right), \tag{1.15}$$

where H^o_{AB} is the coupling matrix element at a reference donor-acceptor distance R^o, and β is the associate decay constant. Using this expression together with Eq. 1.10 and Eq.1.14, the experimentally observable ratio of the CPET rates for the complexes with $n = 1$ and $n = 2$ phenylene linkers is derived to be

$$\frac{k^{(1)}}{k^{(2)}} = e^{-\frac{1}{2k_{\mathrm{B}}T} \Delta\Delta G^o} \frac{\int dR f^{(1)}}{\int dR f^{(2)}}, \tag{1.16}$$

where

$$f^{(n)} = \sqrt{\frac{1}{\lambda^{(n)}(R)}} e^{-\beta R} e^{-\frac{1}{4k_{\mathrm{B}}T} \left(\lambda^{(n)}(R) + 2w_{\mathrm{p}}^{(n)}(R) + 2w_{\mathrm{r}}^{(n)}(R) \right)} \tag{1.17}$$

and

$$\Delta\Delta G^o = \Delta G^{o(1)}_{\mathrm{CPET}} - \Delta G^{o(2)}_{\mathrm{CPET}}. \tag{1.18}$$

1.4 Calculation of the components of the decay constant β

The decay constant β can be obtained by numerical solution of Eq. 1.16 using the experimentally observed rates in Section 1.2. This requires calculation of the terms $w_{\mathrm{r}}(R)$, $w_{\mathrm{p}}(R)$, $\Delta\Delta G^o$, and

$\lambda(R)$. These terms are calculated using a mixture of molecular dynamics and electronic structure techniques, which are described in detail in this section. The computational model employed is presented in Section 1.4.1. The subsequent sections describe the calculation of the individual terms appearing in the CPET rate equation: Section 1.4.2 describes the calculation of the preorganization work terms, Section 1.4.3 describes the calculation of the inner- and outer-sphere reorganization energies, and Section 1.4.4 describes the calculation of the driving forces. The force field parameters of the computational model and optimized molecular geometries are presented in Appendices A and B to this chapter.

1.4.1 Description of the MD simulations

MD simulations of the PCET reactants employ a system comprised of $\mathbf{Fe^{III}PhCO_2^-}$, $\mathbf{Fe^{III}Ph_2CO_2^-}$, and a single TEMPOH molecule; simulations of the products employ a system comprised of $\mathbf{Fe^{II}PhCO_2H}$, $\mathbf{Fe^{II}Ph_2CO_2H}$, and a single TEMPO molecule. In both cases, the system also includes 2225 acetonitrile molecules. The simulation is performed in a 46.8 Å$\times$ 91.2 Å$\times$ 46.8 Å rectangular unit cell that is subject to periodic boundary conditions.

The porphyrin molecules, axial ligands, and TEMPOH/TEMPO molecules are modeled using the Generalized Amber Force Field (GAFF),[21] which is implemented within the DLPOLY molecular dynamics package.[22] The iron atom in both oxidation states is modeled using the Giammona parameters, which are included as the frcmod.hemall contributed parameter set for AMBER.[23] Atom-type assignment (Tables 1.2-1.4) is performed using the Antechamber program.[24] Acetonitrile molecules are represented with the three-site model of Guardia et al.,[25] in which the methyl group is represented as a single particle. In all calculations, the N-methylimidazole axial ligands are replaced by imidazole ligands.

In all MD simulations, short-range interactions are truncated at $r_{\text{cut}} = 12$Å, and force-shifting[26] is employed for the truncation of long-range electrostatic interactions. Trajectories are thermostatted at a temperature of 298 K by resampling all atomic velocities from the Boltzmann distribution every 50 ps, and a timestep of 0.25 fs is employed to ensure accurate integration of the bond-stretching modes.

The charge distributions on the iron porphyrin complexes and the TEMPO/TEMPOH molecules are determined using density functional theory (DFT) calculations, performed using Gaussian 09 (version G09RevB.01).[27] For each species, the molecular geometry is optimized at the B3LYP/ 6-31G(d,p) level of theory. Solvation effects in these DFT calculations are included using the integral

equation formalism of the polarizable continuum model,[28,29] with the default parameter values of the implementation in Gaussian 09.[30] The solute cavity is assembled from atom-centered spheres with radii corresponding to the atomic radii in the Universal Force Field (UFF) scaled by 1.1. The cavity surface is smoothly represented using the GePol-YK scheme,[31] and the acetonitrile static and optical dielectric constants have values of $\epsilon_o = 35.688$ and $\epsilon_\infty = 1.806874$, respectively. Atomic point charges (Tables 1.2-1.4) are determined by fitting the electrostatic potential from the electronic structure calculations using CHelpG (CHarges from Electrostatic Potentials using a Grid based method);[32] the charges for all atoms of the same atom-type are set to the mean value obtained from the CHelpG calculation.

In all MD simulations, the TEMPOH and TEMPO molecules are kept rigid at geometries that are optimized at the B3LYP/6-31G(d,p) level of theory; both molecules are most stable in the chair conformation with the oxygen atom in the equatorial position, and the OH torsion in TEMPOH assumes the anti conformation with respect to the axial methyl groups. The metalated porphyrin ring, the meso substituents, and the axial ligands are also held rigid at the optimal geometry obtained at the B3LYP/6-31G(d,p) level, while the phenylene linker regions are left unrestrained. The NOSQUISH algorithm[33] is employed to integrate the rigid-body equations of motion in the MD simulations. The optimized molecular geometries of TEMPO, TEMPOH, $\mathbf{Fe^{III}PhCO_2^-}$, $\mathbf{Fe^{II}PhCO_2H}$, $\mathbf{Fe^{III}Ph_2CO_2^-}$, and $\mathbf{Fe^{II}Ph_2CO_2H}$, are included in Tables 1.2-1.4.

1.4.2 Calculation of $w_{\mathrm{r}}^{(n)}(R)$ and $w_{\mathrm{p}}^{(n)}(R)$

This section describes the MD simulations that are used to calculate the reactant and product free energy profiles as a function of the electron donor-acceptor distance, $w_{\mathrm{r}}^{(n)}(R)$ and $w_{\mathrm{p}}^{(n)}(R)$, respectively. To robustly and efficiently obtain the relative free-energy profiles for the shorter ($n = 1$) phenylene linker relative to the corresponding profiles for the longer ($n = 2$) linker, some care must be taken in the design of the simulation protocol, as is now described.

Fig. 1.3 presents the simulation setup that is employed for the calculation of the reactant free energy profiles, $w_{\mathrm{r}}^{(1)}(R)$ and $w_{\mathrm{r}}^{(2)}(R)$. The $\mathbf{Fe^{III}PhCO_2^-}$ and $\mathbf{Fe^{III}Ph_2CO_2^-}$ molecules are arranged such that the distance between the iron centers is large (49.1 Å) and the linker region of each porphyrin is oriented toward the other along the y-axis (detailed geometries provided in Tables 1.12 and 1.13). The rigid portions of the iron-porphyrin molecules (i.e., the metalated porphyrin ring, the meso substituents, and the axial ligands) are kept fixed in absolute space during all MD simulations. An analogous simulation setup is used to compute the free-energy profiles for the product species

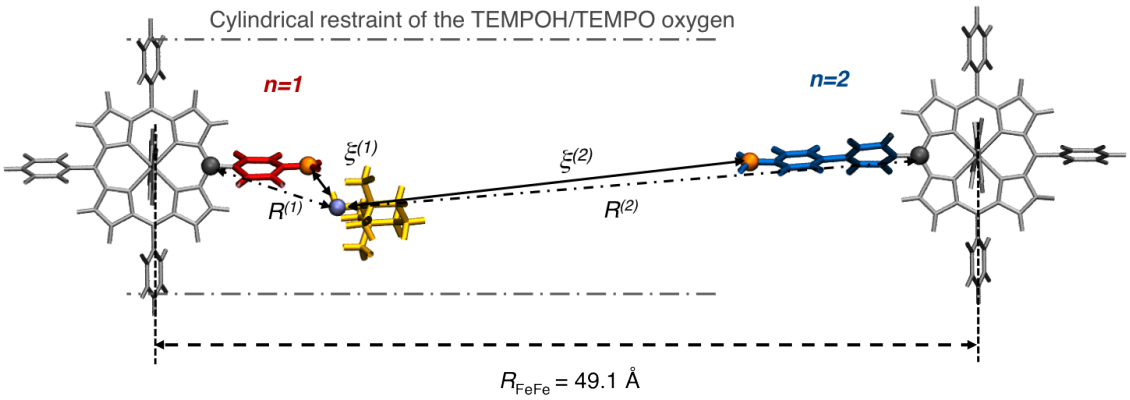

Figure 1.3: The system employed in molecular dynamics calculation of $w_{\mathrm{r}}^{(n)}(R)$. Fixed regions of the porphyrin molecules are indicated in gray, the flexible linker region of $\mathbf{Fe^{III}PhCO_2^-}$ is indicated in red, and the flexible linker region of $\mathbf{Fe^{III}Ph_2CO_2^-}$ is indicated in blue. The rigid TEMPOH molecule is yellow, and the TEMPOH oxygen atom is indicated in purple. The porphyrin 5-carbon atoms defining the $R^{(1)}$ and $R^{(2)}$ distances (see text) are indicated with gray spheres, and the carboxylic carbons defining the $\xi^{(1)}$ and $\xi^{(2)}$ distances are indicated with orange spheres. MeCN molecules are omitted for clarity. The region of the application of cylindrical restraint $V_{\mathrm{cyl}}(d)$ is indicated with gray dashed-dot lines.

(detailed geometries provided in Tables 1.14 and 1.15).

To compute the reactant free energy profiles, we begin by defining collective variables associated with the electron donor-acceptor distance for the $n = 1$ and $n = 2$ complexes in the simulation setup. Specifically, $R^{(1)}$ and $R^{(2)}$ denote the Euclidean distance between the TEMPOH oxygen and the 5-carbon of the porphyrin ring of $\mathbf{Fe^{III}PhCO_2^-}$ or $\mathbf{Fe^{III}Ph_2CO_2^-}$, respectively (Fig. 1.3). We then define $\Delta R = R^{(1)} - R^{(2)}$ and $R = \min(R^{(1)}, R^{(2)})$ in terms of these simple donor-acceptor distances. It is clear that any atomistic configuration for the system corresponds to a particular value for the collective variables ΔR and R. Furthermore, it is clear that the collective variables distinguish between configurations for which the system occupies the basin of stability for the $n = 1$ complex (small R, negative ΔR), for which the system occupies the basin of stability for the $n = 2$ complex (small R, positive ΔR), and for which the system is transferring between these two basins of stability (larger R, $\Delta R \approx 0$).

By sampling the full probability distribution in these two coordinates, $P_{\mathrm{r}}(\Delta R, R)$, we have a direct means of comparing the relative free energies of these two basins of stability (i.e., the difference of the reversible work of association for the $n = 1$ and $n = 2$ TEMPOH-$\mathbf{Fe^{III}Ph_nCO_2^-}$ complexes). Specifically, this relative free energy can be evaluated using

$$-k_{\mathrm{B}}T \ln \int_{-\infty}^{c} d\Delta R \int_{0}^{\infty} dR P_{\mathrm{r}}(\Delta R, R) + k_{\mathrm{B}}T \ln \int_{c}^{\infty} d\Delta R \int_{0}^{\infty} dR P_{\mathrm{r}}(\Delta R, R), \tag{1.19}$$

where $c \approx 0$ is the value of ΔR that is used to distinguish between the two basins of stability. We can also reduce the probability distribution $P_{\mathrm{r}}(\Delta R, R)$ over the configurations associated with $\Delta R < c$ to obtain the reversible work associated with the electron donor-acceptor distance for the $n = 1$ complex,

$$w_{\mathrm{r}}^{(1)}(R) = -k_{\mathrm{B}}T \ln \int_{-\infty}^{c} d\Delta R P_{\mathrm{r}}(\Delta R, R) \tag{1.20}$$

and we can likewise reduce the probability distribution over the configurations associated with $\Delta R > c$ to obtain the reversible work associated with the electron donor-acceptor distance for the $n = 2$ complex,

$$w_{\mathrm{r}}^{(2)}(R) = -k_{\mathrm{B}}T \ln \int_{c}^{\infty} d\Delta R P_{\mathrm{r}}(\Delta R, R) \tag{1.21}$$

The advantage of this approach is that we have avoided any arbitrary shift between the curves $w_{\mathrm{r}}^{(1)}(R)$ and $w_{\mathrm{r}}^{(2)}(R)$, since both curves are obtained from the same full probability distribution $P_{\mathrm{r}}(\Delta R, R)$. That is, the relative energy of these two curves can be directly compared.

In practice, the MD sampling of $P_{\mathrm{r}}(\Delta R, R)$ involves slow timescales that are difficult to converge, and it is more convenient to sample the three-dimensional probability distribution $P_{\mathrm{r}}(\Delta\xi, \xi, R)$. Here, $R = \min(R^{(1)}, R^{(2)})$ as before, $\Delta\xi = \xi^{(1)} - \xi^{(2)}$, and $\xi = \min(\xi^{(1)}, \xi^{(2)})$. The collective variables $\xi^{(1)}$ and $\xi^{(2)}$ denote the distance between the TEMPOH oxygen and the carboxylic carbon of $\mathbf{Fe^{III}PhCO_2^-}$or $\mathbf{Fe^{III}Ph_2CO_2^-}$, respectively (Fig. 1.3). We then reduce this three-dimensional distribution to recover the reversible work profiles,

$$w_{\mathrm{r}}^{(1)}(R) = -k_{\mathrm{B}}T \ln \int_{-\infty}^{c} d\Delta\xi \int_{0}^{\infty} d\xi P_{\mathrm{r}}(\Delta\xi, \xi, R) = -k_{\mathrm{B}}T \ln \int_{-\infty}^{c} d\Delta\xi P_{\mathrm{r}}(\Delta\xi, R) \tag{1.22}$$

and

$$w_{\mathrm{r}}^{(2)}(R) = -k_{\mathrm{B}}T \ln \int_{c}^{\infty} d\Delta\xi \int_{0}^{\infty} d\xi P_{\mathrm{r}}(\Delta\xi, \xi, R) = -k_{\mathrm{B}}T \ln \int_{c}^{\infty} d\Delta\xi P_{\mathrm{r}}(\Delta\xi, R) \tag{1.23}$$

Computation of the three-dimensional probability distribution, $P_{\mathrm{r}}(\Delta\xi, \xi, R)$, is performed using umbrella sampling and the weighted histogram analysis method (WHAM).[34,35] Two-dimensional umbrella sampling is performed with respect to coordinates $\Delta\xi$ and ξ; this consists of 73 independent MD trajectories in the region $\Delta\xi = [-18\text{Å}, 18\text{Å}]$ that are harmonically restrained to uniformly spaced values of $\Delta\xi$, using a restraint force constant of 2.0 kcal/mol/Å^2. Furthermore, the regions of $\xi^{(1)} = [4\text{Å}, 7\text{Å}]$ and $\xi^{(2)} = [4\text{Å}, 7\text{Å}]$ are each sampled with 7 additional simulations restrained to values of ξ spaced every 0.5 Å, using a restraint force constant of 8.0 kcal/mol/Å^2. All umbrella-

sampling simulations are equilibrated for 0.5 ns prior to a 5 ns production run. The $\Delta\xi$, ξ, and R coordinates of the system are then sampled every 500 fs.

To confine the TEMPOH molecule to the vicinity of the iron-porphyrin molecules in the umbrella sampling trajectories, the physical potential energy function is modified to include the cylindrically symmetric term

$$V_{\mathrm{cyl}}(d) = \begin{cases} 0.5k(d - r_{\mathrm{cyl}})^2, & d \geq r_{\mathrm{cyl}} \\ 0, & d < r_{\mathrm{cyl}}, \end{cases} \tag{1.24}$$

where $d = \sqrt{(x_{\mathrm{O}} - x_{\mathrm{C}})^2 + (z_{\mathrm{O}} - z_{\mathrm{C}})^2}$, x_{O} and z_{O} are, respectively, the $x-$ and $z-$coordinates of the TEMPOH oxygen atom, x_{C} and z_{C} are, respectively, the $x-$ and $z-$coordinates of the 5-carbons of the porphyrin rings, $k = 1.0$ kcal/mol/Å^2, and $r_{\mathrm{cyl}} = 8.0$ Å. This term restricts the accessible configuration space of the TEMPOH molecule with respect to the fixed axis that separates the two iron-porphyrin molecules; all other molecules in the system, including the solvent molecules, are unaffected. The parameter r_{cyl} is chosen to be sufficiently large to avoid any biases in the distribution of configurations for which TEMPOH is hydrogen bonded to the iron-porphyrin molecules.

The product free-energy profiles, $w_{\mathrm{p}}^{(1)}(R)$ and $w_{\mathrm{p}}^{(2)}(R)$ are computed using the same approach that is described above for the reactant species. The MD simulations on the product species likewise include the restraining potential in Eq. 1.26 with distances defined in terms of the TEMPO (as opposed to the TEMPOH) oxygen atom. However, to be consistent with the fact that the reactant free-energy profile is obtained with TEMPOH held rigid in its more stable anti conformation of the OH torsion, an additional restraining potential is included in the calculation of the product free-energy profile to enforce the anti conformation of the TEMPO-$\mathbf{Fe^{II}Ph_nCO_2H}$ hydrogen bond. This additional restraining potential is given by

$$V(\phi, r_{\mathrm{OH}}) = V_{\mathrm{dih}}(\phi) S(r_{\mathrm{OH}}), \tag{1.25}$$

where $V_{\mathrm{dih}}(\phi)$ is a piecewise torsional potential

$$V_{\mathrm{dih}}(\phi) = \begin{cases} 0, & \phi_0 - \Delta\phi < \phi < \phi_0 + \Delta\phi \\ 0.5k_\phi \left(\phi - (\phi_0 + \Delta\phi)\right)^2, & \phi > \phi_0 + \Delta\phi \\ 0.5k_\phi \left(\phi - (\phi_0 - \Delta\phi)\right)^2, & \phi < \phi_0 - \Delta\phi \end{cases} \tag{1.26}$$

and $S(r_{\mathrm{OH}})$ is the sigmoid function

$$S(r_{\mathrm{OH}}) = 0.5\left(1 + \mathrm{erf}\left(2.0\left(-r_{\mathrm{OH}} + 3.0\right)\right)\right). \tag{1.27}$$

Here, ϕ is the dihedral angle formed by the TC1, TN, and OC atoms of the TEMPO molecule and the HT atom of the nearest carboxylic acid, and r_{OH} is the distance between the OC atom and the HT atom. This restraint thus applies when TEMPO is hydrogen-bound to the carboxylic acid moiety of $\mathbf{Fe^{II}PhCO_2H}$ or $\mathbf{Fe^{II}Ph_2CO_2H}$, and it does not bias the simulation when TEMPO is free in solution. We use parameters $\Delta\phi = 1.5$ rad, $\phi_0 = 1.5$ rad, and $k_\phi = 3.0$ kcal/mol/rad^2.

Figure 1.4A presents the free energy surface associated with the reduced two-dimensional probability distribution for the reactant species, $-k_{\mathrm{B}}T \ln P_{\mathrm{r}}(\Delta\xi, R)$ (see Eqs. 1.22 and 1.23). The free energy surface is characterized by two pronounced basins of stability; the basin at ($\Delta\xi \approx -20$Å, $R \approx 8$Å) corresponds to the $n = 1$ complex in which TEMPOH is bound to the $\mathbf{Fe^{III}PhCO_2^-}$ molecule, and the basin at ($\Delta\xi \approx 20$Å, $R \approx 12\mathring{A}$) corresponds to the $n = 2$ complex in which TEMPOH is bound to the $\mathbf{Fe^{III}Ph_2CO_2^-}$ molecule. The intermediate, featureless region for which $-20\text{Å} < \Delta\xi < 20\text{Å}$ corresponds to configurations for which the TEMPOH is not directly bound to either iron-porphyrin molecule. Figure 1.4B presents the free energy surface associated with the reduced two-dimensional probability distribution for the product species,$-k_{\mathrm{B}}T \ln P_{\mathrm{p}}(\Delta\xi, R)$, which also shows basins associated with the $n = 1$ and $n = 2$ complexes.

Figure 1.4C presents the one-dimensional free energy surfaces for the reactant species as a function of the electron donor-acceptor distance, $w_{\mathrm{r}}^{(1)}(R)$ and $w_{\mathrm{r}}^{(2)}(R)$, obtained by reducing the two-dimensional results in Figure 1.4A according to Eqs. 1.22 and 1.23. In these calculations, we use the parameter $c = 0$ Å to separate the $n = 1$ and $n = 2$ basins of stability; the plotted results were found to be unchanged with the alternative choices of $c = 1$ Å or 3 Å, indicating that the $n = 1$ and $n = 2$ basins of stability are well separated in the $\Delta\xi$ coordinate. Each curve in Fig. 1.4C shows a single wide basin associated with the conformations of hydrogen-bound complex between TEMPOH the iron-porphyrin molecule. As expected from the presence of the additional phenylene linker, TEMPOH binds at larger values of R in the TEMPOH-$\mathbf{Fe^{III}Ph_2CO_2^-}$ complex than in the TEMPOH-$\mathbf{Fe^{III}PhCO_2^-}$ complex. Furthermore, TEMPOH-$\mathbf{Fe^{III}Ph_2CO_2^-}$ is more stable than TEMPOH-$\mathbf{Fe^{III}PhCO_2^-}$, with a free energy difference of 0.3 kcal/mol at the minimum of the basin. By considering the pairwise interaction energies between TEMPOH, the iron porphyrin molecule, and the acetonitrile solvent, we find that the hydrogen-bonded TEMPOH-$\mathbf{Fe^{III}Ph_2CO_2^-}$ complex is more favorably solvated than the TEMPOH-$\mathbf{Fe^{III}PhCO_2^-}$ complex relative to the separated TEM-

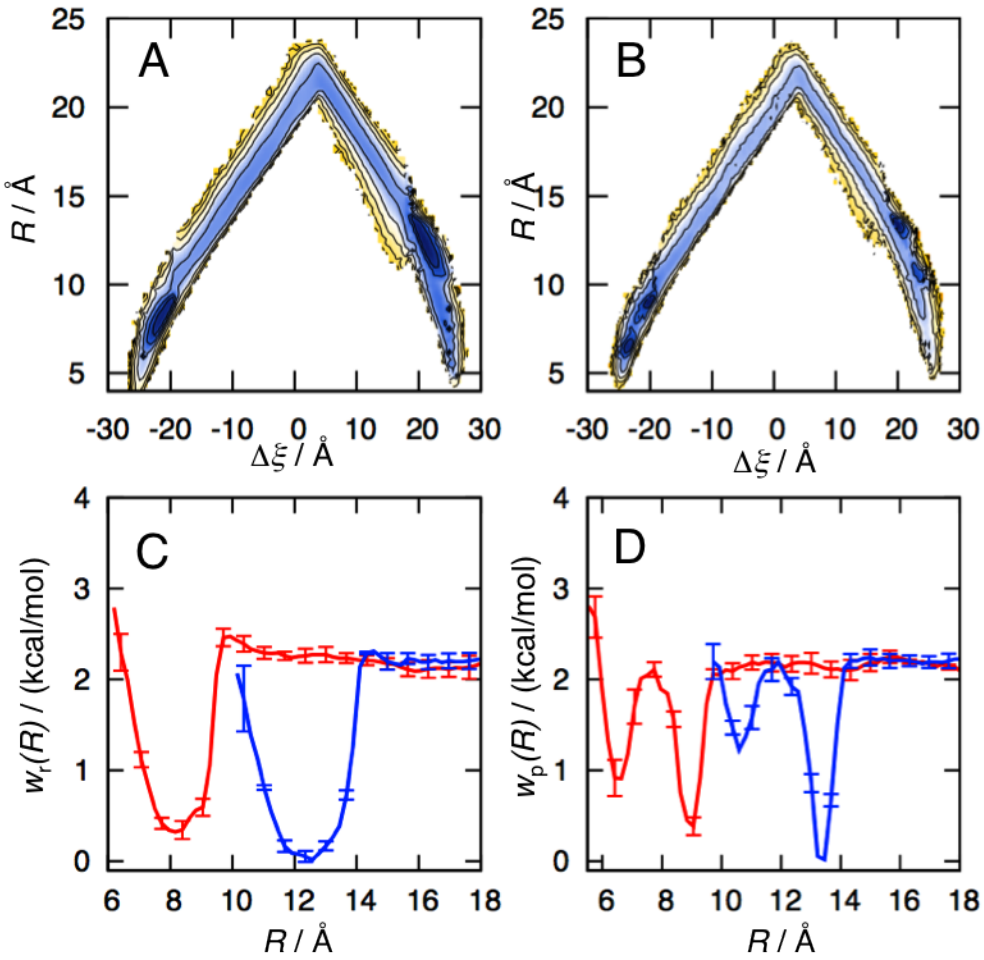

Figure 1.4: Free energy surfaces obtained using MD simulations. **(A)** The two-dimensional reactant free energy surface, $-k_{\mathrm{B}}T \ln P_{\mathrm{r}}(\Delta\xi, R)$. **(B)** The two-dimensional product free energy surface, $-k_{\mathrm{B}}T \ln P_{\mathrm{p}}(\Delta\xi, R)$. In panels A and B, the contour lines denote increments of 1 kcal/mol. **(C)** The reactant free energy profiles, $w_{\mathrm{r}}^{(n)}(R)$, for the $n = 1$ (red) and $n = 2$ (blue) complexes as a function of the electron donor-acceptor distance. **(D)** The product free energy profiles, $w_{\mathrm{p}}^{(n)}(R)$, for the $n = 1$ (red) and $n = 2$ (blue) complexes as a function of the electron donor-acceptor distance. The structures in panel D illustrate configurations of the TEMPO associated with different orientations of the carboxylic acid OH bond.

POH and $\mathbf{Fe^{III}Ph_nCO_2^-}$ molecules.

Figure 1.4D similarly presents the one-dimensional free energy surfaces for the product species as a function of the electron donor-acceptor distance, $w_{\mathrm{p}}^{(1)}(R)$ and $w_{\mathrm{p}}^{(1)}(R)$, obtained by reducing the two-dimensional results in Figure 1.4B. As is the case with the reactant species, the complex with the longer linker, TEMPO-$\mathbf{Fe^{II}Ph_2CO_2H}$ is more stable by approximately 0.3 kcal/mol and favors longer electron donor-acceptor distances than the TEMPO-$\mathbf{Fe^{II}PhCO_2H}$ complex. However, unlike the single, wide basin observed in the $w_{\mathrm{r}}^{(n)}(R)$ profiles, both $w_{\mathrm{p}}^{(1)}(R)$ and $w_{\mathrm{p}}^{(2)}(R)$ exhibit two narrow basins separated by approximately 3 Å. These additional features in the product free energy profiles

are due to the torsional potential associated with rotation of the carboxylic acid OH bond, which exhibits local minima in configurations for which the acidic proton lies in the plane of the other of carboxylate atoms. As a result of this torsional potential, the acidic proton can either point away from the linker into solution, or it can point back towards the linker. The TEMPO molecule, which forms a hydrogen bond with the acidic proton, thus adopts two orientations that are characterized by differing values of the electron donor-acceptor distances. We illustrate these orientations in the inset of Figure 1.4D.

1.4.3 Calculation of the CPET reorganization energies

1.4.3.1 Calculation of λ_{i}

The inner-sphere CPET reorganization energies, $\lambda_{\mathrm{i}}^{(n)}$, are computed as the sum of individual contributions from the iron-porphyrin complex and TEMPOH,[36,37]

$$\lambda_{\mathrm{i}}^{(n)} = \lambda_{\mathrm{i,FePor}}^{(n)} + \lambda_{\mathrm{i,TEMPOH}} \tag{1.28}$$

The inner-sphere reorganization of the iron-porphyrin complex is calculated using[38,39]

$$\lambda_{\mathrm{i,FePor}}^{(n)} = E\left(\mathrm{Fe^{II}Ph_nCO_2H|Fe^{III}Ph_nCO_2^-}\right) - E\left(\mathrm{Fe^{II}Ph_nCO_2H|Fe^{II}Ph_nCO_2H}\right), \tag{1.29}$$

where $E\,(\mathrm{A|B})$denotes the energy of species A at the optimized geometry of species B. (In the calculation of $E\left(\mathrm{Fe^{II}Ph_nCO_2H|Fe^{III}Ph_nCO_2^-}\right)$, the position of the additional proton is optimized while keeping all other atoms fixed.) The corresponding term for TEMPOH is calculated using

$$\lambda_{\mathrm{i,TEMPOH}} = E\,(\mathrm{TEMPO|TEMPOH}) - E\,(\mathrm{TEMPO|TEMPO})\,. \tag{1.30}$$

By treating these contributions separately, we make the usual assumption that the inner-sphere reorganization energies are unaffected by preorganization of the CPET donor and acceptor species. In all cases, the geometry optimizations are performed at the B3LYP/6-31G(d,p) level of theory, with solvation effects included via the polarizable continuum model using the default parameters for Gaussian 09 (version G09RevB.01); final energies are computed using B3LYP/TZVP without implicit solvent effects.

These calculations yield $\lambda_{\mathrm{i,TEMPOH}} = 16.74$ kcal/mol, $\lambda_{\mathrm{i,FePor}}^{(1)} = 8.21$ kcal/mol, and $\lambda_{\mathrm{i,FePor}}^{(2)} = 8.37$ kcal/mol. The majority of the reorganization energy for the porphyrin molecules arises from

the structural rearrangement of the acid moiety upon protonation, with the rearrangements in the porphyrin ring and its substituents contributing only approximately 1 kcal/mol; this is confirmed by repeating the calculation of $E\left(\mathrm{Fe^{II}Ph_nCO_2H|Fe^{III}Ph_nCO_2^-}\right)$ while fixing the position of atoms other than the carboxylic acid moiety. The small inner-sphere reorganization energy for the porphyrin obtained here is consistent with previous studies of model heme compounds, where the total inner-sphere reorganization energy in a self-exchange ET reaction between $\mathrm{Fe^{III}(porphine)(Im)_2}$ and $\mathrm{Fe^{II}(porphine)(Im)_2^-}$ was shown to be only 1.95 kcal/mol.[40] Similarly, the insensitivity of $\lambda_{\mathrm{i,FePor}}^{(n)}$ to number of phenylene linkers is consistent with earlier computational studies of unmetalated N-methylmesoporphyrin, in which the structure of the porphyrin macrocycle was shown to be largely independent of the side chains decorating the ring.[41]

1.4.3.2 Calculation of $\lambda_{\mathrm{o}}(R)$ using all-atom MD simulations

The outer-sphere CPET reorganization energy, $\lambda_{\mathrm{o}}^{(n)}(R)$, is calculated using the MD simulation model described in Sections 1.4.1 and 1.4.2. For a given electron donor-acceptor distance R, the reorganization energy is obtained using[42–44]

$$\lambda_{\mathrm{o}}^{(n)}(R) = \frac{1}{2}\left(\langle\Delta U^{(n)}\rangle_{\mathrm{r}}(R) - \langle\Delta U^{(n)}\rangle_{\mathrm{p}}(R)\right), \tag{1.31}$$

where

$$\langle\Delta U^{(n)}\rangle_{\mu}(R) = Z_R^{-1}\int d\mathbf{x} e^{-\frac{U_\mu(\mathbf{x})}{k_{\mathrm{B}}T}}\delta\left(R(\mathbf{x}) - R\right)\Delta U^{(n)}(\mathbf{x}), \tag{1.32}$$

$$Z_R = \int d\mathbf{x} e^{-\frac{U_\mu(\mathbf{x})}{k_{\mathrm{B}}T}}\delta\left(R(\mathbf{x}) - R\right), \tag{1.33}$$

and

$$\Delta U^{(n)}(\mathbf{x}) = U_{\mathrm{p}}^{(n)}(\mathbf{x}) - U_{\mathrm{r}}^{(n)}(\mathbf{x}). \tag{1.34}$$

Here, $\mathbf{x}$ denotes the configuration of the solute and solvent, $U_\mu(\mathbf{x})$ is the total potential energy function for the system in the reactant (μ = r) or product (μ = p) state, and $U_\mu^{(n)}(\mathbf{x})$ denotes the subset of pairwise interactions between the acetonitrile solvent and the solute complex with n phenylene linkers. Equations 1.31-1.34 are the R-resolved versions of the usual expressions for the outer-sphere reorganization energy, obtained by assuming that the linear response of the solvent holds for each value of the electron donor-acceptor distance, R. We additionally calculate the outer-

sphere reorganization energy without resolving the dependence on R using

$$\lambda_{\mathrm{o}}^{(n)} = \frac{1}{2}\left(\langle \Delta U^{(n)} \rangle_{\mathrm{r}} - \langle \Delta U^{(n)} \rangle_{\mathrm{p}}\right), \tag{1.35}$$

and

$$\langle \Delta U^{(n)} \rangle_{\mu} = Z^{-1} \int d\mathbf{x} e^{-\frac{U_{\mu}(\mathbf{x})}{k_{\mathrm{B}}T}} \Delta U^{(n)}(\mathbf{x}). \tag{1.36}$$

In the calculation of $\Delta U^{(n)}(\mathbf{x})$, the energy functions are evaluated at reactant and product geometries that are identical, except for the position of the transferring proton (HT). In the calculation of $\langle \Delta U^{(n)} \rangle_{\mathrm{r}}(R)$, the position of HT in the product state (needed for the $U_{\mathrm{p}}^{(n)}(\mathbf{x})$ term) is obtained via reflection of its position in the reactant state through the plane that perpendicularly bisects the segment between the TEMPOH oxygen (OC, the proton donor) and the acidic carboxylate oxygen (OA, the proton acceptor). For the calculation of $\langle \Delta U^{(n)} \rangle_{\mathrm{p}}(R)$, the reverse operation is performed to obtain the position of HT in the reactant state.

For the calculation of $\lambda_{\mathrm{o}}^{(1)}(R)$, the equilibrium ensemble for the reactant state is sampled using 1200 uncorrelated snapshots from an unrestrained, 6 ns NVT simulation of the system in the basin of stability for which TEMPOH is hydrogen-bonded to $\mathbf{Fe^{III}PhCO_2^-}$; the equilibrium ensemble for the product state is sampled using 1000 uncorrelated snapshots from an unrestrained, 5 ns NVT simulation of the system in the basin of stability for which TEMPO occupying is hydrogen-bonded to $\mathbf{Fe^{II}PhCO_2H}$. Similarly, for the calculation of $\lambda_{\mathrm{o}}^{(2)}(R)$, the equilibrium ensemble for the reactant state is sampled using 1500 uncorrelated snapshots from an unrestrained, 7.5 ns NVT simulation of the TEMPOH-$\mathbf{Fe^{III}Ph_2CO_2^-}$ complex; the equilibrium ensemble for the product state is sampled using 1000 uncorrelated snapshots from an unrestrained, 5 ns NVT simulation of the TEMPO-$\mathbf{Fe^{II}Ph_2CO_2H}$ complex.

Figure 1.5 presents the computed CPET outer-sphere reorganization energies $\lambda_{\mathrm{o}}^{(1)}(R)$ and $\lambda_{\mathrm{o}}^{(2)}(R)$ as a function of the electron donor-acceptor distance. For a given number of phenylene linkers, the reorganization energy depends only weakly on R. It is also weakly sensitive to the number of linkers, n. If the R-dependence of the outer-sphere reorganization energy is not included (Eqs 1.35-1.36), we obtain $\lambda_{\mathrm{o}}^{(1)} = 17.6 \pm 0.1$ kcal/mol and $\lambda_{\mathrm{o}}^{(2)} = 18.9 \pm 0.1$ kcal/mol.

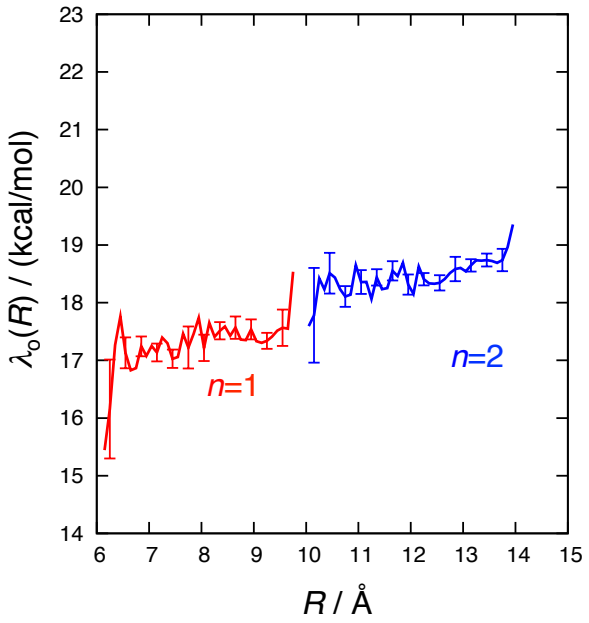

Figure 1.5: Outer-sphere CPET reorganization energies, $\lambda_{\mathrm{o}}^{(n)}(R)$, for the complexes with $n = 1$ (red) and $n = 2$ (blue) phenylene linkers, computing using all-atom MD simulations

1.4.3.3 Calculation of $\lambda_{\mathrm{o}}(R)$ using the frequency-resolved cavity model

For comparison, we also calculated the outer-sphere CPET reorganization energy using a dielectric continuum representation of the solvent. It is obtained using

$$\lambda_{\mathrm{o}}^{(n)}(R) = Z_R^{-1} \int d\mathbf{x} e^{-\frac{U_{\mathrm{T}}(\mathbf{x})}{k_{\mathrm{B}}T}} \delta\left(R(\mathbf{x}) - R\right) \Delta S^{(n)}(\mathbf{x}), \tag{1.37}$$

where

$$\Delta S^{(n)}(\mathbf{x}) = \frac{1}{2}\left[S_{\mathrm{pr}}^{(n)}(\mathbf{x}) - S_{\mathrm{pp}}^{(n)}(\mathbf{x}) + S_{\mathrm{rp}}^{(n)}(\mathbf{x}) - S_{\mathrm{rr}}^{(n)}(\mathbf{x})\right]. \tag{1.38}$$

Here, $S_{\mathrm{AB}}^{(n)}(\mathbf{x})$ denotes the interaction energy between the solute with the charge distribution for state A and the continuum solvent that is polarized in response to the charge distribution for state B. $S_{\mathrm{AB}}^{(n)}(\mathbf{x})$ is computed using the frequency-resolved cavity model (FRCM),[45,46] for which the solute is represented as a set of overlapping atom-centered spherical cavities with sizes that correspond to the optical and static components of the solvent response. The reported calculations employ standard FRCM parameters for acetonitrile, including the global scaling factor for the atomic van der Waals radii used in computation of the solvent optical response ($\kappa = 0.9$) and the solvent-specific additive factor for the atomic van der Waals radii used in computation of the solvent static response ($\delta = 1.8$

Å). The optical and static dielectric constants employed for the acetonitrile solvent are $\epsilon_0 = 37.5$ and $\epsilon_\infty = 1.79$, respectively. The FRCM calculations are performed using the webPCET software package.[47]

For the calculation of $\lambda_o^{(1)}(R)$, the solute configurations are obtained by taking 4000 uncorrelated configurations from an unrestrained, 8 ns simulation of the TEMPOH-$\mathbf{Fe^{III}PhCO_2^-}$ complex. Similarly, for $\lambda_o^{(2)}(R)$ complex, the solute configurations are obtained by taking 3000 uncorrelated configurations from an unrestrained, 6 ns simulation of the TEMPOH-$\mathbf{Fe^{III}Ph_2CO_2^-}$ complex. For each configuration, the reactant and product geometries are identical, except that the position of the transferring proton (HT), which is obtained as in Section 1.4.3.2. The charge distributions for the reactant and product state of both complexes are described in Appendix A.

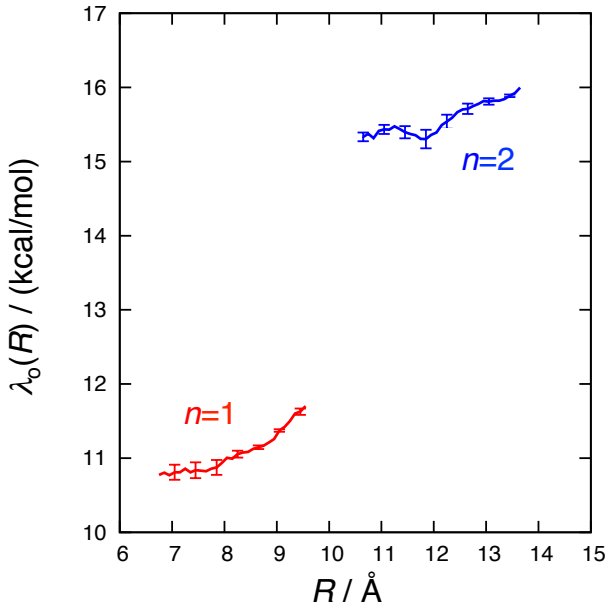

Figure 1.6: Outer-sphere CPET reorganization energies, $\lambda_{o^n}(R)$, for the complexes with $n = 1$ (red) and $n = 2$ (blue) phenylene linkers, computing using the FRCM.

Figure 1.6 presents the computed CPET outer-sphere reorganization energies $\lambda_o^{(1)}(R)$ and $\lambda_o^{(2)}(R)$ as a function of the electron donor-acceptor distance. For a given number of phenylene linkers, the reorganization energy depends relatively weakly on R. However, unlike the results obtained with explicit solvent (Fig. 1.5), the FRCM predicts a stronger difference in the outer-sphere reorganization energy upon changing the number of linkers, n. If the $R-$dependence of the outer-sphere reorganization energy is not included, we obtain $\lambda_o^{(1)} = 11.0 \pm 0.1$ kcal/mol and $\lambda_o^{(2)} = 15.6 \pm 0.1$ kcal/mol.

1.4.4 Calculation of $\Delta G^{o(n)}$ and $\Delta\Delta G^{o}$.

In this section, we validate the assumption that ΔG^{o} is small in comparison to λ for the CPET reactions considered in this study, and we calculate the difference in the reaction driving forces at infinite separation, $\Delta\Delta G^{o}$.

For each complex, the driving force at infinite separation is calculated using

$$\Delta G^{o(n)}_{\mathrm{CPET}} = E(\mathrm{Fe^{II}Ph_nCO_2H}) + E(\mathrm{TEMPO}) - E(\mathrm{Fe^{III}Ph_nCO_2^-}) - E(\mathrm{TEMPOH}), \tag{1.39}$$

where $E(\mathrm{A})$ represents the energy of species A. As before, geometry optimizations are performed at the B3LYP/6-31G(d,p) level of theory, with solvation effects included via the polarizable continuum model using the default parameters for Gaussian 09 (version G09RevB.01); final energies are computed using B3LYP/TZVP with implicit solvent effects included. We compute $\Delta G^{o(1)}_{\mathrm{CPET}} = -3.43$ kcal/mol, and $\Delta G^{o(1)}_{\mathrm{CPET}} = -3.69$ kcal/mol, which are in agreement with the experimental estimates of $\Delta G^{o(1)}_{\mathrm{CPET}} = -3.5 \pm 1.1$ kcal/mol and $\Delta G^{o(2)}_{\mathrm{CPET}} = -3.7 \pm 1.3$ kcal/mol. The values for ΔG^{o} at finite separations, obtained using Eq. 1.10 and the results in Figs. 1.4C and 1.4D, are comparable or smaller in magnitude than the corresponding values for ΔG^{o} at infinite separations.

The difference in the reaction driving forces at infinite separation is calculated as

$$\Delta\Delta G^{o} = \Delta G^{o(1)}_{\mathrm{CPET}} - \Delta G^{o(2)}_{\mathrm{CPET}} \tag{1.40}$$

Using the driving force values described above, we obtain $\Delta\Delta G^{o} = 0.26$ kcal/mol, which is again in agreement with the experimentally measured value of $\Delta\Delta G^{o} = 0.2 \pm 1.4$ kcal/mol.

1.4.5 Decorrelation of the proton and electron donor-acceptor distances, and insensitivity of the proton donor-acceptor distance distribution to phenylene linker length.

Various simplifications in the derivation of the CPET rate expression (Section 1.3) follow from the assumption that the proton donor-acceptor distance, r, and the electron donor-acceptor distance, R, are statistically uncorrelated in the hydrogen-bonded configurations for the TEMPOH/iron-porphyrin system that dominantly contribute to the CPET rate. Furthermore, cancellation of γ terms in Eq. 1.16 is based on the assumption that the distribution of proton donor-acceptor distances is insensitive to the number of phenylene linkers in the iron-porphyrin complex. Here, we validate

these assumptions using MD simulations. Employing the simulation setup for the reactant species that is described in Section 1.4.1, two unrestrained MD trajectories of length 5 ns are performed; for the first of these trajectories, the TEMPOH molecule occupies the basin of stability for which it is hydrogen-bonded to $\mathbf{Fe^{III}PhCO_2^-}$, and for the second trajectory, the TEMPOH molecule occupies the basin of stability for which it is hydrogen-bonded to $\mathbf{Fe^{III}Ph_2CO_2^-}$. Configurations are sampled every 500 fs to construct the one-dimensional probability distributions $P_{\rm r}(r)$ and $P_{\rm r}(R)$, as well as the two-dimensional probability distribution $P_{\rm r}(r, R)$.

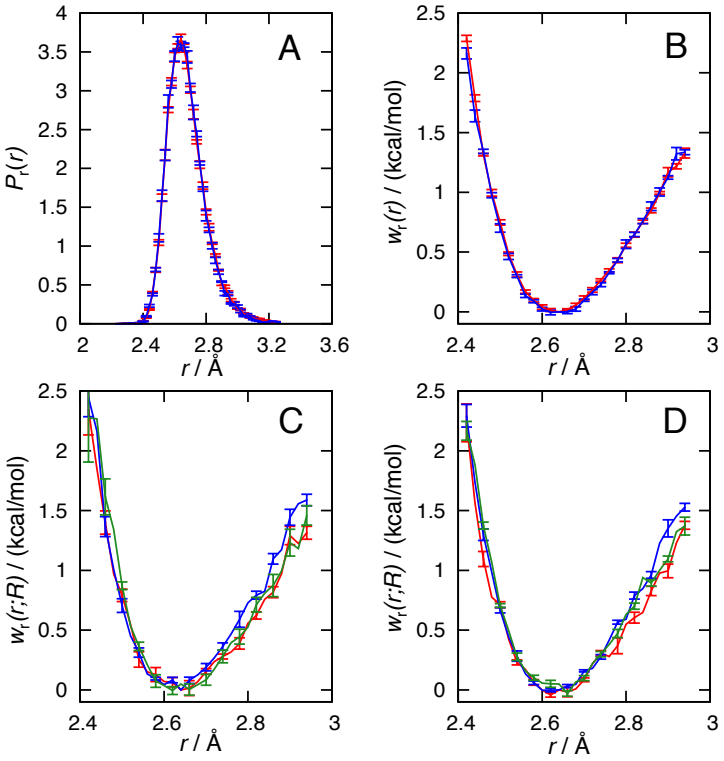

Figure 1.7: **(A)** Distribution of r, the proton donor-acceptor distances in the $n = 1$ (red) and $n = 2$ (blue) TEMPOH/iron-porphyrin complexes. **(B)** $w_{\rm r}^{(n)}(r)$, the free energy as a function of the proton donor-acceptor distance for the $n = 1$ and $n = 2$ complexes. **(C)** $w_{\rm r}^{(1)}(r; R)$ at $R = 7.5$ Å(blue) $R = 8$ Å(red), and $R = 9$ Å(green). **(D)** $w_{\rm r}^{(2)}(r; R)$ at $R = 11.5$ Å(blue) $R = 12$ Å(red), and $R = 13$ Å(green).

Figure 1.7A presents the computed distribution of proton donor-acceptor distances, $P_{\rm r}(r)$, for the TEMPOH-$\mathbf{Fe^{III}PhCO_2^-}$ and TEMPOH-$\mathbf{Fe^{III}Ph_2CO_2^-}$ systems. It is clear that the distributions are essentially identical for the two cases, both of which are peaked about 2.65Å. These data are replotted in Fig.1.7B in terms of the proton donor-acceptor free-energy profiles $w_{\rm r}(r) = -k_{\rm B}T \ln P_{\rm r}(r)$. The results in Fig. 1.7B further emphasize that the work for compression of the proton donor-acceptor distances during the CPET reaction is insensitive to the number of phenylene linkers. These numer-

ical results validate the cancellation of γ in the numerator and denominator of Eq. 1.16, since the distribution of proton donor-acceptor distances is insensitive to the number of phenylene linkers.

Figure 1.7C addresses the issue of statistical decorrelation between the proton and electron donor-acceptor distances in the TEMPOH-$\mathbf{Fe^{III}PhCO_2^-}$ system. Plotted are cross-sections of the two-dimensional free-energy profile in the coordinates r and R, which is obtained using $w_{\rm r}(r;R) = -k_{\rm B}T \ln P_{\rm r}(r;R)$. At various distances for the electron donor-acceptor distances (R = 7.5, 8, and 9 Å), the figure demonstrates that the proton donor-acceptor distribution is essentially unchanged, indicating that the proton and electron donor-acceptor distance distributions are uncorrelated. Figure 1.7D demonstrates that the same lack of correlation is found in the system with $n = 2$ phenylene linkers. These numerical results validate the assumption that the proton and electron donor-acceptor distances are statistically uncorrelated in the hydrogen-bonded configurations of the TEMPOH/iron-porphyrin system.

The results in this section indicate that although the distribution of electron donor-acceptor distances is sensitive to the number of phenylene linkers (Figs. 1.4C and 1.4D), the proton donor-acceptor distance distribution is both insensitive to the number of phenylene linkers (Figs. 1.7A and 1.7B) and uncorrelated with the electron donor-acceptor distance distribution (Figs. 1.7C and 1.7D). The results validate key aspects of the experimental design, which aims to alter the electron donor-acceptor chemistry of the TEMPOH/iron-porphyrin systems through inclusion of phenylene linkers while leaving the proton-transfer interface between the TEMPOH and iron-porphyrin complexes unchanged.

1.5 Determination of the electron transfer decay constant β

Having computed $w_{\rm r}(R)$, $w_{\rm p}(R)$, $\Delta\Delta G^o$, and $\lambda(R)$, we examine the impact of these terms in the calculation of the decay constant β using Eq. 1.16. We consider a series of three cases (I-III), which provide increasingly complete descriptions of these terms.

In the simplest treatment of Eq. 1.16 (Case I), the CPET reaction is assumed to involve only a single electron donor-acceptor distance, $\tilde{R}^{(n)}$, and the terms $w_{\rm p}$, $w_{\rm r}$, and λ are each assumed to be independent of the number of phenylene linkers. For these calculations, we employ the computed value of $\Delta\Delta G^o = 0.26$ kcal/mol. Equation 1.16 then simplifies to a form that resembles what has been employed in the theoretical analysis of ET reactions[15]

$$\frac{k^{(1)}}{k^{(2)}} = e^{-\frac{1}{2k_{\rm B}T}\Delta\Delta G^o} \exp\left[-\beta\left(\tilde{R}^{(1)} - \tilde{R}^{(2)}\right)\right]. \tag{1.41}$$

Table 1.1: Values of electronic decay constant β.

Case	Explicitly calculated terms in Eq. 1.16	$\beta/\text{Å}^{-1}$	$\Delta\beta/\text{Å}^{-1}$
I	$\Delta\Delta G^o$	0.26(4)	-
II	$\Delta\Delta G^o$,$w_\text{r}(R)$, $w_\text{p}(R)$	0.35(6)	$+0.09(4)^\text{b}$
III[a]	$\Delta\Delta G^o$,$w_\text{r}(R)$, $w_\text{p}(R)$, $\lambda(R)$	0.23(7)	$-0.12(4)^\text{c}$

[a] Using the explicit solvent results for $\lambda_\text{o}(R)$.
[b] Relative to Case I.
[c] Relative to Case II.

The electron donor-acceptor distances $\tilde{R}^{(1)}$ and $\tilde{R}^{(2)}$ are estimated from the distances between the metal center and the carboxyl oxygen in the crystal structures of iron(III) tetra-4-carboxyphenylporphyrin chloride and silver(II) 5,10,15,20-tetrakis (4-carboxy-2,6-dimethyl-bi-phenyl)porphyrin, respectively. Inserting the distances $\tilde{R}^{(1)} = 9.9$ Å, $\tilde{R}^{(2)} = 14.1$ Å, and the experimental values for $k^{(1)}$ and $k^{(2)}$ into Eq. 1.16 yields $\beta = 0.26 \pm 0.04\text{Å}^{-1}$.

For Case II, a more detailed treatment of Eq. 1.16 includes the distance dependence of $w_\text{r}(R)$ and $w_\text{p}(R)$, while the dependence of the reorganization energy on the electron donor-acceptor distance and on the linker number is still neglected. Using the experimental values for $k^{(1)}$ and $k^{(2)}$, solution of Eq. 1.16 via numerical quadrature then yields $\beta = 0.35 \pm 0.06\text{Å}^{-1}$.

In the most complete treatment of Eq. 1.16 (Case III), we include the distance dependence of $w_\text{r}^{(n)}(R)$ and $w_\text{p}^{(n)}(R)$, and the distance- and n-dependence of the reorganization energy. Using the values for $\lambda_\text{o}(R)$ obtained from the explicit-solvent MD simulations, solving Eq. 1.16 yields $\beta = 0.23 \pm 0.07\text{Å}^{-1}$. However, using the (physically reasonable) values for $\lambda_\text{o}(R)$ from the continuum-solvent FRCM yields the unphysical result of $\beta = -0.10 \pm 0.06\text{Å}^{-1}$.

Table 1.1 presents a summary of these three analyses. All cases yield values for β that fall within the established range for ET across phenylene bridges ($0.2 - 0.5\text{Å}^{-1}$), but inclusion of the various preorganization and solvent reorganization contributions is found to significantly shift β within that range. Specifically, comparison of Cases I and II indicates that inclusion of the preorganization work for the bimolecular reaction leads to an increase of $0.09 \pm 0.04\text{Å}^{-1}$ in the estimated value of β, emphasizing that even weak n-dependence in the energy of preorganization (~ 0.3 kcal/mol) leads to a substantial difference in the calculated β. Moreover, comparison of Cases II and III indicates that the weak n-dependence in the solvent reorganization energy leads to a decrease of $0.12 \pm 0.04\text{Å}^{-1}$ in the calculated β. Although the combined effects of $w_\text{r}^{(n)}(R)$, $w_\text{p}^{(n)}(R)$, and $\lambda_\text{o}^{(n)}(R)$ in Table 1.1 nearly cancel for the current study, this must be regarded as fortuitous; for systems that do not exhibit this cancellation of error, a careful treatment conformational flexibility and solvent reorganization energy would be necessary to avoid misinterpretation of β. The point is further underscored by our

finding that approximations in the description of the solvent reorganization (i.e., using implicit vs. explicit solvation) can lead to unphysical estimates for β.

1.6 Conclusions

This chapter describes the collaborative theoretical and experimental examinations of the bimolecular PCET reactions of $\mathbf{Fe^{III}PhCO_2^-}$ or $\mathbf{Fe^{III}Ph_2CO_2^-}$ with TEMPOH. It has been experimentally determined that the reaction between $\mathbf{Fe^{III}Ph_nCO_2^-}$ and TEMPOH ($n = 1, 2$) follows a concerted mechanism. Combining the experimental rate measurements with quantities obtained by MD and electronic structure methods yields the first test of the dependence of the CPET rate constant on the electron transfer distance. We demonstrate that common assumptions and simplifications can lead to substantial changes in the interpretation of the electronic decay constant β from experimentally determined reaction rates, and we illustrate the sensitivity of β to the description of the preorganization and solvent reorganization energies. The most detailed treatment provided here yields a value of $\beta \approx 0.23\text{Å}^{-1}$, which is on the low end of the range of values for ET across phenylene bridges ($\beta = 0.2 - 0.5\text{Å}^{-1}$). These results suggest that values of β obtained from ET reactions have direct relevance for vibronically nonadiabatic CPET reactions that are central to biological catalysis and energy production.

Appendix A Parameters of the force field used in the MD simulations

This appendix describes the atom types and charges used in the MD simulations of the iron-porphyrin complexes and TEMPOH/TEMPO molecule.

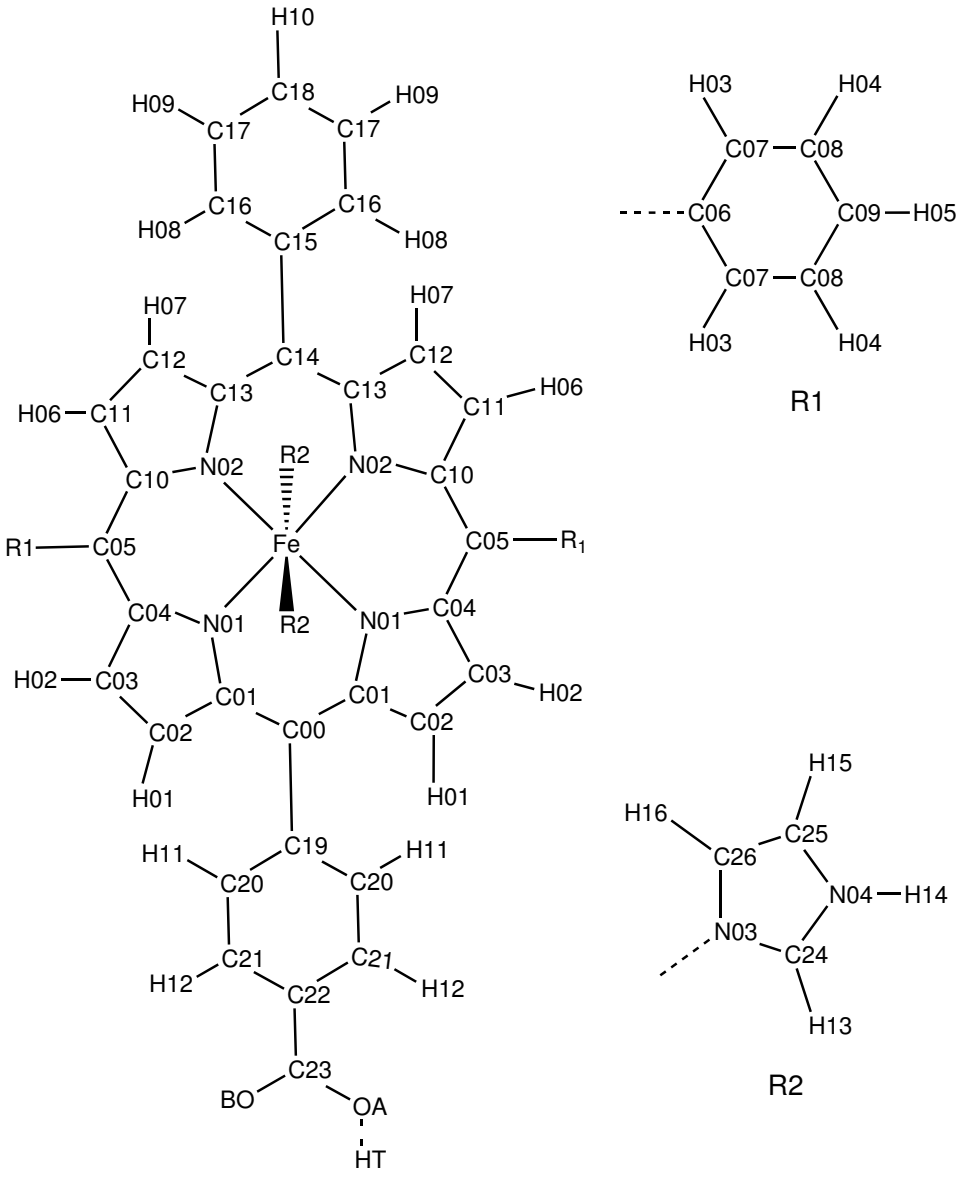

Figure 1.8: Atom types for the $n = 1$ iron-porphyrin complex. R1 and R2 denote the phenyl substituents on the porphyrin ring and the axial imidazole ligands, respectively.

Table 1.2: Atom types and charges in the reactant and product states for the $n = 1$ iron porphyrin complex.

Atom Type	GAFF Atom Type	Reactant Charge	Product Charge
C00	cp	-0.030	-0.090
C01	cc/cd	-0.082	0.069
C02	cc/cd	-0.086	-0.119
C03	cc/cd	-0.228	-0.258
C04	cc/cd	0.250	0.242
C05	cp	-0.144	-0.158
C06	cp	0.226	0.240
C07	ca	-0.192	-0.200
C08	ca	-0.059	-0.061
C09	ca	-0.125	-0.137
C10	cc/cd	0.237	0.233
C11	cc/cd	-0.214	-0.255
C12	cc/cd	-0.099	-0.113
C13	cc/cd	0.107	0.078
C14	cp	-0.080	-0.102
C15	cp	0.174	0.195
C16	ca	-0.133	-0.137
C17	ca	-0.068	-0.073
C18	ca	-0.143	-0.153
C19	cp	0.137	0.198
C20	ca	-0.145	-0.134
C21	ca	-0.089	-0.078
C22	ca	-0.075	-0.095
C23	c	0.682	0.672
C24	cc/cd	0.139	0.13
C25	cc/cd	-0.116	-0.145
C26	cc/cd	-0.050	0.014
Fe	Fe	0.731	0.602
H01	ha	0.097	0.088
H02	ha	0.118	0.108
H03	ha	0.116	0.113
H04	ha	0.099	0.095
H05	ha	0.106	0.105
H06	ha	0.115	0.107
H07	ha	0.095	0.079
H08	ha	0.076	0.071
H09	ha	0.104	0.102
H10	ha	0.113	0.110
H11	ha	0.073	0.081
H12	ha	0.089	0.012
H13	ha	0.060	0.042
H14	ha	0.366	0.356
H15	ha	0.179	0.170
H16	ha	0.063	0.038
N01	nd	-0.287	-0.276
N02	nd	-0.292	-0.278

Continued on next page

Table 1.2 – continued from previous page

Atom Type	GAFF Atom Type	Reactant Charge	Product Charge
N03	nd	-0.251	-0.277
N04	na	-0.233	-0.242
OA	o[a]	-0.749	-0.59
OB	o	-0.749	-0.570
HT	ho	–	0.445

[a] Atom type of OA is set to oh in the simulations of the product species.

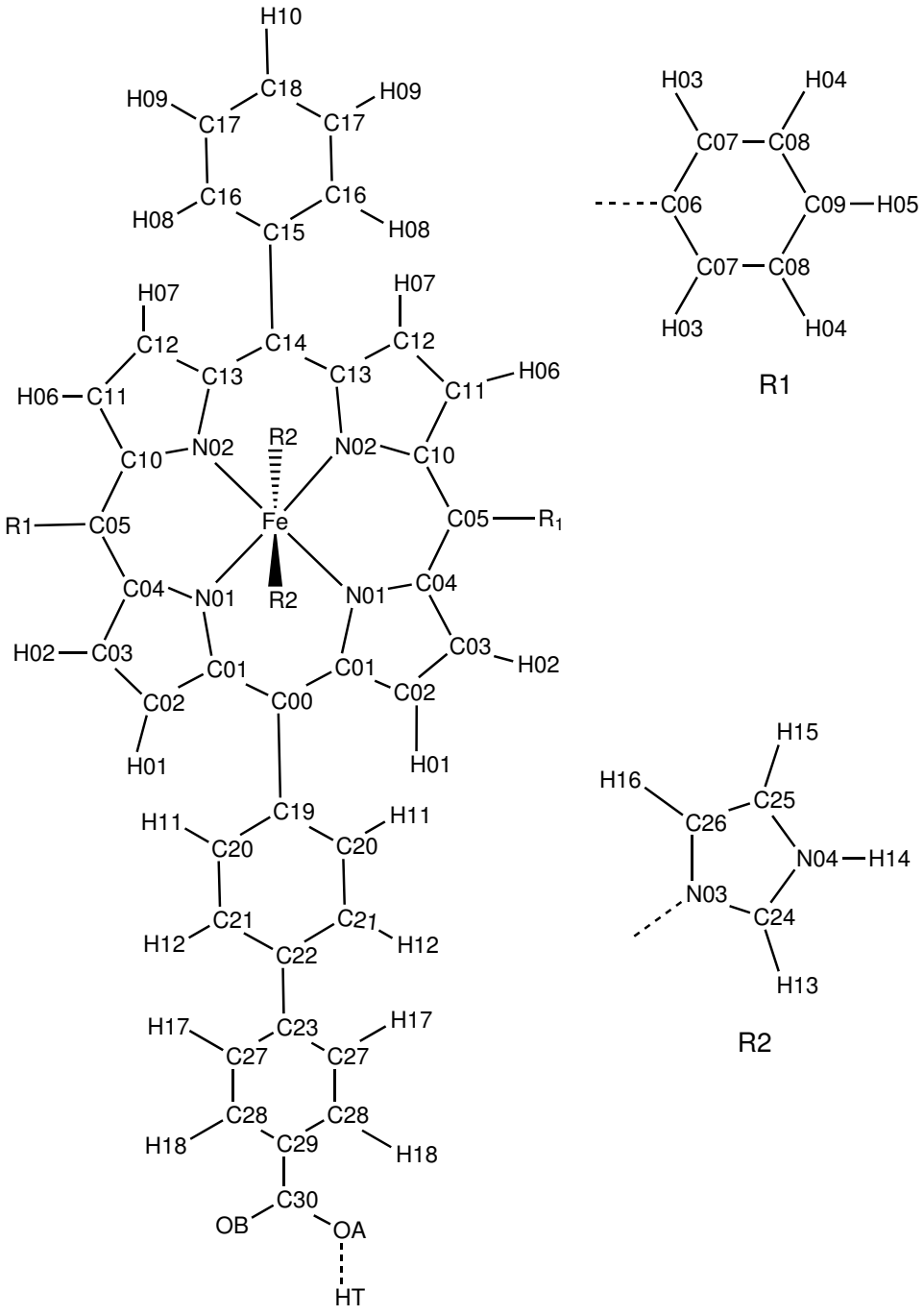

Figure 1.9: Atom types for the $n = 2$ iron-porphyrin complex. R1 and R2 denote the phenyl substituents on the porphyrin ring and the axial imidazole ligands, respectively.

Table 1.3: Atom types and charges in the reactant and product states for the $n = 2$ iron porphyrin complex.

Atom Type	GAFF Atom Type	Reactant Charge	Product Charge
C00	cp	-0.053	-0.102
C01	cc/cd	0.066	0.066
C02	cc/cd	-0.068	-0.098
C03	cc/cd	-0.223	-0.262
C04	cc/cd	0.217	0.239
C05	cp	-0.131	-0.154
C06	cp	0.211	0.231
C07	ca	-0.186	-0.197
C08	ca	-0.062	-0.064
C09	ca	-0.117	-0.127
C10	cc/cd	0.230	0.232
C11	cc/cd	-0.214	-0.258
C12	cc/cd	-0.094	-0.105
C13	cc/cd	0.087	0.074
C14	cp	-0.067	-0.105
C15	cp	0.206	0.193
C16	ca	-0.158	-0.132
C17	ca	-0.062	-0.086
C18	ca	-0.138	-0.129
C19	cp	0.147	0.184
C20	ca	-0.123	-0.127
C21	ca	-0.114	-0.109
C22	cp	0.025	-0.010
C23	cp	0.053	0.123
C24	cc/cd	0.121	0.150
C25	cc/cd	-0.106	-0.140
C26	cc/cd	-0.015	0.028
C27	ca	-0.141	-0.147
C28	ca	-0.099	-0.074
C29	ca	-0.044	-0.063
C30	c	0.656	0.645
Fe	Fe	0.818	0.677
H01	ha	0.083	0.073
H02	ha	0.119	0.107
H03	ha	0.114	0.114
H04	ha	0.100	0.095
H05	ha	0.104	0.101
H06	ha	0.116	0.107
H07	ha	0.093	0.076
H08	ha	0.082	0.07
H09	ha	0.104	0.104
H10	ha	0.108	0.102
H11	ha	0.083	0.080
H12	ha	0.105	0.107
H13	ha	0.070	0.036
H14	ha	0.359	0.358

Continued on next page

Table 1.3 – continued from previous page

Atom Type	GAFF Atom Type	Reactant Charge	Product Charge
H15	ha	0.175	0.169
H16	ha	0.069	0.029
H17	ha	0.086	0.102
H18	ha	0.082	0.112
N01	nd	-0.254	-0.284
N02	nd	-0.277	-0.284
N03	nd	-0.298	-0.310
N04	na	-0.211	-0.253
OA	o[a]	-0.744	-0.584
OB	o	-0.744	-0.563
HT	ho	-	0.444

[a] Atom type of OA is set to oh in the simulations of the product species.

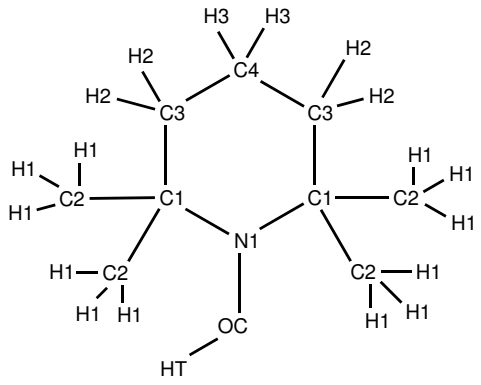

Figure 1.10: Atom types for the TEMPOH molecule.

Table 1.4: TEMPOH atom types and charges in the reactant and product states.

Atom Type	GAFF Atom Type	Reactant Charge	Product Charge
C1	c3	0.800	0.518
C2	c3	-0.306	-0.287
C3	c3	-0.319	-0.262
C4	c3	0.198	0.094
N1	n	-0.730	-0.117
H1	hc	0.057	0.068
H2	hc	0.050	0.060
H3	hc	-0.027	0.005
OC	oh[a]	-0.492	-0.407
HT	ho	0.451	–

[a] Atom type of OC is set to o in the simulations of the product species

Appendix B Optimized molecular geometries of PCET reactant and product species

This appendix describes the optimized molecular geometries of the species employed in the computational model.

Table 1.5: Optimized Cartesian coordinates of the TEMPO molecule

Center Number	Atomic Number	X / Å	Y/ Å	Z / Å
1	1	3.320078	-0.331390	-0.839409
2	1	2.796467	0.162893	1.563010
3	1	2.160467	1.908445	-0.164171
4	6	2.345462	-0.824398	-0.904682
5	1	2.452383	-1.859515	-0.577743
6	1	2.028075	-0.821484	-1.951866
7	6	1.246560	1.398690	-0.488705
8	6	1.761902	-0.176348	1.451656
9	1	1.245477	1.423354	-1.586061
10	6	1.333331	-0.070526	-0.027102
11	1	1.699822	-1.216967	1.779945
12	1	1.136618	0.431737	2.109752
13	1	0.000003	3.158855	-0.353264
14	6	0.000002	2.127117	0.014728
15	1	0.000002	2.191361	1.109223
16	7	0.	-0.746531	-0.199780
17	8	0.	-2.026301	-0.060841
18	6	-1.246555	1.398688	-0.488708
19	1	-1.245465	1.423347	-1.586064
20	1	-1.136637	0.431749	2.109754
21	6	-1.333331	-0.070524	-0.027102
22	6	-1.761906	-0.176346	1.451653
23	1	-2.160463	1.908448	-0.164183
24	1	-1.699817	-1.216964	1.779944
25	6	-2.345462	-0.824393	-0.904681
26	1	-2.028068	-0.821496	-1.951864
27	1	-2.796478	0.162880	1.563000
28	1	-2.452400	-1.859507	-0.577735
29	1	-3.320074	-0.331375	-0.839421

Table 1.6: Optimized Cartesian coordinates of the TEMPOH molecule

Center Number	Atomic Number	X / Å	Y/ Å	Z / Å
1	1	-1.479624	-1.209808	1.801593
2	6	-1.634694	-0.180922	1.469249
3	6	-1.295588	-0.049098	-0.033100
4	6	-1.251300	1.433314	-0.468764
5	1	-1.279652	1.473653	-1.565388
6	1	-2.162053	1.925904	-0.10904
7	6	0.000014	2.169080	0.016436
8	1	0.000039	3.196869	-0.364593
9	6	1.251225	1.433274	-0.468908
10	1	1.279219	1.473324	-1.565547
11	1	2.162039	1.926010	-0.109570
12	6	1.295622	-0.049118	-0.033077
13	6	2.395467	-0.766722	-0.839401
14	1	2.160771	-0.745813	-1.908204
15	1	3.360783	-0.273358	-0.686656
16	1	2.492708	-1.809506	-0.527038
17	6	1.634669	-0.180846	1.469253
18	1	1.037224	0.478138	2.101323
19	1	2.686970	0.075343	1.631307
20	1	1.480860	-1.210026	1.801349
21	1	0.000053	2.248951	1.109867
22	6	-2.395369	-0.766738	-0.839511
23	1	-2.160288	-0.746249	-1.908234
24	1	-3.360615	-0.273092	-0.687241
25	1	-2.493027	-1.809391	-0.526763
26	7	0.000038	-0.665140	-0.446046
27	8	-0.000006	-2.041552	0.011015
28	1	-0.000332	-2.538979	-0.818379
29	1	-1.038231	0.479081	2.101259
30	1	-2.687339	0.074000	1.631093

Table 1.7: Optimized Cartesian coordinates of the $\mathbf{Fe^{III}PhCO_2^-}$ molecule

Center Number	Atomic Number	X / Å	Y/ Å	Z / Å
1	6	2.063901	3.447332	0.079828
2	1	2.206164	4.515452	0.135018
3	6	0.783962	2.789153	0.014438
4	6	-0.441389	3.467466	0.021413
5	6	-0.428342	4.965423	0.043228
6	6	0.016390	5.692989	-1.071868
7	6	0.029354	7.088415	-1.051338
8	1	0.372679	7.635569	-1.924207
9	6	-0.400711	7.777865	0.084403
10	1	-0.389870	8.863490	0.100307
11	6	-0.844516	7.064200	1.199714
12	1	-1.176826	7.592208	2.088505
13	1	0.347735	5.161135	-1.958727
14	6	-0.858860	5.668801	1.179286
15	1	-1.200520	5.117823	2.050448
16	6	-1.676654	2.808877	0.011743
17	6	-2.947243	3.488748	-0.004174
18	1	-3.073581	4.560227	-0.011125
19	6	-3.910129	2.532308	-0.005071
20	1	-4.980635	2.666791	-0.007257
21	6	-3.240278	1.256052	-0.008730
22	6	-3.912803	0.029712	-0.014434
23	6	-5.411658	0.040246	-0.034442
24	6	-6.109262	0.434510	-1.186746
25	1	-5.553634	0.730119	-2.071715
26	6	-7.504910	0.442479	-1.204728
27	1	-8.029308	0.746622	-2.105692
28	6	-8.223611	0.057227	-0.070967
29	1	-9.309323	0.063844	-0.085034
30	6	-7.539300	-0.336707	1.080912
31	1	-8.090567	-0.634577	1.967833
32	6	-6.143663	-0.345799	1.099130
33	1	-5.614813	-0.648563	1.997968
34	6	-3.259799	-1.207086	-0.004966
35	7	-1.896178	-1.415417	0.026256
36	26	-0.467811	0.002403	0.002069
37	7	-0.491767	-0.006921	-2.002898
38	6	-0.428887	1.091288	-2.843615
39	1	-0.359270	2.096582	-2.464383
40	6	-0.469906	0.667266	-4.142533
41	1	-0.444436	1.204039	-5.076534
42	7	-0.558695	-0.706004	-4.082991
43	1	-0.607693	-1.337775	-4.869959
44	6	-0.569634	-1.076787	-2.786858
45	1	-0.633759	-2.101537	-2.461566
46	7	-0.442117	0.011725	2.007483

Continued on next page

Table 1.7 – continued from previous page

Center Number	Atomic Number	X / Å	Y/ Å	Z / Å
47	6	-0.360294	1.081314	2.791480
48	1	-0.296490	2.106101	2.466323
49	7	-0.365199	0.710212	4.087541
50	1	-0.309781	1.341603	4.874386
51	6	-0.453658	-0.663049	4.147133
52	1	-0.473670	-1.200178	5.081062
53	6	-0.501032	-1.086659	2.848314
54	1	-0.571620	-2.091943	2.469354
55	7	0.936895	-1.437453	-0.002120
56	6	2.304347	-1.251115	-0.005187
57	6	2.979200	-0.025106	0.000093
58	6	2.323502	1.211354	0.004824
59	6	4.476720	-0.034441	0.004588
60	6	5.199799	0.405979	-1.116274
61	1	4.661393	0.749017	-1.995728
62	6	6.593969	0.397027	-1.109168
63	1	7.158008	0.731751	-1.973561
64	6	7.308206	-0.046066	0.010357
65	6	8.847374	-0.051436	0.013785
66	6	6.585727	-0.483350	1.126945
67	1	7.143393	-0.822174	1.993883
68	6	5.191482	-0.480466	1.128580
69	1	4.646852	-0.817708	2.006429
70	6	2.973078	-2.527722	-0.020835
71	1	4.043421	-2.661480	-0.034018
72	6	2.010003	-3.483887	-0.007877
73	1	2.136109	-4.555395	-0.003701
74	6	0.739784	-2.803609	-0.007197
75	6	-0.495860	-3.462700	-0.005560
76	6	-0.509047	-4.960917	-0.020054
77	6	-0.092858	-5.669790	-1.158000
78	1	0.238686	-5.123108	-2.035756
79	6	-0.107817	-7.065257	-1.171563
80	1	0.213828	-7.597607	-2.061681
81	6	-0.538218	-7.773466	-0.047532
82	6	-0.954215	-7.078477	1.090037
83	1	-1.286854	-7.621354	1.969700
84	1	-0.549254	-8.859155	-0.058038
85	6	-0.940444	-5.682924	1.103775
86	1	-1.260624	-5.146754	1.992152
87	6	-1.720851	-2.785037	0.002328
88	6	-3.001232	-3.443662	-0.054601
89	1	-3.143569	-4.512350	-0.097495
90	6	-3.948722	-2.471788	-0.058809
91	1	-5.020364	-2.588486	-0.104964
92	7	-1.873410	1.442500	0.005094
93	7	0.959420	1.419987	-0.022491

Continued on next page

Table 1.7 – continued from previous page

Center Number	Atomic Number	X / Å	Y/ Å	Z / Å
94	6	3.011568	2.475596	0.073448
95	1	4.083117	2.590825	0.121601
96	8	9.406957	0.359911	-1.038303
97	8	9.399312	-0.466396	1.068470

Table 1.8: Optimized Cartesian Coordinates of the $\mathbf{Fe^{II}PhCO_2H}$ molecule

Center Number	Atomic Number	X / Å	Y/ Å	Z / Å
1	6	2.050838	3.457774	0.072409
2	1	2.194236	4.526615	0.123998
3	6	0.769848	2.788161	0.009671
4	6	-0.462272	3.460009	0.016105
5	6	-0.449627	4.959147	0.033336
6	6	-0.005848	5.686930	-1.082684
7	6	0.008459	7.082745	-1.068378
8	1	0.352200	7.626301	-1.943721
9	6	-0.421403	7.777802	0.064143
10	1	-0.410539	8.863658	0.076027
11	6	-0.865130	7.066918	1.181423
12	1	-1.197692	7.597973	2.068678
13	1	0.326429	5.151520	-1.967229
14	6	-0.878660	5.671130	1.165245
15	1	-1.221166	5.123653	2.038454
16	6	-1.704905	2.806247	0.009963
17	6	-2.976845	3.495968	-0.001301
18	1	-3.105198	4.567931	-0.005184
19	6	-3.940764	2.540297	-0.002730
20	1	-5.011473	2.678755	-0.002125
21	6	-3.263428	1.261564	-0.010320
22	6	-3.931080	0.028177	-0.013687
23	6	-5.430704	0.037993	-0.027238
24	6	-6.138465	0.449542	-1.168005
25	1	-5.587377	0.760458	-2.050726
26	6	-7.534443	0.457999	-1.180213
27	1	-8.062944	0.776666	-2.074096
28	6	-8.248937	0.054200	-0.050109
29	1	-9.334884	0.060595	-0.058882
30	6	-7.557611	-0.358103	1.091249
31	1	-8.104184	-0.670912	1.976300
32	6	-6.161633	-0.365975	1.101558
33	1	-5.628459	-0.683935	1.992738
34	6	-3.281957	-1.215074	-0.007282
35	7	-1.919195	-1.415960	0.020104
36	26	-0.488308	0.001882	0.000056
37	7	-0.507308	-0.011646	-2.024700
38	6	-0.496580	1.083944	-2.869813
39	1	-0.477522	2.090219	-2.485101
40	6	-0.514446	0.662868	-4.172400
41	1	-0.513766	1.200001	-5.106986
42	7	-0.536384	-0.713728	-4.114545
43	1	-0.553910	-1.346310	-4.901153
44	6	-0.531282	-1.079643	-2.810387
45	1	-0.546261	-2.105340	-2.480556
46	7	-0.468204	0.015430	2.024736

Continued on next page

Table 1.8 – continued from previous page

Center Number	Atomic Number	X / Å	Y/ Å	Z / Å
47	6	-0.444908	1.083459	2.810402
48	1	-0.431269	2.109174	2.480560
49	7	-0.438764	0.717552	4.114554
50	1	-0.421547	1.350151	4.901155
51	6	-0.459378	-0.659063	4.172429
52	1	-0.459135	-1.196188	5.107020
53	6	-0.477494	-1.080167	2.869856
54	1	-0.495894	-2.086461	2.485159
55	7	0.921203	-1.438157	0.000987
56	6	2.286553	-1.259447	0.013048
57	6	2.952422	-0.024434	0.014045
58	6	2.305144	1.220426	0.005153
59	6	4.449677	-0.034253	0.027515
60	6	5.181462	0.414615	-1.085171
61	1	4.649366	0.765521	-1.963605
62	6	6.573526	0.408390	-1.079405
63	1	7.121706	0.753198	-1.948516
64	6	7.269149	-0.049930	0.048653
65	6	8.752509	-0.077801	0.108916
66	6	6.549310	-0.499099	1.164529
67	1	7.093898	-0.846939	2.035544
68	6	5.158813	-0.490815	1.152500
69	1	4.609692	-0.834624	2.023222
70	6	2.963493	-2.538901	0.001638
71	1	4.033721	-2.681218	-0.002169
72	6	1.998917	-3.493739	-0.002107
73	1	2.127087	-4.565702	-0.001338
74	6	0.727434	-2.803526	-0.011433
75	6	-0.514916	-3.456233	-0.016504
76	6	-0.528551	-4.955393	-0.034143
77	6	-0.103128	-5.667341	-1.167404
78	1	0.237240	-5.119858	-2.041453
79	6	-0.117437	-7.063145	-1.183844
80	1	0.212440	-7.594190	-2.072106
81	6	-0.558475	-7.774002	-0.065510
82	6	-0.984853	-7.078935	1.068346
83	1	-1.326484	-7.622497	1.944511
84	1	-0.569967	-8.859849	-0.077575
85	6	-0.969719	-5.683149	1.082929
86	1	-1.299347	-5.147748	1.968470
87	6	-1.747297	-2.783372	-0.008745
88	6	-3.028773	-3.452628	-0.069466
89	1	-3.172374	-4.521598	-0.118275
90	6	-3.977963	-2.482288	-0.067601
91	1	-5.049836	-2.603164	-0.114432
92	7	-1.897370	1.441330	-0.000095
93	7	0.943045	1.420295	-0.020898

Continued on next page

Table 1.8 – continued from previous page

Center Number	Atomic Number	X / Å	Y/ Å	Z / Å
94	6	3.000715	2.488263	0.068978
95	1	4.072059	2.612752	0.119306
96	8	9.340004	0.376474	-1.020588
97	8	9.401384	-0.465301	1.066228
98	1	10.300786	0.318569	-0.882452

Table 1.9: Optimized Cartesian Coordinates of the $\mathbf{Fe^{III}Ph_2CO_2^-}$ molecule

Center Number	Atomic Number	X / Å	Y/ Å	Z / Å
1	6	0.987469	3.457369	0.218613
2	1	1.122587	4.523910	0.310160
3	6	-0.287506	2.793712	0.114915
4	6	-1.515930	3.465496	0.087489
5	6	-1.515046	4.963010	0.125732
6	6	-1.017549	5.704674	-0.957655
7	6	-1.018281	7.099814	-0.924947
8	1	-0.633719	7.657450	-1.773633
9	6	-1.514940	7.775542	0.191701
10	1	-1.514637	8.861024	0.217345
11	6	-2.012196	7.048253	1.275099
12	1	-2.397012	7.565434	2.148924
13	1	-0.635430	5.183635	-1.830332
14	6	-2.013485	5.652997	1.242199
15	1	-2.398020	5.093149	2.089377
16	6	-2.745060	2.799326	0.007603
17	6	-4.017001	3.470017	-0.088097
18	1	-4.150023	4.540617	-0.104507
19	6	-4.971169	2.506585	-0.150664
20	1	-6.040413	2.632930	-0.221172
21	6	-4.293990	1.235371	-0.104402
22	6	-4.957879	0.004695	-0.122204
23	6	-6.453540	0.006777	-0.228989
24	6	-7.079832	0.329327	-1.442646
25	1	-6.471640	0.575530	-2.307994
26	6	-8.471906	0.329875	-1.545406
27	1	-8.941170	0.578507	-2.492610
28	6	-9.257383	0.008509	-0.436348
29	1	-10.340252	0.009088	-0.516361
30	6	-8.643885	-0.313202	0.776208
31	1	-9.247660	-0.560960	1.644137
32	6	-7.251760	-0.314338	0.879568
33	1	-6.778093	-0.561062	1.825093
34	6	-4.300666	-1.226987	-0.042981
35	7	-2.937628	-1.425272	0.038334
36	26	-1.519216	0.000174	0.032269
37	7	-1.504900	-0.013350	-1.970836
38	6	-1.372224	1.078095	-2.811964
39	1	-1.259841	2.079552	-2.432540
40	6	-1.409341	0.652520	-4.110547
41	1	-1.340155	1.184510	-5.045073
42	7	-1.566215	-0.714640	-4.049891
43	1	-1.631391	-1.345324	-4.836571
44	6	-1.620396	-1.080781	-2.753475
45	1	-1.739948	-2.100174	-2.426536
46	7	-1.535522	0.010646	2.039817

Continued on next page

Table 1.9 – continued from previous page

Center Number	Atomic Number	X / Å	Y/ Å	Z / Å
47	6	-1.713870	1.069455	2.822555
48	1	-1.876674	2.082256	2.495529
49	7	-1.662132	0.704795	4.119418
50	1	-1.768889	1.330658	4.905365
51	6	-1.441481	-0.653197	4.181377
52	1	-1.361532	-1.183109	5.116218
53	6	-1.364194	-1.074312	2.883282
54	1	-1.197229	-2.069081	2.507245
55	7	-0.105392	-1.430400	0.044587
56	6	1.260159	-1.235443	0.015077
57	6	1.924580	-0.004299	0.028374
58	6	1.261883	1.227374	0.068154
59	6	3.421780	-0.001723	0.012173
60	6	4.126096	0.442424	-1.117215
61	1	3.576688	0.790570	-1.986865
62	6	5.518808	0.444193	-1.136726
63	6	6.263809	0.004821	-0.028109
64	6	5.552392	-0.435474	1.102057
65	1	6.095225	-0.798295	1.969277
66	6	4.159670	-0.439550	1.122422
67	1	3.637060	-0.788219	2.008185
68	6	1.937121	-2.507615	-0.008616
69	1	3.007760	-2.636250	-0.042874
70	6	0.980871	-3.469946	0.033573
71	1	1.114451	-4.540490	0.044116
72	6	-0.293775	-2.798182	0.053715
73	6	-1.525356	-3.463367	0.086550
74	6	-1.531629	-4.961391	0.119900
75	6	-1.135030	-5.706479	-1.001601
76	1	-0.823521	-5.188576	-1.903831
77	6	-1.144187	-7.101688	-0.967250
78	1	-0.837599	-7.662968	-1.844824
79	6	-1.549986	-7.772749	0.188307
80	6	-1.947507	-7.041124	1.309396
81	1	-2.261747	-7.555029	2.212890
82	1	-1.556740	-8.858196	0.214714
83	6	-1.939112	-5.645824	1.275526
84	1	-2.245346	-5.080211	2.150498
85	6	-2.754264	-2.792806	0.074177
86	6	-4.029643	-3.461645	0.016544
87	1	-4.164746	-4.532157	0.016971
88	6	-4.981531	-2.497146	-0.060439
89	1	-6.050894	-2.622317	-0.131180
90	7	-2.931785	1.431430	-0.006371
91	7	-0.102525	1.427576	0.038867
92	6	1.941841	2.492839	0.183917
93	1	3.012260	2.614195	0.244248

Continued on next page

Table 1.9 – continued from previous page

Center Number	Atomic Number	X / Å	Y/ Å	Z / Å
94	6	7.748307	0.004008	-0.050592
95	6	8.455835	-0.303820	-1.227218
96	6	9.848827	-0.307725	-1.243499
97	1	10.394793	-0.554961	-2.148114
98	6	10.587758	-0.004763	-0.093323
99	6	12.125371	-0.013695	-0.115632
100	8	12.699968	0.264560	0.972023
101	8	12.664924	-0.299443	-1.219169
102	6	9.885633	0.304405	1.078096
103	1	10.459852	0.548309	1.965984
104	6	8.492738	0.308960	1.103809
105	1	7.973442	0.575738	2.020284
106	1	7.907571	-0.567592	-2.127539
107	1	6.035298	0.809936	-2.018704

Table 1.10: Optimized Cartesian Coordinates of the $\mathbf{Fe^{II}Ph_2CO_2H}$ molecule

Center Number	Atomic Number	X / Å	Y/ Å	Z / Å
1	6	0.970265	3.473582	0.054322
2	1	1.106830	4.543674	0.098814
3	6	-0.306668	2.795462	-0.002555
4	6	-1.543464	3.459452	-0.000066
5	6	-1.540952	4.958691	0.008694
6	6	-1.099656	5.683300	-1.110430
7	6	-1.095417	7.079232	-1.104330
8	1	-0.753436	7.620104	-1.982034
9	6	-1.533195	7.777841	0.022977
10	1	-1.530241	8.863805	0.028486
11	6	-1.974651	7.070279	1.143254
12	1	-2.313405	7.604097	2.026513
13	1	-0.761455	5.145123	-1.991040
14	6	-1.977961	5.674348	1.135259
15	1	-2.318850	5.129586	2.010803
16	6	-2.781623	2.797513	-0.004762
17	6	-4.058274	3.478331	-0.024152
18	1	-4.194017	4.549372	-0.033488
19	6	-5.015666	2.516046	-0.025744
20	1	-6.087302	2.647239	-0.030500
21	6	-4.329682	1.241905	-0.024139
22	6	-4.989023	0.003943	-0.024280
23	6	-6.488563	0.003681	-0.048828
24	6	-7.190189	0.403412	-1.197603
25	1	-6.634199	0.712794	-2.077796
26	6	-8.586052	0.402053	-1.221069
27	1	-9.109556	0.711622	-2.121082
28	6	-9.306787	0.000017	-0.094302
29	1	-10.392653	-0.001317	-0.111778
30	6	-8.621729	-0.400479	1.055011
31	1	-9.173196	-0.711776	1.937569
32	6	-7.225836	-0.398405	1.076533
33	1	-6.697686	-0.707275	1.973882
34	6	-4.331590	-1.234873	-0.005356
35	7	-2.967666	-1.426306	0.030920
36	26	-1.546283	0.001078	0.003874
37	7	-1.562342	-0.026074	-2.020594
38	6	-1.563837	1.063645	-2.873290
39	1	-1.557861	2.072705	-2.495431
40	6	-1.574366	0.633284	-4.172932
41	1	-1.578798	1.163816	-5.111280
42	7	-1.579292	-0.743064	-4.105497
43	1	-1.587532	-1.381279	-4.887684
44	6	-1.571775	-1.099753	-2.798732
45	1	-1.574448	-2.123177	-2.461507
46	7	-1.529644	0.028093	2.028679

Continued on next page

Table 1.10 – continued from previous page

Center Number	Atomic Number	X / Å	Y/ Å	Z / Å
47	6	-1.520533	1.101650	2.807020
48	1	-1.518429	2.125129	2.470030
49	7	-1.512534	0.744787	4.113728
50	1	-1.504593	1.382914	4.895990
51	6	-1.516862	-0.631556	4.180974
52	1	-1.512078	-1.162230	5.119240
53	6	-1.527476	-1.061735	2.881281
54	1	-1.533117	-2.070769	2.503413
55	7	-0.127217	-1.429254	0.016161
56	6	1.237272	-1.240501	0.022730
57	6	1.895866	-0.001895	0.014080
58	6	1.238838	1.237501	0.001089
59	6	3.394111	-0.001091	0.019280
60	6	4.119800	0.414283	-1.108411
61	1	3.584101	0.743386	-1.993674
62	6	5.512530	0.413744	-1.109095
63	6	6.237188	0.001121	0.022337
64	6	5.510672	-0.411248	1.152691
65	1	6.038873	-0.754634	2.036837
66	6	4.117793	-0.413754	1.149202
67	1	3.580903	-0.742634	2.033816
68	6	1.923062	-2.514890	0.024145
69	1	2.994528	-2.647706	0.021236
70	6	0.965380	-3.476827	0.033269
71	1	1.101120	-4.547819	0.045853
72	6	-0.311147	-2.795844	0.018076
73	6	-1.549295	-3.457234	0.018162
74	6	-1.552740	-4.956525	0.017269
75	6	-1.118092	-5.678744	-1.105998
76	1	-0.778166	-5.139082	-1.985070
77	6	-1.122587	-7.074703	-1.106239
78	1	-0.785590	-7.613707	-1.987018
79	6	-1.563029	-7.775666	0.018575
80	6	-1.998690	-7.070459	1.142593
81	1	-2.339995	-7.606171	2.023718
82	1	-1.566912	-8.861641	0.019080
83	6	-1.993254	-5.674518	1.140940
84	1	-2.329969	-5.131169	2.018948
85	6	-2.786127	-2.792820	0.015423
86	6	-4.062788	-3.471236	-0.045322
87	1	-4.198956	-4.541590	-0.084905
88	6	-5.018558	-2.507410	-0.058068
89	1	-6.089311	-2.636180	-0.109509
90	7	-2.965021	1.431099	-0.008507
91	7	-0.124946	1.428795	-0.024812
92	6	1.926235	2.509870	0.055174
93	1	2.997173	2.639526	0.101530

Continued on next page

Table 1.10 – continued from previous page

Center Number	Atomic Number	X / Å	Y/ Å	Z / Å
94	6	7.720825	0.000717	0.023069
95	6	8.444483	-0.328089	-1.138307
96	6	9.835075	-0.329194	-1.142644
97	1	10.373649	-0.593343	-2.045310
98	6	10.543774	-0.000523	0.022136
99	6	12.027016	0.013470	0.071895
100	8	12.686249	0.295950	1.058538
101	8	12.602216	-0.323725	-1.104135
102	1	13.564460	-0.285607	-0.969435
103	6	9.833872	0.328119	1.185576
104	1	10.386333	0.589792	2.081383
105	6	8.444721	0.328891	1.185198
106	1	7.912481	0.610237	2.087926
107	1	7.911584	-0.609263	-2.040683
108	1	6.042134	0.758615	-1.991816

Table 1.11: Energies (in hartree) for the optimized geometries provided in Tables 1.7-1.10, using the specified DFT functional and basis set.

Species	B3LYP|6-31G(d,p)	B3LYP|TZVP
TEMPO	−483.750173	−483.862334
TEMPOH	−484.359752	−484.473101
$\mathbf{Fe^{III}PhCO_2^-}$	−3816.774186	−3817.676745
$\mathbf{Fe^{II}PhCO_2H}$	−3817.407030	−3818.292971
$\mathbf{Fe^{III}Ph_2CO_2^-}$	−4047.838889	−4048.805990
$\mathbf{Fe^{II}Ph_2CO_2H}$	−4049.422630	−4048.472463

Table 1.12: Cartesian coordinates of the rigid portion of the iron-porphyrin species $\mathbf{Fe^{III}PhCO_2^-}$ employed in calculation of $w_r^{(1)}(R)$ and $w_r^{(2)}(R)$

Atom Name	X / Å	Y/ Å	Z / Å
C00	-0.07	13.20	-0.25
C01	-1.30	12.53	-0.24
C01	1.17	12.54	-0.27
C02	-2.57	13.20	-0.15
C02	2.44	13.22	-0.29
C03	-3.53	12.24	-0.15
C03	3.40	12.27	-0.30
C04	-2.86	10.97	-0.24
C04	2.74	10.99	-0.31
C05	-3.52	9.74	-0.24
C05	3.41	9.76	-0.33
C06	-5.02	9.73	-0.20
C06	4.91	9.76	-0.36
C07	-5.71	9.28	0.94
C07	-5.76	10.19	-1.30
C07	5.64	9.33	0.76
C07	5.60	10.20	-1.50
C08	-7.10	9.28	0.97
C08	-7.16	10.18	-1.27
C08	7.04	9.33	0.73
C08	7.00	10.20	-1.52
C09	-7.83	9.73	-0.13
C09	7.72	9.77	-0.41
C10	2.74	8.53	-0.33
C10	-2.85	8.51	-0.27
C11	3.42	7.26	-0.41
C11	-3.52	7.23	-0.30
C12	2.46	6.30	-0.42
C12	-2.55	6.28	-0.32
C13	1.18	6.97	-0.34
C13	-1.28	6.96	-0.33
C14	-0.05	6.31	-0.35
C15	-0.04	4.81	-0.39
C16	0.36	4.06	0.73
C16	-0.44	4.12	-1.55
C17	0.37	2.67	0.69
C17	-0.43	2.73	-1.59
C18	-0.03	2.00	-0.47
C24	-1.11	9.81	2.51
C24	1.00	9.70	-3.09
C25	0.65	9.72	3.85
C25	-0.76	9.79	-4.43
C26	1.06	9.69	2.55
C26	-1.17	9.81	-3.12
Fe	-0.10	9.75	-0.29
H01	-2.69	14.27	-0.09
H01	2.56	14.29	-0.29

Continued on next page

Table 1.12 – continued from previous page

Atom Name	X / Å	Y/ Å	Z / Å
H02	-4.60	12.37	-0.08
H02	4.47	12.40	-0.30
H03	-5.14	8.93	1.80
H03	-5.24	10.53	-2.19
H03	5.12	8.99	1.64
H03	5.04	10.54	-2.36
H04	-7.62	8.93	1.86
H04	-7.72	10.53	-2.13
H04	7.59	8.99	1.60
H04	7.52	10.54	-2.41
H05	-8.92	9.73	-0.11
H05	8.81	9.77	-0.43
H06	-4.59	7.09	-0.29
H06	4.49	7.13	-0.46
H07	-2.67	5.21	-0.33
H07	2.58	5.23	-0.48
H08	0.67	4.58	1.63
H08	-0.75	4.68	-2.42
H09	0.68	2.11	1.57
H09	-0.74	2.21	-2.49
H10	-0.02	0.91	-0.49
H13	-2.14	9.87	2.20
H13	2.03	9.64	-2.77
H14	-1.35	9.83	4.60
H14	1.24	9.69	-5.18
H15	1.19	9.69	4.78
H15	-1.30	9.83	-5.36
H16	2.06	9.64	2.16
H16	-2.17	9.87	-2.74
N01	1.37	11.17	-0.29
N01	-1.49	11.16	-0.28
N02	-1.48	8.33	-0.29
N02	1.38	8.34	-0.30
N03	-0.05	9.75	1.72
N03	-0.06	9.75	-2.30
N04	-0.73	9.79	3.80
N04	0.62	9.72	-4.38

Table 1.13: Cartesian coordinates of the rigid portion of the iron-porphyrin species $\mathbf{Fe^{III}Ph_2CO_2^-}$ employed in calculation of $w_r^{(1)}(R)$ and $w_r^{(2)}(R)$

Atom Name	X / Å	Y/ Å	Z / Å
C00	-0.14	-35.72	-0.23
C01	-1.36	-35.05	-0.29
C01	1.10	-35.07	-0.22
C02	-2.63	-35.72	-0.41
C02	2.36	-35.76	-0.18
C03	-3.59	-34.75	-0.45
C03	3.34	-34.81	-0.22
C04	-2.92	-33.48	-0.35
C04	2.68	-33.53	-0.25
C05	-3.58	-32.25	-0.34
C05	3.35	-32.30	-0.29
C06	-5.07	-32.24	-0.38
C06	4.85	-32.31	-0.31
C07	-5.75	-31.74	-1.51
C07	-5.83	-32.72	0.70
C07	5.55	-31.92	-1.46
C07	5.59	-32.71	0.82
C08	-7.15	-31.73	-1.55
C08	-7.22	-32.71	0.65
C08	6.94	-31.92	-1.49
C08	6.98	-32.71	0.79
C09	-7.88	-32.21	-0.47
C09	7.66	-32.32	-0.36
C10	-2.90	-31.03	-0.26
C10	2.69	-31.07	-0.28
C11	3.37	-29.80	-0.23
C11	-3.56	-29.75	-0.17
C12	2.42	-28.84	-0.16
C12	-2.59	-28.80	-0.11
C13	1.14	-29.51	-0.19
C13	-1.32	-29.49	-0.14
C14	-0.09	-28.84	-0.12
C15	-0.07	-27.34	-0.20
C16	0.26	-26.55	-1.13
C16	-0.40	-26.71	1.19
C17	0.27	-25.16	-1.03
C17	-0.39	-25.31	1.28
C18	-0.05	-24.54	0.17
C24	-1.16	-32.09	-3.05
C24	0.95	-32.17	2.54
C25	0.57	-32.38	-4.40
C25	-0.79	-32.36	3.88
C26	0.98	-32.46	-3.10
C26	-1.21	-32.40	2.58
Fe	-0.11	-32.28	-0.26
H01	-2.76	-36.79	-0.46
H01	2.48	-36.83	-0.14

Continued on next page

Table 1.13 – continued from previous page

Atom Name	X / Å	Y/ Å	Z / Å
H02	-4.66	-34.88	-0.55
H02	4.41	-34.95	-0.22
H03	-5.18	-31.36	-2.35
H03	-5.31	-33.10	1.58
H03	4.99	-31.61	-2.34
H03	5.06	-33.01	1.72
H04	-7.65	-31.34	-2.43
H04	-7.79	-33.08	1.50
H04	7.47	-31.62	-2.39
H04	7.53	-33.02	1.68
H05	-8.97	-32.20	-0.50
H05	8.75	-32.32	-0.38
H06	-4.63	-29.60	-0.16
H06	4.44	-29.67	-0.22
H07	-2.70	-27.73	-0.44
H07	2.55	-27.77	-0.98
H08	0.51	-27.03	-2.07
H08	-0.66	-27.31	2.05
H09	0.53	-24.56	-1.90
H09	-0.64	-24.84	2.23
H10	-0.04	-23.45	0.25
H13	-2.17	-31.91	-2.74
H13	1.97	-32.06	2.22
H14	-1.40	-32.04	-5.14
H14	1.20	-32.15	4.62
H15	1.11	-32.47	-5.33
H15	-1.33	-32.42	4.81
H16	1.97	-32.63	-2.71
H16	-2.21	-32.51	2.20
N01	1.31	-33.70	-0.25
N01	-1.55	-33.68	-0.27
N02	-1.53	-30.85	-0.23
N02	1.33	-30.87	-0.26
N03	-0.11	-32.27	-2.26
N03	-0.11	-32.28	1.75
N04	-0.79	-32.15	-4.35
N04	0.58	-32.22	3.83

Table 1.14: Cartesian coordinates of the rigid portion of the iron-porphyrin species $\mathbf{Fe^{II}PhCO_2H}$ employed in calculation of $w_{\mathrm{p}}^{(1)}(R)$ and $w_{\mathrm{p}}^{(2)}(R)$

Atom Name	X / Å	Y/ Å	Z / Å
C00	-0.03	13.19	-0.34
C01	1.20	12.53	-0.34
C01	-1.28	12.54	-0.32
C02	2.48	13.2	-0.42
C02	-2.54	13.24	-0.30
C03	3.44	12.24	-0.43
C03	-3.51	12.29	-0.27
C04	2.75	10.97	-0.34
C04	-2.84	11.01	-0.26
C05	3.40	9.72	-0.35
C05	-3.51	9.78	-0.23
C06	4.90	9.71	-0.38
C06	-5.01	9.78	-0.20
C07	5.59	9.26	-1.52
C07	5.65	10.16	0.72
C07	-5.76	9.34	-1.30
C07	-5.71	10.23	0.94
C08	6.99	9.26	-1.55
C08	7.04	10.15	0.69
C08	-7.16	9.35	-1.27
C08	-7.10	10.24	0.97
C09	7.72	9.7	-0.44
C09	-7.83	9.8	-0.14
C10	-2.86	8.53	-0.24
C10	2.73	8.49	-0.32
C11	-3.55	7.26	-0.16
C11	3.40	7.21	-0.30
C12	-2.59	6.3	-0.16
C12	2.43	6.26	-0.28
C13	-1.31	6.98	-0.24
C13	1.16	6.96	-0.27
C14	-0.08	6.31	-0.24
C15	-0.09	4.81	-0.21
C16	-0.52	4.07	-1.33
C16	0.32	4.113	0.93
C17	-0.53	2.68	-1.31
C17	0.31	2.71	0.96
C18	-0.12	1.99	-0.16
C24	0.99	9.75	-3.11
C24	-1.11	9.75	2.53
C25	-0.76	9.75	-4.45
C25	0.65	9.75	3.87
C26	-1.17	9.75	-3.15
C26	1.06	9.75	2.57
Fe	-0.10	9.75	-0.29
H01	2.62	14.27	-0.48
H01	-2.67	14.31	-0.30

Continued on next page

Table 1.14 – continued from previous page

Atom Name	X / Å	Y/ Å	Z / Å
H02	4.51	12.36	-0.49
H02	-4.58	12.43	-0.26
H03	5.03	8.92	-2.38
H03	5.13	10.51	1.61
H03	-5.24	9	-2.19
H03	-5.14	10.57	1.80
H04	7.50	8.91	-2.44
H04	7.60	10.5	1.56
H04	-7.71	9.01	-2.14
H04	-7.62	10.59	1.86
H05	8.80	9.69	-0.47
H05	-8.92	9.8	-0.11
H06	4.47	7.06	-0.31
H06	-4.62	7.14	-0.09
H07	2.55	5.19	-0.27
H07	-2.73	5.23	-0.10
H08	-0.84	4.60	-2.22
H08	0.65	4.66	1.80
H09	-0.86	2.13	-2.18
H09	0.63	2.19	1.85
H10	-0.13	0.9	-0.14
H13	2.02	9.75	-2.79
H13	-2.14	9.75	2.21
H14	1.24	9.75	-5.21
H14	-1.35	9.75	4.63
H15	-1.31	9.75	-5.38
H15	1.20	9.76	4.80
H16	-2.17	9.75	-2.75
H16	2.06	9.75	2.17
N01	-1.47	11.18	-0.29
N01	1.38	11.16	-0.30
N02	1.36	8.32	-0.29
N02	-1.50	8.34	-0.28
N03	-0.07	9.75	-2.31
N03	-0.05	9.75	1.73
N04	0.61	9.75	-4.41
N04	-0.73	9.75	3.83

Table 1.15: Cartesian coordinates of the rigid portion of the iron-porphyrin species $\mathbf{Fe^{II}Ph_2CO_2H}$ employed in calculation of $w_{\mathrm{p}}^{(1)}(R)$ and $w_{\mathrm{p}}^{(2)}(R)$

Atom Name	X / Å	Y/ Å	Z / Å
C00	0.01	-35.72	-0.22
C01	1.23	-35.02	-0.22
C01	-1.25	-35.10	-0.23
C02	2.52	-35.66	-0.14
C02	-2.50	-35.84	-0.24
C03	3.45	-34.67	-0.14
C03	-3.50	-34.91	-0.25
C04	2.73	-33.41	-0.22
C04	-2.86	-33.61	-0.27
C05	3.34	-32.15	-0.21
C05	-3.57	-32.40	-0.29
C06	4.84	-32.10	-0.19
C06	-5.07	-32.45	-0.31
C07	5.53	-31.63	0.95
C07	5.60	-32.53	-1.29
C07	-5.81	-32.03	0.80
C07	-5.76	-32.92	-1.44
C08	6.92	-31.58	0.97
C08	6.99	-32.48	-1.27
C08	-7.21	-32.07	0.78
C08	-7.15	-32.97	-1.46
C09	7.66	-32.01	-0.13
C09	-7.88	-32.54	-0.35
C10	2.64	-30.94	-0.24
C10	-2.95	-31.14	-0.29
C11	-3.67	-29.89	-0.37
C11	3.27	-29.64	-0.26
C12	-2.74	-28.90	-0.38
C12	2.28	-28.72	-0.28
C13	-1.45	-29.54	-0.30
C13	1.03	-29.45	-0.29
C14	-0.23	-28.84	-0.31
C15	-0.29	-27.34	-0.35
C16	-0.73	-26.61	0.77
C16	0.10	-26.63	-1.50
C17	-0.78	-25.21	0.73
C17	0.05	-25.24	-1.53
C18	-0.39	-24.52	-0.42
C24	0.95	-32.24	2.56
C24	-1.17	-32.31	-3.07
C25	-0.80	-32.30	3.91
C25	0.58	-32.26	-4.42
C26	-1.21	-32.31	2.61
C26	0.99	-32.24	-3.12
Fe	-0.11	-32.28	-0.26
H01	2.69	-36.72	-0.09
H01	-2.59	-36.91	-0.24

Continued on next page

Table 1.15 – continued from previous page

Atom Name	X / Å	Y/ Å	Z / Å
H02	4.52	-34.76	-0.08
H02	-4.56	-35.09	-0.25
H03	4.96	-31.30	1.81
H03	5.08	-32.89	-2.18
H03	-5.30	-31.67	1.68
H03	-5.19	-33.25	-2.31
H04	7.43	-31.22	1.86
H04	7.56	-32.81	-2.13
H04	-7.77	-31.75	1.66
H04	-7.67	-33.33	-2.34
H05	8.75	-31.97	-0.11
H05	-8.97	-32.58	-0.36
H06	4.34	-29.47	-0.25
H06	-4.75	-29.79	-0.43
H07	2.37	-27.64	-0.29
H07	-2.91	-27.83	-0.44
H08	-1.03	-27.14	1.66
H08	0.44	-27.18	-2.37
H09	-1.13	-24.67	1.61
H09	0.35	-24.71	-2.43
H10	-0.43	-23.44	-0.44
H13	1.98	-32.21	2.24
H13	-2.20	-32.34	-2.75
H14	1.20	-32.23	4.65
H14	-1.43	-32.32	-5.17
H15	-1.34	-32.32	4.84
H15	1.12	-32.24	-5.36
H16	-2.22	-32.35	2.22
H16	1.99	-32.21	-2.73
N01	-1.49	-33.75	-0.25
N01	1.37	-33.65	-0.25
N02	1.27	-30.81	-0.26
N02	-1.59	-30.91	-0.26
N03	-0.11	-32.28	1.77
N03	-0.11	-32.28	-2.28
N04	0.58	-32.25	3.86
N04	-0.80	-32.30	-4.38

References

[1] J. Stubbe, D. G. Nocera, C. S. Yee, and M. C. Y. Chang, Chem. Rev. **103**, 2167 (2003).

[2] M. H. V. Huynh and T. J. Meyer, Chem. Rev. **107**, 5004 (2010).

[3] J. J. Warren, T. A. Tronic, and J. M. Mayer, Chem. Rev. **110**, 6961 (2010).

[4] O. S. Wenger, Chem. Soc. Rev. **40**, 3538 (2011).

[5] A. Helms, D. Heiler, and G. McLendon, J. Am. Chem. Soc. **114**, 6227 (1992).

[6] E. A. Weiss, M. J. Ahrens, L. E. Sinks, A. V. Gusev, M. A. Ratner, and M. R. Wasielewski, J. Am. Chem. Soc. **126**, 5577 (2004).

[7] J. J. Warren, A. R. Menzeleev, J. S. Kretchmer, T. F. Miller, H. B. Gray, and J. M. Mayer, J. Phys. Chem. Lett. **4**, 519 (2013).

[8] A. Forneli, M. Planells, M. A. Sarmentero, E. Martinez-Ferrero, B. C. O'Regan, P. Ballester, and E. Palomares, J. Mater. Chem. **18**, 1652 (2008).

[9] R. Quinn, M. Nappa, and J. S. Valentine, J. Am. Chem. Soc. **104**, 2588 (1982).

[10] J. J. Warren and J. M. Mayer, J. Am. Chem. Soc. **130**, 7546 (2008).

[11] S. Hammes-Schiffer and A. A. Stuchebrukhov, Chem. Rev. **110**, 6939 (2010).

[12] C. Costentin, M. Robert, and J.-M. Savéant, J. Am. Chem. Soc. **129**, 9953 (2007).

[13] R. I. Cukier, J. Phys. Chem. **99**, 16101 (1995).

[14] S. J. Edwards, A. V. Soudackov, and S. Hammes-Schiffer, J. Phys. Chem. A **113**, 2117 (2009).

[15] R. A. Marcus and N. Sutin, Biochim. Biophys. Acta **811**, 265 (1985).

[16] H. B. Gray and J. R. Winkler, Biochim. Biophys. Acta **1797**, 1563 (2010).

[17] M. Cordes and B. Giese, Chem. Soc. Rev. **38**, 892 (2009).

[18] E. Hatcher, A. Soudackov, and S. Hammes-Schiffer, Chem. Phys. **319**, 93 (2005).

[19] J. Ulstrup, *Charge Transfer Processes in Condensed Media* (Springer-Verlag, Berlin, 1979).

[20] R. Cukier and D. Nocera, Annu. Rev. Phys. Chem. **49**, 337 (1998).

[21] J. Wang, R. Wolf, J. Caldwell, P. Kollman, and D. Case, J. Comput. Chem **25**, 1157 (2004).

[22] W. Smith and T. Forester, J. Mol. Graph. **14**, 136 (1996).

[23] D. A. Giammona, Ph.D. thesis, University of California, Davis (1984).

[24] J. Wang, W. Wang, P. A. Kollman, and D. A. Case, J. Mol. Graph. Model. **25**, 247 (2006).

[25] E. Guardia, R. Pinzon, J. Casulleras, M. Orozco, and F. Luque, Mol. Simulat. **26**, 287 (2001).

[26] C. L. Brooks, B. M. Pettitt, and M. Karplus, J. Chem. Phys. **83**, 5897 (1985).

[27] M. J. Frisch, G. W. Trucks, H. B. Schlegel, G. E. Scuseria, M. A. Robb, J. R. Cheeseman, G. Scalmani, V. Barone, B. Mennucci, G. A. Petersson, H. Nakatsuji, M. Caricato, X. Li, H. P. Hratchian, A. F. Izmaylov, J. Bloino, G. Zheng, J. L. Sonnenberg, M. Hada, M. Ehara, K. Toyota, R. Fukuda, J. Hasegawa, M. Ishida, T. Nakajima, Y. Honda, O. Kitao, H. Nakai, T. Vreven, J. A. Montgomery, Jr., J. E. Peralta, F. Ogliaro, M. Bearpark, J. J. Heyd, E. Brothers, K. N. Kudin, V. N. Staroverov, R. Kobayashi, J. Normand, K. Raghavachari, A. Rendell, J. C. Burant, S. S. Iyengar, J. Tomasi, M. Cossi, N. Rega, J. M. Millam, M. Klene, J. E. Knox, J. B. Cross, V. Bakken, C. Adamo, J. Jaramillo, R. Gomperts, R. E. Stratmann, O. Yazyev, A. J. Austin, R. Cammi, C. Pomelli, J. W. Ochterski, R. L. Martin, K. Morokuma, V. G. Zakrzewski, G. A. Voth, P. Salvador, J. J. Dannenberg, S. Dapprich, A. D. Daniels, Ö. Farkas, J. B. Foresman, J. V. Ortiz, J. Cioslowski, and D. J. Fox, "Gaussian 09 Revision B.01," (2009).

[28] J. Tomasi, B. Mennucci, and E. Cancés, J. Mol. Struct: Theochem **464**, 211 (1999).

[29] J. Tomasi, B. Mennucci, and R. Cammi, Chem. Rev. **105**, 2999 (2005).

[30] G. Scalmani and M. J. Frisch, J. Chem. Phys. **132** (2010).

[31] J. Pascual-Ahuir, E. Silla, and I. Tunon, J. Comput. Chem. **15**, 1127 (1994).

[32] C. M. Breneman and K. B. Wiberg, J. Comput. Chem. **11**, 361 (1990).

[33] T. F. Miller, M. Eleftheriou, P. Pattnaik, A. Ndirango, D. Newns, and G. Martyna, J. Chem. Phys. **116**, 8649 (2002).

[34] S. Kumar, D. Bouzida, R. Swendsen, P. Kollman, and J. Rosenberg, J. Comput. Chem. **13**, 1011 (1992).

[35] S. Kumar, J. Rosenberg, D. Bouzida, R. Swendsen, and P. Kollman, J. Comput. Chem **16**, 1339 (1995).

[36] E. Hatcher, A. Soudackov, and S. Hammes-Schiffer, J. Am. Chem. Soc. **126**, 5763 (2004).

[37] N. Iordanova, H. Decornez, and S. Hammes-Schiffer, J. Am. Chem. Soc. **123**, 3723 (2001).

[38] S. Nelsen, S. Blackstock, and Y. Kim, J. Am. Chem. Soc. **109**, 677 (1987).

[39] T. F. Markle and J. M. Mayer, Angew. Chem. Int. Ed. **47**, 738 (2008).

[40] E. Sigfridsson, M. Olsson, and U. Ryde, J. Phys. Chem. B **105**, 5546 (2001).

[41] E. Sigfridsson and U. Ryde, JBIC Journal of Biological Inorganic Chemistry **8**, 273 (2003).

[42] A. Warshel, A, J. Phys. Chem. **86**, 2218 (1982).

[43] G. King and A. Warshel, J. Chem. Phys. **93**, 8682 (1990).

[44] D. Small, D. Matyushov, and G. Voth, J. Am. Chem. Soc. **125**, 7470 (2003).

[45] M. V. Basilevsky, I. V. Rostov, and M. D. Newton, Chem. Phys. **232**, 189 (1998).

[46] M. D. Newton, M. V. Basilevsky, and I. V. Rostov, Chem. Phys. **232**, 201 (1998).

[47] WebPCET ApplicationSserver, http://webpcet.scs.uiuc.edu/main.html. University of Illinois at Urbana-Champaign, (2009).

Chapter 2

Ring polymer molecular dynamics beyond the linear response regime: Excess electron injection and trapping in liquids

2.1 Introduction

Excess electron injection and localization in liquids is a prototype for coupled electronic and nuclear dynamics and for solvent dynamics beyond the linear response regime. As such, this process has received both experimental[1–15] and theoretical[16–24] attention. A widely used method for simulating electron injection, as well as many other electronically non-adiabatic processes, is mixed quantum-classical dynamics (MQCD),[16,25–28] in which the excess electron is evolved in the wavefunction representation and the solvent is evolved using classical molecular dynamics. Here, we consider the alternative use of ring polymer molecular dynamics (RPMD)[29,30] to simulate the dynamics of excess electron injection into fluid helium and liquid water.

We recently put forward RPMD as a model for the direct simulation of quantum mechanical systems, and we demonstrated that this model accurately describes the dynamics of an excess electron in dense fluid helium near thermal equilibrium.[31] RPMD, like centroid molecular dynamics (CMD),[32–34] employs the path integral representation[35,36] to yield an approximate classical molecular dynamics model for the real-time simulation of quantum dynamics. The model dynamics rigorously preserves the quantum Boltzmann distribution,[37,38] it allows for the simulation of long dynamical trajectories, and it provides a consistent framework for simulating both quantum mechanical and classical mechanical degrees of freedom. In the current study, we employ RPMD to simulate excess electron injection, a process that involves dynamics far from equilibrium, and we compare the mechanisms and timescales obtained from the RPMD model with those from previous MQCD simulations.

The remainder of the paper is organized as follows. In Section 3.2, we describe our method for simulating the excess electron injection using RPMD. In Section 2.3.1 we discuss the high-energy and low-energy injection of an excess electron into the supercritical helium fluid, a simple model for

a dense classical liquid. In Section 2.3.2, we similarly discuss the injection of an excess electron into ambient liquid water. Concluding remarks are presented in Section 4.6.

2.2 Methods

2.2.1 Ring polymer molecular dynamics

A quantized excess electron is simulated in a classical solvent of either helium or water. For both cases, the RPMD equations of motion are[29]

$$\dot{\mathbf{v}}^{(\alpha)} = \omega_n^2(\mathbf{q}^{(\alpha+1)} + \mathbf{q}^{(\alpha-1)} - 2\mathbf{q}^{(\alpha)}) - \frac{1}{m}\nabla_{\mathbf{q}^{(\alpha)}} U(\mathbf{q}^{(\alpha)}, \mathbf{Q}_1, \ldots, \mathbf{Q}_N), \quad \alpha = 1 \ldots n, \tag{2.1}$$

$$\dot{\mathbf{V}}_j = -\frac{1}{nM_j}\sum_{\alpha=1}^{n} \nabla_{\mathbf{Q}_j} U(\mathbf{q}^{(\alpha)}, \mathbf{Q}_1, \ldots, \mathbf{Q}_N), \quad j = 1 \ldots N. \tag{2.2}$$

Here, n is the number of ring polymer beads for the quantized electron, N is the number of atoms in the classical solvent, and $\mathbf{q}^{(\alpha)}$ and $\mathbf{Q}_j$ are the respective positions of the electron beads and solvent atoms, such that $\mathbf{q}^{(0)} = \mathbf{q}^{(n)}$. Similarly, $\mathbf{v}^{(\alpha)}$ and $\mathbf{V}_j$ are the respective velocities of the electron beads and solvent atoms, and m and M_j are the corresponding masses. The intra-bead harmonic frequency is given by $\omega_n = n/(\beta\hbar)$, where β is the reciprocal temperature. The notation $\{\mathbf{q}\} = \{\mathbf{q}^{(1)}, \ldots, \mathbf{q}^{(n)}\}$ and $\{\mathbf{Q}\} = \{\mathbf{Q}_1, \ldots, \mathbf{Q}_N\}$ will hereafter be used to describe the full set of ring polymer bead positions and solvent atom positions, respectively. Eqs. 2.1 and 2.2 generate a classical dynamics that we employ as a model for the real-time dynamics of the system.[31]

The system is described using a potential energy function, $U(\mathbf{q}, \{\mathbf{Q}\})$, that is a sum of solvent-solvent, $U_{\text{s-s}}(\{\mathbf{Q}\})$, and electron-solvent, $U_{\text{e-s}}(\mathbf{q}, \{\mathbf{Q}\})$, interactions. As in our previous study,[31] we describe the electron-helium system using the interaction potentials adopted by Berne, Coker, and coworkers.[39,40] For the case of an excess electron in water, we employed the simple point charge (SPC) rigid water model[41] and the Schnitker-Rossky pseudopotential for the electron-water interactions.[42] Although more recent water-electron pseudopotentials have been developed,[43–46] and issues related to the accuracy of the Schnitker-Rossky pseudopotential have been raised,[47,48] our choice was made to aid comparison with previous simulations of electron injection.[17,19,22]

2.2.2 RPMD model for electron injection

Experimental electron injection can be achieved using photo-ionization of a solvent molecule or another donor species.[1,2,13,49] This process can be theoretically modeled as the sudden introduction of an excess electron to a configuration of the neat fluid that is drawn from its equilibrium Boltzmann distribution at temperature T,[19]

$$P_T(\{\mathbf{Q}\}) \propto \exp[-U_{\text{s-s}}(\{\mathbf{Q}\})/(k_{\text{B}}T)]. \tag{2.3}$$

Previous MQCD simulation studies initialized the excess electron in Born-Oppenheimer states within a specified energy range,[17,21] but the RPMD model represents the electron in the position basis rather than the basis of electronic states. Although it would be possible to project the distribution of electrons onto a specific energy eigenstate, we instead modulate the energy of the injected electron via its initial temperature. The excess electron and solvent are initially distributed according to

$$P_0(\mathbf{q}, \{\mathbf{Q}\}; T, T') = P_T(\{\mathbf{Q}\}) P_{T'}(\mathbf{q}|\{\mathbf{Q}\}), \tag{2.4}$$

where the second term is a conditional probability distribution function for the electron at temperature T' subject to a given solvent configuration,

$$P_{T'}(\mathbf{q}|\{\mathbf{Q}\}) = \frac{\int d\mathbf{q}^{(1)} \dots d\mathbf{q}^{(n)}\ \delta(\mathbf{q} - \bar{\mathbf{q}})\ \exp[S(\{\mathbf{q}\}, \{\mathbf{Q}\}; T')]}{\int d\mathbf{q}^{(1)} \dots d\mathbf{q}^{(n)}\ \exp[S(\{\mathbf{q}\}, \{\mathbf{Q}\}; T')]}. \tag{2.5}$$

Here, $S(\{\mathbf{q}\}, \{\mathbf{Q}\}; T)$ describes the action for the electron ring polymer coupled to the liquid at temperature T,[50]

$$S(\{\mathbf{q}\}, \{\mathbf{Q}\}; T) = -\frac{1}{nk_{\text{B}}T} \sum_{\alpha=1}^{n} \left(\frac{1}{2} m\omega_n^2 (\mathbf{q}^{(\alpha)} - \mathbf{q}^{(\alpha+1)})^2 + U(\mathbf{q}^{(\alpha)}, \{\mathbf{Q}\}) \right), \tag{2.6}$$

and $\bar{\mathbf{q}} = n^{-1} \sum_{\alpha=1}^{n} \mathbf{q}^{(\alpha)}$ is the position of the ring polymer centroid.

We consider initial distributions corresponding to both high-energy ("hot") and low-energy ("cold") electron injection. For hot electron injection, we choose T' to ensure that the Boltzmann distribution occupies a significant fraction of electronically excited states. For cold electron injection, we choose $T' = T$, such that the excess electron is initialized at the same temperature as the neat liquid. Following previous simulations,[16,19–21] we employ $T = 309$ K for the simulations

with helium and $T = 300$ K for the simulations with water. For hot injection into both solvents, we employed $T' = 5000$ K. For the potential energy functions employed here, these parameters ensure that cold electron injection leads to an initial excess electron population that is almost entirely in the ground state. However, for hot electron injection into helium, approximately 75% of the initial excess electron population occupies electronically excited states; for hot electron injection into water, approximately 85% of the population initially occupies electronically excited states.

The RPMD simulation protocol for electron injection is implemented as follows: (1) Representative configurations of the neat liquid at equilibrium are generated from long molecular dynamics trajectories at constant temperature T. Independent solvent configurations are sampled from these trajectories. (2) Keeping the solvent configuration fixed, the ring polymer for an excess electron is introduced to the system and equilibrated using molecular dynamics at constant temperature T'. (3) Keeping both the solvent configuration and the centroid of the ring polymer fixed, the internal modes of the ring polymer are equilibrated at temperature T. This step is redundant, and thus skipped, for the cold electron injection simulations where $T = T'$. (4) The combined electron-solvent dynamics are evolved according to the RPMD equations of motion in Eqs. 2.1 and 2.2. The initial velocities for the solvent atoms and the ring polymer beads are drawn from the Maxwell-Boltzmann distribution at temperature T.

Our model for electron injection is inspired by the path integral molecular dynamics work of Parrinello and Rahman, in which an excess electron localizes in a molten KCl salt.[37] Of course, these earlier simulations were taken as a demonstration of the thermodynamic favorability of the localized electron, whereas we emphasize the ring polymer trajectory as a model for real-time dynamics. The details of our RPMD initialization protocol were chosen so that the ensemble of RPMD trajectories are equivalent in the short-time limit to the ensemble of partially adiabatic CMD trajectories[51,52] initialized from the non-equilibrium distribution in Eq. 2.4. In the Appendix, we provide further justification for this protocol by demonstrating that it is consistent with the RPMD approximation for a Kubo-transformed correlation function for which the system is initialized in a non-equilibrium distribution.

2.2.3 One-electron energy eigenvalue calculations

As a means of analyzing the dynamics of electron injection and localization, the excess electron energy levels and eigenfunctions were calculated for the time-series of solvent configurations harvested from the RPMD trajectories. At each configuration, the one-electron eigenvalue problem was solved

using the iterative-and-block Lanczos scheme put forward by Webster, et. al.[16] It is emphasized that these eigenvalue calculations are not necessary for evolving the RPMD equations of motion; the time-series of eigenvalues for the excess electron are extracted *a posteriori* from the completed trajectories.

2.2.4 Simulation details

Simulations were performed by implementing the RPMD method within the DL_POLY2.19 molecular dynamics package.[53] The equations of motion were integrated using the velocity Verlet algorithm.[54] As in previous RPMD applications,[31,55–61] the ring polymer coordinates were updated at each timestep due to the forces arising from the solvent potential ($-\nabla_{\mathbf{q}^\alpha} U(\mathbf{q}^\alpha, \mathbf{Q}_1, \ldots, \mathbf{Q}_\mathrm{N})$) and due to the exact evolution of the purely harmonic portion of the ring polymer potential. The resulting integration algorithm is time reversible and symplectic.[62]

The helium-electron simulation employed periodic boundary conditions with a cubic simulation cell of side length $L = 26.47$ Å. The system consists of 1000 helium atoms and a single ring polymer. These parameters correspond to a reduced solvent density of $\rho^* = 0.9$. All interactions were truncated at 6.4 Å. As is discussed in the results section, additional simulations for the electron in helium were also employed using 4096 helium atoms in a cubic simulation box of side length $L = 42.36$ Å, which corresponds to the same helium density.

The water-electron simulation employed periodic boundary conditions with a cubic simulation cell of side length of $L = 31.08$ Å. The system consists of 1000 classical SPC water molecules and the ring polymer for a single excess electron. Short-ranged interactions were truncated and shifted with a cutoff distance of 9 Å. Long-range electrostatic interactions between water molecules were included via Ewald summation. Following previous simulations of the excess electron in water,[17,19,22,63] electrostatic interactions between the electron and the water molecules were truncated and shifted, and rigid-body constraints for the water molecules were enforced via the RATTLE algorithm.[64]

Unless otherwise specified, the electron was represented in all simulations by a ring polymer of $n = 1024$ beads, which has been shown to yield adequate convergence for the path integral discretization in both systems.[40,65] The real-time RPMD trajectories were evolved with a timestep of 5×10^{-4} fs. For both hot and cold electron injection in both water and helium solvents, one hundred injection trajectories (step 4 in the above protocol) were each evolved for 1 picosecond. The system configuration was recorded during the trajectories at every femtosecond. We note that by employing a classical treatment of the water and helium solvent, we avoid the possibility of

unphysical coupling between the electron ring polymer dynamics and internal ring polymer modes of the solvent degrees of freedom.[61]

The details for the equilibration of the injected electron (steps 2 and 3 in the above protocol) are as follows. For hot injection, step 2 was performed using an RPMD simulation of length 150 fs for the electron with fixed solvent positions. Step 3 was performed using an RPMD simulation of length 300 fs, fixing the solvent positions and the ring polymer centroid position. For cold injection, steps 2 and 3 were combined into a single RPMD trajectory of length 300 fs with fixed solvent positions. These equilibration runs were thermostatted by resampling the velocities from the Maxwell-Boltzmann distribution every 3 fs. To more efficiently sample the ring polymer particle density for cold electron injection, the equilibration runs in step 2 were initialized with the ring polymer in the region of the large ground-state wavefunction density. As a convergence check, the length of the equilibration trajectories for both solvents were doubled, and it was confirmed that the average for the ring polymer radius of gyration in the equilibration trajectories was converged.

For the simulations in both solvents, the electronic energy eigenstates were calculated once every two femtoseconds using a uniform grid of $32 \times 32 \times 32$ points that spanned the simulation cell. The grid density and the interaction cutoffs are consistent with those employed in previous MQCD simulations of electron injection and photoexcitation.[17,20–22,66,67] The iterative Lanczos calculation of the adiabatic eigenstates employed 650 Krylov vectors with the exponential transform parameter (β in Ref. 16) of 0.1. The block Lanczos correction used ten blocks of 16 vectors. For the case of an excess electron in water, the eigenvalue calculations employed a smooth spherical cutoff[68] for all interactions between 7.5 and 8.0 Å, and for the eigenvalue calculations of an electron in helium, interactions were truncated and shifted at 6.4 Å. The analysis of Turi and Borgis indicates that these parameters lead to adequate convergence.[43]

Finally, we note that for a small fraction of trajectories, our hot injection protocol led to configurations in which the electron ring polymer spans the entire periodic simulation cell. In one extreme case, a single periodic replica of the ring polymer was stretched between two different periodic replicas of a solvent cavity; this unphysical configuration was metastable on the timescale of picoseconds. To mitigate this system size effect, we systematically discarded any trajectory in which a given solvent atom was within a distance s of beads from two different periodic replicas of the ring polymer for a combined time of more than 20 fs. For helium, we used $s = 3$ Å, and for water, we used $s = 4$ Å. This led to the rejection of approximately 3% of trajectories for helium simulations and 1% for water. A larger simulation cell would naturally lead to an ensemble of trajectories that

is less biased by this artifact.

2.3 Results and discussion

We employ the RPMD model to investigate electron injection and localization in dense molecular liquids. Both the short-time limit upon injection and the long-time limit following injection are well understood from a statistical perspective.[69] The process by which the system responds after electron injection, however, involves additional challenges due to coupled electronic and nuclear dynamics on the subpicosecond timescale.

For the simulations in both water and helium, the electron is injected into a solvent configuration that is characteristic of the neat liquid. At short times, the electron experiences a rugged potential energy landscape with cavities that correspond to density fluctuations in the liquid. The electronic ground state is spatially localized in the disordered solvent environment,[70] but higher excited states form a conduction band of extended electronic eigenstates.[18,71]

In the limit of long simulation times, the system equilibrates with the electron strongly localized, or trapped, in a cage of solvent molecules.[69] The thermodynamic driving force for the trapping of the excess electron arises from a tradeoff between stabilizing the electronic eigenstates and the penalty of creating a solvent cavity that is large enough to confine the excess electron. The lowest energy electronic states correspond to a nearly spherical s-type state and up to three p-type states for the solvents considered here.[17,18]

The dynamics of electron injection in liquids involves large-scale solvent rearrangements coupled to the non-adiabatic dynamics of the excess electron. It is a benchmark for the simulation of coupled electronic and nuclear dynamics, following the seminal MQCD work of Coker, Berne, and coworkers for an electron in helium[18,20,21] and by Rossky, Friesner, and coworkers for an electron in water,[16,17,19] and it remains a topical challenge for both theory and experiment. These earlier MQCD trajectories identified mechanisms and timescales for the localization dynamics of the excess electron that provide a basis for comparison with the RPMD model employed here.

2.3.1 Injection of an excess electron into supercritical helium

2.3.1.1 From the perspective of the electron

Figure 2.1 presents a typical RPMD trajectory for cold electron injection into the helium fluid. Fig. 2.1(a) displays the time-series for the ring polymer radius of gyration and the excess electron

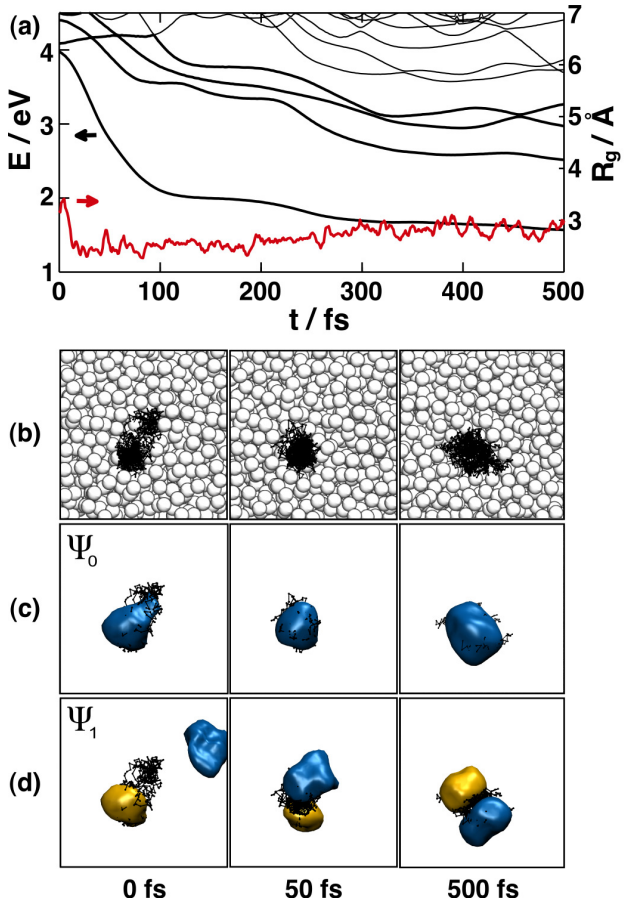

Figure 2.1: A typical RPMD trajectory for cold electron injection into supercritical helium. **(a)** The time-series for the lowest excess electron eigenenergies (black) and the ring polymer radius of gyration (red). **(b)** Snapshots of the ring polymer (black) and solvent configurations from the RPMD trajectory. **(c)** and **(d)** The corresponding snapshots of the ground state (c) and first excited state (d) excess electron wavefunctions, visualized as 95% isosurfaces.

eigenspectrum. The radius of gyration, R_g, is calculated from the configuration of the ring polymer using

$$R_{\mathrm{g}}^2 = \frac{1}{n}\sum_{\alpha=1}^{n}(\mathbf{q}^{(\alpha)} - \bar{\mathbf{q}})^2. \tag{2.7}$$

Fig. 2.1(b) shows snapshots of the ring polymer at various times along the injection trajectory, and Figs. 2.1(c) and (d) show the corresponding snapshots for the ground state (Ψ_0) and first excited state (Ψ_1) eigenfunctions. As was previously discussed, the trajectory is evolved according to the RPMD equations of motion, and the eigenstates for the excess electron are calculated afterwards for the purpose of analysis.

For cold electron injection, the ground state dominates the initial electron population. It is thus

reasonable in Fig. 2.1 that the ring polymer occupies the region of space for which the ground-state wavefunction is most probable. As the RPMD trajectory evolves in time, $R_g(t)$ for the ring polymer rapidly decreases and approaches the equilibrium average value of 2.6 Å. On a similar timescale, the solvent molecules rearrange to accommodate the excess electron in a solvent cavity. Formation of the solvent cavity is indicated by the decreasing energy of the lowest eigenstates that form the trapped states for the electron. The instantaneous configurations of the solvent cavity are not perfectly symmetrical, so the p-like excited states of the trapped electron are nondegenerate.

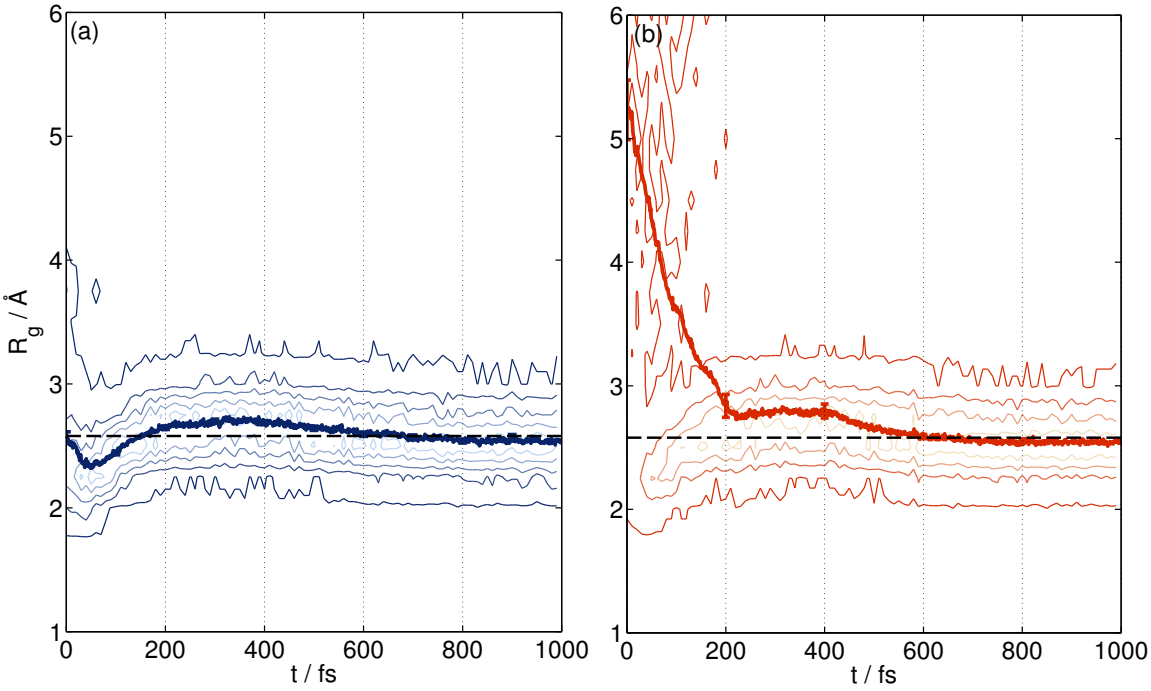

Figure 2.2: Ring polymer radius of gyration following **(a)** cold injection and **(b)** hot injection of the excess electron in helium. The contour plot indicates the distribution of $R_g(t)$ from the ensemble of RPMD trajectories, the heavy colored lines indicates the non-equilibrium average taken over trajectories $\langle R_g(t) \rangle$, and the black dashed line indicates the average from an equilibrium simulation.

The majority of trajectories following cold electron injection are qualitatively similar to that shown in Fig. 2.1. To extract a statistically meaningful description, however, we consider the ensemble of RPMD trajectories for electron injection. In Fig. 2.2(a), we present the radius of gyration of the excess electron in fluid helium, $\langle R_g(t) \rangle$, where the angle-brackets indicate the non-equilibrium average over RPMD trajectories at time t after injection. Also shown in this figure is the contour plot for the distribution of $R_g(t)$ from the ensemble of trajectories. Both the average and the distribution exhibit behavior that is consistent with the trajectory in Fig. 2.1. The electron initially collapses into a nascent solvent cavity within 50 fs, the solvent cavity then expands so that

$\langle R_g(t) \rangle$ exceeds the equilibrium value at approximately 300 fs, and the system subsequently relaxes towards equilibrium at longer times.

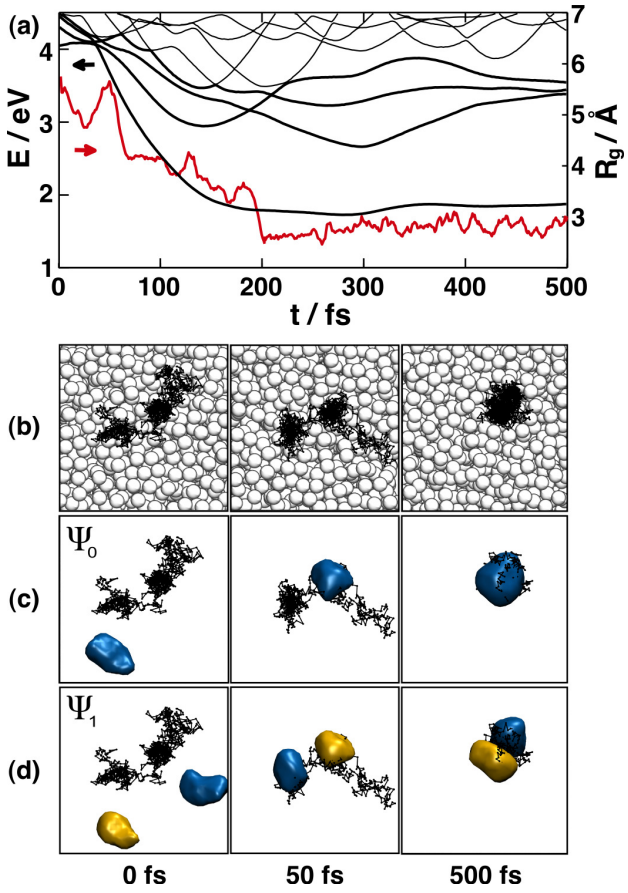

Figure 2.3: A typical RPMD trajectory for hot electron injection into supercritical helium. **(a)** The time-series for the lowest excess electron eigenenergies (black) and the ring polymer radius of gyration (red). **(b)** Snapshots of the ring polymer (black) and solvent configurations from the RPMD trajectory. **(c)** and **(d)** The corresponding snapshots of the ground state (c) and first excited state (d) excess electron wavefunctions.

Hot electron injection exhibits an additional mechanism for localization. Along with the one-cavity localization pathway seen in cold electron injection, the hot injection trajectories reveal that the electron transiently occupies multiple solvent cavities at the same time. Fig. 2.3 presents one such trajectory. Fig. 2.3(b) shows that the ring polymer is initially extended in the solvent, and it collapses into a metastable, multi-cavity configuration within 50 fs. As the solvent undergoes further rearrangement, the ring polymer collapses into two distinct solvent cavities at 70 fs and then a single cavity at approximately 200 fs. Figs. 2.3(c) and 2.3(d) reveal that the ring polymer configuration

is more consistent with the density of the first excited state wavefunction than the ground state wavefunction at 50 fs following injection.

This multi-cavity mechanism for localization following hot injection is further illustrated in Fig. 2.2(b). In a large fraction of the hot injection trajectories, the ring polymer fully localizes on the 50 fs timescale, as was seen in cold injection. However, a significant number of trajectories exhibit extended ring polymer configurations that survive for hundreds of femtoseconds. The longest multi-cavity configurations persist for approximately 400 fs in our ensemble of hot injection trajectories for helium.

2.3.1.2 From the perspective of the solvent

The solvent dynamics during electron localization was investigated by computing the time-resolved electron-helium radial distribution function, $\langle g_{\mathrm{e-He}}(r,t)\rangle$, for the distance between the ring polymer centroid and the solvent helium atoms. Here, $g_{\mathrm{e-He}}(r,t)$ refers to the radial distribution function from a single configuration of the system at time t after injection, and the angle-brackets indicate the non-equilibrium average over RPMD trajectories at time t. Fig. 2.4(a) presents $\langle g_{\mathrm{e-He}}(r,t)\rangle$ for cold electron injection. Even at very short times, the electron ring polymer is localized within a solvent cavity, as is seen by the depletion of helium atom density near the centroid of the ring polymer. However, the initial solvent cavity is smaller than at equilibrium, and it expands rapidly as the solvent atoms are expelled from the neighborhood of the electron. As is seen from the 80% contour line plotted in the figure, the solvent cavity expands to a radius of approximately 4.5 Å by 200 fs, and this rapid expansion creates a compression wave in the helium fluid (indicated by the dashed line in the figure). The wave of high solvent density travels outward at 28 Å/ps, reaching the edge of the periodic simulation cell by approximately 350 fs. The solvent cavity subsequently contracts to a radius of approximately 4 Å at 800 fs, at which time a recurrence of high solvent density at the edge of the electron cavity is also observed. The origin of this interesting recurrence will be discussed below. The creation of compression waves during electron localization and solvent cavity expansion was previously explored in density functional theory calculations involving liquid helium at lower density and temperature.[23] We expect that solvent compression waves also appear in MQCD simulations of electron injection in helium, although to our knowledge, Fig. 2.4 presents the first report of these waves in a simulation with explicit solvent. The corresponding plot for hot electron injection (Fig. 2.4(b)) shows significant density near $r = 0$ at short times following injection. Furthermore, the 80% contour line in Fig. 2.4(b) intercepts the y-axis at a considerably smaller value

than in Fig. 2.4(a). These features indicate the presence of helium atoms near the centroid of the ring polymer due to trajectories in which the electron ring polymer initially spans multiple solvent cavities. By 200 fs, this feature has disappeared, which is consistent with the timescale for the ring polymer localization in Fig. 2.2(b). At longer times, solvent dynamics for hot injection are similar to those for cold electron injection.

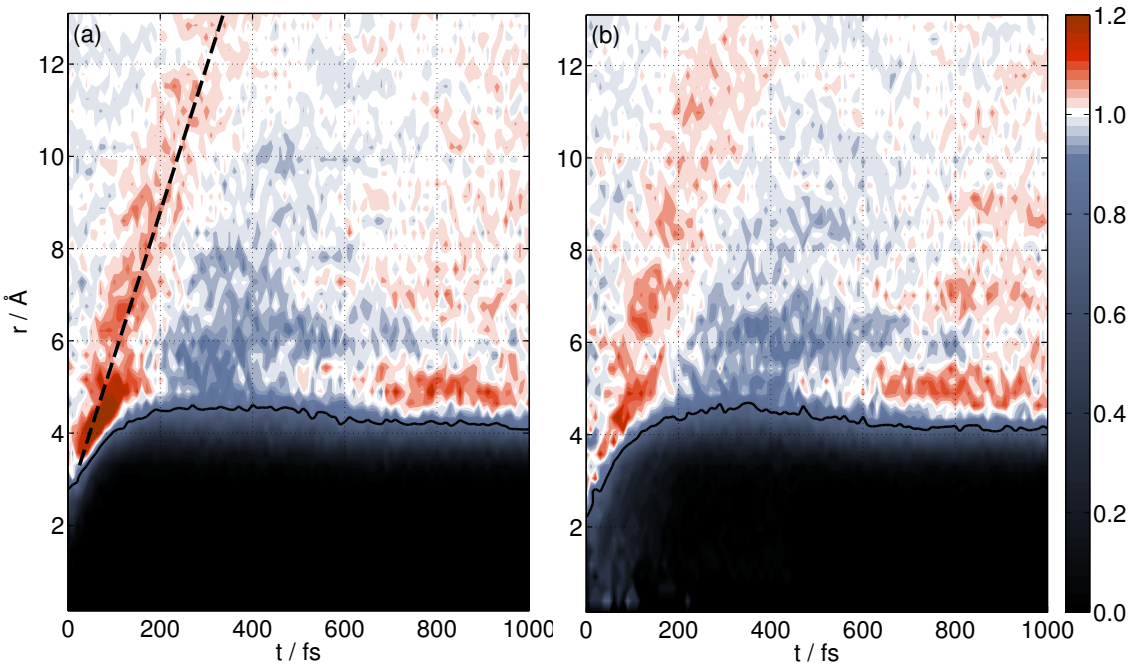

Figure 2.4: Time-resolved radial distribution function $\langle g_{\mathrm{e-He}}(r,t)\rangle$ for the helium atoms with respect to the electron ring polymer centroid as a function of time for **(a)** cold injection and **(b)** hot injection. In both parts, the contour line indicates 80% of the average solvent density. The dashed line in part (a) indicates the outward solvent compression wave following electron localization.

The eigenenergies of the excess electron provide another means of analyzing the solvent dynamics. In Fig. 2.5, we present the excess electron energy eigenstates following both cold and hot electron injection, obtained from the non-equilibrium average over the ensemble of RPMD trajectories. As was seen in the individual trajectories in Figs. 2.1 and 2.3, the lowest states rapidly drop in energy as the electron localizes. Past 200 fs, the average eigenenergies oscillate on the same timescale as the solvent cavity size seen in Fig. 2.4. This relationship between the electron energy levels and the size of the solvent cavity is expected from a simple square-well picture for the localized electron. Solvent cavity oscillations have been experimentally observed following electron cavity expansion in low-temperature, low-density liquid helium,[72] but it is not obvious that such a large effect would survive in the more dense and viscous solvent regime considered here.[23,24,72]

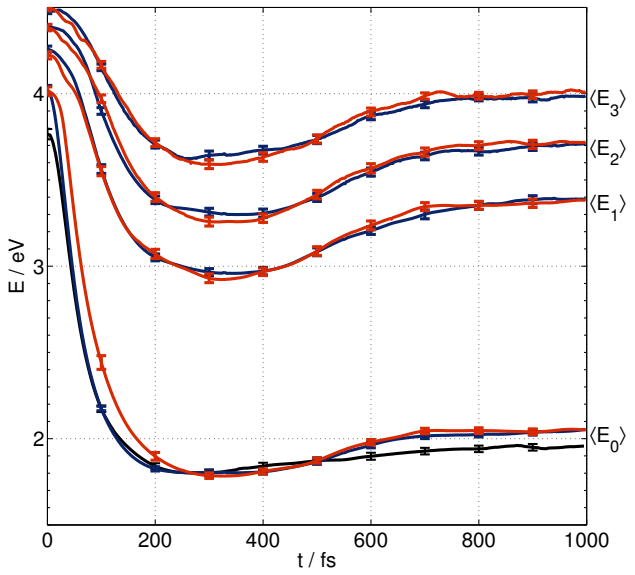

Figure 2.5: The four lowest electron eigenenergies, obtained from the non-equilibrium average for RPMD trajectories following cold (blue) and hot (red) injection into the helium fluid. The black curve shows the corresponding ground-state result from the cold injection simulations with 4096 helium atoms. The black line exhibits a lower initial ground state energy for the electron because the larger system size supports larger solvent density fluctuations in the neat fluid, even at the same average fluid density.

At 800 fs following electron injection, both Figs. 2.4(a) and 2.4(b) exhibit a pronounced recurrence of solvent density at the edge of the solvent cavity. One possible explanation for this feature is that electron localization drives atoms in the first solvation shell of the electron to collide with atoms in the second shell and ballistically rebound, causing a recurrence of solvent density at the cavity edge. But it is also possible that this feature appears when the outgoing solvent compression wave from the electron reaches its periodic neighbor. (Note that at 28 Å/ps, the solvent compression will begin arriving at the neighboring solvent cavity image at approximately 650 fs.) To determine whether the result is physically significant or a simulation artifact, we repeated the cold electron injection trajectories at the same solvent density but in a simulation cell for which the side length is increased by approximately 60%.

In Fig. 2.6, we present the $\langle g_{\mathrm{e-He}}(r,t)\rangle$ obtained from these larger simulations in helium. The initial solvent dynamics are similar to those found in the smaller cell. A solvent cavity rapidly expands, driven by the localization of the excess electron, and a solvent compression wave propagates outward from the cavity at the same rate. However, for the larger simulations, the oscillation in the cavity size is less dramatic, and the recurrence of large solvent density at the edge of the solvent cavity is significantly delayed in comparison to Fig. 2.4. This result suggests that while the outgoing

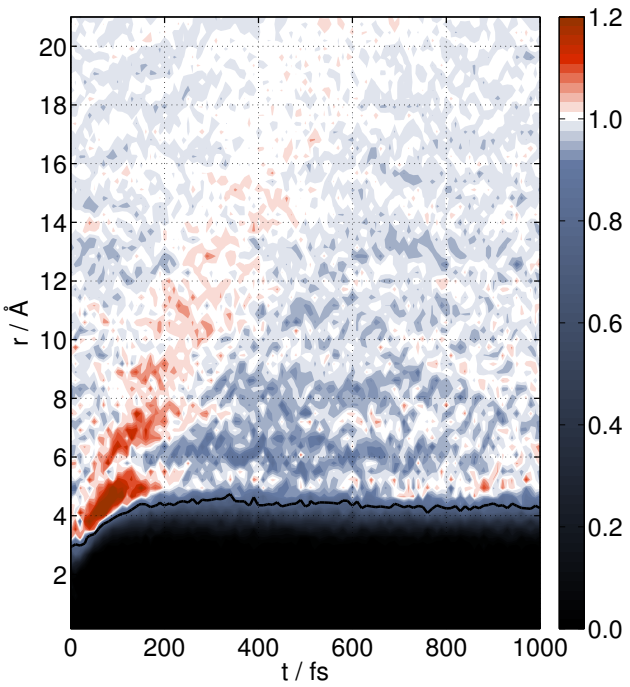

Figure 2.6: Time-resolved radial distribution function $\langle g_{\mathrm{e-He}}(r,t)\rangle$ following cold injection in the larger simulations with 4096 helium atoms, to be compared with Fig. 2.4(a).

compression wave is physically genuine, the pronounced recurrence of solvent density at the cavity edge is caused by the finite system size of the simulations. The conclusion is further supported by our calculation of the trajectory-averaged electron ground-state energy for the larger system, plotted as a black line in Fig. 2.5. The rebound of the ground state energy is much less dramatic at 800 fs in the larger system, because the compression wave from the neighboring periodic replica has not yet arrived. We emphasize that the system size effect is not an artifact of the RPMD model, and we expect that it also appears in MQCD simulations.

The qualitative mechanisms and timescales observed in our RPMD simulations are similar to those reported previously in MQCD simulations of electron injection into helium.[21] Injecting hot electrons at an energy of 0.5 eV above the instantaneous ground state energy, Space and Coker also found two distinct pathways for electron localization. For an ensemble of 15 MQCD trajectories, most trajectories exhibited non-adiabatic electron relaxation of the electron to single-cavity state in $50-100$ fs, followed by solvent cavity expansion over the next $100-200$ fs. In a few trajectories, however, the electron was trapped in an excited state, and remained in a two-cavity configuration for $300-400$ fs before ultimately completing its relaxation in a single cavity. The total excited-state survival time for such "hung" trajectories was $600-700$ fs. While we do observe a similar

multi-cavity relaxation mechanism in the RPMD simulation, our timescale for the relaxation of these configurations is more rapid, with all 100 RPMD trajectories collapsing into a single cavity within 400 fs.

2.3.1.3 Adiabatic versus non-adiabatic dynamics

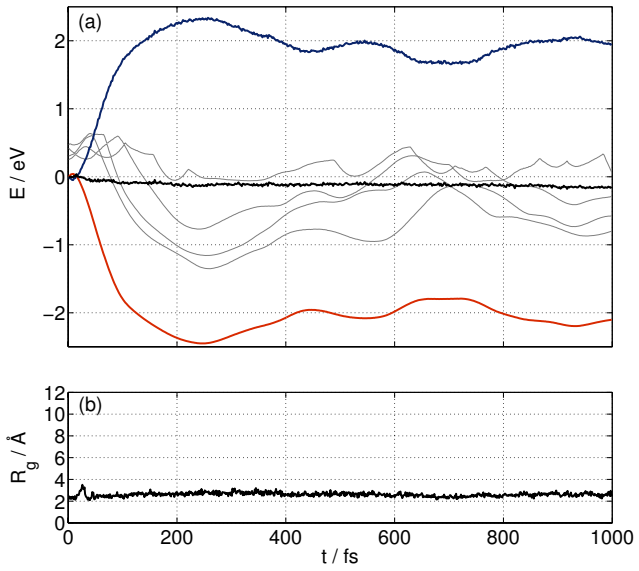

Figure 2.7: An illustrative cold injection trajectory in helium, showing the time-series for **(a)** various energy components and **(b)** the ring polymer radius of gyration. In part (a), the blue curve presents $K_{\mathrm{s}}(\{\mathbf{V}(t)\}) + U_{\text{s-s}}(\{\mathbf{Q}(t)\})$, the sum of the solvent kinetic energy term and the solvent-solvent potential energy term, the red curve plots the electronic ground state energy $E_0(\{\mathbf{Q}(t)\})$, the gray curve plots other low-lying electronic eigenenergies, and the heavy black curve plots the ground-state Born-Oppenheimer Hamiltonian, $H_{\mathrm{BO}}(t) = K_{\mathrm{s}}(\{\mathbf{V}(t)\}) + U_{\text{s-s}}(\{\mathbf{Q}(t)\}) + E_0(\{\mathbf{Q}(t)\})$. Energy components are shifted by constant values for graphical clarity.

We employ an energy conservation measure to directly compare the RPMD model with adiabatic Born-Oppenheimer dynamics. Fig. 2.7(a) presents various energy components for a typical cold injection RPMD trajectory in helium. The blue curve presents $K_{\mathrm{s}}(\{\mathbf{V}(t)\}) + U_{\text{s-s}}(\{\mathbf{Q}(t)\})$, the sum of the solvent kinetic energy term and the solvent-solvent potential energy term that are obtained from the RPMD trajectory. Also plotted are the electronic eigenstates for the excess electron that are calculated from solvent configurations along the RPMD trajectory, with the red curve corresponding to the electron ground state energy $E_0(\{\mathbf{Q}(t)\})$, and the gray curves corresponding to low-lying excited state energies. Finally, the black curve represents $H_{\mathrm{BO}}(t) = K_{\mathrm{s}}(\{\mathbf{V}(t)\}) + U_{\text{s-s}}(\{\mathbf{Q}(t)\}) + E_0(\{\mathbf{Q}(t)\})$, which is the energy function that would be conserved if the trajectory evolved according to the ground-state Born-Oppenheimer Hamiltonian. In cold electron injection, as was earlier discussed, the initial population of the excess electron is dominated by the electronic ground state. The con-

servation of $H_{\mathrm{BO}}(t)$ in Fig. 2.7(a) indicates that the RPMD model is consistent with the adiabatic ground state dynamics throughout the cold electron injection trajectory.

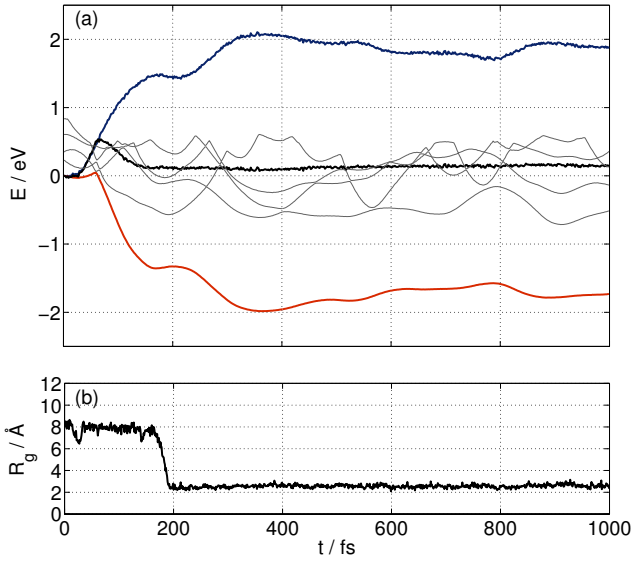

Figure 2.8: An illustrative hot injection trajectory in helium, presented as in Fig. 2.7.

Figure 2.8 presents the corresponding analysis for a typical hot injection trajectory that exhibits the two-cavity localization pathway. At short times, the ground-state Born-Oppenheimer Hamiltonian is clearly not conserved along the RPMD trajectory. However, after the ring polymer localizes into a single solvent cavity at 200 fs (Fig. 2.8(b)), then $H_{\mathrm{BO}}(t)$ becomes a constant of the motion. Although the RPMD model does not evolve the electron in its eigenstate representation, it clearly exhibits the transition from an initial excited-state population to ground state dynamics as a function of time.

A more extensive analysis of the ensemble of RPMD trajectories for hot electron injection and cold electron injection yields results that are entirely consistent with the illustrative trajectories presented in Figs. 2.7 and 2.8.

2.3.1.4 Energy dissipation and slow equilibration timescales

Although the solvent bath of 1000 helium atoms might seem an ample reservoir for dissipating the energy associated with the electron injection and localization, Fig. 2.9(a) reveals that this is not the case. The dashed line in this figure presents the temperature of the solvent atoms following cold electron injection, obtained from the non-equilibrium average over the ensemble of RPMD trajectories. Initially, the solvent temperature is 309 K, as is required by our injection protocol, but

this temperature rises to over 320 K as the electron relaxes and forms a solvent cavity. This is yet another finite size effect that should be considered in simulations of electron injection. Given that the RPMD trajectories are essentially reproducing ground-state adiabatic dynamics for the case of cold electron injection (Fig. 2.7(a)), it is almost certain that this effect also appears in MQCD simulations (although we find that the greater heat capacity of water leads to a less pronounced increase in temperature than for helium).

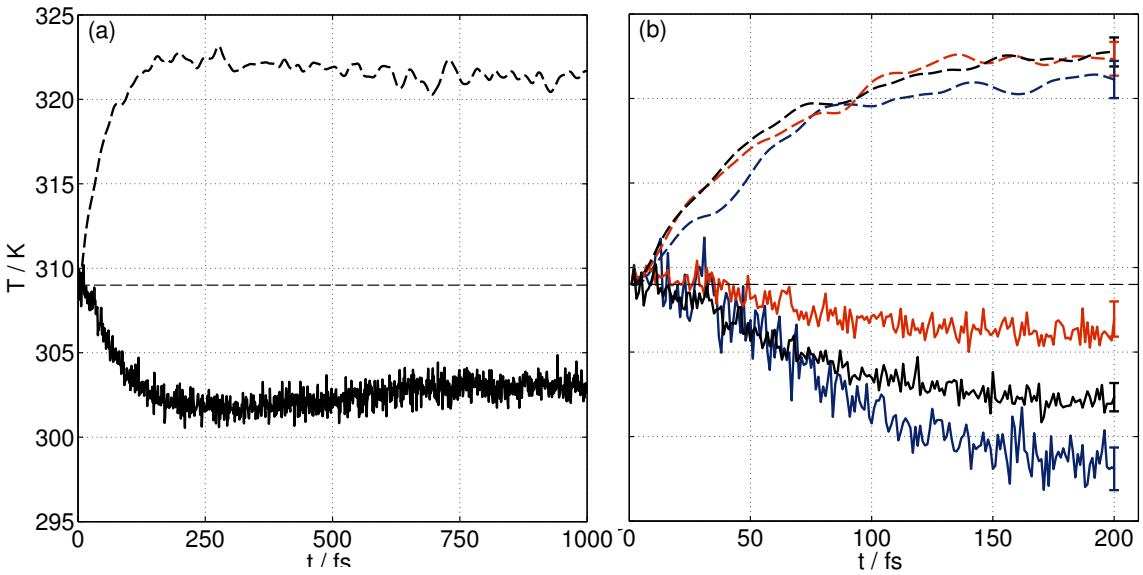

Figure 2.9: The non-equilibrium average temperature for the helium solvent atoms (dashed) and for the ring polymer beads (solid) following cold electron injection. **(a)** Results obtained over 1 ps using 1024 ring polymer beads and **(b)** obtained for a shorter period using 512 (blue), 1024 (black), and 2048 (red) ring polymer beads. Error bars indicate the standard deviation of the mean.

The solid line in Fig. 2.9(a) shows the corresponding evolution of the temperature of the ring polymer beads, also obtained from the non-equilibrium average over RPMD trajectories. At short times, the temperature of the ring polymer beads drops as the electron adiabatically expands during the formation of the solvent cavity. However, even after a picosecond of dynamics, the ring polymer temperature remains very different from that of the solvent atoms. This slow equilibration timescale, which is a well-known hindrance to the convergence of path integral molecular dynamics simulations,[73] arises from the separation of timescales between the motions of the ring polymer beads and the solvent atoms. Interestingly, slow equilibration between the ring polymer and the solvent seems to be a necessary feature of the RPMD model's correct description of the adiabatic Born-Oppenheimer dynamics for cold electron injection (Fig. 2.7(a)); if the internal modes of the

ring polymer rapidly equilibrated with the solvent atoms, then the average solvent kinetic energy would have dropped and $H_{\mathrm{BO}}(t)$ would not have been a constant of the motion.

The dashed lines in Fig. 2.9(b) show that the calculated rise in solvent temperature following electron injection is independent of the number of ring polymer beads (in the limit that the bead number is converged with respect to the path integral discretization, of course). This is not surprising, but it does confirm that the coupling between the solvent and ring polymer dynamics does not significantly depend upon this parameter. The solid lines in Fig. 2.9(b) also show that increasing the number of ring polymer beads diminishes the amount to which the time-evolved ring polymer temperature deviates from its initial value. This is also easily understood. The similarity of the dashed lines in Fig. 2.9(b) suggests that the amount of energy exchanged between the solvent and ring polymer beads during electron localization is independent of the number of beads. Increasing the number of beads, which undergo relatively fast equilibration with respect to each other, simply decreases the fraction of this fixed amount of energy that is withdrawn from the average energy of each bead.

We conclude this section by noting that if a sufficiently large solvent bath were employed, then the average rise in the solvent temperature in Fig. 2.9(a) would not have occurred. Also, if a sufficient number of ring polymer beads were employed, then the corresponding drop in the ring polymer temperature in Fig. 2.9(b) would not have been observed. These features, while interesting, are artifacts of our finite simulation size, rather than fundamental drawbacks of the RPMD model.

2.3.2 Injection of an excess electron into liquid water

Liquid water provides a more complex environment for electron injection than helium by introducing solvent hydrogen-bonding and rotational motion. Nonetheless, many features of the water simulations will be familiar from our analysis of electron injection into helium.

Figure 2.10 presents the ring polymer radius of gyration following injection into liquid water. As was seen for helium, the ring polymer is initially more extended for the case of hot injection. The figure also shows that the hot injection trajectories in water exhibit a slower timescale for relaxation of the ring polymer than cold injection trajectories. For cold injection, $\langle R_g(t) \rangle$ approaches its equilibrium value within 30 fs, on the timescale of the librational motion of the water molecules. However, a fraction of the hot injection trajectories exhibit a slower relaxation pathway in which the ring polymer transiently occupies multiple solvent cavities. In general, we find that these multi-cavity configurations survive for less time in water than in helium, suggesting that the water solvent

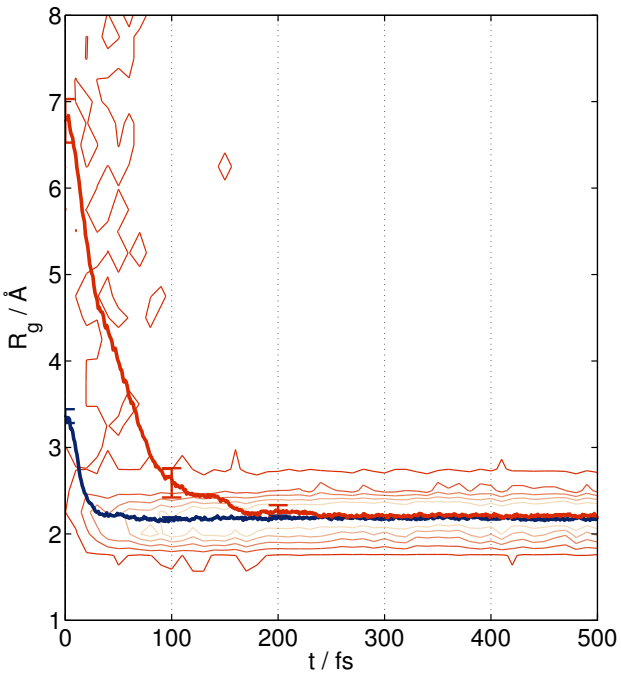

Figure 2.10: Ring polymer radius of gyration following excess electron injection into water. The contour plot indicates the distribution of $R_g(t)$ from the ensemble RPMD trajectories for hot injection, the heavy lines indicates the non-equilibrium average $\langle R_g(t) \rangle$ taken over cold injection (blue) and hot injection (red) trajectories.

allows for more facile rearrangement of the electron solvation environment at short times.

To further investigate the dynamics of the solvent, Fig. 2.11 presents the electron-hydrogen radial distribution function $\langle g_{\mathrm{e-H}}(r,t) \rangle$ and the electron-oxygen radial distribution function $\langle g_{\mathrm{e-O}}(r,t) \rangle$ for cold electron injection; both are calculated in terms of the distance between the ring polymer centroid and the corresponding solvent atoms. As was the case in cold helium injection, the initial absence of both oxygen and hydrogen atoms near the electron centroid indicates that the injected electron occupies a pre-solvation environment that is depleted of water molecules.[74,75] For times shorter than 100 fs following injection, the primary solvent rearrangements correspond to the reorientation of the solvent hydrogen atoms in the vicinity of the electron. However, another significant solvent rearrangement occurs on the 300 fs timescale, as the first peak in $\langle g_{\mathrm{e-O}}(r,t) \rangle$ bifurcates to form the first two distinct shells of the solvent cage. Also on this timescale, $\langle g_{\mathrm{e-H}}(r,t) \rangle$ gains a new peak at approximately 2 Å that corresponds to water OH bonds pointed towards the localized electron. Once the solvent relaxation is complete, at timescales beyond 1 ps, the radial distribution plots in Fig. 2.11 are entirely consistent with those previously reported from equilibrium simulations.[19,63] Comparison of Fig. 2.11 with the corresponding results for helium in Figs. 2.4(a) and 2.6(a)

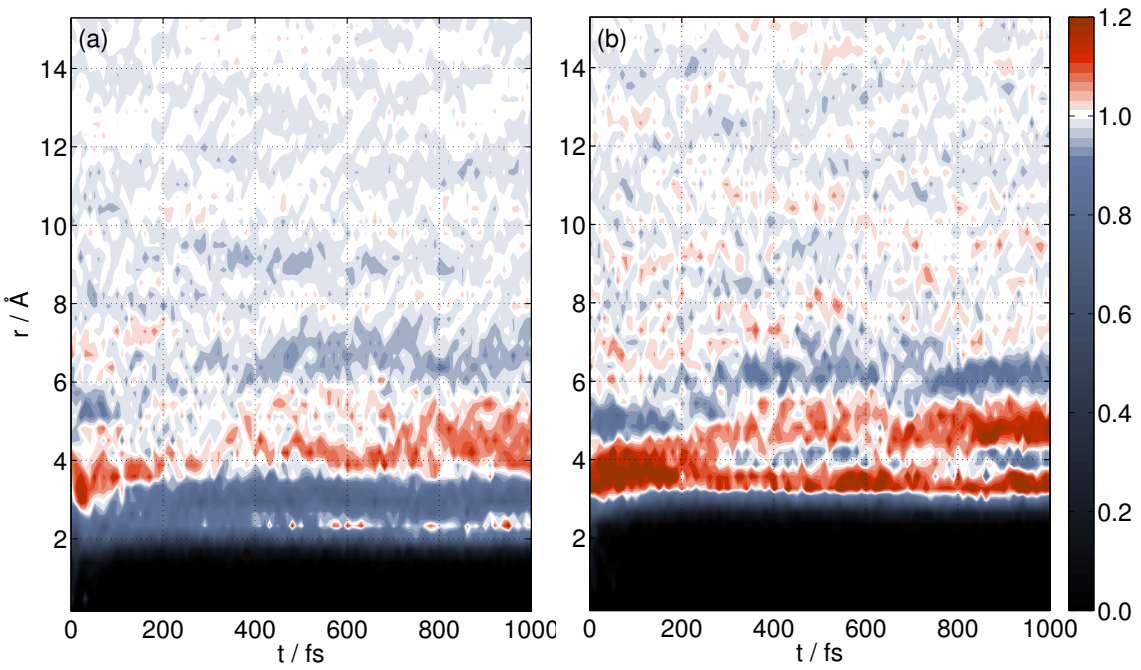

Figure 2.11: Solvent dynamics following cold electron injection into water. **(a)** The time-resolved electron-hydrogen radial distribution function $\langle g_{\mathrm{e-H}}(r,t)\rangle$. **(b)** The time-resolved electron-oxygen radial distribution function $\langle g_{\mathrm{e-O}}(r,t)\rangle$.

emphasizes that water introduces new features during electron localization associated with hydrogen bonding reorientation on the 300 fs timescale.

Another difference between water and helium is that the water dynamics in Fig. 2.11 does not exhibit the pronounced solvent compression wave that was observed as the excess electron localizes in the helium solvent. This is explained by the fact that water creates the solvent cavity on short timescales by primarily undergoing rotational motions of the individual molecules (Fig. 2.11) whereas the helium atoms in the vicinity of the localizing electron undergo significant translational motions on short timescales (Fig. 2.4). These rapid translational impulses in the helium solvent, as well as the hard repulsions between the helium atoms, facilitate the initiation and outward propagation of the solvent compression wave; the absence of translational impulses to the water molecules during electron localization leads to the corresponding absence of the compression wave.

The most prominent difference between the electron-solvent radial distributions for hot (Fig. 2.12) and cold (Fig. 2.11) excess electron injection appears at short times. As was observed in the helium simulations, the initial configurations of the electron ring polymer for hot injection are not confined to a single solvent cavity, which leads to an initial non-zero density for the electron-solvent distribution functions at $r = 0$, as is consistent with the timescale for ring polymer localization

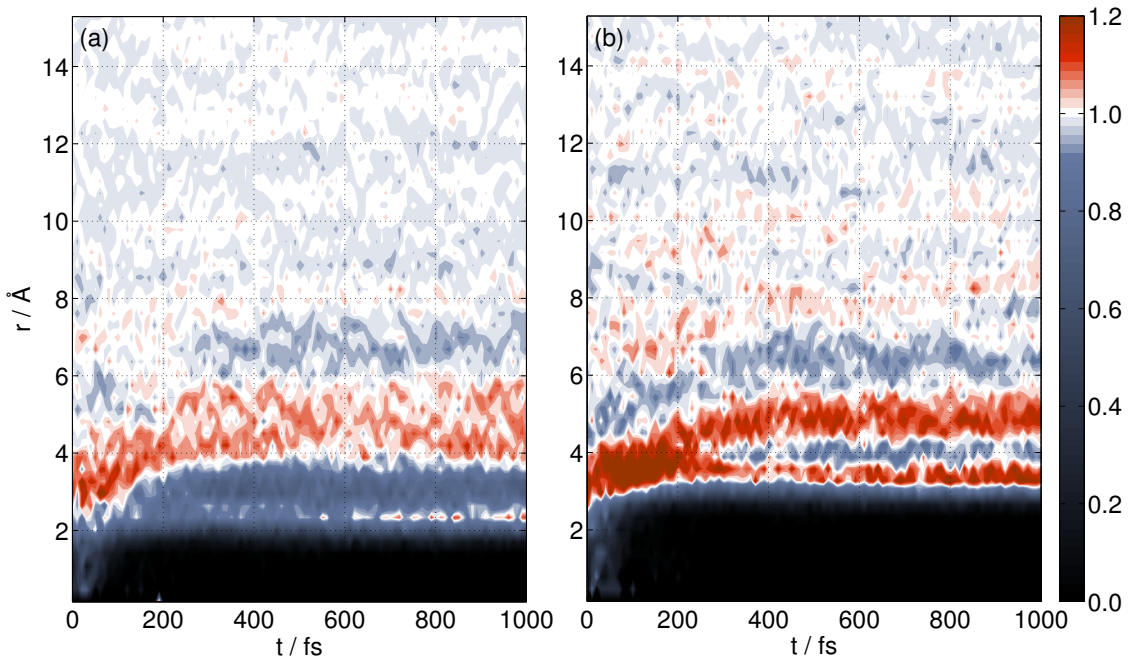

Figure 2.12: Solvent dynamics following hot electron injection into water. **(a)** The time-resolved electron-hydrogen radial distribution function $\langle g_{\mathrm{e-H}}(r,t)\rangle$. **(b)** The time-resolved electron-oxygen radial distribution function $\langle g_{\mathrm{e-O}}(r,t)\rangle$.

in Fig. 2.10. At longer times, the electron-solvent distribution functions for hot injection closely resemble those for cold injection.

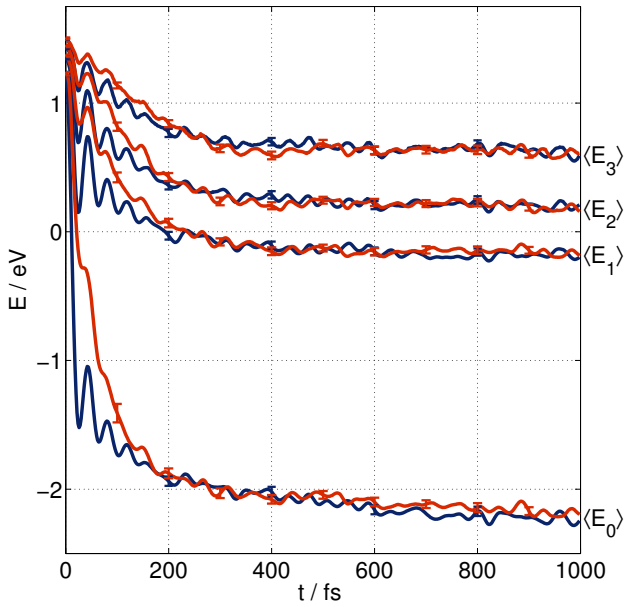

Figure 2.13: The four lowest electron eigenenergies, obtained from the non-equilibrium average for RPMD trajectories following cold (blue) and hot (red) injection into the liquid water.

Figure 2.13 presents the trajectory-averaged excess electron eigenenergies for cold (blue) and hot (red) electron injection into water. As was seen for helium in Fig. 2.5, the energies for cold electron injection exhibit a rapid initial decline, with the energy of the ground state dropping by 2.5 eV within the first 30 fs following injection. This initial relaxation timescale is somewhat slower in the hot injection results, due to the ring polymer configurations that transiently occupy multiple solvent cavities. A new feature of the water simulations are the oscillations in the eigenenergies on the 30 fs timescale, associated with the librational motion of the water molecules neighboring the excess electron. On the timescales of 200-400 fs, the eigenenergies for both the hot and cold injection simulations continue to relax as distinct water solvent shells appear in Figs. 2.11 and 2.12.

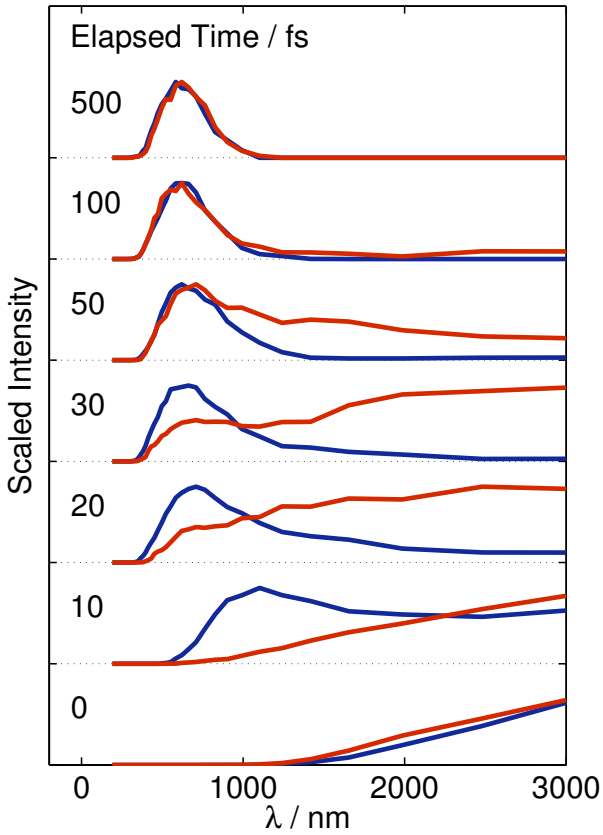

Figure 2.14: Transient electron absorption spectra for cold (blue) and hot (red) excess electron injection into water, normalized by the maximum value. Spectra for each waiting time are vertically shifted for clarity.

In Fig. 2.14, the transient absorption spectrum for the electron following hot and cold injection

are computed using[76]

$$I(E,t) = \left\langle \frac{2\pi}{\hbar} \sum_n w(n,t) \sum_{n' \neq n} |\langle \psi_n(t)|\mu|\psi_{n'}(t)\rangle|^2 \, \delta[E - (E_n(t) - E_{n'}(t))] \right\rangle, \tag{2.8}$$

where μ is the dipole operator, the large angle brackets indicate the non-equilibrium average over the ensemble of RPMD trajectories, and the energy eigenvalues and functions are calculated from the solvent configurations along the trajectories. We employ $w(n,t) = Q(t)^{-1}\exp[-E_n(t)/(k_\mathrm{B}T)]$ to be the instantaneous Boltzmann weights, where $Q(t) = \sum_n \exp[-E_n(t)/(k_\mathrm{B}T)]$. Alternative choices for $w(n,t)$, including expressions that account for the overlap between the ring polymer bead positions and the density of the corresponding eigenfunction, do not lead to significant changes in the figure.

Upon initial electron injection, both spectra are necessarily identical within statistical error, featuring a broad absorption band that extends into the infrared. However, the spectrum for cold injection develops an additional peak at 1000 nm within 10 fs. Even though it is clear from Fig. 2.13 that the electron eigenenergies continue to relax for hundreds of femtoseconds, the ground- to excited-state energy gaps that dominate the cold electron injection spectrum in Fig. 2.14 change little after 30 fs. The transient absorption spectrum for hot electron injection in Fig. 2.14 again illustrates the slower relaxation timescale associated with electron localization via multiple solvent cavities. Significant differences between the hot and cold injection trajectories persist for approximately 100 fs, after which the electron localization into the ground state is completed and the spectra together approach the equilibrium absorption spectrum.

Many of the features of the RPMD simulations reported here agree well with previous MQCD simulations of electron injection into water. In particular, ground-state simulations of electron injection[19] find that the excess electron localizes to nearly its equilibrium radius within 30 fs, while solvent reordering occurs on a timescale of 200 fs. These are the same timescales for cold electron injection obtained from the RPMD model, and as is expected, the transient absorption spectrum for cold electron injection in Fig. 2.14 is essentially identical to that reported previously.[19] (We have confirmed that the only significant difference, which appears at $t = 0$, is due to the larger system size used in our simulations and the use of a criterion to exclude initially delocalized states in the earlier work.[19,77?]) The slower relaxation timescale observed in the RPMD simulations of hot electron injection is also similar to that found in non-adiabatic MQCD simulations.[17] These earlier studies found that roughly half of the initially excited electrons relax to the ground state within $50 - 150$ fs.[17] Our simulations predict a similar timescale of $30 - 150$ fs for electron localization following hot injection (Fig. 2.10).

However, in a notable difference from our results, a large fraction of non-adiabatic MQCD trajectories exhibit a timescale of up to 1 ps for the survival of excited electronic states following high-energy injection.[16,17,22] This slow timescale arises in the MQCD simulations from the slow internal conversion of localized, p-type electronic states to the ground state.[17,22] It is possible that the classical isomorphic model of RPMD simply fails to capture this highly non-adiabatic feature of the collapse dynamics. However, we note that subsequent MQCD simulations that employed a flexible water model find that the slowest non-adiabatic relaxation timescales is approximately 164 fs. Furthermore, ultrafast transient absorptions spectra following electron injection also indicate that the original 1 ps timescale is too long, with recent results and interpretations finding a timescale for non-adiabatic collapse of less than 150 fs,[9–11] and experimental studies that probe the lifetime of the p-type first excited state following photo-excitation of the hydrated electron in water clusters find a short timescale for $p \rightarrow s$ internal conversion of 50 fs.[78–80]

2.4 Conclusions

We have employed the RPMD model to directly simulate the non-equilibrium injection and relaxation of an excess electron in into supercritical helium fluid and ambient liquid water. A temperature-based method for modulating the initial energy of the excess electron in the RPMD model is presented and used to study both low-energy (cold) and high-energy (hot) electron injection.

For cold injection into fluid helium, the RPMD model is shown to be consistent with electronically adiabatic dynamics with the excess electron in its ground state. The radius of gyration of the ring polymer rapidly approaches its equilibrium value, driving the formation of a solvent compression wave that travels outward and eventually reaches the neighboring periodic replicas of the excess electron. For hot injection into fluid helium, similar solvent dynamics is observed, but the localization of the ring polymer exhibits an additional mechanism for localization via multiple solvent cavities on the timescale of approximately 200 fs. Our comparison of the instantaneous temperature of the solvent and ring polymer beads for the injection simulations in helium illustrates the slow timescale for equilibration between the ring polymer modes and the solvent atoms, as well as simulation artifacts arising from the finite number of ring polymer beads and the finite solvent bath.

For the simulations in liquid water, cold electron injection again leads to the adiabatic localization of the excess electron into a solvent cavity on the timescale of 50 fs, whereas hot electron injection leads to an additional 150 fs relaxation timescale due to metastable ring polymer configurations that occupy multiple solvent cavities. No solvent compression is observed in water, because the

formation of the solvent cavity involves rotational movements of water molecules rather than rapid translational motion. The water solvent dynamics reveals that distinct first- and second-solvation shells around the electron appear at approximately 300 fs after the initial injection. Our calculation of the transient absorption spectra for the excess electron following injection in water shows clear differences between hot and cold injection at times less than 100 fs, but these spectra show little signature of the solvent relaxation dynamics that continues at longer times.

Comparison of the RPMD simulations with prior MQCD simulations reveal broad agreement, both with regard to the observed mechanisms and timescales for solvent and electron relaxation dynamics. Although the RPMD model, along with recent ultrafast spectroscopy studies, does not find evidence for the picosecond-lifetime electronic excited states that are predicted in the MQCD simulations, the similarity between the results obtained with these very different theoretical approaches is encouraging.

Appendix A Alternative justification for the electron injection protocol

Here, we provide an alternative justification for the electron injection protocol in Sec. 2.2.2 by demonstrating that it is closely related to the RPMD approximation to a real-time Kubo-transformed correlation function for which the system is initially in a non-equilibrium distribution.

Suppose that the initial probability distribution in Eq. 2.4 is replaced with

$$P_0(\mathbf{q},\{\mathbf{Q}\};T,T') = P_T(\{\mathbf{Q}\})\mathcal{P}_{T'}(\mathbf{q}|\{\mathbf{Q}\}), \tag{2.9}$$

where $\mathcal{P}_{T'}(\mathbf{q}|\{\mathbf{Q}\})$ is the conditional probability distribution for the particle density of the electron,

$$\mathcal{P}_{T'}(\mathbf{q}|\{\mathbf{Q}\}) = \frac{\int d\mathbf{q}^{(1)}\dots d\mathbf{q}^{(n)}\ \delta(\mathbf{q}-\mathbf{q}^{(1)})\ \exp[S(\{\mathbf{q}\},\{\mathbf{Q}\};T')]}{\int d\mathbf{q}^{(1)}\dots d\mathbf{q}^{(n)}\ \exp[S(\{\mathbf{q}\},\{\mathbf{Q}\};T')]}, \tag{2.10}$$

rather than the ring polymer centroid density. Then, consider the real-time Kubo-transformed correlation function for which the initial particle density is restricted to be $P_0(\mathbf{q},\{\mathbf{Q}\};T,T')$, namely

$$\tilde{C}_{A_0B}(t) = \frac{1}{\beta}\int_0^\beta d\lambda\ \mathrm{Tr}\left[e^{-\lambda\hat{H}}\hat{A}_0(\hat{\mathbf{q}},\{\hat{\mathbf{Q}}\})e^{-(\beta-\lambda)\hat{H}}e^{i\hat{H}t/\hbar}\hat{B}(\hat{\mathbf{q}},\{\hat{\mathbf{Q}}\})e^{-i\hat{H}t/\hbar}\right], \tag{2.11}$$

where $\beta = (k_\mathrm{B}T)^{-1}$, $\hat{H}$ is the Hamiltonian operator for the system, and $\hat{A}_0$ and $\hat{B}$ are position-dependent operators such that

$$\hat{A}_0(\hat{\mathbf{q}},\{\hat{\mathbf{Q}}\}) = \int d\mathbf{q}'d\mathbf{Q}'_1\dots d\mathbf{Q}'_N\ P_0(\mathbf{q}',\{\mathbf{Q}'\};T,T')\ \hat{A}(\hat{\mathbf{q}},\{\hat{\mathbf{Q}}\})\left(\delta(\mathbf{q}'-\hat{\mathbf{q}})\prod_{k=1}^{N}\delta(\mathbf{Q}'_k-\hat{\mathbf{Q}}_k)\right). \tag{2.12}$$

In the limit that the solvent degrees of freedom are treated classically, the RPMD approximation to this correlation function is

$$\begin{aligned}\widetilde{C}_{A_0B}(t) = \left(\frac{n}{2\pi\hbar}\right)^{3n}\left(\frac{1}{2\pi\hbar}\right)^{3N}\int d\{\mathbf{q}\}d\{\mathbf{p}\}d\{\mathbf{Q}\}d\{\mathbf{P}\}\ e^{-\beta H(\{\mathbf{q}\},\{\mathbf{p}\},\{\mathbf{Q}\},\{\mathbf{P}\})}\\ \times A_0(\mathbf{q}^{(1)}(0),\{\mathbf{Q}(0)\})B_n(\{\mathbf{q}(t)\},\{\mathbf{Q}(t)\}),\end{aligned} \tag{2.13}$$

where

$$H(\{\mathbf{q}\},\{\mathbf{p}\},\{\mathbf{Q}\},\{\mathbf{P}\}) = \sum_{\alpha=1}^{n} \frac{(\mathbf{p}^{(\alpha)})^2}{2m_n} + \sum_{j=1}^{N} \frac{\mathbf{P}_j^2}{2M_j} + \sum_{\alpha=1}^{n} \left[\frac{1}{2} m_n \omega_n^2 (\mathbf{q}^{(\alpha)} - \mathbf{q}^{(\alpha+1)})^2 + \frac{1}{n} U(\mathbf{q}^{(\alpha)}, \{\mathbf{Q}\}) \right] \tag{2.14}$$

is the classical Hamiltonian that gives rise to the ring polymer equations of motion (Eqs. 2.1 and 2.2), $\{\mathbf{q}(t)\}$ and $\{\mathbf{Q}(t)\}$ are the positions of the electron ring polymer beads and solvent atoms evolved in time according to these dynamics, $m_n = m/n$, and

$$B_n(\{\mathbf{q}\},\{\mathbf{Q}\}) = n^{-1} \sum_{\alpha=1}^{n} B(\mathbf{q}^{(\alpha)},\{\mathbf{Q}\}). \tag{2.15}$$

Eq. 2.13 can be rearranged to obtain

$$\tilde{C}_{A_0 B}(t) = \int d\mathbf{q}' d\mathbf{Q}'_1 \ldots d\mathbf{Q}'_N \; P_0(\mathbf{q}',\{\mathbf{Q}'\};T,T') \; \tilde{C}_{AB}(t;\mathbf{q}',\{\mathbf{Q}'\}), \tag{2.16}$$

where

$$\tilde{C}_{AB}(t;\mathbf{q}',\{\mathbf{Q}'\}) = \left(\frac{n}{2\pi\hbar}\right)^{3n} \left(\frac{1}{2\pi\hbar}\right)^{3N} \int d\{\mathbf{q}\} d\{\mathbf{p}\} d\{\mathbf{Q}\} d\{\mathbf{P}\} \; e^{-\beta H(\{\mathbf{q}\},\{\mathbf{p}\},\{\mathbf{Q}\},\{\mathbf{P}\})} \times \left(A(\mathbf{q}^{(1)}(0),\{\mathbf{Q}(0)\}) \; \delta(\mathbf{q}' - \mathbf{q}^{(1)}(0)) \prod_{k=1}^{N} \delta(\mathbf{Q}'_k - \mathbf{Q}_k(0)) \right) B_n(\{\mathbf{q}(t)\},\{\mathbf{Q}(t)\}). \tag{2.17}$$

The correlation function in Eq. 2.17 corresponds to a system that is initially constrained with respect to the solvent position and the position of one ring-polymer bead. Subject to these constraints, the remaining bead positions and the momenta are sampled from the distribution proportional to $e^{-\beta H(\{\mathbf{q}\},\{\mathbf{p}\},\{\mathbf{Q}\},\{\mathbf{P}\})}$, which corresponds to temperature T. RPMD correlation functions of this form are familiar from the flux-side formulation of the RPMD rate theory, where one bead of the ring polymer is initially pinned to a transition state dividing surface.[57]

The full correlation function in Eq. 2.16 weights the $\tilde{C}_{AB}(t;\mathbf{q}',\{\mathbf{Q}'\})$ according to the initial particle density distribution $P_0(\mathbf{q}',\{\mathbf{Q}'\};T,T')$. As for other correlation functions of non-linear, position-dependent operators, the RPMD approximation in Eq. 2.16 is exact to $O(t^3)$ at short times.[30]

The protocol for initializing trajectories to calculate the RPMD correlation function in Eq. 2.16 is the same as the protocol put forward in Section 2.2.2, except that Step 3 is modified as follows to

account for the difference between the particle density and the centroid density: $(3')$ Keeping both the solvent configuration and one bead of the ring polymer fixed, the positions of the remaining ring polymer beads are equilibrated at temperature T.

Both the analysis presented in this appendix and the earlier comparison with CMD support the same conclusion: The ring polymer bead positions and velocities that are not determined by the initial distribution $P_0(\mathbf{q}, \{\mathbf{Q}\}; T, T')$ are most naturally sampled at temperature T, rather than T'.

References

[1] A. Migus, Y. Gauduel, J. L. Martin, and A. Antonetti, Phys. Rev. Lett. **58**, 1559 (1987).

[2] H. Lu, F. H. Long, and K. B. Eisenthal, J. Opt. Soc. Am. B **7**, 1511 (1990).

[3] X. L. Shi, F. H. Long, H. Lu, and K. B. Eisenthal, J. Phys. Chem. **100**, 11903 (1996).

[4] F. H. Long, H. Lu, and K. B. Eisenthal, Phys. Rev. Lett. **64**, 1469 (1990).

[5] A. Hertwig, H. Hippler, and A. N. Unterreiner, Phys. Chem. Chem. Phys. **1**, 5633 (1999).

[6] A. Hertwig, H. Hippler, and A. N. Unterreiner, J. Phys.: Condens. Matter **12**, A165 (2000).

[7] D. Madsen, C. L. Thomsen, J. Thogersen, and S. R. Keiding, J. Chem. Phys. **113**, 1126 (2000).

[8] C. R. Wang, T. Luow, and Q. B. Lu, Phys. Chem. Chem. Phys. **10**, 4463 (2008).

[9] M. Mizuno, S. Yamaguchi, and T. Tahara, J. Phys. Chem. A **109**, 5257 (2005).

[10] V. H. Vilchiz, J. A. Kloepfer, A. C. Germaine, V. A. Lenchenkov, and S. E. Bradforth, J. Phys. Chem. A **105**, 1711 (2001).

[11] R. Lian, R. A. Crowell, and I. A. Shkrob, J. Phys. Chem. A **109**, 1510 (2005).

[12] T. W. Kee, D. H. Son, P. Kambhampati, and P. F. Barbara, J. Phys. Chem. A **105**, 8434 (2001).

[13] P. Kambhampati, D. H. Son, T. W. Kee, and P. F. Barbara, J. Phys. Chem. A **106**, 2374 (2002).

[14] R. Laenen, T. Roth, and A. Laubereau, Phys. Rev. Lett. **85**, 50 (2000).

[15] C. Pepin, T. Goulet, D. Houde, and J. P. Jay-Gerin, J. Phys. Chem. A **101**, 4351 (1997).

[16] F. Webster, P. J. Rossky, and R. A. Friesner, Comput. Phys. Commun. **63**, 494 (1991).

[17] F. J. Webster, J. Schnitker, M. S. Friedrichs, R. A. Friesner, and P. J. Rossky, Phys. Rev. Lett. **66**, 3172 (1991).

[18] D. F. Coker and B. J. Berne, J. Chem. Phys. **89**, 2128 (1988).

[19] P. J. Rossky and J. Schnitker, J. Phys. Chem. **92**, 4277 (1988).

[20] B. Space and D. F. Coker, J. Chem. Phys. **94**, 1976 (1991).

[21] B. Space and D. F. Coker, J. Chem. Phys. **96**, 652 (1992).

[22] T. H. Murphrey and P. J. Rossky, J. Chem. Phys. **99**, 515 (1993).

[23] J. Eloranta and V. A. Apkarian, J. Chem. Phys. **117**, 10139 (2002).

[24] M. Rosenblit and J. Jortner, J. Phys. Chem. A **101**, 751 (1997).

[25] H. D. Meyer and W. H. Miller, J. Chem. Phys. **72**, 2272 (1980).

[26] J. C. Tully, J. Chem. Phys. **93**, 1061 (1990).

[27] J. C. Tully, Faraday Discuss. **110**, 407 (1998).

[28] S. Nielsen, R. Kapral, and G. Ciccotti, J. Chem. Phys. **115**, 5805 (2001).

[29] I. R. Craig and D. E. Manolopoulos, J. Chem. Phys. **121**, 3368 (2004).

[30] B. J. Braams and D. E. Manolopoulos, J. Chem. Phys. **125**, 124105 (2006).

[31] T. F. Miller, J. Chem. Phys. **129**, 194502 (2008).

[32] S. Jang and G. A. Voth, J. Chem. Phys. **111**, 2371 (1999).

[33] J. S. Cao and G. A. Voth, J. Chem. Phys. **100**, 5106 (1994).

[34] S. M. Jang, Y. Pak, and G. A. Voth, J. Phys. Chem. A **103**, 10289 (1999).

[35] R. P. Feynman and A. R. Hibbs, *Quantum mechanics and path integrals* (McGraw-Hill, New York, New York, 1965).

[36] D. Chandler and P. G. Wolynes, J. Chem. Phys. **74**, 4078 (1981).

[37] M. Parrinello and A. Rahman, J. Chem. Phys. **80**, 860 (1984).

[38] B. Deraedt, M. Sprik, and M. L. Klein, J. Chem. Phys. **80**, 5719 (1984).

[39] N. R. Kestner, J. Jortner, M. H. Cohen, and S. A. Rice, Phys. Rev. A **140**, A56 (1965).

[40] D. F. Coker, B. J. Berne, and D. Thirumalai, J. Chem. Phys. **86**, 5689 (1987).

[41] H. Berendsen, J. P. M. Postma, W. van Gunsteren, and J. Hermans, in *The Jerusalem symposia on quantum chemistry and biochemistry*, Vol. 14, edited by B. Pullman (D. Reidel, 1981).

[42] J. Schnitker and P. J. Rossky, J. Chem. Phys. **86**, 3462 (1987).

[43] L. Turi and D. Borgis, J. Chem. Phys. **117**, 6186 (2002).

[44] T. Sommerfeld and K. D. Jordan, J. Phys. Chem. A **109**, 11531 (2005).

[45] T. Sommerfeld, A. DeFusco, and K. D. Jordan, J. Phys. Chem. A **112**, 11021 (2008).

[46] L. D. Jacobson, C. F. Williams, and J. M. Herbert, J. Chem. Phys. **130**, (2009).

[47] R. E. Larsen, W. J. Glover, and B. J. Schwartz, J. Chem. Phys. **131**, (2009).

[48] J. Schnitker and P. J. Rossky, J. Chem. Phys. **131**, (2009).

[49] X. Y. Chen and S. E. Bradforth, Annu. Rev. Phys. Chem. **59**, 203 (2008).

[50] D. Chandler, "Theory of quantum processes in liquids," in *Liquids, Freezing and Glass Transition*, edited by D. Levesque, J. P. Hansen, and J. Zinn-Justin (Elsevier, New York, 1991) pp. 193–285.

[51] T. D. Hone, P. J. Rossky, and G. A. Voth, J. Chem. Phys. **124**, (2006).

[52] E. Geva, Q. Shi, and G. A. Voth, J. Chem. Phys. **115**, 9209 (2001).

[53] W. Smith and T. R. Forester, J. Mol. Graphics **14**, 136 (1996).

[54] W. C. Swope, H. C. Andersen, P. H. Berens, and K. R. Wilson, J. Chem. Phys. **76**, 637 (1982).

[55] T. F. Miller and D. E. Manolopoulos, J. Chem. Phys. **123**, 154504 (2005).

[56] T. F. Miller and D. E. Manolopoulos, J. Chem. Phys. **122**, 184503 (2005).

[57] I. R. Craig and D. E. Manolopoulos, J. Chem. Phys. **122**, 084106 (2005).

[58] I. R. Craig and D. E. Manolopoulos, Chem. Phys. **322**, 236 (2006).

[59] T. E. Markland, S. Habershon, and D. E. Manolopoulos, J. Chem. Phys. **128**, 194506 (2008).

[60] R. Collepardo-Guevara, I. R. Craig, and D. E. Manolopoulos, J. Chem. Phys. **128**, 144502 (2008).

[61] S. Habershon, G. S. Fanourgakis, and D. E. Manolopoulos, J. Chem. Phys. **129**, 074501 (2008).

[62] M. Tuckerman, B. J. Berne, and G. J. Martyna, J. Chem. Phys. **97**, 1990 (1992).

[63] J. Schnitker and P. J. Rossky, J. Chem. Phys. **86**, 3471 (1987).

[64] H. C. Andersen, J. Comput. Phys. **52**, 24 (1983).

[65] A. Wallqvist, D. Thirumalai, and B. J. Berne, J. Chem. Phys. **86**, 6404 (1987).

[66] B. J. Schwartz and P. J. Rossky, J. Chem. Phys. **101**, 6917 (1994).

[67] B. J. Schwartz and P. J. Rossky, J. Chem. Phys. **101**, 6902 (1994).

[68] O. Steinhauser, Mol. Phys. **45**, 335 (1982).

[69] D. Chandler and K. Leung, Annu. Rev. Phys. Chem. **45**, 557 (1994).

[70] P. W. Anderson, Phys. Rev. **109**, 1492 (1958).

[71] J. Schnitker, K. Motakabbir, P. J. Rossky, and R. Friesner, Phys. Rev. Lett. **60**, 456 (1988).

[72] A. V. Benderskii, J. Eloranta, R. Zadoyan, and V. A. Apkarian, J. Chem. Phys. **117**, 1201 (2002).

[73] R. W. Hall and B. J. Berne, J. Chem. Phys. **81**, 3641 (1984).

[74] J. Schnitker, P. J. Rossky, and G. A. Kenneywallace, J. Chem. Phys. **85**, 2986 (1986).

[75] K. A. Motakabbir, J. Schnitker, and P. J. Rossky, J. Chem. Phys. **97**, 2055 (1992).

[76] B. J. Berne and R. Pecora, *Dynamic light scattering*, dover ed. (Dover Publications, Mineola, N.Y., 2000).

[77] K. A. Motakabbir and P. J. Rossky, Chem. Phys. **129**, 253 (1989).

[78] A. E. Bragg, J. R. R. Verlet, A. Kammrath, O. Cheshnovsky, and D. M. Neumark, Science **306**, 669 (2004).

[79] A. E. Bragg, J. R. R. Verlet, A. Kammrath, O. Cheshnovsky, and D. M. Neumark, J. Am. Chem. Soc. **127**, 15283 (2005).

[80] O. T. Ehrler and D. M. Neumark, Acc. Chem. Res. **42**, 769 (2009).

Chapter 3

Direct simulation of electron transfer using ring polymer molecular dynamics: Comparison with semiclassical instanton theory and exact quantum methods

3.1 Introduction

Condensed-phase electron transfer (ET) reactions are central to many biological and synthetic pathways for energy conversion and catalysis.[1–4] The development of accurate, robust, and scalable methods for the study of such reactions is thus a key objective in theoretical chemistry. Although transition state theories and rate models for ET have been successfully applied in complex systems,[5–8] methods for the direct simulation and mechanistic study of ET dynamics in general systems remain less fully developed. To this end, we explore the use of ring polymer molecular dynamics (RPMD) for the description of prototypical ET reactions between mixed-valence transition metal ions in water, and we compare the RPMD approach against benchmark semiclassical and quantum dynamics methods.

Fundamental theoretical challenges in the direct simulation of ET reactions arise due to the coupling of the intrinsically quantum mechanical electronic transitions with slower, classical motions of the surrounding environment. Numerous semiclassical and mixed quantum-classical dynamics methods have been developed for the investigation of electronically non-adiabatic reactions,[9–19] but existing methods do not enable mechanistic studies that are independent of dividing surface assumptions in general systems; nor do they yield dynamical trajectories that preserve the equilibrium Boltzmann distribution[20,21] and allow for the use of rare-event sampling methodologies.[22] New methods are needed to accurately describe coupled electronic and nuclear dynamics and to enable the efficient and robust simulation of long trajectories that bridge the multiple timescales of ET reactions in complex systems.

RPMD[23] is an approximate quantum dynamical method that is based on the imaginary-time path integral formulation of statistical mechanics.[24,25] It provides an isomorphic classical molecular

dynamics model for the real-time evolution of a quantum mechanical system. Previous applications of RPMD include studies of molecular liquids,[26–31] hydrogen transfer rates,[32–35] and tunneling processes in low-dimensional systems.[36–38] A key feature of the RPMD method is that it yields real-time molecular dynamics trajectories that preserve the exact quantum Boltzmann distribution and exhibit time-reversal symmetry.[23,39] These properties allow RPMD to be used in combination with rare-event sampling methods for the trajectory-based analysis of quantum mechanical tunneling processes in systems involving thousands of atoms.[35,40] We have recently extended RPMD to describe electronic and nuclear dynamics, including solvated electron diffusion[41] and non-adiabatic electron injection into liquid water.[40]

In the current paper, RPMD is used to directly simulate ET dynamics in both atomistic and system-bath representations for mixed-valence ET in water. The calculated rates and mechanisms are analyzed in the context of semiclassical and exact quantum methods. A description of the employed methodologies is provided in Section 3.2, and Section 3.3 presents the details of the atomistic and system-bath representations. Calculation details are given in Section 3.4, and a discussion of the results is presented in Section 4.5.

3.2 Methods

Several methods are utilized to investigate ET rates and mechanisms, including RPMD, semiclassical instanton theory, exact quantum-mechanical dynamics, and the classical Marcus rate theory for ET. These methods are summarized below.

3.2.1 Ring polymer molecular dynamics

The RPMD equations of motion for a quantized electron and N classical particles are[23,41]

$$\dot{\mathbf{v}}^{(\alpha)} = \omega_n^2 \left(\mathbf{q}^{(\alpha+1)} + \mathbf{q}^{(\alpha-1)} - 2\mathbf{q}^{(\alpha)} \right) - \frac{1}{m_\mathrm{e}} \nabla_{\mathbf{q}^{(\alpha)}} U_\mathrm{ext} \left(\mathbf{q}^{(\alpha)}, \mathbf{Q}_1, \ldots, \mathbf{Q}_N \right) \tag{3.1}$$

and

$$\dot{\mathbf{V}}_j = -\frac{1}{nM_j} \sum_{\alpha=1}^{n} \nabla_{\mathbf{Q}_j} U_\mathrm{ext}(\mathbf{q}^{(\alpha)}, \mathbf{Q}_1, \ldots, \mathbf{Q}_N), \tag{3.2}$$

where $\mathbf{q}^{(\alpha)}$ and $\mathbf{v}^{(\alpha)}$ are the position and velocity vectors of α^{th} ring polymer bead, $\mathbf{Q}_j$ and $\mathbf{V}_j$ are the position and velocity vectors of the j^{th} classical particle, and n is the number of imaginary-time ring-polymer beads. The intra-bead harmonic frequency is $\omega_n/(\beta\hbar)$, where β is

the reciprocal temperature. The masses of electron and classical particles are m_{e} and M_j, respectively, $U_{\mathrm{ext}}(\mathbf{q}^{(\alpha)}, \mathbf{Q}_1, \ldots, \mathbf{Q}_N)$ is the potential energy function of the system, and $\mathbf{q}^{(0)} = \mathbf{q}^{(n)}$. Eqs. 3.1 and 3.2 generate a classical dynamics that we employ as a model for the real-time dynamics of the system.[41] In the limit of large n, these dynamics preserve the exact Boltzmann distribution.[39]

As in classical formulations of the thermal rate constant,[42–44] the RPMD rate can be expressed as[32,38]

$$k_{\mathrm{RPMD}} = \lim_{t\to\infty} \kappa(t) k_{\mathrm{TST}}. \tag{3.3}$$

Here, k_{TST} is the transition state theory (TST) approximation for the rate for a dividing surface $\xi(\mathbf{r}) = \xi^{\ddagger}$, where $\xi(\mathbf{r})$ is a collective variable, $\mathbf{r} = \left\{\mathbf{q}^{(1)}, \ldots, \mathbf{q}^{(n)}, \mathbf{Q}\right\}$ is the full position vector for the system, and $\mathbf{Q} = \{\mathbf{Q}_1, \ldots, \mathbf{Q}_N\}$ denotes the set of classical particle positions. The prefactor, $\kappa(t)$, is the time-dependent transmission coefficient that accounts for recrossing of trajectories through the dividing surface. An important feature of RPMD is that calculated rates and mechanisms are independent of the choice of TST dividing surface, as in exact quantum and exact classical dynamics.[32,38,45]

The TST rate in Eq. 3.3 is calculated using[33,46,47]

$$k_{\mathrm{TST}} = (2\pi\beta)^{-1/2} \langle g_\xi \rangle_{\mathrm{c}} \frac{e^{-\beta \Delta F(\xi^{\ddagger})}}{\int_{-\infty}^{\xi^{\ddagger}} d\xi e^{-\beta \Delta F(\xi)}}. \tag{3.4}$$

Here, $F(\xi)$ is the free energy (FE) along ξ

$$e^{-\beta \Delta F(\xi')} = \frac{\langle \delta(\xi(\mathbf{r}) - \xi') \rangle}{\langle \delta(\xi(\mathbf{r}) - \xi_r) \rangle}, \tag{3.5}$$

where ξ_r is a reference point in the reactant region, and[48–50]

$$g_\xi(\mathbf{r}) = \left[\sum_{i=1}^{d} \frac{1}{m_i} \left(\frac{\partial \xi(\mathbf{r})}{\partial r_i} \right)^2 \right]^{1/2}. \tag{3.6}$$

The scalar $r_i \in \{\mathbf{r}\}$ in this equation indicates either a ring-polymer or classical particle degree of freedom, m_i is the corresponding mass, and d is the total number of degrees of freedom in the system. In Eqs. 3.4 and 3.5, $\langle \ldots \rangle$ denotes the equilibrium ensemble average

$$\langle \ldots \rangle = \frac{\int d\mathbf{r} \int d\mathbf{v}\, e^{-\beta H_n(\mathbf{r},\mathbf{v})} (\ldots)}{\int d\mathbf{r} \int d\mathbf{v}\, e^{-\beta H_n(\mathbf{r},\mathbf{v})}}, \tag{3.7}$$

and $\langle \dots \rangle_{\mathrm{c}}$ denotes the average in the constrained ensemble

$$\langle \dots \rangle_{\mathrm{c}} = \frac{\int d\mathbf{r} \int d\mathbf{v}\; e^{-\beta H_n(\mathbf{r},\mathbf{v})}(\dots)\delta(\xi(\mathbf{r}) - \xi^{\ddagger})}{\int d\mathbf{r} \int d\mathbf{v}\; e^{-\beta H_n(\mathbf{r},\mathbf{v})}\delta(\xi(\mathbf{r}) - \xi^{\ddagger})}. \tag{3.8}$$

Here,

$$H_n(\mathbf{r},\mathbf{v}) = \sum_{j=1}^{N} \frac{1}{2} M_j \mathbf{V}_j^2 + \sum_{\alpha=1}^{n} \frac{1}{2} m_{\mathrm{b}} \left(\mathbf{v}^{(\alpha)}\right)^2 + U_n(\mathbf{r}), \tag{3.9}$$

where m_{b} is the fictitious Parrinello-Rahman mass,[39] $\mathbf{v} = \left\{\mathbf{v}^{(1)}, \dots, \mathbf{v}^{(n)}, \mathbf{V}_1, \dots, \mathbf{V}_N\right\}$, and

$$U_n(\mathbf{r}) = \frac{1}{n} \sum_{\alpha=1}^{n} \frac{1}{2} m_{\mathrm{e}} \omega_n^2 \left(\mathbf{q}^{(\alpha)} - \mathbf{q}^{(\alpha-1)}\right)^2 + \frac{1}{n} \sum_{\alpha=1}^{n} U_{\mathrm{ext}}\left(\mathbf{q}^{(\alpha)}, \mathbf{Q}\right) \tag{3.10}$$

is the full potential energy function for the ring polymer.

The transmission coefficient in Eq. 3.3 is obtained from the flux-side correlation function using

$$\kappa(t) = \frac{\left\langle \dot{\xi}_0\; h\big(\xi(\mathbf{r}_t) - \xi^{\ddagger}\big)\right\rangle_{\mathrm{c}}}{\left\langle \dot{\xi}_0\; h\Big(\dot{\xi}_0\Big)\right\rangle_{\mathrm{c}}}, \tag{3.11}$$

where $h(\xi)$ is the Heaviside function, $\dot{\xi}_0$ is the initial velocity of the collective variable in an RPMD trajectory released from the dividing surface, and $\mathbf{r}_t$ is the time-evolved position of the system along that trajectory.[33]

3.2.2 Semiclassical instanton theory

The "Im F" premise in semiclassical rate theory relates the thermal rate constant in the deep-tunneling regime to the analytical continuation of the partition function into the complex plane,[51–56]

$$k \approx \frac{2}{\beta\hbar Q_{\mathrm{r}}} \mathrm{Im}\, R, \tag{3.12}$$

where Q_{r} is the reactant partition function and Im R is the imaginary part of the analytical continuation of the partition function for the full system. In the steepest-descent limit, the "Im F" description is equivalent to the flux-side time correlation formulation[57] of semiclassical instanton (SCI) theory.[58] We adapt this approach to describe the transfer of a single quantized electron in a classical solvent.

The partition function for the full system in the ring-polymer representation can be expressed

$$Q_n = c \int d\mathbf{Q}\; I_n(\mathbf{Q}) \tag{3.13}$$

where $c = \prod_{j=1}^{N} \frac{M_j}{2\pi\beta\hbar^2}$,

$$I_n(\mathbf{Q}) = \left(\frac{m_e \omega_n}{2\pi\hbar}\right)^{-n/2} \int d\{q^{(\alpha)}\} e^{-A(\{q^{(\alpha)}\};\mathbf{Q})/\hbar}, \tag{3.14}$$

and

$$A(\{q^{(\alpha)}\};\mathbf{Q}) = (\beta\hbar) U_n(\mathbf{r}) \tag{3.15}$$

is the classical action for a periodic trajectory in imaginary time. The notation presented here assumes that the quantized electron moves in a single dimension. At each solvent configuration, the steepest-descent approximation to $I_n(\mathbf{Q})$ is obtained by expanding $A(\{q^{(\alpha)}\};\mathbf{Q})$ to second order about its global minimum $\{\tilde{q}^{(\alpha)}\}$, for which the electron ring-polymer coordinates obey the stationary condition

$$\frac{1}{n}\sum_{\alpha=1}^{n} \left| \frac{\partial}{\partial q^{(\alpha)}}\, U_{\text{ext}}\left(q^{(\alpha)},\mathbf{Q}\right)\Big|_{q^{(\alpha)}=\tilde{q}^{(\alpha)}} - \omega_n^2 \left(\tilde{q}^{(\alpha+1)} + \tilde{q}^{(\alpha-1)} - 2\tilde{q}^{(\alpha)}\right) \right| = 0. \tag{3.16}$$

The steepest-descent approximation yields

$$I_n(\mathbf{Q}) = \frac{1}{\sqrt{\det\, \mathbf{K}}} e^{-A(\{\tilde{q}^{(\alpha)}\};\mathbf{Q})/\hbar}, \tag{3.17}$$

where $\mathbf{K}$ is the Hessian matrix given by

$$K_{\mu\nu} = \frac{\omega_n}{\hbar} \frac{\partial^2}{\partial q^{(\mu)} \partial q^{(\nu)}}\; A(\{\tilde{q}^{(\alpha)}\};\mathbf{Q})\Big|_{\{q^{(\alpha)}\}=\{\tilde{q}^{(\alpha)}\}}, \tag{3.18}$$

and where $(\det\, \mathbf{K}) = \prod_{i=1}^{n} \eta_i^2$ is obtained from the normal mode frequencies, $\{\eta_i\}$.

For a reaction with a barrier, a saddle point satisfies the stationary condition in Eq. 3.16, and the Hessian matrix exhibits an imaginary normal-mode frequency, η_1. By analytically continuing η_1 onto the real axis, and by integrating out the zero-frequency normal mode that is associated with

the cyclic permutation of the ring-polymer beads, we obtain the steepest-descent SCI rate[58]

$$k_{\mathrm{SCI}} = \frac{c}{Q_{\mathrm{r}}} \int d\mathbf{Q}\, \mathcal{I}_n(\mathbf{Q})\,, \tag{3.19}$$

where

$$\mathcal{I}_n(\mathbf{Q}) = \left(\frac{m_e B_n \omega_n^3}{2\pi\hbar}\right)^{1/2} \frac{1}{\sqrt{\det{}'\ \mathbf{K}}} e^{-A(\{\tilde{q}^{(\alpha)}\};\mathbf{Q})/\hbar}, \tag{3.20}$$

$(\det{}'\ \mathbf{K}) = \prod\limits^{\prime} |\eta_i|^2$ is obtained from a product that excludes the zero-frequency mode, and

$$B_n = \sum_{\alpha=1}^{n} (\tilde{q}^{(\alpha+1)} - \tilde{q}^{(\alpha)})^2. \tag{3.21}$$

Formal connections between path-integral statistics and reactive tunneling have long been recognized.[25,58–62] In particular, Althorpe and coworkers[37] have recently emphasized the connection between the TST limit of RPMD and the reversible action work (RAW) formulation of SCI theory.[54,63] To the extent that Eq. 3.19 is an harmonic approximation to the RAW SCI formulation,[37]

$$k_{\mathrm{RPMD}} = \left(\frac{\kappa_{\mathrm{o}}}{\alpha}\right) k_{\mathrm{SCI}}, \tag{3.22}$$

where $\alpha = 2\pi(\beta\hbar|\eta_1|)^{-1}$, and κ_{o} is the transmission coefficient through a dividing surface that minimizes the recrossing of RPMD trajectories.

3.2.3 Exact quantum dynamics

We obtain numerically exact quantum dynamics for ET using the Quasi-Adiabatic Path Integral method (QUAPI).[64–68] The method is applied to a redox system composed of two diabatic electronic states and a coordinate representing polarization of the solvent dipole field; the solvent coordinate is in turn linearly coupled to a harmonic oscillator bath.

The Hamiltonian for the redox system[65]

$$H_{\mathrm{S}} = \frac{p_s^2}{2m_{\mathrm{s}}} + \begin{pmatrix} V_{11}(s) & V_{12}(s) \\ V_{12}(s) & V_{22}(s) \end{pmatrix}, \tag{3.23}$$

where s is the solvent coordinate, p_s is the conjugate momentum, and m_{s} is the effective solvent mass. Here, $V_{11}(s)$ and $V_{22}(s)$ are diabatic states corresponding to reactant and product states for ET, and $V_{12}(s)$ is the electronic coupling. The Hamiltonian describing the bath modes and their

coupling to the solvent coordinate is

$$H_{\mathrm{B}} = \sum_{j=1}^{f} \frac{P_j^2}{2M_j} + \sum_{j=1}^{f} \frac{1}{2} M_j \omega_j^2 \left(Q_j - \frac{c_j s}{M_j \omega_j^2} \right)^2 , \tag{3.24}$$

where M_j, ω_j, and Q_j are the mass, frequency and the position of the j^{th} bath mode, respectively, and c_j is the strength of the coupling between the j^{th} bath mode and the solvent coordinate.

The exact quantum mechanical rate constant can be expressed in terms of the symmetrized real-time flux-flux correlation function,[69]

$$k_{\mathrm{Q}} = \lim_{t' \to \infty} \frac{1}{Q_{\mathrm{R}}} \int_0^{t'} C_{\mathrm{FF}}(t) dt, \tag{3.25}$$

where

$$C_{\mathrm{FF}}(t) = \mathrm{Tr}[\mathcal{F} e^{iHt_{\mathrm{c}}^*/\hbar} \mathcal{F} e^{-iHt_{\mathrm{c}}/\hbar}], \tag{3.26}$$

and Q_{R} is the reactant partition function. Here, $H = H_{\mathrm{S}} + H_{\mathrm{B}}$ is the full ET Hamiltonian, $\mathcal{F} = \frac{i}{\hbar}[H, \mathcal{P}_2]$ is the operator for the flux between the reactant and product electronic states, $\mathcal{P}_2 = |2\rangle\langle 2|$ is the projection operator for the product electronic state, and $t_{\mathrm{c}} = t - i\beta\hbar/2$ is the complex time. The propagators are discretized into $\mathcal{N}$ time slices of length Δt_{c}, and the trace in Eq. 3.26 is expanded to yield

$$\begin{aligned} C_{\mathrm{FF}}(t) = \int_{-\infty}^{\infty} d\mathbf{Q}_0 \Bigg\langle \mathbf{Q}_0 \Bigg| \langle s_1, \sigma_1 | \mathcal{F} | s_{2\mathcal{N}+2}, \sigma_{2\mathcal{N}+2} \rangle \prod_{k=\mathcal{N}+3}^{2\mathcal{N}+2} \langle \sigma_k, s_k | e^{iH\Delta t_{\mathrm{c}}^*/\hbar} | \sigma_{k-1}, s_{k-1} \rangle \\ \times \langle s_{\mathcal{N}+2}, \sigma_{\mathcal{N}+2} | \mathcal{F} | s_{\mathcal{N}+1}, \sigma_{\mathcal{N}+1} \rangle \prod_{k=2}^{\mathcal{N}+1} \langle \sigma_k, s_k | e^{-iH\Delta t_{\mathrm{c}}/\hbar} | \sigma_{k-1}, s_{k-1} \rangle \Bigg| \mathbf{Q}_0 \Bigg\rangle , \end{aligned} \tag{3.27}$$

where $\mathbf{Q}_0$ represents the bath degrees of freedom, s_k is the solvent coordinate, and σ_k is the electronic state at complex time slice k.

The propagators in Eq. 3.27 are factorized using the quasi-adiabatic short-time approximation[64]

$$e^{-iH\Delta t_{\mathrm{c}}/\hbar} \approx e^{-iH_{\mathrm{B}}\Delta t_{\mathrm{c}}/2\hbar} e^{-iH_{\mathrm{S}}\Delta t_{\mathrm{c}}/\hbar} e^{-iH_{\mathrm{B}}\Delta t_{\mathrm{c}}/2\hbar}. \tag{3.28}$$

Analytical integration over the bath modes then yields

$$C_{\mathrm{FF}}(t) = \frac{1}{\hbar^2} \mathrm{Re} \left[C_1(2,2,1,1;t_{\mathrm{c}}) - C_2(2,1,2,1;t_{\mathrm{c}}) + C_3(1,1,2,2;t_{\mathrm{c}}) - C_4(1,2,1,2;t_{\mathrm{c}}) \right], \tag{3.29}$$

where

$$C_i(\sigma_1,\sigma_{\mathcal{N}+1},\sigma_{\mathcal{N}+2},\sigma_{2\mathcal{N}+2};t_{\rm c}) = \int ds_1 \cdots \int ds_{\mathcal{N}} \int ds_{\mathcal{N}+2} \cdots \int ds_{2\mathcal{N}+1} \times \sum_{\sigma_2=1}^{2} \cdots \sum_{\sigma_{\mathcal{N}}=1}^{2} \sum_{\sigma_{\mathcal{N}+3}=1}^{2} \cdots \sum_{\sigma_{2\mathcal{N}+1}=1}^{2} I_i(\mathbf{s},\boldsymbol{\sigma};t_{\rm c}) \tag{3.30}$$

and

$$I_i(\mathbf{s},\boldsymbol{\sigma};t_{\rm c}) = V_{12}(s_1)\, V_{12}(s_{\mathcal{N}+2}) K(\mathbf{s},\boldsymbol{\sigma};t_{\rm c}) \mathcal{I}(\mathbf{s}). \tag{3.31}$$

Here, $s_{2\mathcal{N}+2} = s_1$, $s_{\mathcal{N}+2} = s_{\mathcal{N}+1}$, and we have introduced the notation $\mathbf{s} = \{s_1,\ldots,s_{2\mathcal{N}+2}\}$ and $\boldsymbol{\sigma} = \{\sigma_1,\ldots,\sigma_{2\mathcal{N}+2}\}$.

In Eq. 3.31, the path-integral expression for the complex-time propagators of the system Hamiltonian is given by

$$K(\mathbf{s},\boldsymbol{\sigma};t_{\rm c}) = \prod_{k=\mathcal{N}+3}^{2\mathcal{N}+2} \langle \sigma_k, s_k | e^{iH_{\rm S}\Delta t_{\rm c}^*/\hbar} | \sigma_{k-1}, s_{k-1}\rangle \prod_{k=2}^{\mathcal{N}+1} \langle \sigma_k, s_k | e^{-iH_{\rm S}\Delta t_{\rm c}/\hbar} | \sigma_{k-1}, s_{k-1}\rangle. \tag{3.32}$$

The matrix elements in Eq. 3.32 are obtained using the numerically exact expression

$$\langle s_k,\sigma_k | e^{-iH_{\rm S}\Delta t_{\rm c}/\hbar} | s_{k-1},\sigma_{k-1}\rangle = \sum_{m=1}^{M_0} \phi_m(s_k,\sigma_k)\phi_m^*(s_{k-1},\sigma_{k-1}) e^{-iE_m\Delta t_{\rm c}/\hbar}, \tag{3.33}$$

where $\phi_m(s,\sigma)$ and E_m are the eigenstates and eigenenergies of $H_{\rm S}$, respectively, and M_0 is the number of eigenstates included in the expansion.

The discretized form of the non-local influence functional in Eq. 3.31, which accounts for bath-induced electronic transitions in the system, is

$$\mathcal{I}(\mathbf{s}) = \mathcal{I}_0 \exp\left(- \sum_{k=1}^{2\mathcal{N}+2} \sum_{k'=1}^{k} B_{kk'} s_k\ s_{k'} \right), \tag{3.34}$$

where $\mathcal{I}_0$ is the partition function of the uncoupled bath oscillators.[64,70,71] The diagonal elements of $\{B_{kk'}\}$ describe local contributions to the bath response function from a particular complex time slice k along the adiabatic path, and the off-diagonal elements describe non-local contributions. For the case of linear system-bath coupling, the diagonal matrix elements are given by

$$B_{kk} = \sum_{j=1}^{f} \frac{c_j^2}{M_j\omega_j^3 \sinh(\beta\omega_j/2)} \sin\left(\frac{\omega_j(t_{k+1}-t_k)}{2}\right) \sin\left(\frac{\omega_j(t_{k+1}-t_k+i\beta)}{2}\right), \tag{3.35}$$

Table 3.1: Complex times t_k used to calculate the $\{B_{kk'}\}$.

k	t_k
1	0
$2,\ldots,\mathcal{N}+1$	$(k-1/2)\Delta t_{\rm c}$
$\mathcal{N}+2$	$t-i\beta\hbar/2$
$\mathcal{N}+3,\ldots,2\mathcal{N}+2$	$(2\mathcal{N}+3/2-k)\Delta t_{\rm c}^{*}-i\beta\hbar$
$2\mathcal{N}+3$	$-i\beta\hbar$

and the off-diagonal matrix elements are given by

$$B_{kk'} = \sum_{j=1}^{f} \frac{c_j^2}{M_j\omega_j^3 \sinh(\beta\omega_j/2)} \sin\left(\frac{\omega_j(t_{k+1}-t_k)}{2}\right) \times \cos\left(\frac{\omega_j(t_{k+1}-t_{k'+1}+t_k-t_{k'}+i\beta)}{2}\right) \sin\left(\frac{\omega_j(t_{k'+1}-t_{k'})}{2}\right). \tag{3.36}$$

The complex times t_k in Eqs. 3.35 and 3.36 are provided in Table 3.1.

3.2.4 Marcus theory for ET in a classical solvent

In the Marcus theory for ET,[3,72–74] electronic transitions occur at solvent geometries for which the donor and acceptor electronic states are isoenergetic. In the limit of weak electronic coupling and classical solvent motions, the ET rate is thus

$$k_{\rm MT} = \frac{2\pi}{\hbar}|V_{12}|^2 \left(\frac{\beta}{4\pi\lambda}\right)^{1/2} e^{-\beta\Delta G^{*}}, \tag{3.37}$$

where V_{12} is the electronic coupling matrix element,

$$\Delta G^{*} = \frac{(\Delta G^0+\lambda)^2}{4\lambda}, \tag{3.38}$$

λ is the solvent reorganization energy, and $-\Delta G^0$ is the thermodynamic driving force for the ET reaction. The rate expression in Eq. 3.37 exhibits three distinct regimes of behavior as the driving force is varied relative to λ. In the normal regime, where $-\Delta G^0 < \lambda$, the rate increases with increasing driving force. A turnover in this trend occurs in the activationless regime, for which $-\Delta G^0 \approx \lambda$. In the inverted regime, for which $-\Delta G^0 > \lambda$, the rate decreases with increasing driving force.

In the current study, we use implementations for Marcus theory, SCI theory, and RPMD in which the solvent degrees of freedom are treated classically; the role of nuclear quantum effects in

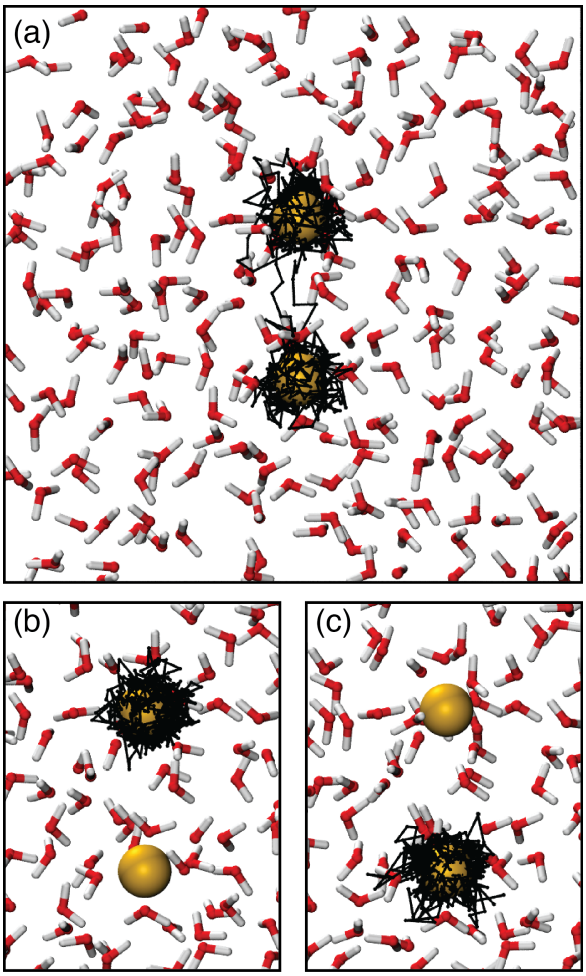

Figure 3.1: Snapshots of the atomistic representation for the ET reaction, with the donor and acceptor metal ions shown in yellow, the electron ring polymer in black, and the water molecules in red and white. Typical configurations of the symmetric ET system are presented with the electron ring polymer (a) in transition between the redox sites, (b) in the reactant basin, and (c) in the product basin.

diminishing the degree of turnover for the ET rate in the inverted regime[3,75] is not considered here.

3.3 Systems

ET dynamics is studied using both all-atom and system-bath representations for mixed-valence transition metal ions in water. These representations are described in this section.

Table 3.2: Parameters for the atomistic representation of ET.

Parameter	Value
$\mathbf{Q}_{\mathrm{A}}$ /Å	$(0, 0, -3.25)$
$\mathbf{Q}_{\mathrm{D}}$ /Å	$(0, 0, 3.25)$
$r_{\mathrm{cut}}^{\mathrm{H}}$ /Å	1.0
$r_{\mathrm{cut}}^{\mathrm{M}}$ /Å	1.1
q_{O} /e	-0.84
q_{H} /e	0.42
q_{M} /e	3.0
γ_{O} / (kcal/mol Å^9)	6392.7

3.3.1 Atomistic representation for ET

The atomistic representation for the ET reaction (Fig. 3.1) is described using the potential energy function[76]

$$U_{\mathrm{ext}}(\mathbf{q}, \mathbf{Q}) = U_{\mathrm{sol}}(\mathbf{Q}) + U_{\text{e-sol}}(\mathbf{q}, \mathbf{Q}) + U_{\text{e-M}}(\mathbf{q}, \mathbf{Q}) + U_{\text{M-sol}}(\mathbf{Q}), \tag{3.39}$$

where $\mathbf{q}$ is the electron position and $\mathbf{Q}$ is the set of N classical solvent atom positions. Solvent-solvent interactions, $U_{\mathrm{sol}}(\mathbf{Q})$, are described using the simple point charge (SPC) model[77] for explicit, rigid water molecules. The remaining interactions are described below, with the values of the parameters provided in Table 3.2.

The electron-water interactions are described using the pairwise pseudopotential[78]

$$U_{\text{e-sol}}(\mathbf{r}) = \sum_{k=1}^{N} U_{\text{e-sol}}^{k}(r_k),$$

where $r_k = |\mathbf{q} - \mathbf{Q}_k|$. For cases in which the atom index k corresponds to a hydrogen atom,

$$U_{\text{e-sol}}^{k}(r_k) = \begin{cases} -\dfrac{\mathrm{q}_{\mathrm{H}} e}{4\pi\varepsilon_0 r_{\mathrm{cut}}^{\mathrm{H}}}, & r_k \leq r_{\mathrm{cut}}^{\mathrm{H}} \\ -\dfrac{\mathrm{q}_{\mathrm{H}} e}{4\pi\varepsilon_0 r_k}, & r_k > r_{\mathrm{cut}}^{\mathrm{H}}, \end{cases} \tag{3.40}$$

and when k corresponds to an oxygen atom,

$$U_{\text{e-sol}}^{k}(r_k) = -\frac{\mathrm{q}_{\mathrm{O}} e}{4\pi\varepsilon_0 r_k}. \tag{3.41}$$

Electron-ion interactions are described using

$$U_{\text{e-M}}(\mathbf{q}) = U_{\text{e-D}}(|\mathbf{q} - \mathbf{Q}_{\mathrm{D}}|) + U_{\text{e-A}}(|\mathbf{q} - \mathbf{Q}_{\mathrm{A}}|), \tag{3.42}$$

Table 3.3: Values of the asymmetry parameter ϵ considered in the atomistic representation and the corresponding thermodynamic driving force regimes.

Case	ϵ / e	ET Regime
I	0.0	Symmetric
II	0.1	Normal
III	0.2	Normal
IV	0.3	Activationless
V	0.4	Inverted
VI	0.6	Inverted
VII	0.7	Inverted

where $\mathbf{Q}_\mathrm{D}$ and $\mathbf{Q}_\mathrm{A}$ denote the respective positions of the donor and acceptor metal ions, which are held fixed at a separation of 6.5 Å. These interactions are described using Shaw-type pairwise pseudopotentials.[79] For the acceptor metal ion,

$$U_{\text{e-A}}(r) = \begin{cases} -\dfrac{(\mathrm{q_M} + \epsilon)\, e}{4\pi\varepsilon_0 r_{\mathrm{cut}}^{\mathrm{M}}}, & r \leq r_{\mathrm{cut}}^{\mathrm{M}} \\ -\dfrac{(\mathrm{q_M} + \epsilon)\, e}{4\pi\varepsilon_0 r}, & r > r_{\mathrm{cut}}^{\mathrm{M}}, \end{cases} \tag{3.43}$$

where $r = |\mathbf{q} - \mathbf{Q}_\mathrm{A}|$, and for the donor metal ion,

$$U_{\text{e-D}}(r) = \begin{cases} -\dfrac{\mathrm{q_M} e}{4\pi\varepsilon_0 r_{\mathrm{cut}}^{\mathrm{M}}}, & r \leq r_{\mathrm{cut}}^{\mathrm{M}} \\ -\dfrac{\mathrm{q_M} e}{4\pi\varepsilon_0 r}, & r > r_{\mathrm{cut}}^{\mathrm{M}}, \end{cases} \tag{3.44}$$

with $r = |\mathbf{q} - \mathbf{Q}_\mathrm{D}|$. The asymmetry parameter, ϵ, adjusts the thermodynamic driving force for the ET reaction while leaving the solvent reorganization energy unchanged. The values of ϵ considered in this study and the corresponding ET regimes are presented in Table 3.3.

The ion-water interactions are given by

$$U_{\text{M-sol}}(\mathbf{Q}) = \sum_{k=1}^{N} \left(U_{\text{D-sol}}^{k}(\mathbf{Q}_k) + U_{\text{A-sol}}^{k}(\mathbf{Q}_k) \right). \tag{3.45}$$

For cases in which atom index k corresponds to a hydrogen atom,

$$U_{\text{D-sol}}^{k}(\mathbf{Q}_k) = \frac{\mathrm{q_H q_M}}{4\pi\varepsilon_0 |\mathbf{Q}_\mathrm{D} - \mathbf{Q}_k|}, \tag{3.46}$$

and when k corresponds to an oxygen atom,

$$U^{k}_{\text{D-sol}}(\mathbf{Q}_k) = \frac{\gamma_{\text{O}}}{|\mathbf{Q}_{\text{D}} - \mathbf{Q}_k|^9} + \frac{\text{q}_{\text{O}}\text{q}_{\text{M}}}{4\pi\varepsilon_0|\mathbf{Q}_{\text{D}} - \mathbf{Q}_k|}. \tag{3.47}$$

The potential energy functions associated with the acceptor ion, $U^{k}_{\text{A}-\text{sol}}(\mathbf{Q})$, are obtained by replacing $\mathbf{Q}_{\text{D}}$ with $\mathbf{Q}_{\text{A}}$ in Eqs. 3.46 and 3.47. These ion-water potential energy functions include electrostatic interactions combined with short-range repulsive terms that reproduce the octahedral coordination structure of the solvated ions.[76]

3.3.2 System-bath representations for ET

The system-bath representation for the ET reaction is described in the position basis using the potential energy function

$$U_{\text{ext}}(q, s, \mathbf{Q}) = U_{\text{e}-\text{M}}(q) + U_{\text{e}-\text{sol}}(q, s) + U_{\text{B}}(s, \mathbf{Q}), \tag{3.48}$$

where the first two terms comprise the system potential, and U_{B} is the potential energy contribution due to the bath. The scalar coordinates q and s are the positions of the electron and the solvent mode, respectively.

The first term in the system potential energy function models the ion-electron interaction,

$$U_{\text{e-M}}(q) = \begin{cases} a_{\text{L}}q^2 + b_{\text{L}}q + c_{\text{L}}, & r_{\text{L}}^{\text{out}} \leq q \leq r_{\text{L}}^{\text{in}} \\ a_{\text{R}}q^2 + b_{\text{R}}q + c_{\text{R}}, & r_{\text{R}}^{\text{in}} \leq q \leq r_{\text{R}}^{\text{out}} \\ -\dfrac{(3+\epsilon)}{|q - r_{\text{A}}|} - \dfrac{3}{|q - r_{\text{B}}|}, & \text{otherwise.} \end{cases} \tag{3.49}$$

This one-dimensional (1D) potential energy function consists of two Coulombic wells capped by parabolic functions to remove the singularity; it is continuous, and its derivative is piecewise continuous over the full range of q. The coefficients in Eq. 3.49 are provided in Appendix 3.1, and the values of ϵ considered for the system-bath representation are presented in Table 3.4.

The second term in the system potential energy function models the solvent and its interactions with the transferring electron,

$$U_{\text{e-sol}}(q, s) = \mu s \tanh(\phi q) + \frac{1}{2}m_{\text{s}}\omega_{\text{s}}^2 s^2. \tag{3.50}$$

Table 3.4: Values of the asymmetry parameter ϵ considered in the system-bath representation, the corresponding thermodynamic driving force regimes, and the electronic coupling matrix element, V_{12}.[a]

Case	Model SB1		Model SB2		ET Regime
	ϵ	$\lvert V_{12}\rvert$	ϵ	$\lvert V_{12}\rvert$	
I	0.0	6.6860	0.0	2.0662	Symmetric
II	0.05	6.4837	−0.015	2.0916	Normal
III	0.10	6.1300	−0.025	2.1088	Normal
IV	0.20	5.4840	−0.050	2.1524	Activationless
V	0.30	4.9120	−0.075	2.1971	Inverted
VI	0.40	4.4040	−0.100	2.2427	Inverted

[a] The coupling $|V_{12}|$ is given in units of a.u./10^7 for Model SB1 and a.u./10^5 for Model SB2; ϵ is in atomic units.

The first term on the RHS of this equation describes the coupling of the electronic dipole of the redox system to the solvent dipole, and $\omega_{\rm s}$ is the effective frequency of the solvent coordinate.

The harmonic oscillator bath potential in Eq. 3.49 has the same form as in Eq. 3.24,

$$U_{\rm B}(s,\mathbf{Q}) \quad = \quad \sum_{j=1}^{f}\left[\frac{1}{2}M\omega_j^2\left(Q_j-\frac{c_j s}{M\omega_j^2}\right)^2\right]. \tag{3.51}$$

The bath exhibits Ohmic spectral density with cutoff frequency $\omega_{\rm c}$,

$$J(\omega)=\eta\omega e^{-\omega/\omega_{\rm c}}, \tag{3.52}$$

where the dimensionless parameter η determines the strength of coupling between the system and the bath modes.[55] The continuous spectral density is discretized into f oscillators with frequencies[32]

$$\omega_j=-\omega_{\rm c}\log\left(\frac{j-0.5}{f}\right) \tag{3.53}$$

and coupling constants

$$c_j=\omega_j\left(\frac{2\eta M\omega_{\rm c}}{f\pi}\right)^{1/2}, \tag{3.54}$$

where $j=1\ldots f$.

In the current paper, we use two sets of parameters for the system-bath representation. Model SB1 is constructed to reproduce the energy-scales of the atomistic representation, and Model SB2 uses parameters that are numerically less demanding for the QUAPI calculations. The parameters for the models are given in Table 3.5.

As indicated previously, the QUAPI method is implemented using a discrete representation

Table 3.5: Parameters for the system-bath representation of ET.

Parameter[a]	Model SB1	Model SB2
r_{A}/Å	3.25	2.72435
r_{B}/Å	−3.25	−2.72435
μ	0.0230725	0.0114265
f	12	
ω_{s}	0.00228	
ω_{c}	0.00228	
M	1836.0	
m_{s}	1836.0	
$\eta/M\omega_{\mathrm{c}}$	1.0	
ϕ/r_{A}	3.0	

[a] Parameters given in atomic units, unless otherwise specified.

for the diabatic states of the redox system (Eq. 3.23). The system representation in the position basis described in Eq. 3.48 is therefore transformed to the electronic diabatic basis for the QUAPI calculations. The resulting diagonal matrix elements for the system potential energy are

$$V_{11}(s) = a_1 s^2 + b_1 s + c_1 \tag{3.55}$$

and

$$V_{22}(s) = a_2 s^2 + b_2 s + c_2, \tag{3.56}$$

and the constant off-diagonal elements V_{12} are reported in Table 3.4. The details of this transformation and the values of the coefficients in Eqs. 3.55 and 3.56 are given in Appendix 3.2.

3.4 Calculation details

3.4.1 Atomistic representation

The atomistic system includes 430 SPC water molecules in a cubic simulation cell with periodic boundary conditions. The side-length of the cell is $L = 23.46$ Å. All calculations are performed at a temperature of $T = 300$ K, and all pairwise interactions are truncated at a distance of $r_{\mathrm{cut}} = L/2$. Long-range electrostatics are treated by the force-shifting algorithm,[80] where the Coulombic portion of each potential is multiplied by a damping function $S(r)$, such that both the potential and its

derivative smoothly vanish at $r = r_{\mathrm{cut}}$. Specifically,

$$S(r) = \begin{cases} 1 - \dfrac{2r}{r_{\mathrm{cut}}} + \dfrac{r^2}{{r_{\mathrm{cut}}}^2}, & r \leq r_{\mathrm{cut}} \\ 0, & r > r_{\mathrm{cut}} \end{cases} . \tag{3.57}$$

Force-shifting reduces the unphysical structuring of water near the cutoff radius,[80] and it is found to have little effect on the solvent environment of the redox system.

3.4.1.1 RPMD

The atomistic RPMD simulations are implemented in the DL_POLY molecular dynamics package.[81] In all simulations, the RPMD equations of motion are evolved using the velocity Verlet algorithm,[82] and the constraints in the rigid-body water model are implemented using the RATTLE algorithm.[83] The electron is quantized with $n = 1024$ ring-polymer beads. As in previous RPMD simulations, each timestep for the electron ring polymer involves separate coordinate updates due to forces arising from the physical potential and due to exact evolution of the purely harmonic portion of the ring-polymer potential. The resulting integration algorithm is time-reversible and symplectic.

Several collective variables are used to characterize the ET reaction in the atomistic representation. The position of the electron is described by a ring-polymer progress variable, or "bead-count" coordinate, defined as

$$f_{\mathrm{b}}(\mathbf{q}^{(1)}, \ldots, \mathbf{q}^{(n)}) = \frac{1}{n} \sum_{\alpha=1}^{n} \frac{1}{2} \left(\tanh\left(b q_z^{(\alpha)} \right) + 1 \right), \tag{3.58}$$

where $b = 1.25$ Å^{-1}, and the metal ions are symmetrically positioned on the z-axis. We also consider the solvent collective variable

$$\Delta U(\mathbf{Q}) = -\frac{e}{4\pi\varepsilon_0} \sum_{k=1}^{N} \left(\frac{\mathrm{q_k}}{|\mathbf{Q}_{\mathrm{D}} - \mathbf{Q}_k|} - \frac{\mathrm{q_k}}{|\mathbf{Q}_{\mathrm{A}} - \mathbf{Q}_k|} \right), \tag{3.59}$$

where $q_k \in \{\mathrm{q_H}, \mathrm{q_O}\}$ is the charge on solvent atom k. This solvent collective variable, which is familiar from earlier simulation studies of Marcus theory,[76,84] describes the energy difference between the electronic diabatic states in the tight-binding approximation.

The RPMD rate in Eq. 3.3 is calculated from the product of the TST rate and the transmission coefficient. The TST rate described in Eq. 3.4 is obtained from $F(f_{\mathrm{b}})$, the FE profile in the bead-count coordinate. This FE profile is calculated using umbrella sampling and the weighted histogram

analysis method (WHAM), as described below.[85,86]

For each value of the asymmetry parameter ϵ, the following umbrella sampling protocol is used. The region $f_{\mathrm{b}} = 0.06 - 0.94$ is sampled with 22 trajectories that are harmonically restrained to uniformly spaced values of f_{b} using a restraint force constant of 1.195×10^4 kcal/mol. Likewise, the regions $f_{\mathrm{b}} = 0.945 - 1.0$ and $f_{\mathrm{b}} = 0.0 - 0.055$ are each sampled with 11 uniformly spaced windows using a higher force constant of 1.195×10^5 kcal/mol. The regions of $f_{\mathrm{b}} = 0.986 - 0.991$ and $f_{\mathrm{b}} = 0.009 - 0.015$ are each sampled with 5 uniformly spaced windows using a force constant of 1.195×10^5 kcal/mol. The equilibrium sampling trajectories are performed using path-integral molecular dynamics (PIMD) with a Parrinello-Rahman mass of 364.6 a.u., which allows for a timestep of 0.025 fs; this choice of mass does not affect the calculated FE profile or any other equilibrium ensemble average.[39,87] Each sampling trajectory is run for at least 50 ps, and thermostatting is performed during the trajectory calculations by resampling the particle velocities from the Maxwell-Boltzmann (MB) distribution every 1.25 ps.

The transmission coefficient in Eq. 3.11 is calculated using RPMD trajectories that are released from the dividing surface at $f_{\mathrm{b}}^{\ddagger}$. For each value of ϵ, the dividing surface is chosen to coincide with the maximum along the FE profile, $F(f_{\mathrm{b}})$. The positions of the dividing surfaces are set to $f_{\mathrm{b}}^{\ddagger} = (0.5,\ 0.7,\ 0.8,\ 0.96,\ 0.98,\ 0.98,\ 0.98)$ for the different ϵ-cases (I, II, ..., VI) in Table 3.3. Between 400 and 1200 trajectories are released for each value of ϵ. Each RPMD trajectory is evolved for 40 fs with a timestep of 5×10^{-5} fs and with the initial velocities sampled from the MB distribution. Initial configurations for the released RPMD trajectories are selected every 100 fs from eight long, independent PIMD sampling trajectories that are constrained to the dividing surface $\xi^{\ddagger}$. These sampling trajectories are thermostatted by resampling the velocities every 200 fs, and the constraint to the dividing surface is enforced using the RATTLE algorithm.

Two-dimensional (2D) FE surfaces in the ring-polymer centroid coordinate and the solvent coordinate, $F(\bar{z}, \Delta U)$, are used for the analysis of the ET reaction mechanism. For a given value of ϵ, the 2D FE surface is constructed using PIMD sampling trajectories that are harmonically restrained in both $\bar{z}$ and ΔU coordinates. The $\bar{z}$ coordinate is sampled using 43 uniformly spaced windows in the region of -3.575 Å to $+3.575$ Å with a harmonic restraint force constant of 169.7 kcal/mol Å^{-2}. To ensure adequate sampling of ring-polymer configurations spanning both metal ions, we use four additional sampling trajectories that are harmonically restrained to $\bar{z} = \pm 2.7625$ Å and $\bar{z} = \pm 2.925$ Å with a force constant of 452.5 kcal/mol Å^{-2}. The solvent coordinate is sampled with 15 uniformly spaced windows in the range -130 to $+150$ kcal/mol using a harmonic restraint force

constant of 0.023 $(\text{kcal/mol})^{-1}$. Each sampling trajectory is run for at least 50 ps, with velocities resampled from the MB distribution every 500 fs. We note that f_b is a good progress variable for ET throughout the entire regime of the thermodynamic driving forces, whereas the ring-polymer centroid is not. In the ET inverted regime, the centroid does not fully distinguish between ring-polymer configurations in the reactant and product basins; no such difficulty is experienced in the calculations reported here.

3.4.1.2 Marcus theory

Marcus theory rates are calculated using Eqs. 3.37 and 3.38. The driving force, $-\Delta G^0$, is obtained from $F(\Delta U)$ as the difference between the free energies of the reactant and product minima; these values are reported in Table 3.6. To the extent that the tight-binding approximation holds, the reorganization energy, λ, is identical for all ϵ, and we confirm that this is very nearly the case in our calculations. For the case of symmetric ET ($\epsilon = 0$), the reorganization energy is calculated using $\lambda = 4F(\Delta U)|_{\Delta U=0}$ and is found to be 69.7 ± 0.7 kcal/mol.

The coupling matrix element in Eq. 3.37, $|V_{12}|$, is calculated as $2|V_{12}| = E_1 - E_0$, where E_0 and E_1 are the two lowest eigenenergies of the electron in the potential of the isolated metal ions with $\epsilon = 0$. These eigenenergies are obtained with an iterative, block Lanczos scheme,[88] performed on a uniform grid of $64 \times 64 \times 64$ points spanning the cubic simulation cell. The iterative Lanczos calculation employs 200 Krylov vectors and an exponential transform parameter of $\beta_\text{L} = 0.1$. The block Lanczos refinement uses ten blocks of five Krylov vectors. This yields a value for the tunnel splitting of $|V_{12}| = 0.0403$ kcal/mol (6.43×10^{-5} a.u.), which is consistent with previous calculations.[76] This value for the tunnel splitting was assumed to be insensitive to presence of solvent, as has been previously demonstrated,[89], and independent of the value of the asymmetry parameter ϵ. The validity of this latter assumption is confirmed for the system-bath models (see Table 3.4).

3.4.2 System-bath representation

As in the atomistic representation, the calculations in the system-bath representation are performed at $T = 300$ K. The harmonic bath is discretized using $f = 12$ modes.

3.4.2.1 RPMD

RPMD rates for the system-bath models are also calculated with the electron quantized using $n = 1024$ ring-polymer beads. For each value of ϵ, the FE profile, $F(f_\text{b})$, is obtained from um-

brella sampling along the f_{b} coordinate. For both system-bath models, SB1 and SB2, $F(f_{\mathrm{b}})$ is sampled with two sets of harmonically restrained PIMD trajectories. The region of $f_{\mathrm{b}} = 0.06 - 0.94$ is sampled with 45 trajectories that are harmonically restrained to uniformly spaced values of f_{b} using a force constant of 20 a.u. The regions of $f_{\mathrm{b}} = 0.0 - 0.05$ and $f_{\mathrm{b}} = 0.095 - 1.00$ are each sampled with 51 uniformly spaced windows using a harmonic restraint force constant of 3000 a.u. All sampling trajectories are performed using PIMD with the masses of the classical particles set to $m_{\mathrm{s}} = M = 0.01$ a.u; as before, the altered masses in the PIMD sampling trajectories allow for larger timesteps while having no effect on calculated ensemble averages. Each sampling trajectory is run for at least 12.09 ps, the PIMD timestep is 2.42×10^{-4} fs, and thermostatting is performed by resampling velocities from the MB distribution every 2.42 fs. The FE profiles are constructed from the sampling trajectories using WHAM.

For each value of ϵ, the transmission coefficient in Model SB1 is calculated from 2400 RPMD trajectories released from the dividing surface and evolved for 121 fs with the timestep of 1.21×10^{-4} fs. The position of the dividing surface is $f_{\mathrm{b}}^{\ddagger} = (0.5,\ 0.385,\ 0.2345,\ 0.014,\ 0.014,\ 0.014)$ for the ϵ-cases (I, II, ..., VI). In Model SB2, 1600 RPMD trajectories are released at each value of ϵ; each trajectory is evolved for 121 fs using a timestep of 2.42×10^{-4} fs; and the dividing surface is located at $f_{\mathrm{b}}^{\ddagger} = (0.5,\ 0.65,\ 0.75,\ 0.986,\ 0.986,\ 0.986)$ for ϵ-cases (I, II, ..., VI). Initial configurations for the released RPMD trajectories are sampled every 14.5 fs from eight long, independent PIMD sampling trajectories that are constrained to the dividing surface. The velocities of the PIMD sampling trajectories are resampled every 48.4 fs from the MB distribution. The dividing surface constraint is implemented using the RATTLE algorithm.

We note that RPMD results can be affected by coupling of fictitious internal ring-polymer modes to physical frequencies in the system.[90] We thus performed test calculations of the ET rate in these and similar systems using partially adiabatic centroid molecular dynamics (PACMD).[90,91] The PACMD calculations revealed no significant changes from the RPMD results, confirming that this issue does not impact our conclusions.

3.4.2.2 Marcus Theory

For the calculation of Marcus theory rates, the reorganization energy and the thermodynamic driving force for each value of epsilon are obtained analytically from the diabatic states for the donor and acceptor, $V_{11}(s)$ and $V_{22}(s)$. For Model SB1, we obtain a solvent reorganization energy of $\lambda = 68.9$ kcal/mol, and for Model SB2, we obtain $\lambda = 17.0$ kcal/mol. The values of $|V_{12}|$ for both

system-bath models is given in Table 3.4.

3.4.2.3 Semiclassical instanton theory

For the SB models, contributions from the linearly-coupled harmonic bath can be factorized and cancelled from the RHS of Eq. 3.12, yielding expressions that depend only on the electron ring-polymer coordinates and the single classical solvent coordinate, s. Calculation of k_{SCI} then consists of *(i)* determination of saddle-point configurations for the classical action, $A\left(\{q^{(\alpha)}\}; s\right)$, on a numerical grid in the solvent coordinate s, *(ii)* evaluation of the steepest-descent approximation for $\mathcal{I}_n(s)$ at each point on the solvent grid, and *(iii)* integration over the solvent coordinate in Eq. 3.19 via numerical quadrature. The reactant partition function, Q_r, was similarly obtained by evaluating $I_n(s)$ via steepest-decent expansion around the minimum-action configuration in the reactant basin. All calculations were performed using $n = 2048$ beads for the electron ring polymer.

For Model SB1, the grid in the solvent coordinate s consists of 200 uniformly spaced points in the range of -4 to 4 a.u.; for Model SB2, this grid consists of 150 uniformly spaced points in the range -3 to 3 a.u. At each value of s, the saddle-point configuration on the surface $A\left(\{q^{(\alpha)}\}; s\right)$ corresponds to the maximum along the path of minimum action that connects the reactant and product basins. This path of minimum action is obtained using the string method,[92] with the path discretized into $L = 1000$ equidistant slices and with minimization performed using Euler integration and a timestep of 2.4×10^{-3} fs. Initial convergence of the path is achieved when this minimization results in a change of less than 5.3×10^{-8} Å in each degree of freedom. The path is then iteratively refined in the vicinity of the saddle point: a 20-slice subsection of the path about the saddle point is extracted, the number of slices used to describe the path is doubled, and the subsection of the path is re-minimized with its endpoints fixed. Iterative refinement of the path is complete when the slice of maximum action (i.e., the saddle point configuration) satisfies Eq. 3.16 to within 10^{-5} a.u.

3.4.2.4 QUAPI

The QUAPI calculation for Model SB2 requires construction of the short-time system propagator followed by two independent Monte Carlo (MC) simulations to evaluate the flux-flux correlation function in Eq. 3.29.

The complex-time propagator in Eq. 3.33 is calculated using eigenvalues and eigenfunctions obtained from a 2D discrete variable representation (DVR) grid calculation[93] in the solvent coordinate, s, and the electronic state variable, σ. The DVR Hamiltonian is diagonalized on a grid of 40 uni-

formly spaced points over a range of -4 to $+4$ a.u. in s and $\sigma = 1, 2$. The number of eigenvalues and eigenvectors used in these calculations (M_0 in Eq. 3.33) ranges from 30 to 50 for the values of ϵ considered in this study.

The flux-flux correlation function in Eq. 3.29 is obtained from standard path-integral Monte Carlo (PIMC) sampling performed on the 2D DVR grid. In a first PIMC simulation, the correlation function is obtained using

$$C_{\rm FF}(t) = D_\rho \left\langle \, \mathrm{sgn}\{\mathrm{Re}\left[I_1(\mathbf{s},\boldsymbol{\sigma};t_{\rm c}) - I_2(\mathbf{s},\boldsymbol{\sigma};t_{\rm c}) + I_3(\mathbf{s},\boldsymbol{\sigma};t_{\rm c}) - I_4(\mathbf{s},\boldsymbol{\sigma};t_{\rm c})\right]\} \, \right\rangle_{\rho(\mathbf{s},\boldsymbol{\sigma};t_{\rm c})}, \tag{3.60}$$

where importance sampling is performed using the distribution

$$\rho(s,\sigma;t_{\rm c}) = \mathrm{Abs}\left\{\mathrm{Re}\left[I_1\mathbf{s}(\boldsymbol{\sigma};t_{\rm c}) - I_2(\mathbf{s},\boldsymbol{\sigma};t_{\rm c}) + I_3(\mathbf{s},\boldsymbol{\sigma};t_{\rm c}) - I_4(\mathbf{s},\boldsymbol{\sigma};t_{\rm c})\right]\right\}, \tag{3.61}$$

and the function $I_i(\mathbf{s},\boldsymbol{\sigma};t_{\rm c})$ is defined in Eq. 3.31. Convergence is achieved with 10^8 MC steps. The normalization constant, D_ρ, is obtained from a second, independent PIMC simulation, using

$$D_\rho = D_\Lambda \left\langle \, \frac{\rho(\mathbf{s},\boldsymbol{\sigma};t_{\rm c})}{\Lambda(\mathbf{s},\boldsymbol{\sigma};t_{\rm c})} \, \right\rangle_{\Lambda(\mathbf{s},\boldsymbol{\sigma};t_{\rm c})}. \tag{3.62}$$

Here, importance sampling is performed on the distribution

$$\Lambda(\mathbf{s},\boldsymbol{\sigma};t_{\rm c}) = \prod_{k=\mathcal{N}+3}^{2\mathcal{N}+2} \left|\langle\sigma_k, s_k|e^{iH_{\rm S}\Delta t_{\rm c}^*/\hbar}|\sigma_{k-1}, s_{k-1}\rangle\right| \prod_{k=2}^{\mathcal{N}+1} \left|\langle\sigma_k, s_k|e^{-iH_{\rm S}\Delta t_{\rm c}/\hbar}|\sigma_{k-1}, s_{k-1}\rangle\right|, \tag{3.63}$$

where $\sigma_1 = 2$, $\sigma_{\mathcal{N}+1} = 2$, $\sigma_{\mathcal{N}+2} = 1$, and $\sigma_{2\mathcal{N}+2} = 1$. Convergence is achieved with 10^6 MC steps, and the normalization constant D_Λ is obtained by direct matrix multiplication. A maximum of $\mathcal{N} = 4$ path beads are required to converge the flux-flux correlation function over a timescale of 25 fs; no significant changes are observed between calculations performed using $\mathcal{N} = 4$ and $\mathcal{N} = 8$.

The reactant partition function is obtained from a single PIMC calculation using the expression

$$Q_{\rm R} = \mathrm{Tr}[e^{-\beta H}\mathcal{P}_1], \tag{3.64}$$

where $\mathcal{P}_1 = |1\rangle\langle 1|$ is the projection operator for the reactant electronic state.

The QUAPI calculations for case IV are performed using a larger value for the coupling between the solvent coordinate and the bath modes, $\eta/M\omega_c = 30$. This change leads to lower-amplitude oscillations in the flux-flux correlation function and improved numerical convergence of the ET rate

Table 3.6: ET reaction rates for the atomistic representation, obtained using RPMD and Marcus theory.[a]

Case	$-\Delta G^o$	$\log k_{\mathrm{MT}}$	$\log k_{\mathrm{RPMD}}$
I	0.0	-2.2(1)	-1.7(2)
II	22(1)	4.6(3)	4.6(4)
III	43(1)	8.7(2)	8.4(2)
IV	63(1)	10.40(4)	10.17(9)
V	84(1)	10.0(1)	11.21(4)
VI	124(3)	2.9(8)	11.48(8)
VII	138(2)	-1.8(9)	11.80(7)

[a] ET rates are given in s^{-1}, and the $-\Delta G^0$ are given in kcal/mol. The numbers in parentheses denote the statistical uncertainty in the last reported digit.

calculation. Other features of the flux-flux correlation function, including the timescales for the real-time oscillations and the decorrelation time, are unchanged. The invariance of these features suggests that the parameters used in the current study correspond to the regime in which the ET reaction rate is independent of the solvent-bath coupling.[65,94] RPMD rate calculations performed using different values for $\eta/M\omega_c$ also support this conclusion.

3.5 Results

3.5.1 Atomistic simulations

The atomistic representation for ET (Fig. 3.1) is investigated using direct RPMD simulations and the Marcus rate theory. For each case of the thermodynamic driving force, Fig. 3.2(a) presents FE profiles for the reactant and product diabatic electronic states as a function of the solvent collective variable, $\Delta U(\mathbf{Q})$ (Eq. 3.59). The FE profiles are obtained by reducing the corresponding 2D surfaces, $F(f_{\mathrm{b}}, \Delta U)$, where the reactant and product diabats are associated with ring-polymer configurations for which $f_{\mathrm{b}} > 0.995$ and $f_{\mathrm{b}} < 0.005$, respectively. The results in Fig. 3.2(a) are graphically identical to those obtained using the tight-binding approximation, and the FE profiles exhibit the anticipated parabolic form, although no assumptions regarding the linear response of the solvent have been made.[76,84] These data, in combination with the calculated tunnel splitting for the transferring electron, are used to calculate the Marcus rates in Table 3.6.

Fig. 3.2(b) presents the corresponding FE profiles as a function of the bead-count coordinate, f_{b} (Eq. 3.58). These profiles are used in the statistical component of the RPMD rate calculation (Eqs. 3.3 and 3.4). As is seen from the inset, all of the profiles behave similarly in the vicinity of $f_{\mathrm{b}} \approx 1$. The steep rise in the FE profile between 0.980 and 0.999 is associated with the formation

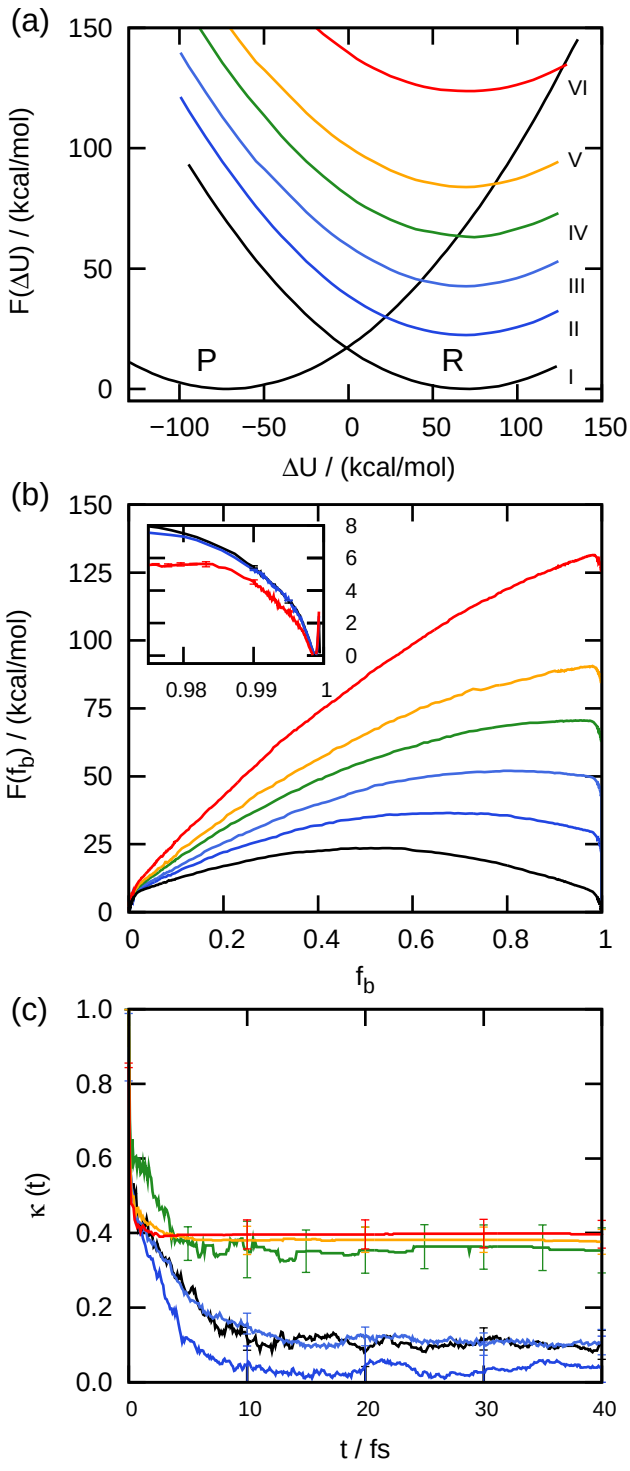

Figure 3.2: **(a)** FE profiles, $F(\Delta U)$, for the reactant (colored, at right) and product (left) diabatic electronic states as a function of the solvent collective variable in the atomistic representation. The various cases of the thermodynamic driving force for the ET reaction are labeled; see Tables 3.3 and 3.6 for details. For each case, the FE profiles are vertically shifted to align the minima of the product basin. **(b)** The corresponding FE profiles as a function of the bead-count coordinate, $F(f_\mathrm{b})$. In the main panel, the profiles are vertically shifted to align the product basin; in the inset, the profiles are vertically shifted to align the reactant basin. **(c)** The corresponding RPMD transmission coefficients for the ET reaction, $\kappa(t)$. In panels (b) and (c), the curves retain the same color scheme introduced in panel (a).

of "kink-pair" configurations, in which the ring polymer spans both redox sites;[25,95,96] a typical kink-pair configuration is illustrated in Fig. 3.1(a).

The dynamical component of the RPMD rate calculation (Eq. 3.11) is obtained from the long-time plateau[46] of the RPMD transmission coefficient shown in Fig. 3.2(c). Each transmission coefficient is calculated with respect to a dividing surface at a fixed value of $f_{\rm b}$, as is described in Sec. 3.4.1. Plateau values in the range of 0.1-0.4 indicate modest recrossing of the RPMD trajectories through these surfaces. For cases in which the thermodynamic driving force corresponds to ET in the normal and activationless regimes, Fig. 3.2(c) illustrates that the RPMD trajectories commit to the reactant or product basins within 10-20 fs, the timescale for local solvent motion between librational rebounds. At thermodynamic driving forces corresponding to the inverted regime, the transmission coefficient plateaus on faster timescales than those involving the rigid solvent molecules.

Fig. 3.3(a) presents a direct comparison of the RPMD and Marcus theory rates throughout the normal and activationless regime for ET in the atomistic representation. The RPMD rates, which are also reported in Table 3.6, quantitatively agree with the Marcus theory results over 12 orders of magnitude in the ET reaction rate. Unlike the Marcus rates, which are based on a TST description for the reaction, the calculated RPMD rates are independent of any *a priori* assumptions about the ET reaction mechanism.

Figs. 3.3(b) and (c) illustrate the ET reaction mechanism that is predicted from the RPMD simulations. Representative RPMD trajectories are projected onto the $(\bar{z}, \Delta U)$ plane, where $\bar{z}$ is the component of the ring-polymer centroid that lies along the axis of the metal ions in the system; also shown are FE profiles for the system in these collective variables. For symmetric ET (Case I), Fig. 3.3(b) reveals that the RPMD trajectories involve three distinct steps that will be familiar from the Marcus rate theory: *(i)* solvent fluctuation to a configuration for which the reactant and product diabats are nearly degenerate (indicated by the dashed line), *(ii)* formation of a kink-pair in the ring-polymer configuration and rapid transfer of the electron from one redox site to the other, and *(iii)* relaxation of the solvent coordinate in the product basin following the ET event. For ET approaching the activationless regime (Case IV), Fig. 3.3(c) shows the latter two steps in the mechanism remain, but only a small initial solvent fluctuation is needed to reach solvent configurations for which the electronic diabats are degenerate.

To understand the connection between RPMD and the Marcus theory rate expression, we note that Eq. 3.37 includes two key terms – an Arrhenius-type contribution that is associated with free energy of solvent reorganization to bring reactant and product diabats into degeneracy and a prefactor

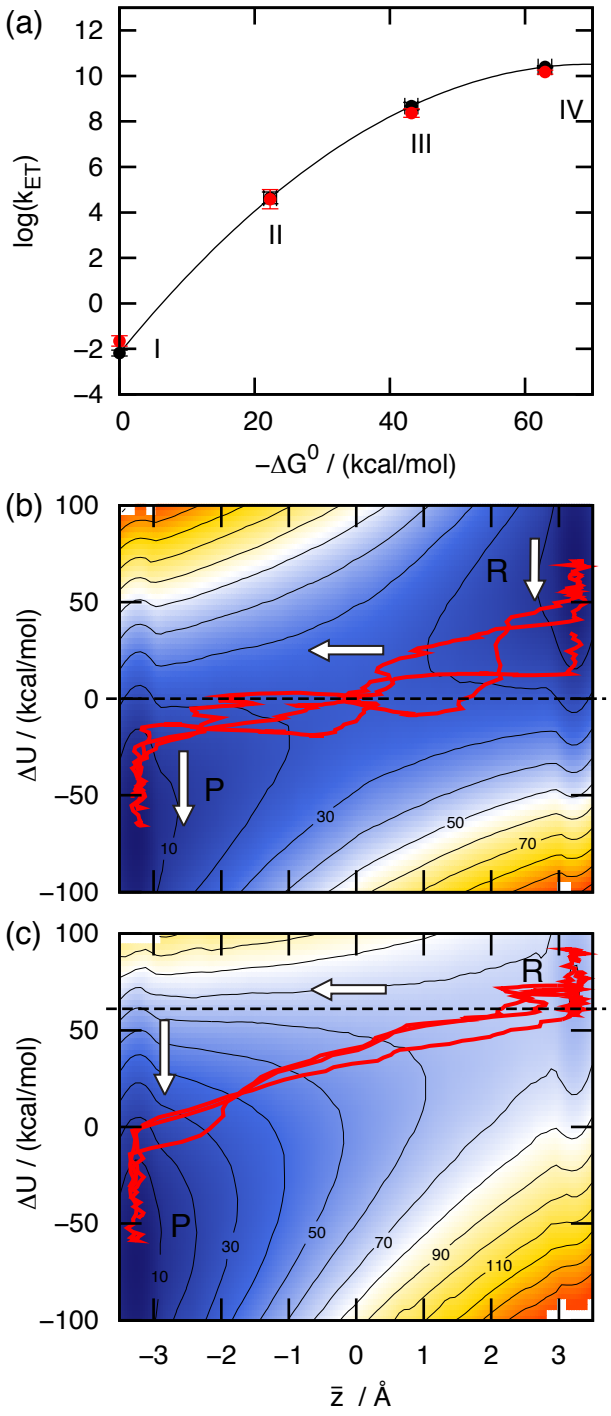

Figure 3.3: **(a)** ET reaction rates for the atomistic representation in the normal and activationless regimes, computed using RPMD (red) and Marcus theory (black). The various cases for the thermodynamic driving force are labeled. **(b)** Representative trajectories (red) from the ensemble of reactive RPMD trajectories for symmetric ET (Case I). The trajectories are plotted as a function of the ring-polymer centroid, $\bar{z}$, and the solvent collective variable, ΔU. The FE profile in these collective variables is also presented, with contour lines indicating FE increments of 10 kcal/mol. **(c)** Representative RPMD trajectories for activationless ET (Case IV) and the corresponding FE profile. The white arrows in panels (b) and (c) indicate the solvent reorganization mechanism for ET that is anticipated in the Marcus rate theory, and the dashed lines indicate values of ΔU at which the reactant and product diabats cross in Fig. 3.2(a).

that depends on the coupling between the diabatic states. RPMD captures the solvent reorganization energetics because the path-integral-based method preserves exact quantum statistics.[39,87] The RPMD rate also correctly accounts for the tunneling contribution to the ET reaction rate, which can likewise be attributed to the path-integral basis of the method; the tunnel splitting for the electron between degenerate redox sites is analytically related to the reversible work for forming a kink-pair in the ring-polymer configuration.[25,89,96] Given that the ensemble of reactive RPMD trajectories exhibit the dual rare events of solvent reorganization and kink-pair formation, and given that the FE barriers associated with these two steps are analytically related to the key terms in the Marcus rate expression, it is reasonable that Fig. 3.3(a) finds good agreement between RPMD and Marcus theory. The RPMD method succeeds in the normal and activationless regimes because it captures the correct physics of the ET reaction.

Fig. 3.4 demonstrates that the success of the RPMD method does not extend into the inverted regime for ET, with both the RPMD rates and reaction mechanism deviating from the predictions of Marcus theory. In Fig. 3.4(a), the RPMD rates are seen to be only weakly dependent on the increasing driving force, rather than exhibiting the characteristic turnover in this inverted regime. The RPMD trajectories also deviate from the reaction mechanism that is assumed in the Marcus TST, as is seen in Fig. 3.4(b). The reactive trajectories exhibit kink-pair formation directly from solvent configurations that are characteristic of the reactant basin; the expected solvent reorganization to configurations for which the electronic diabats are degenerate (indicated by the dashed line in the figure) is not observed.

To further explore the successes and failures of RPMD in these various regimes for ET, we compare the method with semiclassical instanton theory and exact quantum dynamics in the following section.

3.5.2 System-Bath Simulations

In this section, we employ system-bath representations for ET to allow for the comparison of RPMD with other simulation techniques, including semiclassical instanton and exact quantum dynamics methods.

Fig. 3.5(a) and Table 3.7 present a comparison of the RPMD and Marcus rates for Model SB1, which is parameterized to match the energy-scales for the atomistic representation (Sec. 3.3.2). As before, the RPMD method reproduces the Marcus rates throughout the normal and activationless regimes, while failing to predict the turnover of the ET rate in the inverted regime. Analysis of the

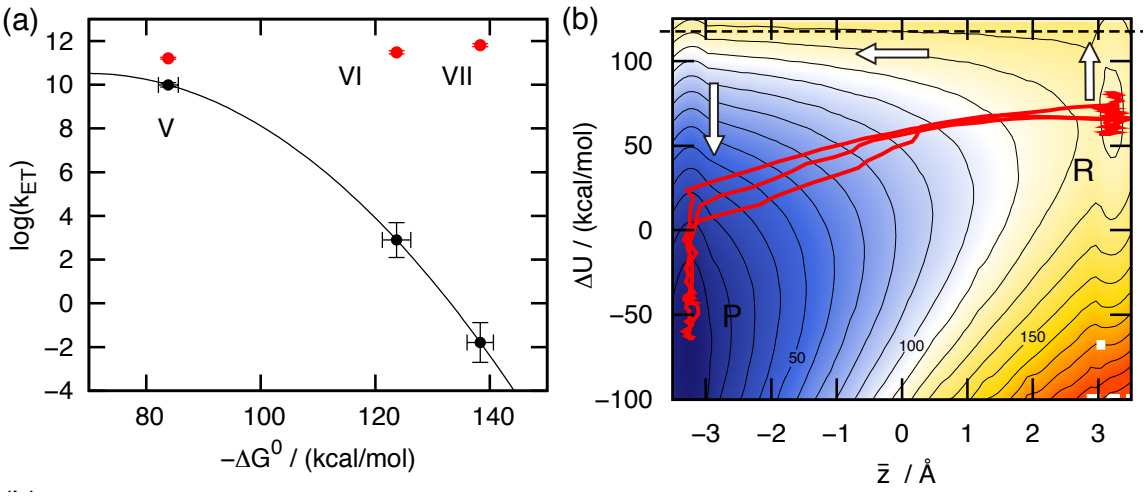

Figure 3.4: **(a)** ET reaction rates for the atomistic representation in the inverted regime, computed using RPMD (red) and Marcus theory (black). The various cases for the thermodynamic driving force are labeled. **(b)** Representative trajectories (red) from the ensemble of reactive RPMD trajectories for inverted ET (Case VI). The trajectories are plotted as a function of the ring-polymer centroid, $\bar{z}$, and the solvent collective variable, ΔU. The FE profile in these collective variables is also presented, with contour lines indicating FE increments of 10 kcal/mol. The white arrows indicate the solvent reorganization mechanism for ET that is anticipated in the Marcus rate theory, and the dashed line indicates the value of ΔU at which the reactant and product diabats cross in Fig. 3.2(a).

RPMD reactive trajectories in this system reveals mechanisms that are entirely analogous to those observed in Figs. 3.3(b), 3.3(c), and 3.4(b) for the atomistic system. Specifically, for the normal and activationless regimes, the RPMD trajectories exhibit solvent reorganization to configurations for which the electronic diabats are degenerate, followed by rapid transfer of the electron between redox sites; and for the inverted regime, RPMD predicts ET without prior solvent reorganization. These data confirm that Model SB1 exhibits the same essential physics as the atomistic representation.

ET rates from the steepest-descent SCI theory (Eq. 3.19) are also included in Fig. 3.5(a) and Table 3.7. Throughout the full range of thermodynamic driving forces, the instanton method tracks

Table 3.7: ET reaction rates for Model SB1, obtained using RPMD, Marcus theory, and SCI theory.[a]

Case	$-\Delta G^0$	$\log k_{\mathrm{MT}}$	$\log k_{\mathrm{RPMD}}$	$\log k_{\mathrm{SCI}}$	$\log \alpha k_{\mathrm{RPMD}}$
I	0.0	−6.0	−6.55(4)	−7.9	−7.3
II	18.5	−0.2	−0.33(3)	−1.9	−0.9
III	36.9	3.7	3.52(8)	2.4	2.8
IV	73.9	6.3	6.19(5)	5.6	5.4
V	110.9	1.6	6.44(1)	5.8	5.8
VI	148.0	−10.4	6.69(3)	5.9	5.9

[a] ET rates are given in s^{-1}, and the $-\Delta G^0$ are given in kcal/mol.

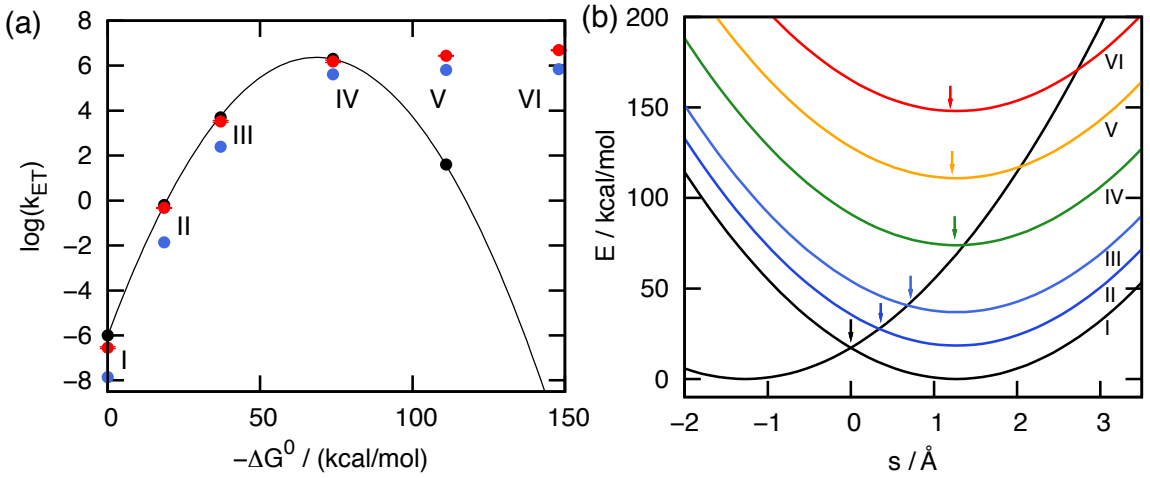

Figure 3.5: **(a)** ET reaction rates for Model SB1, computed using RPMD (red), Marcus theory (black), and SCI theory (blue). **(b)** FE profiles, $F(\Delta U)$, for the reactant (colored, at right) and product (left) diabatic electronic states as a function of the solvent coordinate, s. The various cases of the thermodynamic driving force for the ET reaction are labeled; see Table 3.4 for details. The arrow indicates the value of the solvent coordinate that maximizes $\mathcal{I}_n(s)$, which corresponds to the dominant contribution to the SCI rate in Eq. 3.19.

the RPMD results, including deviation from the Marcus predictions in the inverted regime. As is shown in Table 3.7, α-correction of the RPMD rates (Eq. 3.22, assuming $\kappa_o \approx 1$) further improves their agreement with the SCI rates. These results underscore that the failure of RPMD does not arise from a breakdown in its formal connection with SCI theory;[37] instead, the comparison suggests that both RPMD and the SCI theory share the same underlying flaw in the inverted regime. [a]

The mechanistic predictions from SCI theory also show similarities with the RPMD results. Fig. 3.5(b) presents the Marcus parabolas for the electronic diabats of Model SB1 as a function of the solvent coordinate, s. Also shown are the solvent configurations that correspond to the SCI predictions for the ET transition state. For each value of the thermodynamic driving force, the arrow in the figure indicates the solvent configuration that maximizes $\mathcal{I}_n(s)$, which corresponds to the largest contribution to the rate in Eq. 3.19. For the normal and activationless regimes, SCI theory correctly predicts an ET transition state at the crossing of the electronic diabats. However, in the inverted regime, the SCI transition state is instead located at the minimum of the reactant basin. These mechanistic results from SCI theory are consistent with the observed pathways for the RPMD trajectories, which suggests that in the inverted regime, both RPMD and SCI theory overestimate the degree of ET from solvent configurations in the reactant basin.

[a] Additional calculations performed using the RAW formulation of SCI theory [54,63] were found to be fully consistent with the SCI results in Fig. 3.5(a), but much more numerically unstable in the deep-tunneling regime considered here.

Table 3.8: ET reaction rates for a 1D asymmetric double well, obtained using SCI theory. [a]

ϵ	ΔE	$\log k_{\mathrm{SCI}}$
0.0	0.0	−11.0
0.05	0.02940	−10.9
0.10	0.05884	−10.8
0.20	0.11776	−10.6
0.30	0.17676	−10.3
0.40	0.23584	−10.3

[a] The Golden Rule for the symmetric case yields $\log k = -11.55$. ΔE is the difference between the two lowest eigenenergies for the system. All quantities reported in atomic units.

To further illustrate this issue, we present SCI rate calculations for deep tunneling in a 1D asymmetric double well. Table 3.8 presents ET reaction rates calculated on the potential energy surface $U_{\text{e-M}}(q)$ (Eq. 3.49), with parameters from Model SB1. Although this is a non-dissipative 1D system, the SCI rate is still well-defined, and it is reported as a function of the potential energy asymmetry. The rates plateau to a finite value with increasing asymmetry, which is consistent with rates for deep tunneling between a bound state and a continuum.[97–99] However, this behavior is qualitatively incorrect for tunneling rates between bound states, which should vanish for non-degenerate states in accord with Fermi's Golden Rule.[100] We conclude that SCI theory, as well as the closely related RPMD method, significantly overestimate the tunneling probability between asymmetric bound states, leading to an incorrect ET mechanism and overestimation of the reaction rate in the inverted regime.

The results for the simple double-well system can be used to deduce a more general argument for the applicability of the RPMD and SCI calculations in ET problems. Table 3.8, combined with the condition of detailed balance for the thermal reaction rate, indicates that the SCI rate for transfer in an asymmetric double-well system is approximately

$$k \approx \frac{2\pi}{\hbar}|V_{12}|^2 \, \min\left(1, e^{-\beta \Delta E}\right). \tag{3.65}$$

For the Marcus-type ET mechanism in which electron tunneling is gated via solvent reorganization that symmetrizes the double-well system, Eq. 3.65 leads to the TST rate in Eq. 3.37. However, for an unphysical "direct" ET mechanism in which electron tunneling proceeds from solvent configurations in the reactant basin (i.e., without prior solvent reorganization), Eq. 3.65 leads to the following TST expression for the ET rate,

$$k_{\text{direct}} = \frac{2\pi}{\hbar}|V_{12}|^2 \left(\frac{\beta}{4\pi\lambda}\right)^{\frac{1}{2}} \min\left(1, e^{-\beta\left(\lambda + \Delta G^0\right)}\right). \tag{3.66}$$

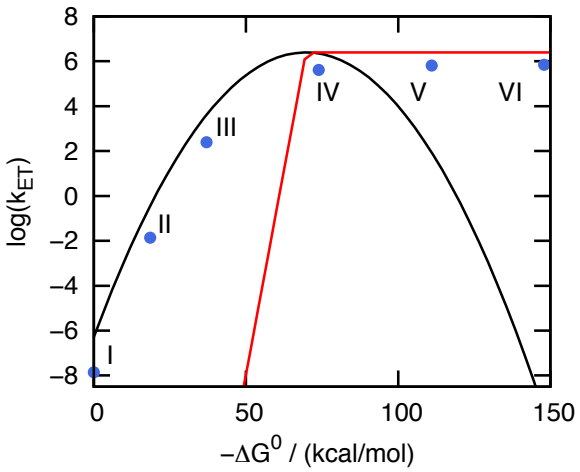

Figure 3.6: The ET rates for Model SB1 corresponding to a Marcus-like mechanism (black) and the "direct" mechanism in Eq. 3.66 (red). SCI rates (blue) correspond to the kinetically favorable mechanism in all regimes. See text for details.

Fig. 3.6 presents the ET reaction rates for Model SB1, assuming either the Marcus-type mechanism (Eq. 3.37, black) or the direct mechanism (Eq. 3.66, red). Also plotted are the rates calculated using SCI theory (Eq. 3.19, blue). Throughout the normal and activationless regimes, the rate for the Marcus-type mechanism dominates; in the inverted regime, the rate for the direct mechanism dominates; and the results from SCI theory closely track the larger of these two rates. It is clear that SCI theory (as well as RPMD) features a competition between the correct, Marcus-type mechanism for ET and the unphysical, direct mechanism for ET, and the prevailing mechanism is that which is predicted to be faster. This analysis is fully consistent with the earlier discussions of the RPMD trajectories (Figs. 3.3b, 3.3c, and 3.4b) and the SCI transition state configurations (Fig. 3.5b) for ET in the various regimes. Furthermore, this analysis provides a general basis for expecting the SCI and RPMD methods to accurately describe ET rates in the normal and activationless regimes, and for expecting these methods to significantly overestimate the ET rate in the inverted regime.

Table 3.9 presents ET rates for Model SB2, including results obtained using the QUAPI exact quantum dynamics method. Comparison of the RPMD, Marcus theory, and SCI theory rates for ET in Table 3.9 confirms that Model SB2 exhibits all of the previously discussed trends for these approximate methods. Fig. 3.7 presents the flux-flux correlation functions used to obtain the exact quantum rates for Model SB2.

The results in Fig. 3.7 emphasize the role of electronic state quantization in the ET reaction dynamics. At larger thermodynamic driving forces, the correlation functions become increasingly oscillatory, with a resonance frequency that matches the electronic state energy gap between the ET

Table 3.9: ET reaction rates for Model SB2, obtained using RPMD, Marcus theory, SCI theory, and exact quantum dynamics. [a]

Case	$-\Delta G^0$	$\log k_{\mathrm{MT}}$	$\log k_{\mathrm{RPMD}}$	$\log k_{\mathrm{SCI}}$	$\log k_{\mathrm{Q}}$
I	0.0	6.7	6.05(3)	5.1	6.7(1)
II	5.3	8.3	7.73(5)	6.6	8.5(1)
III	8.8	9.1	8.54(3)	7.4	9.0(3)
IV	17.6	9.8	9.27(2)	8.6	10.8(9)
V	26.5	8.9	9.40(3)	8.8	–
VI	35.3	6.3	9.52(2)	8.8	–

[a] ET rates are given in s^{-1}, and the $-\Delta G^0$ are given in kcal/mol.

reactant and product.[101,102] Integration over this increasingly oscillatory time correlation function (Eq. 3.25) contributes to the turnover in the ET reaction rate in the inverted regime. The RPMD approximation to the real-time dynamics of the system, which is not expected to capture coherent quantum effects,[23,41] does not fully enforce the quantization of electronic dynamics and leads to the observed inaccuracies in the inverted regime. Approximate quantum dynamical methods that explicitly enforce electronic quantization by using either a discrete electronic state basis or by exactly mapping to a continuous electronic basis are thus expected to provide a better starting point for describing state-to-state electronic dynamics and ET in the inverted regime.[12,14,16,19,103] Further investigation of this point is in progress.

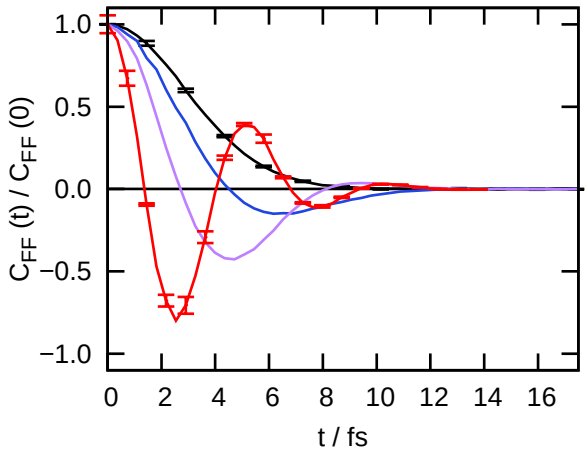

Figure 3.7: Normalized flux-flux autocorrelation functions $C_{\mathrm{FF}}(t)$ for Model SB2, calculated using exact quantum dynamics for Cases I (black), II (blue), III (purple) and IV (red).

3.6 Conclusions

The current paper demonstrates the applicability of RPMD for the direct simulation of ET reaction dynamics in complex systems. Using both atomistic and system-bath representations for ET in a polar solvent, we compare RPMD results with those obtained using Marcus theory, semiclassical instanton theory, and exact quantum dynamics. Throughout the normal and activationless regimes for ET, RPMD correctly predicts the ET reaction mechanism and quantitatively describes the ET reaction rate over 12 orders of magnitude, without invoking any prior mechanistic or transition state assumptions. Analysis of the RPMD trajectories reveals that the accuracy of the method lies in its exact description of statistical fluctuations, with regard to both solvent reorganization and the formation of kink-pair configurations during the electron tunneling event. However, for ET in the inverted regime, both RPMD and SCI theory fail to predict the turnover in the ET reaction rate with increasing thermodynamic driving force. In this regime, both methods overestimate the probability of electronic tunneling from solvent configurations in the reactant basin, leading to an overestimation of the corresponding reaction rates. Exact quantum dynamics calculations illustrate that the limitations of the RPMD method in the inverted regime arise from the inadequate quantization of the real-time electronic-state dynamics; analogous breakdowns of the method have been identified in other applications to strongly coherent quantum systems, including low-dimensional quantum oscillators[23] and electron-scattering in dilute fluids.[41]

We conclude by emphasizing that the normal and activationless regimes encompass the vast majority ET reactions in biological and synthetic systems.[104] The results presented here thus constitute a significant success for the RPMD method, demonstrating that it allows for the robust, direct simulation of thermally activated ET in systems with over 1000 atoms, leading to the quantitative prediction of ET reaction rates and the potential discovery and characterization of ET reaction mechanisms in complex systems. A comparable demonstration using other approximate real-time quantum simulation methods has not, to our knowledge, been previously reported. Having established both the applicability and limitations of RPMD for ET reactions dynamics, this work provides the foundation for future studies of ET and proton-coupled ET reactions in enzymes and other condensed-phase systems.

Appendix A System-Bath Potential Energy Parameters

Table 3.10: Parameters for the left Coulombic well in the electron-ion potential energy function of Eq. 3.49 for Model SB1. [a]

Case	a_{L}	b_{L}	c_{L}	$r_{\mathrm{L}}^{\mathrm{in}}$	$r_{\mathrm{L}}^{\mathrm{out}}$
I	0.164567	2.002721	3.683127	−4.062912	−8.106702
II	0.164520	2.001856	3.675494	−4.062912	−8.104948
III	0.164472	2.000989	3.667859	−4.062912	−8.103197
IV	0.164377	1.999251	3.652576	−4.062912	−8.099709
V	0.164280	1.997506	3.637280	−4.062912	−8.096237
VI	0.164183	1.995754	3.621971	−4.062912	−8.092782

[a] Unless otherwise noted, parameters are given in atomic units

Table 3.11: Parameters for the right Coulombic well in the electron-ion potential energy function of Eq. 3.49 for Model SB1. [a]

Case	a_{R}	b_{R}	c_{R}	$r_{\mathrm{R}}^{\mathrm{in}}$	$r_{\mathrm{R}}^{\mathrm{out}}$
I	0.164567	−2.002721	3.683127	4.062912	8.106702
II	0.167357	−2.036963	3.752141	4.062912	8.108432
III	0.170147	−2.071204	3.821152	4.062912	8.110110
IV	0.175726	−2.139680	3.959165	4.062912	8.113319
V	0.181304	−2.208150	4.097166	4.062912	8.116346
VI	0.186882	−2.276615	4.235157	4.062912	8.119207

[a] Unless otherwise noted, parameters are given in atomic units

Table 3.12: Parameters for the left Coulombic well in the electron-ion potential energy function of Eq. 3.49 for Model SB2. [a]

Case	a_{L}	b_{L}	c_{L}	$r_{\mathrm{L}}^{\mathrm{in}}$	$r_{\mathrm{L}}^{\mathrm{out}}$
I	0.157480	1.596286	1.609286	−3.050000	−7.086414
II	0.157507	1.596671	1.612042	−3.050000	−7.087150
III	0.157525	1.596927	1.613880	−3.050000	−7.087642
IV	0.157569	1.597568	1.618474	−3.050000	−7.088871
V	0.157613	1.598208	1.623065	−3.050000	−7.090102
VI	0.157657	1.598848	1.627656	−3.050000	−7.091336

[a] Unless otherwise noted, parameters are given in atomic units

Table 3.13: Parameters for the right Coulombic well in the electron-ion potential energy function of Eq. 3.49 for Model SB2. [a]

Case	a_{R}	b_{R}	c_{R}	$r_{\mathrm{R}}^{\mathrm{in}}$	$r_{\mathrm{R}}^{\mathrm{out}}$
I	0.157480	−1.596286	1.609286	3.050000	7.086414
II	0.156666	−1.587919	1.598482	3.050000	7.085675
III	0.156124	−1.582341	1.591280	3.050000	7.085179
IV	0.154767	−1.568396	1.573273	3.050000	7.083924
V	0.153410	−1.554450	1.555265	3.050000	7.082650
VI	0.152053	−1.540504	1.537256	3.050000	7.081357

[a] Unless otherwise noted, parameters are given in atomic units

Appendix B Transformation to Diabatic Basis

The QUAPI method is implemented in an electronic diabatic state representation of the ET reaction. In this appendix, we describe the procedure for transforming the potential energy function for Model SB2 from a position basis for the electron (Eq. 3.48) to a diabatic basis where the reactant and product electronic states are maximally localized on the donor and acceptor metal atoms.

We begin by calculating the two lowest adiabatic electronic eigenstates ($\psi_0(q;s)$ and $\psi_1(q;s)$) and eigenenergies ($E_0(s)$ and $E_1(s)$) of the system Hamiltonian at fixed values of the solvent coordinate in the range -8 a$_0$ $\leq s \leq$ 8 a$_0$. For each value of s, the system Hamiltonian is diagonalized on a uniform DVR grid of 1024 electron positions in the range -25 a$_0$ $\leq q \leq 25$ a_0.

For each value of s, reactant and product electronic wavefunctions in the diabatic basis are obtained via rotation of the two lowest-energy adiabatic wavefunctions, using

$$\phi_{\mathrm{R}}(q;s) = \cos(\theta_s)\psi_0(q;s) - \sin(\theta_s)\psi_1(q;s) \tag{3.67}$$

and

$$\phi_{\mathrm{P}}(q;s) = \sin(\theta_s)\psi_0(q;s) + \cos(\theta_s)\psi_1(q;s), \tag{3.68}$$

where

$$\theta_s = \frac{1}{2}\arctan\left(\frac{S_{10}+S_{01}}{S_{11}-S_{00}}\right) \tag{3.69}$$

and $S_{\mu\nu} = \int_{-\infty}^{0} \psi_\mu(q;s)^* \psi_\nu(q;s)\, dq$. This choice of the rotation angle, θ_s, maximizes $\int_{-\infty}^{0} |\phi_{\mathrm{R}}(q;s)|^2\, dq$, the probability that the reactant diabatic state is positioned on the donor ion. Maximization of the probability that the product diabatic state is positioned on the acceptor ion yields an identical choice for θ_s.

The corresponding potential energy matrix elements in the diabatic basis (Eq. 3.23) are thus

$$V_{11}(s) = E_0(s)\cos^2\theta_s + E_1(s)\sin^2\theta_s, \tag{3.70}$$

$$V_{22}(s) = E_0(s)\sin^2\theta_s + E_1(s)\cos^2\theta_s, \tag{3.71}$$

$$V_{21}(s) = V_{12}(s) = (E_0(s) - E_1(s))\cos\theta_s \sin\theta_s. \tag{3.72}$$

The diagonal elements are found to be parabolic functions of s, and the off-diagonal element are found to be nearly constant with respect to s. We fit $V_{11}(s)$ and $V_{22}(s)$ to second-order polynomials

functions (Eqs. 3.55 and 3.56) and employ a constant value for V_{12} that corresponds to the $s = 0$ result. The polynomial expansion coefficients for $V_{11}(s)$ and $V_{22}(s)$ are provided in Table 3.14, and the constant value for V_{12} is provided in Table 3.4.

Table 3.14: The diagonal elements of the diabatic potential matrix, $V_{11}(s)$ and $V_{22}(s)$ in Eqs. 3.55 and 3.56, for Model SB2. [a]

Case	$a_1 \times 10^3$	$b_1 \times 10^2$	c_1	$a_2 \times 10^3$	$b_2 \times 10^2$	c_2
I	4.7722	1.1308	−2.1576	4.7722	1.1308	−2.1576
II	4.7722	1.1308	−2.1477	4.7722	1.1308	−2.1561
III	4.7722	1.1308	−2.1411	4.7721	1.1308	−2.1551
IV	4.7720	1.1307	−2.1245	4.7720	1.1308	−2.1526

[a] Unless otherwise noted, parameters are given in atomic units

References

[1] M. H. V. Huynh and T. J. Meyer, Chem. Rev. (Washington, DC, U.S.) **107**, 5004 (2007).

[2] N. S. Lewis and D. G. Nocera, Proc. Natl. Acad. Sci. U. S. A. **103**, 15729 (2006).

[3] R. A. Marcus and N. Sutin, Biochim. Biophys. Acta **811**, 265 (1985).

[4] H. B. Gray and J. R. Winkler, Annu. Rev. Biochem. **65**, 537 (1996).

[5] O. Miyashita, M. Y. Okamura, and J. N. Onuchic, Proc. Natl. Acad. Sci. U. S. A. **102**, 3558 (2005).

[6] J. M. Jean, R. A. Friesner, and G. R. Fleming, J. Chem. Phys. **96**, 5827 (1992).

[7] J. Blumberger, I. Tavernelli, M. L. Klein, and M. Sprik, J. Chem. Phys. **124** (2006).

[8] L. W. Ungar, M. D. Newton, and G. A. Voth, J. Phys. Chem. B **103**, 7367 (1999).

[9] P. Ehrenfest, Z. Phys **45**, 455 (1927).

[10] A. D. Mclachlan, Mol. Phys. **8**, 39 (1964).

[11] J. C. Tully, J. Chem. Phys. **93**, 1061 (1990).

[12] J. C. Tully, Faraday Discuss. , 407 (1998).

[13] M. Ben-Nun, J. Quenneville, and T. J. Martinez, J. Phys. Chem. A **104**, 5161 (2000).

[14] H. D. Meyer and W. H. Miller, J. Chem. Phys. **70**, 3214 (1979).

[15] H. D. Meyer and W. H. Miller, J. Chem. Phys. **72**, 2272 (1980).

[16] G. Stock and M. Thoss, Phys. Rev. Lett. **78**, 578 (1997).

[17] J. S. Cao and G. A. Voth, J. Chem. Phys. **105**, 6856 (1996).

[18] J. S. Cao and G. A. Voth, J. Chem. Phys. **106**, 1769 (1997).

[19] N. Ananth and T. F. Miller, J. Chem. Phys. **133** (2010).

[20] S. Nielsen, R. Kapral, and G. Ciccotti, J. Chem. Phys. **115**, 5805 (2001).

[21] J. R. Schmidt, P. V. Parandekar, and J. C. Tully, J. Chem. Phys. **129** (2008).

[22] P. G. Bolhuis, D. Chandler, C. Dellago, and P. L. Geissler, Annu. Rev. Phys. Chem. **53**, 291 (2002).

[23] I. R. Craig and D. E. Manolopoulos, J. Chem. Phys. **121**, 3368 (2004).

[24] R. P. Feynman and A. R. Hibbs, *Quantum mechanics and path integrals* (McGraw-Hill, New York, New York, 1965).

[25] D. Chandler and P. G. Wolynes, J. Chem. Phys. **74**, 4078 (1981).

[26] T. F. Miller and D. E. Manolopoulos, J. Chem. Phys. **122**, 184503 (2005).

[27] T. F. Miller and D. E. Manolopoulos, J. Chem. Phys. **123**, 154504 (2005).

[28] B. J. Braams, T. F. Miller, and D. E. Manolopoulos, Chem. Phys. Lett. **418**, 179 (2006).

[29] S. Habershon, T. E. Markland, and D. E. Manolopoulos, J. Chem. Phys. **131** (2009).

[30] T. E. Markland, J. A. Morrone, B. J. Berne, K. Miyazaki, E. Rabani, and D. R. Reichman, Nat. Phys. **7**, 134 (2011).

[31] I. R. Craig and D. E. Manolopoulos, Chem. Phys. **322**, 236 (2006).

[32] I. R. Craig and D. E. Manolopoulos, J. Chem. Phys. **122**, 084106 (2005).

[33] R. Collepardo-Guevara, I. R. Craig, and D. E. Manolopoulos, J. Chem. Phys. **128**, 144502 (2008).

[34] T. E. Markland, S. Habershon, and D. E. Manolopoulos, J. Chem. Phys. **128**, 194506 (2008).

[35] N. Boekelheide, R. Salomón-Ferrer, and T. F. Miller, Proc. Natl. Acad. Sci. U. S. A. **108**, 16159 (2011).

[36] R. Collepardo-Guevara, Y. V. Suleimanov, and D. E. Manolopoulos, J. Chem. Phys. **130** (2009).

[37] J. O. Richardson and S. C. Althorpe, J. Chem. Phys. **131**, 214106 (2009).

[38] I. R. Craig and D. E. Manolopoulos, J. Chem. Phys. **123**, 034102 (2005).

[39] M. Parrinello and A. Rahman, J. Chem. Phys. **80**, 860 (1984).

[40] A. R. Menzeleev and T. F. Miller, J. Chem. Phys. **132**, 034106 (2010).

[41] T. F. Miller, J. Chem. Phys. **129**, 194502 (2008).

[42] E. Wigner, Z. Phys. Chem. B **19**, 203 (1932).

[43] H. Eyring, J. Chem. Phys. **3**, 107 (1935).

[44] J. C. Keck, J. Chem. Phys. **32**, 1035 (1960).

[45] W. H. Miller, J. Chem. Phys. **58**, 1664 (1973).

[46] D. Chandler, J. Chem. Phys. **68**, 2959 (1978).

[47] C. H. Bennett, in *Algorithms for Chemical Computations*, ACS Symposium Series, Vol. 46, edited by R. E. Christofferson (American Chemical Society, 1977) Chap. 4, p. 63.

[48] E. A. Carter, G. Ciccotti, J. T. Hynes, and R. Kapral, Chem. Phys. Lett. **156**, 472 (1989).

[49] G. K. Schenter, B. C. Garrett, and D. G. Truhlar, J. Chem. Phys. **119**, 5828 (2003).

[50] J. B. Watney, A. V. Soudackov, K. F. Wong, and S. Hammes-Schiffer, Chem. Phys. Lett. **418**, 268 (2006).

[51] V. A. Benderskii, D. E. Makarov, and A. C. Wight, in *Advances in Chemical Physics*, Vol. 88 (John Wiley & Sons, Inc., 1994).

[52] S. Chapman, B. C. Garrett, and W. H. Miller, J. Chem. Phys. **63**, 2710 (1975).

[53] C. G. Callan and S. Coleman, Phys. Rev. D. **16**, 1762 (1977).

[54] G. Mills, G. K. Schenter, D. E. Makarov, and H. Jonsson, Chem. Phys. Lett. **278**, 91 (1997).

[55] A. O. Caldeira and A. J. Leggett, Ann. Phys. **149**, 374 (1983).

[56] P. Hanggi and W. Hontscha, J. Chem. Phys. **88**, 4094 (1988).

[57] W. H. Miller, J. Chem. Phys. **62**, 1899 (1975).

[58] S. C. Althorpe, J. Chem. Phys. **134**, 114104 (2011).

[59] D. M. Ceperley and G. Jacucci, Phys. Rev. Lett. **58**, 1648 (1987).

[60] A. Kuki and P. G. Wolynes, Science **236**, 1647 (1987).

[61] C. Alexandrou and J. W. Negele, Phys. Rev. C **37**, 1513 (1988).

[62] J. O. Richardson and S. C. Althorpe, J. Chem. Phys. **134**, 054109 (2011).

[63] G. Mills, G. K. Schenter, D. E. Makarov, and H. Jonsson, in *Proceedings of the International School of Physics*, edited by B. J. Berne, G. Ciccotti, and D. F. Coker (World Scientific, 1997) p. 405.

[64] N. Makri, Chem. Phys. Lett. **193**, 435 (1992).

[65] M. Topaler and N. Makri, J. Phys. Chem. **100**, 4430 (1996).

[66] M. Topaler and N. Makri, Chem. Phys. Lett. **210**, 285 (1993).

[67] M. Topaler and N. Makri, Chem. Phys. Lett. **210**, 448 (1993).

[68] D. E. Makarov and N. Makri, Phys. Rev. A **48**, 3626 (1993).

[69] W. H. Miller, S. D. Schwartz, and J. W. Tromp, J. Chem. Phys. **79**, 4889 (1983).

[70] R. P. Feynman and F. L. Vernon, Ann. Phys. **24**, 118 (1963).

[71] E. Sim, G. Krilov, and B. J. Berne, J. Phys. Chem. A **105**, 2824 (2001).

[72] R. A. Marcus, J. Chem. Phys. **24**, 966 (1956).

[73] R. A. Marcus, Discuss. Faraday. Soc. , 21 (1960).

[74] R. A. Marcus, J. Chem. Phys. **43**, 679 (1965).

[75] J. Ulstrup and J. Jortner, J. Chem. Phys. **63**, 4358 (1975).

[76] R. A. Kuharski, J. S. Bader, D. Chandler, M. Sprik, M. L. Klein, and R. W. Impey, J. Chem. Phys. **89**, 3248 (1988).

[77] H. Berendsen, J. P. M. Postma, W. van Gunsteren, and J. Hermans, in *The Jerusalem symposia on quantum chemistry and biochemistry*, Vol. 14, edited by B. Pullman (D. Reidel, 1981).

[78] M. Sprik, R. W. Impey, and M. L. Klein, J. Stat. Phys. **43**, 967 (1986).

[79] R. W. Shaw, Phys. Rev. **174**, 769 (1968).

[80] C. L. Brooks, B. M. Pettitt, and M. Karplus, J. Chem. Phys. **83**, 5897 (1985).

[81] W. Smith and T. R. Forester, J. Mol. Graphics **14**, 136 (1996).

[82] L. Verlet, Phys. Rev. **159**, 98 (1967).

[83] H. C. Andersen, J. Comput. Phys. **52**, 24 (1983).

[84] G. King and A. Warshel, J. Chem. Phys. **93**, 8682 (1990).

[85] S. Kumar, D. Bouzida, R. H. Swendsen, P. A. Kollman, and J. M. Rosenberg, J. Comput. Chem. **13**, 1011 (1992).

[86] S. Kumar, J. M. Rosenberg, D. Bouzida, R. H. Swendsen, and P. A. Kollman, J. Comput. Chem. **16**, 1339 (1995).

[87] B. Deraedt, M. Sprik, and M. L. Klein, J. Chem. Phys. **80**, 5719 (1984).

[88] F. Webster, P. J. Rossky, and R. A. Friesner, Comput. Phys. Commun. **63**, 494 (1991).

[89] M. Marchi and D. Chandler, J. Chem. Phys. **95**, 889 (1991).

[90] S. Habershon, G. S. Fanourgakis, and D. E. Manolopoulos, J. Chem. Phys. **129** (2008).

[91] T. D. Hone, P. J. Rossky, and G. A. Voth, J. Chem. Phys. **124** (2006).

[92] E. Weinan, W. Q. Ren, and E. Vanden-Eijnden, J. Chem. Phys. **126** (2007).

[93] D. T. Colbert and W. H. Miller, J. Chem. Phys. **96**, 1982 (1992).

[94] R. E. Cline and P. G. Wolynes, J. Chem. Phys. **88**, 4334 (1988).

[95] D. Chandler, "Theory of quantum processes in liquids," in *Liquids, Freezing and Glass Transition*, edited by D. Levesque, J. P. Hansen, and J. Zinn-Justin (Elsevier, New York, 1991) pp. 193–285.

[96] D. M. Ceperley, Rev. Mod. Phys. **67**, 279 (1995).

[97] S. Jang and G. A. Voth, J. Chem. Phys. **111**, 2371 (1999).

[98] S. Jang and G. A. Voth, J. Chem. Phys. **112**, 8747 (2000).

[99] W. Hontscha, P. Hanggi, and E. Pollak, Phys. Rev. B. **41**, 2210 (1990).

[100] J. J. Sakurai and S. F. Tuan, *Modern quantum mechanics*, rev. ed. (Addison-Wesley Pub. Co., Reading, Mass., 1994).

[101] D. Egorova and W. Domcke, J. Photochem. Photobiol. A **166**, 19 (2004).

[102] D. Egorova, M. Thoss, W. Domcke, and H. B. Wang, J. Chem. Phys. **119**, 2761 (2003).

[103] J. R. Klauder, Ann. Phys. **254**, 419 (1997).

[104] R. A. Marcus, Rev. Mod. Phys. **65**, 599 (1993).

Chapter 4

Kinetically constrained ring polymer molecular dynamics for non-adiabatic chemical reactions

4.1 Introduction

A central challenge in chemical dynamics is the accurate and robust description of non-adiabatic processes in the condensed phase. Important target applications include charge-transfer and energy-transfer processes that are fundamental to biological and inorganic catalysis. A variety of simulation methods have been developed to address this challenge, including those based on mean-field,[1–5] surface hopping,[6–8] and semiclassical dynamics[9–12] approaches. In the current study, we provide a novel extension of the ring-polymer molecular dynamics (RPMD) method that is well suited to addressing electronically non-adiabatic dynamics and nuclear quantization for chemical reactions in large systems.

RPMD is an approximate quantum dynamics method[13,14] that is based on the path-integral formalism of statistical mechanics.[15] It provides an isomorphic classical model for the real-time evolution of a quantum mechanical system. RPMD yields real-time molecular dynamics trajectories that preserve the exact quantum Boltzmann distribution and exhibit time-reversal symmetry, thus enabling the method to be readily used in combination with classical rare-event sampling methods and for the direct simulation of quantum-mechanical processes in systems involving thousands of atoms. Numerous applications of the RPMD method have been reported to date,[14] including the study of chemical reactions in the gas phase,[16–19] in solution,[20–24] and in enzymes;[25] the simulation of diffusive processes in liquids,[26–32] glasses,[33,34] solids,[31] and on surfaces;[35,36] and the calculation of neutron diffraction patterns[37] and absorption spectra.[38,39]

We have recently employed the RPMD method to investigate condensed-phase electron transfer (ET)[23] and proton-coupled electron transfer (PCET)[24] reaction dynamics. This work utilized the usual path-integral formulation in the position representation,[15,40–42] such that the transferring electron is treated as a distinguishable particle. Although this approach allows for the robust de-

scription of condensed-phase charge transfer, it is clearly limited to non-adiabatic processes that can be realistically described using a one-electron pseudopotential, rather than general, many-electron wavefunctions.[23,24] Recent efforts have been made to extend RPMD to more general non-adiabatic chemistries, such as combining the path-integral methods with fewest-switches surface hopping[43] or approaches[44–46] based on the Meyer-Miller-Stock-Thoss Hamiltonian.[2,47] However, the development of electronic-state-representation (or simply "state-representation") RPMD methods that provide accuracy and scalability while strictly preserving detailed balance remains an ongoing challenge.

In this work, we extend RPMD to allow for the description of non-adiabatic, multi-electron processes in large systems. The new kinetically constrained (KC) RPMD method employs a coarse-graining procedure that reduces discrete electronic-state variables to a single continuous coordinate, as well as a "kinetic constraint" modification of the equilibrium distribution to address known failures of path-integral-based estimates for tunneling rates. This kinetically constrained distribution is rigorously preserved using continuous equations of motion, yielding a real-time model for the non-adiabatic dynamics that retains all the useful features of the conventional position-representation RPMD method, such as detailed balance, time-reversal symmetry, and invariance of reaction rate calculations to the choice of dividing surface. We demonstrate that the method yields excellent numerical results for a range of model systems, including a simple avoided-crossing reaction and condensed-phase ET reactions across multiple regimes for the electronic coupling and thermodynamic driving force.

4.2 Theory

4.2.1 Path-integral discretization in a two-level system

We begin by reviewing imaginary-time path integration for a general, two-level system in the diabatic representation. Consider a Hamiltonian operator of the form $\hat{H} = \hat{T} + \hat{V}$, where

$$\hat{T} = \sum_{j=1}^{d} \frac{p_j^2}{2m_j} \tag{4.1}$$

describes the kinetic energy for a system of d nuclear degrees of freedom and

$$\hat{V}(\mathbf{R}) = \begin{pmatrix} V_0(\mathbf{R}) & K(\mathbf{R}) \\ K(\mathbf{R}) & V_1(\mathbf{R}) \end{pmatrix} \tag{4.2}$$

is the potential energy in the diabatic representation as a function of the nuclear coordinates, $\mathbf{R}$.

The canonical partition function for the two-level system is

$$Z = \mathrm{Tr}[e^{-\beta\hat{H}}] = \int d\mathbf{R} \sum_{i=0,1} \langle \mathbf{R}, i|e^{-\beta\hat{H}}|\mathbf{R}, i\rangle. \tag{4.3}$$

By resolving the identity in the product space of the electronic and nuclear coordinates, we discretize the trace into the ring-polymer representation with n beads,

$$Z = \int d\{\mathbf{R}^{(\alpha)}\} \sum_{\{i^{(\alpha)}\}} \prod_{\alpha=1}^{n} \langle \mathbf{R}^{(\alpha)}, i^{(\alpha)}|e^{-\beta_n\hat{H}}|\mathbf{R}^{(\alpha+1)}, i^{(\alpha+1)}\rangle, \tag{4.4}$$

where $\beta_n = \beta/n$ and $\left(\mathbf{R}^{(\alpha)}, i^{(\alpha)}\right)$ indicates the nuclear position and electronic state of the α^{th} ring-polymer bead, such that $\left(\mathbf{R}^{(n+1)}, i^{(n+1)}\right) = \left(\mathbf{R}^{(1)}, i^{(1)}\right)$. Finally, employing the short-time approximations

$$\langle \mathbf{R}, i|e^{-\beta_n\hat{H}}|\mathbf{R}', i'\rangle \approx \langle \mathbf{R}|e^{-\beta_n\hat{T}}|\mathbf{R}'\rangle\langle i|e^{-\beta_n\hat{V}(\mathbf{R})}|i'\rangle \tag{4.5}$$

and

$$\langle i|e^{-\beta_n\hat{V}(\mathbf{R})}|i'\rangle \approx [\mathbf{M}(\mathbf{R})]_{i,i'}, \tag{4.6}$$

where[48]

$$\mathbf{M}(\mathbf{R}) = \begin{pmatrix} e^{-\beta_n V_0(\mathbf{R})} & -\beta_n K(\mathbf{R}) e^{-\beta_n V_0(\mathbf{R})} \\ -\beta_n K(\mathbf{R}) e^{-\beta_n V_1(\mathbf{R})} & e^{-\beta_n V_1(\mathbf{R})} \end{pmatrix}, \tag{4.7}$$

we obtain the familiar result,

$$Z_n = \int d\{\mathbf{R}^{(\alpha)}\} \sum_{\{i^{(\alpha)}\}} \rho_n^{\mathrm{RP}}(\{\mathbf{R}^{(\alpha)}\}, \{i^{(\alpha)}\}), \tag{4.8}$$

such that $Z = \lim_{n\to\infty} Z_n$. The ring-polymer distribution in Eq. 4.8 is given by

$$\rho_n^{\mathrm{RP}}(\{\mathbf{R}^{(\alpha)}\},\{i^{(\alpha)}\}) = \Omega e^{-\beta U_{\mathrm{int}}(\{\mathbf{R}^{(\alpha)}\})} \prod_{\alpha=1}^{n} M_{i^{(\alpha)},i^{(\alpha+1)}}(\mathbf{R}^{(\alpha)}). \tag{4.9}$$

Here, we have introduced the notation $\Omega = \prod_{j=1}^{d} \left(\frac{nm_j}{2\pi\hbar^2\beta}\right)^{n/2}$ and $[\mathbf{M}(\mathbf{R})]_{i,i'} = M_{i,i'}(\mathbf{R})$, as well as the internal ring-polymer potential

$$U_{\mathrm{int}}(\{\mathbf{R}^{(\alpha)}\}) = \frac{1}{2n} \sum_{\alpha=1}^{n} \sum_{j=1}^{d} m_j\omega_n^2 \left(R_j^{(\alpha)} - R_j^{(\alpha+1)}\right)^2, \tag{4.10}$$

where $\omega_n = (\beta_n \hbar)^{-1}$.

4.2.2 Mean-field (MF) non-adiabatic RPMD

Equation 4.8 can be rewritten in the form of a classical configuration integral,

$$Z_n = \int d\{\mathbf{R}^{(\alpha)}\}\ \rho_n^{\mathrm{MF}}(\{\mathbf{R}^{(\alpha)}\}), \tag{4.11}$$

where $\rho_n^{\mathrm{MF}}(\{\mathbf{R}^{(\alpha)}\})$ is a quantized equilibrium distribution that depends only on the ring-polymer nuclear coordinates,

$$\rho_n^{\mathrm{MF}}(\{\mathbf{R}^{(\alpha)}\}) = \Omega e^{-\beta V_{\mathrm{eff}}^{\mathrm{MF}}(\{\mathbf{R}^{(\alpha)}\})}, \tag{4.12}$$

and

$$V_{\mathrm{eff}}^{\mathrm{MF}}(\{\mathbf{R}^{(\alpha)}\}) = U_{\mathrm{int}}(\{\mathbf{R}^{(\alpha)}\}) - \frac{1}{\beta} \ln \left[\sum_{\{i^{(\alpha)}\}} \prod_{\alpha=1}^{n} M_{i^{(\alpha)}, i^{(\alpha+1)}}(\mathbf{R}^{(\alpha)}) \right].$$

Here, $V_{\mathrm{eff}}^{\mathrm{MF}}(\{\mathbf{R}^{(\alpha)}\})$ is an effective potential for the ring-polymer nuclear coordinates in which all fluctuations over the electronic state variables are thermally averaged; in this sense, it provides a mean-field (MF) description of the electronic degrees of freedom. For all systems considered in the current study, the argument of the logarithm in Eq. 4.13 is strictly positive.

As is familiar from applications of path-integral statistical mechanics,[41,42] the quantized equilibrium distribution can be sampled by running appropriately thermostatted classical molecular dynamics trajectories on the effective ring-polymer potential. Specifically, the classical equations of motion that sample $\rho_n^{\mathrm{MF}}(\{\mathbf{R}^{(\alpha)}\})$ are

$$\dot{v}_j^{(\alpha)} = -\frac{1}{\tilde{m}_j} \frac{\partial}{\partial R_j^{(\alpha)}} V_{\mathrm{eff}}^{\mathrm{MF}}(\{\mathbf{R}^{(\alpha)}\}), \tag{4.13}$$

where $v_j^{(\alpha)}$ is the velocity for the αth ring-polymer bead associated with the jth nuclear degree of freedom. We use a notation for the masses in Eq. 4.13 that emphasizes that they need not correspond to the physical masses of the system; any positive values for these masses will yield trajectories that correctly sample the path-integral distribution. However, to employ these trajectories as a model for the real-time dynamics of the system, it is sensible, as in previous implementations of RPMD,[14] to utilize masses for the nuclear degrees of freedom that correspond to the physical masses of the system (i.e., $\tilde{m}_j = m_j/n$). This choice is sufficient to fully specify the MF version of non-adiabatic

RPMD dynamics for two-level systems,

$$\dot{v}_j^{(\alpha)} = -\frac{n}{m_j}\frac{\partial}{\partial R_j^{(\alpha)}} V_{\text{eff}}^{\text{MF}}(\{\mathbf{R}^{(\alpha)}\}). \tag{4.14}$$

MF non-adiabatic RPMD, described in Eq. 4.14, has the appealing feature that it involves simple, continuous equations of motion that rigorously preserve the exact quantum Boltzmann distribution.[a] However, as we will illustrate with later results, these MF equations of motion fail to accurately describe non-adiabatic processes in the regime of weak electronic coupling, due to the neglect of fluctuations in the electronic state variables. The aim of the next section is thus to develop a continuous RPMD that preserves the kinetically important fluctuations in the electronic variables (*i.e.*, ring-polymer "kink-pair" formation).

4.2.3 Kinetically constrained (KC) RPMD

This section describes the central methodological contribution of the paper. We present a state-representation RPMD method that retains the robust features of the position-representation RPMD while also including the kinetically important fluctuations in the electronic degrees of freedom. The development of this method involves three basic components, which are sequentially presented in the following subsections. First, we introduce a continuous auxiliary variable, y, that reports on kink-formation in the ring polymer, and its associated effective potential. Second, we introduce a kinetic constraint on the ring-polymer equilibrium distribution that inhibits the formation of instanton paths across non-degenerate double wells, thus correcting a known failure of instanton-based methods in the deep tunneling regime. And third, we derive an appropriate mass for the auxiliary variable, y.

4.2.3.1 A collective variable that reports on kinks

The expression for the partition function in Eq. 4.8 includes a sum over the ensemble of ring-polymer configurations associated with all possible combinations of the electronic-state variables $\{i^{(\alpha)}\}$, namely

$$\sum_{\{i^{(\alpha)}\}} \prod_{\alpha=1}^{n} M_{i^{(\alpha)},i^{(\alpha+1)}}(\mathbf{R}^{(\alpha)}). \tag{4.15}$$

As is illustrated in Fig. 4.1, this ensemble includes configurations for which all of the state variables assume the same value (i.e., $i^{(\alpha)} = 0$ for all α, or $i^{(\alpha)} = 1$ for all α), as well as "kinked" ring-polymer

[a] The mean-field RPMD approximation is not a new idea; it has been used previously to benchmark non-adiabatic PI methods by D. E. Manolopoulos, T. F. Miller III, J. C. Tully, and I. R. Craig.

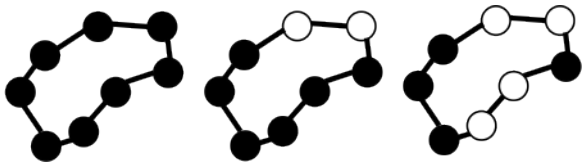

Figure 4.1: A schematic illustration of ring-polymer configurations that exhibit either zero (left), one (center), or two (right) kink-pairs. Ring-polymer beads shown in white correspond to the electronic state $i^{(\alpha)} = 0$, whereas those in black correspond to $i^{(\alpha)} = 1$.

configurations in which the electronic-state variable changes value as a function of the bead index, α. Because of the cyclic boundary condition for the ring-polymer coordinates, the number of kinks that is exhibited by a given configuration must be even; we thus refer to the number of "kink-pairs" in describing the ring-polymer configuration.

The thermal weight of kinked ring-polymer configurations is closely related to the process of reactive tunneling. Indeed, for nuclear configurations in which the diabatic potentials are degenerate (i.e., $V_0(\mathbf{R}) = V_1(\mathbf{R})$), the combined thermal weight of all ring-polymer configurations with k kink-pairs is proportional to $(\beta K)^{2k}$.[49–51] This connection between imaginary-time path-integral statistics and the diabatic coupling K lies at the heart of semiclassical instanton (SCI) theory,[52–57] and it underpins the accuracy of the RPMD method for the description of thermal reaction rates in the deep-tunneling regime.[58–60]

For these reasons, the formation of kink-pairs during non-adiabatic transitions is an important feature to preserve in any extension of the RPMD method to multi-level systems. We thus introduce a discrete collective variable that reports on the existence of kink-pairs in the ring-polymer configuration,

$$\theta(\{i^{(\alpha)}\}) = \begin{cases} -1, & i^{(\alpha)} = 0 \text{ for all } \alpha, \\ 1, & i^{(\alpha)} = 1 \text{ for all } \alpha, \\ 0, & \text{otherwise.} \end{cases} \tag{4.16}$$

Furthermore, we introduce a continuous dummy variable y that is tethered to $\theta(\{i^{(\alpha)}\})$ via a square-well restraining potential $V_{\mathrm{r}}(y, \{i^{(\alpha)}\})$, such that

$$e^{-\beta V_{\mathrm{r}}(y,\{i^{(\alpha)}\})} = f(y, \theta(\{i^{(\alpha)}\})), \tag{4.17}$$

where

$$f(y,\theta) = \lim_{b\to\infty} \frac{1}{2}\left(1 - \tanh\left[b\left(|y-\theta| - \frac{1}{2}\right)\right]\right). \tag{4.18}$$

Finally, the ring-polymer probability distribution in Eq. 4.9 is reduced with respect to the discrete

electronic variables $\{i^{(\alpha)}\}$, yielding a distribution that depends only on the ring-polymer nuclear coordinates and on the coordinate y that smoothly reports on the existence of kink-pairs in the electronic coordinates,

$$\rho_n(\{\mathbf{R}^{(\alpha)}\}, y) = \Omega e^{-\beta V_{\text{eff}}(\{\mathbf{R}^{(\alpha)}\}, y)}, \tag{4.19}$$

such that

$$Z_n = \int d\{\mathbf{R}^{(\alpha)}\} \int dy \; \rho_n(\{\mathbf{R}^{(\alpha)}\}, y), \tag{4.20}$$

and

$$V_{\text{eff}}(\{\mathbf{R}^{(\alpha)}\}, y) = U_{\text{int}}(\{\mathbf{R}^{(\alpha)}\}) - \frac{1}{\beta} \ln \left[\sum_{\{i^{(\alpha)}\}} e^{-\beta V_{\text{r}}(y, \{i^{(\alpha)}\})} \prod_{\alpha=1}^{n} M_{i^{(\alpha)}, i^{(\alpha+1)}}(\mathbf{R}^{(\alpha)}) \right].$$

Since y is restrained to the collective variable $\theta(\{i^{(\alpha)}\})$, it is straightforward to obtain the free energy (FE) of kink-pair formation via integration of $\rho_n(\{\mathbf{R}^{(\alpha)}\}, y)$ over all values of $\{\mathbf{R}^{(\alpha)}\}$ and all values of y that fall below a threshold magnitude, (i.e., $|y| < \epsilon$). In practice, for a given number of ring-polymer beads n, the parameter b is selected to be sufficiently large that this FE of kink-pair formation is invariant with respect to further increasing b. This criterion leads to a well-defined limit for the convergence of both n and b.

Note that the effective potential in Eq. 4.21 introduces no approximation to the equilibrium statistics of the system; since the LHS of Eq. 4.17 is normalized with respect to integration over y, then the expression for Z_n in Eq. 4.20 is unchanged from Eq. 4.8. Eqs. 4.19 - 4.21 thus correspond to a coarse-graining of the electronic degrees of freedom in a manner that is familiar from the description of large, purely classical systems[61–64] and that is not unlike the formulation of the centroid effective potential that appears in the centroid molecular dynamics (CMD) method for describing the quantized dynamics of nuclei.[65,66] The auxiliary variable y preserves key aspects of the fluctuations of the electronic coordinates by distinguishing kinked and unkinked ring-polymer configurations. As before, we can introduce classical equations of motion that rigorously preserve the quantized equilibrium distribution $\rho_n(\{\mathbf{R}^{(\alpha)}\}, y)$, namely

$$\begin{aligned} \dot{v}_j^{(\alpha)} &= -\frac{n}{m_j} \frac{\partial}{\partial R_j^{(\alpha)}} V_{\text{eff}}(\{\mathbf{R}^{(\alpha)}\}, y) \\ \dot{v}_y &= -\frac{1}{m_y} \frac{\partial}{\partial y} V_{\text{eff}}(\{\mathbf{R}^{(\alpha)}\}, y), \end{aligned} \tag{4.21}$$

where we again utilize masses for the nuclear degrees of freedom that correspond to the physical masses of the system. We will shortly (in Subsection 4.2.3.3) introduce a criterion for the mass

associated with the auxiliary electronic variable, m_y.

The equations of motion in Eq. 4.21, with an appropriate selection of m_y, fully specify an RPMD method for non-adiabatic systems that preserves the exact quantum Boltzmann distribution and that explicitly accounts for fluctuations in the electronic degrees of freedom. However, like the conventional position-representation RPMD method, these dynamics would overestimate ET rates in the Marcus inverted regime;[23] to address this problem, the following subsection introduces a small modification to the quantized equilibrium distribution $\rho_n(\{\mathbf{R}^{(\alpha)}\}, y)$ that penalizes ring-polymer kink-pair formation between non-degenerate electronic states, thus yielding RPMD equations of motion that correctly describe non-adiabatic reactions across multiple regimes.

4.2.3.2 A kinetic constraint on the quantum Boltzmann distribution

Recent work has established that many of the successes and failures of the RPMD method in the deep tunneling regime arise from its close connection to semiclassical instanton theory.[23,58–60] In a particularly striking failure of instanton-based methods, the rate of deep-tunneling across strongly asymmetric barriers is significantly overestimated in RPMD and steepest-descent SCI calculations, which manifests in incorrect rate coefficients for ET in the Marcus inverted regime.[23,67] A simple and methodologically suggestive way to understand this overestimation is to recognize that ring-polymer configurations associated with transitions between asymmetric potential wells (i.e., kinked ring-polymer configurations across non-degenerate diabatic surfaces, such that $|V_0(\mathbf{R}) - V_1(\mathbf{R})| \gg |K(\mathbf{R})|$) appear with greater probability in the equilibrium distribution than is appropriate for an accurate transition-state theory (TST) description of the deep-tunneling process.[23]

To address this failure of instanton-based rate theories, we propose a simple modification of the path-integral distribution in Eq. 4.19 that explicitly penalizes the formation of kink-pairs at ring-polymer configurations for which the diabatic surfaces are non-degenerate, such that

$$\rho_n^{\mathrm{KC}}(\{\mathbf{R}^{(\alpha)}\}, y) = \Omega e^{-\beta V_{\mathrm{eff}}^{\mathrm{KC}}(\{\mathbf{R}^{(\alpha)}\}, y)}, \tag{4.22}$$

where

$$V_{\mathrm{eff}}^{\mathrm{KC}}(\{\mathbf{R}^{(\alpha)}\}, y) = U_{\mathrm{int}}(\{\mathbf{R}^{(\alpha)}\}) - \frac{1}{\beta}\ln\left[\sum_{\{i^{(\alpha)}\}} g(\{i^{(\alpha)}\}, \{\mathbf{R}^{(\alpha)}\}) e^{-\beta V_{\mathrm{r}}(y, \{i^{(\alpha)}\})} \prod_{\alpha=1}^{n} M_{i^{(\alpha)}, i^{(\alpha+1)}}(\mathbf{R}^{(\alpha)})\right],$$

and

$$g(\{i^{(\alpha)}\},\{\mathbf{R}^{(\alpha)}\}) = \begin{cases} 1, & i^{(\alpha)} = 0 \text{ for all } \alpha, \\ 1, & i^{(\alpha)} = 1 \text{ for all } \alpha, \\ \left(\frac{a}{\pi}\right)^{\frac{1}{2}} \eta e^{-a(w(\bar{\mathbf{R}}))^2}, & \text{otherwise.} \end{cases} \tag{4.23}$$

The function $w(\mathbf{R}) = (V_0(\mathbf{R}) - V_1(\mathbf{R}))/K(\mathbf{R})$ is the scaled difference in the diabatic potential surfaces, $\bar{\mathbf{R}} = \frac{1}{n}\sum_{\alpha=1}^{n} \mathbf{R}^{(\alpha)}$ is the ring-polymer centroid coordinate, a is a unitless convergence parameter, and

$$\eta = \langle |\nabla w(\mathbf{R})| \rangle_{\mathrm{c}}. \tag{4.24}$$

The brackets denote an ensemble average constrained to the intersection of the diabatic surfaces, such that

$$\langle (...) \rangle_{\mathrm{c}} = \frac{\int d\mathbf{R} \delta(w(\mathbf{R}))(...) \left|K(\mathbf{R})\right|^2 e^{-\beta V_0(\mathbf{R})}}{\int d\mathbf{R} \delta(w(\mathbf{R})) \left|K(\mathbf{R})\right|^2 e^{-\beta V_0(\mathbf{R})}}. \tag{4.25}$$

The exponential term in $g(\{i^{(\alpha)}\},\{\mathbf{R}^{(\alpha)}\})$ penalizes the formation of ring-polymer kink-pairs as a function of the difference of the diabatic surfaces, and the associated prefactor ensures that the FE of kink-pair formation at the crossing of the diabatic surfaces is the same in the modified and unmodified distributions. In Appendix 4.1, we present the detailed derivation of the penalty function $g(\{i^{(\alpha)}\},\{\mathbf{R}^{(\alpha)}\})$; in Appendix 4.2, we demonstrate that this form of the penalty function enables the effective potential in Eq. 4.23 and its derivatives to be factorized and efficiently evaluated in $\mathcal{O}(n)$ operations, which is essential for practical applications.

A consequence of including the penalty function $g(\{i^{(\alpha)}\},\{\mathbf{R}^{(\alpha)}\})$ is that the resulting partition function

$$Z_n^{\mathrm{KC}} = \int d\{\mathbf{R}^{(\alpha)}\} \int dy \rho_n^{\mathrm{KC}}(\{\mathbf{R}^{(\alpha)}\}, y) \tag{4.26}$$

is no longer identical to the result in Eq. 4.8; the penalty function thus introduces an approximation to the true quantum Boltzmann statistics of the system. However, two points are worth noting about this. Firstly, the configurations that are explicitly excluded via the penalty function constitute only a subset of those for which the ring polymer exhibits kinks in the electronic variables. If these excluded configurations are statistically unfavorable relative to unkinked configurations, which is generally true for cases in which the diabatic basis is a good representation for the electronic structure of a physical system, then we may expect that the penalty function introduces little bias to the equilibrium properties of the system; regardless, the impact of the penalty function is easily tested by sampling the path-integral statistics both with and without this modification to the ring-polymer distribution. Secondly, we note that the ring-polymer configurations that are

excluded via the penalty function are precisely those that give rise to the breakdown of the instanton approximation for tunneling across asymmetric barriers. In this sense, we are introducing a targeted kinetic constraint on the accessible ring-polymer configurations with the aim of eliminating a known pathology of the semiclassical instanton theory upon which RPMD rests in the deep-tunneling regime.

The parameter a in Eq. 4.23 dictates the strength of the kinetic constraint that is introduced via the penalty function. Convergence with respect to this parameter requires that the statistical weight of kinked ring-polymer configurations that violate the kinetic constraint must become negligible in comparison to the statistical weight of kinked configurations that satisfy the kinetic constraint. We thus choose a to be sufficiently large to converge the FE of kink-pair formation in the kinetically constrained ring-polymer distribution, which is given by $\Delta F^{\mathrm{KC}} = F^{\mathrm{KC}}(0) - F^{\mathrm{KC}}(-1)$, where

$$F^{\mathrm{KC}}(y) = -\frac{1}{\beta} \ln \int d\{\mathbf{R}^{(\alpha)}\} \rho_n^{\mathrm{KC}}(\{\mathbf{R}^{(\alpha)}\}, y). \tag{4.27}$$

This criterion provides a simple basis for the determination of a in a given application. However, it should also be noted that if a is chosen to be greater than unity, then kink-pair formation will be hindered at ring-polymer configurations for which $|V_0(\mathbf{R}) - V_1(\mathbf{R})| < |K(\mathbf{R})|$. Therefore, in addition to requiring that a be sufficiently large to converge the FE of kink-pair formation in the kinetically constrained ring-polymer distribution, we also require that the parameter not exceed a value of unity. In principle, systems for which this range of convergence does not exist fall outside the realm of applicability of the current method and are likely to be better described using the MF non-adiabatic RPMD in Eq. 4.14. However, all of the systems considered in the current paper exhibit this range of convergence with $a < 1$, suggesting that the existence of a range of convergence for this parameter is a relatively minor concern.

The classical equations of motion associated with the equilibrium distribution $\rho_n^{\mathrm{KC}}(\{\mathbf{R}^{(\alpha)}\}, y)$ are

$$\begin{aligned} \dot{v}_j^{(\alpha)} &= -\frac{n}{m_j} \frac{\partial}{\partial R_j^{(\alpha)}} V_{\mathrm{eff}}^{\mathrm{KC}}(\{\mathbf{R}^{(\alpha)}\}, y) \\ \dot{v}_y &= -\frac{1}{m_y} \frac{\partial}{\partial y} V_{\mathrm{eff}}^{\mathrm{KC}}(\{\mathbf{R}^{(\alpha)}\}, y). \end{aligned} \tag{4.28}$$

Eq. 4.28 specifies the kinetically constrained RPMD (KC-RPMD) method for non-adiabatic dynamics, which explicitly accounts for fluctuations in the electronic degrees of freedom and which addresses the failing of instanton-based methods in describing deep-tunneling across asymmetric

barriers. As before, these equations utilize the physical masses for the nuclear degrees of freedom, and m_y will be described in the following Subsection 4.2.3.3.

We emphasize that since the trajectories generated by Eq. 4.28 rigorously preserve a well-defined (albeit approximate) equilibrium distribution, the KC-RPMD method exhibits all of the robust features of the usual position-representation RPMD method, including detailed balance, time-reversibility, invariance of thermal rate coefficient calculations to the choice of dividing surface, and the ability to immediately utilize the full machinery of classical MD simulations.[14] However, unlike the position-representation RPMD method, KC-RPMD allows for the description of non-adiabatic processes involving many-electron wavefunctions and will be shown to overcome the previous failures of instanton-based methods for ET reactions in the Marcus inverted regime.

4.2.3.3 The mass of the auxiliary variable

For the position-representation RPMD method,[13,14] the correspondence between the ring-polymer bead masses and the physical masses of the particles in the system has been justified in several ways. These include the demonstration that the RPMD mass choice leads to both *(i)* optimal agreement in the short-time limit between general, real-time quantum mechanical correlation functions and their RPMD approximations[68] and *(ii)* an RPMD TST that corresponds to the $t \to 0^+$ limit of an appropriately transformed quantum-mechanical flux-side correlation function, and therefore yields the exact quantum rate coefficient in the absence of recrossing.[58,69,70]

In the current study, we employ a justification similar to *(ii)* for the determination of m_y, the mass of the auxiliary variable that reports on ring-polymer kink formation. Specifically, we choose m_y such that the resulting KC-RPMD TST exactly recovers the multi-dimensional Landau-Zener TST rate expression for non-adiabatic transitions in the weak-coupling regime.[71] The resulting expression, which is derived in Appendix 4.3, is

$$m_y = \frac{\beta^3 \hbar^2}{2\pi^3} \left[\frac{\langle |\nabla w(\mathbf{R})| \rangle_c}{\langle |K(\mathbf{R})|^{-1} \rangle_c} \right]^2 , \tag{4.29}$$

where the constrained ensemble average is defined in Eq. 4.25. For simple potentials, this expression can be evaluated analytically; however, for general systems, the evaluation of m_y involves only a constrained ensemble average, which can be performed using well-established classical simulation methods[72] and which is already required for most RPMD (or classical mechanical) rate calculations.[14]

4.2.3.4 Summary of the KC-RPMD method

Before proceeding, we summarize the steps that are needed to implement the KC-RPMD method for a given application, which emphasizes the relative simplicity of this non-adiabatic extension of RPMD.

1. Determine the number of ring-polymer beads, n, needed to converge the equilibrium properties of the system in the path-integral representation, as is typically necessary in path-integral calculations.

2. Converge the coefficient b that appears in the potential of restraint (Eq. 4.17) between the auxiliary variable y and the collective variable that reports on the existence of kinks in the ring-polymer configuration. As is described in Subsection 4.2.3.1, the coefficient b should be sufficiently large to converge the FE of kink-pair formation ΔF^{KC}.

3. Compute the mass m_y (Eq. 4.29) and η (Eq. 4.24) from a single, constrained ensemble average.

4. Converge the coefficient a that appears in the function that penalizes the weight of kinked ring-polymer configurations across non-degenerate diabatic surfaces (Eq. 4.23). As is described in Subsection 4.2.3.2, the coefficient a should be sufficiently large to converge ΔF^{KC} but should not exceed a value of unity.

5. As for the usual position-representation RPMD method, model the real-time dynamics of the system by integrating classical equations of motion in an extended phase space, as defined by Eq. 4.28.

4.3 Model Systems

Numerical results are presented for model systems with potential energy functions of the form

$$\hat{V}(\mathbf{R}) = \hat{V}_{\mathrm{S}}(\mathbf{R}) + \mathbb{1} V_{\mathrm{B}}(\mathbf{R}), \tag{4.30}$$

where $\mathbb{1}$ is the identity operator,

$$\hat{V}_{\mathrm{S}}(\mathbf{R}) = \begin{pmatrix} V_0(s) & K \\ K & V_1(s) \end{pmatrix}, \tag{4.31}$$

K is a constant, s is a one-dimensional (1D) system coordinate, and the full set of nuclear position coordinates $\mathbf{R} = \{s, \mathbf{x}\}$ includes a set of f bath modes, $\mathbf{x}$. We use atomic units throughout, unless otherwise noted.

System A models a simple avoided-crossing reaction in the absence of a dissipative bath, for which

$$\hat{V}_{\mathrm{S}}(s) = \begin{pmatrix} Ae^{Bs} & K \\ K & Ae^{-Bs} \end{pmatrix} \tag{4.32}$$

and $V_{\mathrm{B}}(\mathbf{R}) = 0$. Parameters for this model are presented in Table 4.1, and the quantities η and m_y are analytically evaluated from Eqs. 4.24 and 4.29, such that $\eta = 8 \times 10^{-2}$ and the values for m_y are given in Table 4.2.

System B models a condensed-phase ET reaction in various regimes, with the redox system described using

$$\hat{V}_{\mathrm{S}}(\mathbf{R}) = \begin{pmatrix} As^2 + Bs & K \\ K & As^2 - Bs + \epsilon \end{pmatrix}, \tag{4.33}$$

where s corresponds to the local solvent dipole. This solvent coordinate is linearly coupled to a bath of harmonic oscillators, such that

$$V_{\mathrm{B}}(s, \mathbf{x}) \quad = \quad \sum_{j=1}^{f} \left[\frac{1}{2} M\omega_j^2 \left(x_j - \frac{c_j s}{M\omega_j^2} \right)^2 \right], \tag{4.34}$$

with oscillators of mass M. The bath exhibits an Ohmic spectral density with cutoff frequency ω_{c},

$$J(\omega) = \gamma\omega e^{-\omega/\omega_{\mathrm{c}}}, \tag{4.35}$$

where γ is a dimensionless parameter that controls the strength of coupling between the system and the bath modes and that is chosen to be characteristic of a condensed-phase environment. The spectral density in Eq. 4.35 is discretized into f oscillators with frequencies[20]

$$\omega_j = -\omega_{\mathrm{c}} \ln \left(\frac{j - 0.5}{f} \right) \tag{4.36}$$

and coupling constants

$$c_j = \omega_j \left(\frac{2\gamma M \omega_{\mathrm{c}}}{f\pi} \right)^{1/2}, \tag{4.37}$$

where $j = 1 \ldots f$. The additional parameters for System B are provided in Table 4.3, and $m_y =$

Table 4.1: Parameters for System A.

Parameter	Value Range[a]
A	0.02
B	2.0
K	5×10^{-5}
m_s	2000
$1000/T$(K)	$1.5 - 5.5$

[a] Unless otherwise noted, values are reported in atomic units.

Table 4.2: Values of m_y for the KC-RPMD simulations of System A.

$1000/T$(K)	m_y[a]
1.5	2.74×10^3
2.0	6.50×10^3
2.5	1.27×10^4
3.0	2.19×10^4
3.5	3.48×10^4
4.0	5.20×10^4
4.5	7.40×10^4
5.0	1.02×10^5
5.5	1.35×10^5

[a] Unless otherwise noted, values are reported in atomic units.

3.94×10^4 is again evaluated using Eq. 4.29. Using Eq. 4.29, we obtain and $\eta = 6.86 \times 10^4$ for results in Fig 4.3 and $\eta = 6.86 \times 10^4 - 5.76$ for results presented in Fig 4.5.

In the following, we consider examples in which the system coordinate s is either quantized or treated in the classical limit. However, to enable straightforward comparison with other methods, we will in all cases consider the classical limit for the nuclear degrees of freedom associated with the harmonic oscillator bath. As is usual for applications of RPMD,[14] the classical limit for nuclear degrees of freedom is obtained by requiring the associated ring-polymer bead positions to coincide.

Table 4.3: Parameters for System B.

Parameter	Value Range[a]
A	4.772×10^{-3}
B	2.288×10^{-2}
ϵ	$0 - 0.236$
K	$6.67 \times 10^{-7} - 7.5 \times 10^{-3}$
m_s	1836.0
M	1836.0
ω_c	2.28×10^{-3}
$\gamma/M\omega_c$	1.0
f	12
T	300 K

[a] Unless otherwise noted, values are reported in atomic units.

4.4 Calculation of reaction rates

4.4.1 Calculation of KC-RPMD rates

As for the position-representation RPMD method,[14] the KC-RPMD method involves classical equations of motion in an extended phase space (Eq. 4.28). Accordingly, standard methods for the calculation of classical reaction rates can be employed to compute KC-RPMD reaction rate coefficients,[72] and the KC-RPMD rate can be separated into statistical and dynamical contributions as[73,74]

$$k^{\mathrm{KC-RPMD}} = k_{\mathrm{TST}}^{\mathrm{KC-RPMD}} \lim_{t\to\infty} \kappa(t), \tag{4.38}$$

where $k_{\mathrm{TST}}^{\mathrm{KC-RPMD}}$ is the TST estimate for the rate associated with the dividing surface $\xi(\mathbf{r}) = \xi^{\ddagger}$, and $\kappa(t)$ is the time-dependent transmission coefficient that corrects for dynamical recrossing at the dividing surface. Here, $\xi(\mathbf{r})$ is a collective variable that distinguishes between reactant and product basins of stability, defined as a function of the position vector of the full system in the ring-polymer representation, $\mathbf{r} = \left\{\{\mathbf{R}^{(\alpha)}\}, y\right\}$.

The KC-RPMD TST rate is calculated using the usual expression,[14]

$$k_{\mathrm{TST}}^{\mathrm{KC-RPMD}} = \frac{1}{\sqrt{2\pi\beta}} \langle \chi_{\xi} \rangle^{\ddagger} \frac{e^{-\beta \Delta F(\xi^{\ddagger})}}{\int_{-\infty}^{\xi^{\ddagger}} d\xi e^{-\beta \Delta F(\xi)}}. \tag{4.39}$$

Here, $F(\xi)$ is the FE along ξ relative to a reference value ξ°, such that

$$e^{-\beta \Delta F(\xi^{\ddagger})} = \frac{\langle \delta(\xi(\mathbf{r}) - \xi^{\ddagger}) \rangle}{\langle \delta(\xi(\mathbf{r}) - \xi^{\circ}) \rangle}, \tag{4.40}$$

and[75–77]

$$\chi_{\xi}(\mathbf{r}) = \left[\sum_{j}^{nd+1} \frac{1}{m_j} \left(\frac{\partial \xi(\mathbf{r})}{\partial r_j} \right)^2 \right]^{1/2}. \tag{4.41}$$

The sum in Eq. 4.41 runs over all the $nd+1$ degrees of freedom for the ring-polymer representation used here, and m_j denotes the mass associated with each degree of freedom. The angle brackets indicate an equilibrium ensemble average

$$\langle \dots \rangle = \frac{\int d\mathbf{r} \int d\mathbf{v}\ e^{-\beta H(\mathbf{r},\mathbf{v})} (\dots)}{\int d\mathbf{r} \int d\mathbf{v}\ e^{-\beta H(\mathbf{r},\mathbf{v})}}, \tag{4.42}$$

where $\mathbf{v} = \left\{\left\{v^{(\alpha)}\right\}, v_y\right\}$ is the velocity vector for the full system in the ring-polymer representation

and $H(\mathbf{r}, \mathbf{v})$ is the ring-polymer Hamiltonian associated with the KC-RPMD effective potential. Similarly,

$$\langle \dots \rangle^{\ddagger} = \frac{\int d\mathbf{r} \int d\mathbf{v}\ e^{-\beta H(\mathbf{r},\mathbf{v})} \delta(\xi(\mathbf{r}) - \xi^{\ddagger})(\dots)}{\int d\mathbf{r} \int d\mathbf{v}\ e^{-\beta H(\mathbf{r},\mathbf{v})} \delta(\xi(\mathbf{r}) - \xi^{\ddagger})} \tag{4.43}$$

is the ensemble average constrained to the dividing surface. For the case of $\xi(\mathbf{r}) = y$, the KC-RPMD TST rate expression takes a particularly concise form,

$$k_{\mathrm{TST}}^{\mathrm{KC-RPMD}} = \frac{1}{\sqrt{2\pi\beta m_y}} \frac{e^{-\beta \Delta F(y^{\ddagger})}}{\int_{-\infty}^{y^{\ddagger}} dy e^{-\beta \Delta F(y)}}. \tag{4.44}$$

The transmission coefficient in Eq. 4.38 is calculated as

$$\kappa(t) = \frac{\langle \dot{\xi}_0 h\left(\xi(\mathbf{r}_t) - \xi^{\ddagger}\right) \rangle^{\ddagger}}{\langle \dot{\xi}_0 h(\dot{\xi}_0) \rangle^{\ddagger}}, \tag{4.45}$$

where $h(x)$ is the Heaviside function, and the subscripts 0 and t denote evaluation of the quantity from the trajectory at its initiation and after evolution for time t, respectively.

4.4.1.1 KC-RPMD rate calculation in System B

The KC-RPMD reaction rate for System B is calculated as the product of the KC-RPMD TST rate (Eq. 4.44) and the transmission coefficient (Eq. 4.45). In all cases, the TST dividing surface is defined as an isosurface of the auxiliary variable, y.

We perform two sets of KC-RPMD reaction rate calculations for System B. In the first, the diabatic coupling $K = 6.67 \times 10^{-7}$ is held fixed, $T = 300$ K, and the driving force parameter ϵ is varied. The ring polymer is discretized using $n = 32$ beads. For cases in which the solvent dipole coordinate s is treated classically, the ring-polymer bead positions for this solvent coordinate are restricted to coincide; in all cases, the degrees of freedom associated with the harmonic oscillator bath are treated classically. Convergence checks with respect to the strength of the kinetic constraint, a, are provided in the Results Section. Unless otherwise stated, the results for this set of calculations are reported using $a = 5 \times 10^{-8}$. The coefficient b was found to be converged for all calculations on System B with a value of $b = 400$.

The KC-RPMD TST rate (Eq. 4.44) is obtained from $F(y)$, the FE profile in the continuous auxiliary variable. For cases in which the solvent coordinate s is treated classically, the FE profile is obtained by direct numerical integration; for cases in which the solvent coordinate is quantized, the FE profile is calculated using umbrella sampling and the weighted histogram analysis method

(WHAM).[72,78–80] In the latter case, for each value of ϵ, $F(y)$ is obtained by reducing the two-dimensional (2D) FE surface computed with respect to y and the ring-polymer centroid for the solvent coordinate, $\bar{s}$.

The 2D FE profile $F(\bar{s}, y)$ is sampled using independent KC-RPMD trajectories with a potential that restrains $\bar{s}$ and y to s_0 and y_0, respectively, such that

$$V_{\text{map}}\left(\{s^{(\alpha)}\}, y\right) = V_{\text{eff}}^{\text{KC}}\left(\{s^{(\alpha)}\}, y\right) + 0.5k_s(\bar{s} - s_0)^2 + \left(0.5k_y(y - y_0)^2 + 10k_y(y - y_0)^6\right). \quad (4.46)$$

The KC-RPMD sampling trajectories are grouped into two sets. The first set is comprised of 1100 trajectories that primarily sample the reactant and product basins, with s_0 and y_0 assuming values on a square grid. The parameter s_0 assumes 22 uniformly spaced values in the region $s_0 = [-4, 9]$, and the associated force constant is $k_s = 0.04$. For each value of s_0, the parameter y_0 assumes 10 equally-spaced values in the range $y_0 = [-1.5, -0.5]$ with $k_y = 0.2$, 10 equally-spaced values in the range $y_0 = [1.5, 0.5]$ with $k_y = 0.2$, 15 equally-spaced values in the range $y_0 = [-0.5, -0.2]$ with $k_y = 16.0$, and 15 equally-spaced values in the range $y_0 = [0.5, 0.2]$ with $k_y = 16.0$. The second set of sampling trajectories is comprised of 506 KC-RPMD trajectories that primarily sample the region of the intersection of the diabatic surfaces, denoted $s^\ddagger$, with s_0 and y_0 assuming values on a square grid. The parameter s_0 assumes 11 uniformly spaced values in the region $s_0 = [s^\ddagger - 0.2, s^\ddagger + 0.2]$, and the associated force constant is $k_s = 4.0$. For each value of s_0, the parameter y_0 assumes 13 equally-spaced values in the range $y_0 = [0.40, 0.52]$ with $k_y = 64.0$, 13 equally-spaced values in the range $y_0 = [-0.40, -0.52]$ with $k_y = 64.0$, and 20 equally-spaced values in the range $y_0 = [-0.4, 0.4]$ with $k_y = 6.0$. Each sampling trajectory is evolved for at least 20 ps using a timestep of $dt = 0.02$ fs. Thermostatting is performed by resampling the velocities from the Maxwell-Boltzmann (MB) distribution every 200 fs.

The transmission coefficients (Eq. 4.45) are calculated using KC-RPMD trajectories that are released from the dividing surface associated with $y^\ddagger = 0$. For each value of the driving force ϵ, a total of 1000 trajectories are released. Each KC-RPMD trajectory is evolved for 200 fs using a timestep of $dt = 0.02$ fs and with the initial velocities sampled from the MB distribution. The initial configurations for the KC-RPMD trajectories are generated from long KC-RPMD trajectories that are constrained to the dividing surface using the RATTLE algorithm;[81] the constrained trajectories are at least 200 ps in time and are thermostatted by resampling the velocities from the MB distribution every 200 fs.

In the second set of KC-RPMD reaction rate calculations for System B, $\epsilon = 0$, $T = 300$ K, and

the diabatic coupling K is varied from the weak-coupling to the strong-coupling regimes, such that $-\log(K) \in \{6.18, 6.00, 5.50, 5.00, 4.50, 4.00, 3.30, 3.00, 2.70, 2.30, 2.10\}$. For these couplings, the calculations are performed using $-\log(a) \in \{7.3, 5.0, 4.0, 3.0, 2.0, 2.0, 1.5, 1.0, 0.5, 0.5, 0.5\}$, respectively. At each coupling, it is confirmed that the FE barrier in $F(y)$ and the KC-RPMD rate are robust with respect to increasing the convergence parameter a, although at larger couplings, the plateau range for a becomes more narrow. The ring-polymer is discretized using $n = 128$ beads, which is sufficient for convergence at all values of the diabatic coupling; the solvent coordinate and the harmonic bath are treated classically.

4.4.1.2 KC-RPMD rate calculation in System A

The form of the potential energy surface in System A precludes the use of the factorization shown in Eq. 4.38, which assumes that the reactant and product basins are bound. The KC-RPMD rate in System A is instead evaluated directly as the long-time limit of the flux-side correlation function,

$$k^{\mathrm{KC-RPMD}} = \frac{1}{Q_{\mathrm{R}}(T)} \lim_{t\to\infty} C_{\mathrm{fs}}(t), \tag{4.47}$$

where

$$C_{\mathrm{fs}}(t) = \Omega \int d\mathbf{r}_0 \int d\mathbf{v}_0 e^{-\beta H(\mathbf{r},\mathbf{v})} \delta(y_0) v_y h(y_t). \tag{4.48}$$

Here, $\mathbf{r} = \left\{\{s^{(\alpha)}\}, y\right\}$, $\mathbf{v} = \left\{\{v^{(\alpha)}\}, v_y\right\}$, and the subscripts denote the values of the ring-polymer positions and velocities at times 0 and t, respectively. The reactant partition function for the unbound system is the inverse de Broglie thermal wavelength, $Q_{\mathrm{R}}(T) = \sqrt{\frac{m_s}{2\pi\beta\hbar^2}}$, and

$$\Omega = \left(\frac{m_{\mathrm{s}}}{2\pi\hbar}\right)^n \sqrt{\frac{m_{\mathrm{y}}\beta}{2\pi}}. \tag{4.49}$$

Efficient Monte Carlo sampling of the initial conditions in the flux-side correlation function is accomplished by introducing two reference distributions,

$$\rho_+^{\mathrm{ref}}(\mathbf{r},\mathbf{v}) = e^{-\beta H_{\mathrm{ref}}(\mathbf{r},\mathbf{v})} \delta(y) h(v_y) v_y \tag{4.50}$$

and

$$\rho_-^{\mathrm{ref}}(\mathbf{r},\mathbf{v}) = e^{-\beta H_{\mathrm{ref}}(\mathbf{r},\mathbf{v})} \delta(y) h(-v_y) v_y, \tag{4.51}$$

where

$$H_{\mathrm{ref}}(\mathbf{r},\mathbf{v}) = \sum_{\alpha=1}^{n} \frac{1}{2}\tilde{m}_{\mathrm{s}} {v^{(\alpha)}}^2 + \frac{1}{2} m_y v_y^2 + U_{\mathrm{int}}(\{s^{(\alpha)}\}) + V_{\mathrm{ref}}(\bar{s}) \tag{4.52}$$

and

$$V_{\mathrm{ref}}(\bar{s}) = -\frac{\bar{s}^2}{\sigma^2}. \tag{4.53}$$

The difference between the reference and system Hamiltonians is thus given by

$$\Delta V(\mathbf{r},\mathbf{v}) = H(\mathbf{r},\mathbf{v}) - H_{\mathrm{ref}}(\mathbf{r},\mathbf{v}). \tag{4.54}$$

The KC-RPMD rate is then evaluated using

$$k^{\mathrm{KC-RPMD}}(T) = \lim_{t\to\infty} \frac{\Omega}{Q_{\mathrm{R}}(T)} \left[\Phi_+ \left\langle e^{-\beta \Delta V(\mathbf{r}_0,\mathbf{v}_0)} h(y_t) \right\rangle_+ + \Phi_- \left\langle e^{-\beta \Delta V(\mathbf{r}_0,\mathbf{v}_0)} h(y_t) \right\rangle_- \right], \tag{4.55}$$

where the angle brackets denote sampling over the initial positions and velocities of the system using the distributions described by Eqs. 4.50 and 4.51,

$$\langle (\dots) \rangle_\pm = \frac{\int d\mathbf{r}_0 \int d\mathbf{v}_0 \ (\dots)\ \rho_\pm^{\mathrm{ref}}(\mathbf{r}_0,\mathbf{v}_0)}{\int d\mathbf{r}_0 \int d\mathbf{v}_0 \ \rho_\pm^{\mathrm{ref}}(\mathbf{r}_0,\mathbf{v}_0)}, \tag{4.56}$$

and $\Phi_\pm$ denote the value of the reference distributions integrated over all space,

$$\Phi_\pm = \int d\mathbf{r}_0 \int d\mathbf{p}_0 \ \rho_\pm^{\mathrm{ref}}(\mathbf{r}_0,\mathbf{v}_0). \tag{4.57}$$

The reference distributions involve integration over separable degrees of freedom, and Eq. 4.57 can be evaluated analytically.

For each temperature T, 2×10^5 initial configurations are sampled from the distribution in Eq. 4.56, and KC-RPMD trajectories are evolved for 500 fs with a timestep of $dt = 0.02$ fs. We employ $n = 64$ ring-polymer beads and $a = 5 \times 10^{-6}$; it is confirmed that varying a over two orders of magnitude leads to graphically indistinguishable differences in the results. The coefficient b was found to be converged for all calculations on System A with a value of $b = 100$.

4.4.2 Calculation of reference TST rate expressions

The exact quantum-mechanical thermal rate coefficient for System A is

$$k^{\mathrm{ex}}(T) = \frac{1}{Q_{\mathrm{R}}(T)} \frac{1}{2\pi\hbar} \int_0^\infty dE e^{-\beta E} N(E), \tag{4.58}$$

where $N(E)$ denotes the microcanonical reaction probability at energy E. These probabilities are evaluated directly by solving the scattering problem for the potential in Eq. 4.32 using the log-derivative method.[82,83]

Reference values for the thermal reaction rates for System B are evaluated using rate expressions for adiabatic and non-adiabatic ET. The TST expression for adiabatic ET with classical solvent is[84,85]

$$k_{\mathrm{ET}}^{\mathrm{ad}} = \frac{\omega_{\mathrm{s}}}{2\pi} \exp\left[-\beta G_{\mathrm{ad}}^{\ddagger}\right], \tag{4.59}$$

where ω_{s} and $G_{\mathrm{ad}}^{\ddagger}$ are, respectively, the solvent frequency and the FE barrier to reaction, calculated along the solvent coordinate. The expression for non-adiabatic ET with classical solvent is given by the classical Marcus Theory (MT) expression[85]

$$k_{\mathrm{ET}}^{\mathrm{nad}} = \frac{2\pi}{\hbar} |K|^2 \sqrt{\frac{\beta}{4\pi\lambda}} \exp\left[-\beta \frac{(\lambda + \Delta G^o)^2}{4\lambda}\right], \tag{4.60}$$

where λ, ΔG°, and K are the solvent reorganization energy, the driving force, and the electronic coupling, respectively. The expression for non-adiabatic ET with quantized solvent is given by the golden-rule expression[85–87]

$$k_{\mathrm{ET}}^{\mathrm{nad}} = \frac{2\pi}{\hbar Q_{\mathrm{R}}} |K|^2 \sum_\mu \sum_\nu e^{-\beta E_\mu^{(\mathrm{a})}} |\langle \chi_\mu | \chi_\nu \rangle|^2 \delta(E_\mu^{(\mathrm{a})} - E_\nu^{(\mathrm{b})}), \tag{4.61}$$

where χ_μ and χ_ν denote the reactant and product vibrational eigenstates for the solvent coordinate, respectively, with associated energies $E_\mu^{(\mathrm{a})}$ and $E_\nu^{(\mathrm{b})}$. If the reactant and product solvent potential energy surfaces are represented by displaced harmonic oscillators with frequency ω_{s}, as is the case for System B, this equation can be transformed into the analytical form,[86,87]

$$k_{\mathrm{ET}}^{\mathrm{nad}} = \frac{2\pi}{\hbar\omega_{\mathrm{s}}} |K|^2 e^{vz - S\coth(z)} I_v(S\ \mathrm{csch}(z)), \tag{4.62}$$

where $z = \beta\omega_{\mathrm{s}}/2$, $v = -\epsilon/\omega_{\mathrm{s}}$, I_v is a modified Bessel function of the first kind, and $S = (2\hbar)^{-1} m_{\mathrm{s}} \omega_{\mathrm{s}} {\Delta_{\mathrm{s}}}^2$,

with Δ_s and ϵ denoting the relative horizontal displacement of the diabatic potential energy surfaces and the reaction driving force, respectively.

4.5 Results

We present numerical results obtained using the new KC-RPMD method, including comparisons with reaction rates obtained using exact quantum mechanics (Eq. 4.58), position-representation RPMD, MF non-adiabatic RPMD (Eq. 4.14), and TST rate expressions (Eqs. 4.59-4.61). These results demonstrate the performance of the KC-RPMD method in models for a simple avoided-crossing reaction and for condensed-phase ET. We examine these models in a variety of regimes to demonstrate the performance of the KC-RPMD in describing electronically adiabatic vs. non-adiabatic reactions, classical vs. quantized nuclei, and normal vs. inverted ET.

4.5.1 Simple avoided-crossing reaction

We begin by considering numerical results for System A, which models a non-dissipative avoided-crossing reaction in 1D. Figure 4.2 presents the thermal reaction rate for this system over the range of temperatures from 187 to 667 K, which corresponds to spanning from the weak- to moderate-coupling regimes (i.e., $\beta K = 0.02 - 0.1$). The reaction rates are computing using the KC-RPMD and MF non-adiabatic RPMD methods. For comparison, we also include the rates calculated with position-representation RPMD on the lower adiabatic surface, and exact rates computed using the log-derivative method.

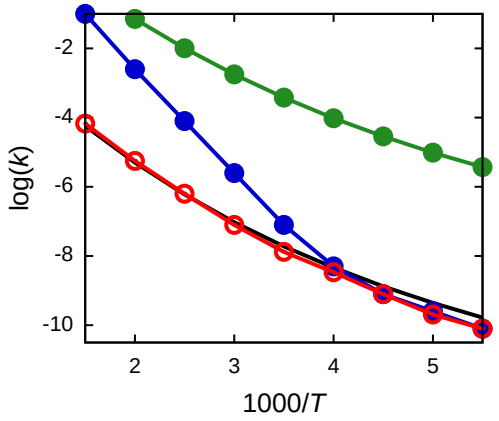

Figure 4.2: Thermal reaction rate coefficients for System A as a function of temperature, obtained using KC-RPMD (red), MF non-adiabatic RPMD (blue), position-representation RPMD on the lower adiabatic surface (green), and exact quantum mechanics (black).

Comparison of the position-representation RPMD rates and the exact quantum rates illustrate the importance of non-adiabatic effects in this model. The MF non-adiabatic RPMD method, which incorporates non-adiabatic effects via the thermal average of fluctuations in the electronic degrees of freedom, does well in regimes of stronger coupling but breaks down when the statistical weight of ring-polymer configurations with kink-pairs becomes small relative to the weight of configurations without kink-pairs. In contrast, KC-RPMD performs well throughout the entire range of temperatures, accurately capturing the regime for which the mean-field result is accurate as well as the weak-coupling regime for which explicit fluctuations in the electronic degrees of freedom are important.

4.5.2 Condensed-phase electron transfer

We next present numerical results for System B, a system-bath model for condensed-phase ET. We consider the effects of varying the diabatic coupling, changing the driving force, and including quantum-mechanical effects in the treatment of the solvent coordinate.

Figure 4.3(a) presents thermal reaction rates for this system in the weak-coupling regime ($\beta K \approx 7\times10^{-4}$) and for a broad range of the thermodynamic driving force, obtained using KC-RPMD (red), position-representation RPMD (blue), and the non-adiabatic MT relation in Eq. 4.60. For this set of results, the solvent coordinate is treated classically, such that the classical MT relation provides the appropriate reference result. The position-representation RPMD results in this figure are reproduced from Ref. 23. Comparison of the MT results and the position-representation RPMD results in the figure reiterate the observations from Ref. 23; this previous implementation of the RPMD method provides an accurate description of the ET rate throughout the normal and activationless regimes of the driving force, but the breakdown of the instanton tunneling rate for strongly asymmetric double-well systems leads to the absence of the rate turnover in the inverted regime. Correction of this breakdown via introduction of the kinetic constraint in the KC-RPMD method (red) leads to quantitative agreement with the reference results across the full range of driving forces. Fig. 4.3(a) clearly demonstrates that, in addition to enabling the use of many-electron wavefunctions in the diabatic representation, the KC-RPMD method successfully avoids the most dramatic known failure of the position-representation RPMD method.

Figure 4.3(b) presents numerical results for System B that include quantization of the solvent coordinate. The KC-RPMD results are plotted in red, and the results for MT with the classical solvent are re-plotted for reference. Also included are the golden-rule ET rates from Eq. 4.60, which explicitly include the quantization of the solvent coordinate. Just as KC-RPMD quantitatively

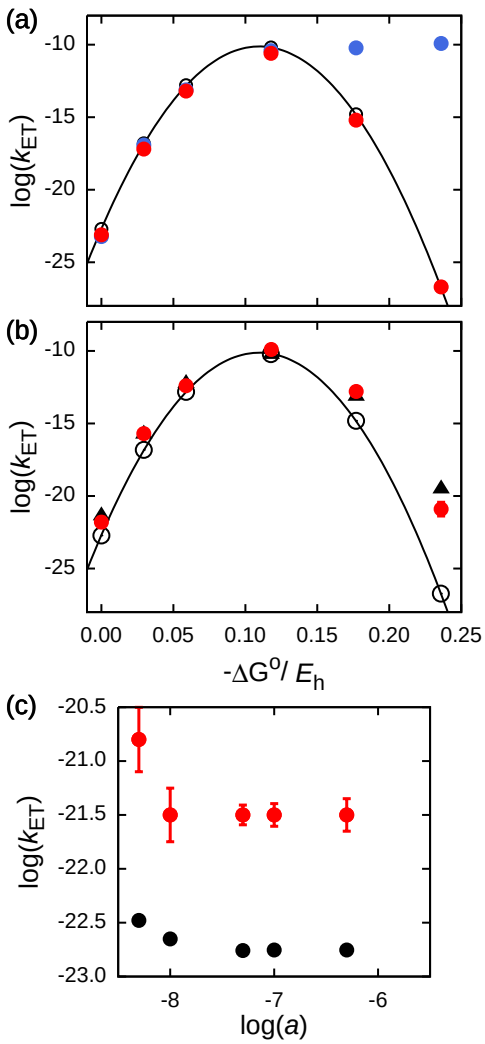

Figure 4.3: **(a)** ET reaction rate coefficients for System B with a classical description of the solvent coordinate, obtained as a function of ET driving force using KC-RPMD (red), classical MT (Eq. 4.60, black open circles), and position-representation RPMD (Ref. 23, blue). **(b)** The corresponding results for System B with a quantized description of the solvent coordinate, obtained using KC-RPMD (red) and the golden-rule expression in Eq. 4.62 (black triangles). Results obtained using classical MT are also included for comparison (black open circles). **(c)** The convergence of the KC-RPMD reaction rate for symmetric ET with respect to the strength of kinetic constraint, a, including both classical (black) and quantized (red) descriptions of the solvent.

reproduced the MT relation in the limit of classical nuclei (Fig. 4.3(a)), Fig. 4.3(b) demonstrates that KC-RPMD reproduces the effects of nuclear quantization on the ET reaction rate throughout the full range of driving forces. In particular, nuclear quantization enhances the KC-RPMD rate in the normal regime far less than in the inverted regime, as is consistent with Eq. 4.61.

Figure 4.3(c) presents convergence tests for the symmetric ET reaction rate with ($\beta K \approx 7\times10^{-4}$), including both classical (black) and quantized (red) descriptions of the solvent. Specifically, we plot

the KC-RPMD rate as a function of the strength of the kinetic restraint, a. In both cases, it is seen that for small values of a, the rate varies with a since the kinetic constraint is not fully enforced. However, for sufficiently large values of a, the kinetic constraint is enforced and the rate converges with respect to this parameter. Similar results are obtained for the cases with non-zero driving force.

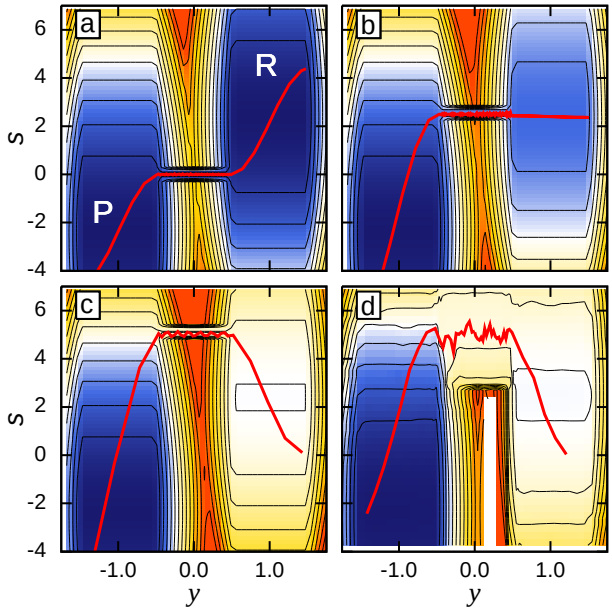

Figure 4.4: **(a)-(c)** Representative trajectories (red) from the ensemble of reactive KC-RPMD trajectories for the (a) symmetric, (b) activationless, and (c) inverted regimes of ET, obtained using the classical description of the solvent coordinate. The trajectories are projected onto the plane of the solvent coordinate s and the auxiliary variable y. The trajectories overlay the FE surface $F(s, y)$, with contour lines indicating increments of 0.0475 $E_{\rm h}$ (50 $k_{\rm B}T$). The ET reactant and product basins are indicated using "R" and "P," respectively. **(d)** The corresponding results for the inverted regime, obtained using the quantized description of the solvent coordinate. To more clearly illustrate the effect of solvent quantization, the trajectories and FE profile are plotted as a function of the solvent ring-polymer bead position, $s^{(\alpha)}$, rather than the centroid position.

Figures 4.4(a)-(c) present representative reactive KC-RPMD trajectories for System B in the symmetric ($\epsilon = 0$), activationless ($\epsilon = 0.1178$), and inverted ($\epsilon = 0.236$) regimes for ET. The solvent is treated classically, and the illustrative trajectories overlay the 2D FE profile $F(s, y)$. In each case, the KC-RPMD trajectories exhibit the reaction mechanism that is anticipated in MT, with distinct components of the trajectories undergoing *(i)* solvent reorganization to configurations for which the electronic diabatic states are nearly degenerate, *(ii)* reactive tunneling of the electron between the redox sites at solvent configurations for which the electronic diabatic states are nearly degenerate, and *(iii)* solvent relaxation in the product basin following reactive tunneling. As was emphasized in Ref. 23, these features of MT emerge clearly for position-representation RPMD in the normal and activationless regimes, but they do not correctly appear in the inverted regime. By penalizing

ring-polymer configurations that lead to the overestimation of reactive tunneling via the kinetic constraint, the KC-RPMD method correctly predicts the solvent-reorganization reaction mechanism for all regimes of the ET driving force.

Figure 4.4(d) reproduces the results for the inverted regime using the quantized description for the solvent coordinate. As for the results obtained with classical solvent (Fig. 4.4(c)), the reactive trajectory exhibits the solvent-reorganization reaction mechanism for the inverted regime. However, comparison of Figs. 4.4(c) and 4.4(d) reveals in the quantized description for the solvent, widening of the transition channel significantly reduces the degree to which solvent reorganization is needed for reactive tunneling. By allowing for a degree of "corner-cutting" in the solvent coordinate, this quantum effect gives rise to the significant weakening of the turnover in the ET reaction rate in the inverted regime that is observed in Fig. 4.3(b).

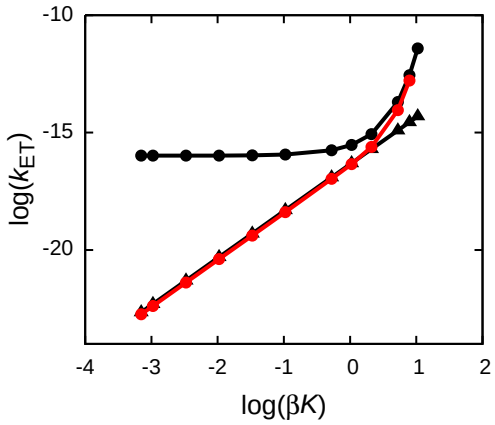

Figure 4.5: ET reaction rate coefficients for System B with a classical description of the solvent coordinate, obtained as a function of the diabatic coupling using KC-RPMD (red), the non-adiabatic rate expression in Eq. 4.60 (black triangles), and the adiabatic rate expression in Eq. 4.59 (black circles).

Finally, Figure 4.5 presents rate coefficients for System B obtained over a range of values for the diabatic coupling K that span from the weak-coupling to the strong-coupling regimes. In all cases, $\epsilon = 0$, and the solvent degree of freedom is treated classically. For comparison with the KC-RPMD reaction rates (red), reference results are included from rate expressions that are derived in the non-adiabatic regime (Eq. 4.60, black triangles) and in the adiabatic regime (Eq. 4.59, black circles). Although the KC-RPMD method makes no *a priori* assumption about the coupling regime for the reaction, it is seen that the method quantitatively reproduces the reference results in the appropriate regimes, and the KC-RPMD method correctly transitions from the non-adiabatic result to the adiabatic result in the regime of intermediate coupling ($\log(\beta K) \approx 0$).

4.6 Concluding Remarks

The development of accurate and robust methods for describing non-adiabatic chemistries in complex, condensed-phase systems is a central methodological challenge for the field of molecular simulation. In this work, we present an extension of RPMD that is well suited to addressing this challenge for broad classes of donor-acceptor chemistries. The KC-RPMD method is a path-integral-based method that provides continuous equations of motion to model the non-adiabatic molecular dynamics of systems that are quantized with respect to both electronic and nuclear degrees of freedom. The method generates trajectories that rigorously preserve a well-defined equilibrium distribution, such that KC-RPMD exhibits the appealing features of the previously formulated position-representation RPMD method, including detailed balance, time-reversal symmetry, and invariance of reaction rate calculations to the choice of dividing surface. The distribution that is preserved in KC-RPMD is modified from the exact quantum Boltzmann distribution by introducing a kinetic constraint to penalize ring-polymer configurations that make a small contribution to the thermal ensemble but that lead to the overestimation of deep-tunneling rates across asymmetric barriers. KC-RPMD yields very encouraging results for a range of condensed-phase charge-transfer chemistries, as is demonstrated using model systems that investigate the performance of the method for adiabatic vs. non-adiabatic reactions, classical vs. quantized nuclei, and normal vs. inverted ET. We emphasize that KC-RPMD is computationally efficient (with force-evaluations that scale linearly with the number of ring-polymer beads), relatively easy to perform (as it simply involves the integration of continuous classical-like equations of motion), naturally interfaced with electronic structure packages (as the electronic states correspond to general, many-electron wavefunctions in the diabatic representation), and free of uncontrolled parameters. Furthermore, the method enables the immediate and straightforward utilization of the full toolkit of classical molecular dynamics simulation, including rare-event sampling methods, and it is robustly scalable to large, complex systems. We expect that it will prove useful for the simulation of charge-transfer and non-adiabatic chemistries in a range of future applications.

Appendix A Derivation of the penalty function

In this appendix, we derive the specific form of the penalty function, g, that appears in Eq. 4.23. The penalty function enforces the kinetic constraint by restraining the formation of kinked configurations of the ring polymer to the region of the crossing of the diabatic surfaces (thereby excluding ring-polymer configurations that have low thermodynamic weight in the equilibrium ensemble but which contribute substantially to the incorrect instanton TST estimate for the rate). This is accomplished by a Gaussian function that is centered at the intersection of diabatic surfaces, with the energy scale set by the diabatic coupling, K, such that

$$g(\{i^{(\alpha)}\},\{\mathbf{R}^{(\alpha)}\}) = \begin{cases} 1, & i^{(\alpha)} = 0 \text{ for all } \alpha, \\ 1, & i^{(\alpha)} = 1 \text{ for all } \alpha, \\ Ce^{-a(w(\bar{\mathbf{R}}))^2}, & \text{otherwise}, \end{cases} \tag{4.63}$$

where C is a multiplicative prefactor, and w is defined in the main text (after Eq. 4.23). We choose a form for the penalty function in which the intersection of the diabatic surfaces is defined in terms of the centroid of the ring polymer, which is convenient and has a natural classical limit; however, other sensible choices of the penalty function are possible.

To avoid biasing the rate of reactive tunneling at the nuclear configurations for which the diabats cross, we require that the FE of kink-pair formation is unchanged by the kinetic constraint at these nuclear configurations, and we derive the expression for C based on this condition. Specifically, we consider the FE cost of going from unkinked configurations of the ring polymer in the reactant basin to kinked configurations at the crossing of the diabatic surfaces, and we equate this to the FE cost of kink-pair formation at the intersection of the diabats in the unmodified distribution.

For simplicity, we first present the detailed derivation for a 1D redox system with constant coupling, K, in the classical limit for the nuclear coordinate. We then outline the analogous derivations for a 1D redox system with quantized nuclei and for a general multi-dimensional system.

4.A.1 1D redox system with constant K and classical nuclei

For a 1D system with classical nuclei, the kinetically constrained ring-polymer distribution (Eq. 4.22) has the form

$$\rho_n^{\mathrm{KC}}(x,y) = \Omega \sum_{\{i^\alpha\}} g(\{i^{(\alpha)}\},x) e^{-\beta V_{\mathrm{r}}(y,\{i^{(\alpha)}\})} \Gamma(\{i^{(\alpha)}\},x), \tag{4.64}$$

where $\Gamma(\{i^{(\alpha)}\},x)=\prod_{\alpha=1}^{n} M_{i^{(\alpha)},i^{(\alpha+1)}}(x)$, and the penalty function in this case takes the form

$$g(\{i^{(\alpha)}\},x)=\begin{cases} 1, & i^{(\alpha)}=0 \text{ for all } \alpha, \\ 1, & i^{(\alpha)}=1 \text{ for all } \alpha, \\ Ce^{-a(w(x))^2}, & \text{otherwise.} \end{cases} \tag{4.65}$$

In the kinetically constrained distribution, the FE cost of going from unkinked configurations of the ring polymer in the reactant basin to kinked configurations at the crossing of the diabatic surfaces is $F^{\ddagger}=-\frac{1}{\beta}\ln P^{\mathrm{KC}}(y=y^{\ddagger})$, where

$$P^{\mathrm{KC}}(y=y^{\ddagger})=Z_0^{-1}e^{-\beta\Delta F(y^{\ddagger})}, \tag{4.66}$$

$$Z_0=\int_{-\infty}^{y^{\ddagger}} dy' e^{-\beta\Delta F(y')}, \tag{4.67}$$

$$e^{-\beta\Delta F(y)}=\int d\{\mathbf{R}^{(\alpha)}\}\; e^{-\beta V_{\mathrm{eff}}(\{\mathbf{R}^{(\alpha)}\},y)}, \tag{4.68}$$

and $y^{\ddagger}=0$.

For kinked ring-polymer configurations (i.e., $y = y^{\ddagger}$), the numerator on the right-hand side (RHS) of Eq. 4.66 simplifies to

$$\begin{aligned} e^{-\beta\Delta F(y^{\ddagger})} &= \int dx\; e^{-\beta V_{\mathrm{eff}}(x,y^{\ddagger})} \\ &= C\int dx \sum_{\{i^{\alpha}\}} \mathcal{P}_k(\{i^{(\alpha)}\}) e^{-a(w(x))^2}\Gamma(\{i^{(\alpha)}\},x) \\ &= C\int dx\; e^{-a(w(x))^2} \sum_{k=1}^{n/2} \frac{(\beta K)^{2k}}{\phi_n(k)} \frac{e^{-\beta V_0(x)}-e^{-\beta V_1(x)}}{\beta(V_1(x)-V_0(x))}, \end{aligned} \tag{4.69}$$

where $\phi_n(k)=\left(\frac{2}{n^{2k}}\binom{n}{2k}\right)^{-1}$, and $\mathcal{P}_k(\{i^{(\alpha)}\})$ is unity for configurations characterized by $k>0$ kink-pairs and 0 otherwise. The last equality in Eq. 4.69 is obtained by evaluating the sum over ring-polymer configurations in the limit of large n.[88]

A consequence of the penalty function is that only nuclear configurations in the vicinity of the intersection of the diabatic surfaces contribute to the integral over x. Therefore, for sufficiently large

values of a, the penalty function tends to a Dirac δ-function,

$$\lim_{a\to\infty} e^{-a(w(x))^2} = \delta(w(x))\sqrt{\frac{\pi}{a}}. \tag{4.70}$$

Using this identity and performing the integral over x, Eq. 4.69 becomes

$$\begin{aligned} e^{-\beta\Delta F(y^\ddagger)} &= C\sqrt{\frac{\pi}{a}}\sum_{k=1}^{n/2}\frac{(\beta K)^{2k}}{\phi_n(k)}\int dx\ \delta(w(x))\frac{e^{-\beta V_0(x)}-e^{-\beta V_1(x)}}{\beta(V_1(x)-V_0(x))} \\ &= C\sqrt{\frac{\pi}{a}}\sum_{k=1}^{n/2}\frac{(\beta K)^{2k}}{\phi_n(k)}\ e^{-\beta V_0(x^\ddagger)}\left|w'(x^\ddagger)\right|^{-1}, \end{aligned} \tag{4.71}$$

where $x^\ddagger$ denotes the point of the intersection of the diabatic surfaces (the solution of $w(x)=0$), and the prime denotes differentiation with respect to the nuclear coordinate.

We now consider the denominator Z_0 in Eq. 4.66, which is dominated by the statistical weight of unkinked configurations. For these configurations, the penalty function makes no contribution, such that

$$\begin{aligned} Z_0 &= \int_{-\infty}^{y^\ddagger} dy \int dx e^{-\beta V_{\text{eff}}(x,y)} \\ &= \int_{-\infty}^{y^\ddagger} dy \int dx\ f(y,-1)\ \Gamma(\{0\},x), \end{aligned} \tag{4.72}$$

where we have used the definition of $f(y,\theta(\{i^\alpha\}))$ from Eq. 4.17, and $\{0\}$ denotes ring-polymer configurations which have $i^{(\alpha)}=0$ for all α. Inserting the definition of $\Gamma(\{0\},x)$ into the RHS of Eq. 4.72 yields

$$\begin{aligned} Z_0 &= \int_{-\infty}^{y^\ddagger} dy \int dx\ f(y,-1)\ e^{-\beta V_0(x)} \\ &= \int dx\ e^{-\beta V_0(x)}. \end{aligned} \tag{4.73}$$

Combining the results of Eqs. 4.66, 4.71, and 4.73, we obtain the probability of forming kinked ring-polymer configurations at the crossing of the diabatic surfaces in the kinetically constrained distribution,

$$P^{\text{KC}}(y=y^\ddagger) = \frac{e^{-\beta V_0(x^\ddagger)}}{\int dx\ e^{-\beta V_0(x)}}\frac{C}{|w'(x^\ddagger)|}\sqrt{\frac{\pi}{a}}\ \sum_{k=1}^{n/2}\frac{(\beta K)^{2k}}{\phi_n(k)} \tag{4.74}$$

Here, the first term on the RHS corresponds to the FE cost of reorganizing the nuclear coordinates to configurations for which the diabatic surfaces are degenerate, and the second term corresponds

to the FE cost for ring-polymer kink-pair formation at the reorganized nuclear configurations and in the presence of the penalty function. The analog of Eq. 4.74 for the ring-polymer distribution without the kinetic constraint (i.e., in the absence of the penalty function) is

$$P(y=y^{\ddagger},x=x^{\ddagger})=\frac{e^{-\beta V_0(x^{\ddagger})}}{\int dx\ e^{-\beta V_0(x)}}\sum_{k=1}^{n/2}\frac{(\beta K)^{2k}}{\phi_n(k)}. \tag{4.75}$$

Finally, enforcing the condition that the probabilities in Eqs. 4.74 and 4.75 are identical yields the final expression for the multiplicative prefactor in a 1D redox system with constant K and classical nuclei,

$$C=\sqrt{\frac{a}{\pi}}|w'(x^{\ddagger})|. \tag{4.76}$$

4.A.2 1D redox system with constant K and quantized nuclei

We now repeat the derivation of C for the case of a 1D redox system with constant K and quantized nuclei. In this case, the steps outlined in Eqs. 4.69-4.71 yield

$$\begin{aligned}e^{-\beta\Delta F(y^{\ddagger})}&=C\sqrt{\frac{\pi}{a}}\int d\mathbf{x}\ \delta(w(\bar{x}))e^{-\beta U_{\rm int}(\mathbf{x})}\Phi(\mathbf{x})\\&=C\sqrt{\frac{\pi}{a}}\int d\mathbf{x}\ \delta(\bar{x}-x^{\ddagger})e^{-\beta U_{\rm int}(\mathbf{x})}\frac{\Phi(\mathbf{x})}{|w'(\bar{x})|}.\end{aligned} \tag{4.77}$$

where $\mathbf{x}$ denotes the vector of ring-polymer position coordinates $\{x^{(\alpha)}\}$, $\bar{x}$ is the centroid of the ring polymer, and

$$\Phi(\mathbf{x})=\left(\mathrm{Tr}\prod_{\alpha=1}^{n}\mathbf{M}(x^{(\alpha)})-\prod_{\alpha=1}^{n}M_{0,0}(x^{(\alpha)})-\prod_{\alpha=1}^{n}M_{1,1}(x^{(\alpha)})\right). \tag{4.78}$$

As before, Z_0 in Eq. 4.66 is unaffected by the penalty function, and it simplifies in this case to

$$Z_0=\int d\mathbf{x}e^{-\beta U_{\rm int}(\mathbf{x})}\prod_{\alpha=1}^{n}M_{0,0}(x^{(\alpha)}). \tag{4.79}$$

Combining the results of Eqs. 4.66, 4.77, and 4.79, we obtain the probability of forming kinked ring-polymer configurations at the crossing of the diabatic surfaces in the kinetically constrained distribution,

$$P^{\rm KC}(y=y^{\ddagger})=\frac{C}{Z_0}\sqrt{\frac{\pi}{a}}\int d\mathbf{x}\ \delta(\bar{x}-x^{\ddagger})e^{-\beta U_{\rm int}(\mathbf{x})}\frac{\Phi(\mathbf{x})}{|w'(\bar{x})|}. \tag{4.80}$$

The analog of Eq. 4.80 for the ring-polymer distribution without the kinetic constraint is

$$P(y = y^{\ddagger}, \bar{x} = x^{\ddagger}) = Z_0^{-1} \int d\mathbf{x}\ \delta(\bar{x} - x^{\ddagger}) e^{-\beta U_{\text{int}}(\mathbf{x})} \Phi(\mathbf{x}) \tag{4.81}$$
$$= Z_0^{-1} \int d\mathbf{x}\ \delta(w(\bar{x})) |w'(\bar{x})| e^{-\beta U_{\text{int}}(\mathbf{x})} \Phi(\mathbf{x}).$$

Finally, enforcing the condition that the probabilities in Eqs. 4.80 and 4.81 are identical yields the final expression for the multiplicative prefactor in a 1D redox system with constant K and quantized nuclei,

$$C = \sqrt{\frac{a}{\pi}} \frac{\int d\mathbf{x}\ \delta(w(\bar{x})) |w'(\bar{x})| e^{-\beta U_{\text{int}}(\mathbf{x})} \Phi(\mathbf{x})}{\int d\mathbf{x}\ \delta(w(\bar{x})) e^{-\beta U_{\text{int}}(\mathbf{x})} \Phi(\mathbf{x})}. \tag{4.82}$$

Equation 4.82 has the form of a constrained ensemble average, which can be evaluated using standard methods.

If the ring-polymer nuclear coordinates are approximated by the centroid position, $\Phi(\mathbf{x})$ can be further simplified as follows,

$$\Phi(\mathbf{x}) = \frac{e^{-\beta V_0(\bar{x})} - e^{-\beta V_1(\bar{x})}}{\beta(V_1(\bar{x}) - V_0(\bar{x}))} \sum_{k=1}^{n/2} \frac{(\beta K)^{2k}}{\phi_n(k)}. \tag{4.83}$$

Inserting Eq. 4.83 into Eq. 4.82 yields the final result for the multiplicative prefactor in a 1D redox system with quantized nuclei,

$$C = \sqrt{\frac{a}{\pi}} |w'(x^{\ddagger})|. \tag{4.84}$$

Note that this result is identical to that obtained for a system with classical nuclei in Eq. 4.76. Furthermore, note that Eqs. 4.82 and 4.84 are identical in the limit of classical nuclei or for a quantized system with constant coupling and harmonic diabatic potentials.

4.A.3 Multi-dimensional redox system with position-dependent $K(\mathbf{R})$

For the case of a general multi-dimensional system with classical nuclei and $\mathbf{R}$-dependent diabatic coupling $K(\mathbf{R})$, the previously outlined derivation yields

$$C = \sqrt{\frac{a}{\pi}} \langle |\nabla w(\mathbf{R})| \rangle_{\Sigma}, \tag{4.85}$$

where the brackets denote a constrained ensemble average constrained to at the hypersurface $w(\mathbf{R}) = 0$,

$$\langle \dots \rangle_{\Sigma} = \frac{\sum_{k=1}^{n/2} \frac{(\beta)^{2k}}{\phi_n(k)} \int d\mathbf{R}\ \delta(w(\mathbf{R}))(\dots)|K(\mathbf{R})|^{2k} e^{-\beta V_0(\mathbf{R})}}{\sum_{k=1}^{n/2} \frac{(\beta)^{2k}}{\phi_n(k)} \int d\mathbf{R}\ \delta(w(\mathbf{R}))|K(\mathbf{R})|^{2k} e^{-\beta V_0(\mathbf{R})}}. \tag{4.86}$$

This expression can be further simplified if it is assumed that terms associated with more than one kink-pair ($k = 1$) can be neglected in both the numerator and denominator. The resulting expression is

$$C = \sqrt{\frac{a}{\pi}} \langle |\nabla w(\mathbf{R})| \rangle_{\mathrm{c}}, \tag{4.87}$$

where the brackets denote an ensemble average constrained to the intersection of the diabatic surfaces, as described in Eq. 4.25. We note that Eqs. 4.85 and 4.87 are identical for the case of constant diabatic coupling, K, and Eq. 4.87 reduces to Eq. 4.76 for the case of a 1D redox system.

Finally, following the approach described in Section 4.A.2, the multiplicative prefactor for the case of a general multi-dimensional system with quantized nuclei and $\mathbf{R}$-dependent diabatic coupling is derived to be

$$C = \sqrt{\frac{a}{\pi}} \frac{\int d\{\mathbf{R}^{(\alpha)}\}\ \delta(w(\bar{\mathbf{R}}))|\nabla w(\bar{\mathbf{R}})| e^{-\beta U_{\mathrm{int}}(\{\mathbf{R}^{(\alpha)}\})} \Phi(\{\mathbf{R}^{(\alpha)}\})}{\int d\{\mathbf{R}^{(\alpha)}\}\ \delta(w(\bar{\mathbf{R}})) e^{-\beta U_{\mathrm{int}}(\{\mathbf{R}^{(\alpha)}\})} \Phi(\{\mathbf{R}^{(\alpha)}\})}. \tag{4.88}$$

Employing the approximation for $\Phi(\{\mathbf{R}^{(\alpha)}\})$ described in Eq. 4.83 and again truncating the sums in the numerator and denominator at terms associated with a single kink-pair, we arrive at the same result that was obtained for a system with classical nuclei in Eq. 4.87,

$$C = \sqrt{\frac{a}{\pi}} \langle |\nabla w(\mathbf{R})| \rangle_{\mathrm{c}}. \tag{4.89}$$

This expression for the multiplicative prefactor appears in the main text in Eq. 4.23.

Appendix B KC-RPMD forces and the Bell algorithm

In this appendix, we illustrate the terms that arise in the calculation of forces associated with the KC-RPMD effective potential ($V_{\text{eff}}^{\text{KC}}(\{\mathbf{R}^{(\alpha)}\}, y)$ in Eq. 4.21), and we review a computational algorithm[89] that enables the evaluation of these forces with a cost that scales linearly with the number of ring-polymer beads.

Without approximation, the KC-RPMD effective potential can be factorized to obtain

$$V_{\text{eff}}^{\text{KC}}(\{\mathbf{R}^{(\alpha)}\}, y) = U_{\text{int}}(\{\mathbf{R}^{(\alpha)}\}) - \frac{1}{\beta}\ln\left[f(y,-1)\prod_{\alpha=1}^{n}M_{0,0}(\mathbf{R}^{(\alpha)}) + f(y,1)\prod_{\alpha=1}^{n}M_{1,1}(\mathbf{R}^{(\alpha)})\right. \tag{4.90}$$
$$\left. + f(y,0)\left(\frac{a}{\pi}\right)^{\frac{1}{2}}\eta e^{-a(w(\bar{\mathbf{R}}))^2}\left(\text{Tr}\prod_{\alpha=1}^{n}\mathbf{M}(\mathbf{R}^{(\alpha)}) - \prod_{\alpha=1}^{n}M_{0,0}(\mathbf{R}^{(\alpha)}) - \prod_{\alpha=1}^{n}M_{1,1}(\mathbf{R}^{(\alpha)})\right)\right].$$

Differentiation of this term with respect to a given nuclear coordinate $\xi^{(\alpha)}$ leads to terms of the form

$$\frac{\partial}{\partial\xi^{(\alpha)}}\left[\ln\left(\text{Tr}\prod_{\alpha=1}^{n}\mathbf{M}(\mathbf{R}^{(\alpha)})\right)\right] = \frac{\text{Tr}\left[\mathbf{F}_{\alpha-1}\mathbf{D}_{\alpha}^{\xi}\mathbf{G}_{\alpha+1}\right]}{\text{Tr}\left[\prod_{\alpha}^{n}\mathbf{M}(\mathbf{R}^{(\alpha)})\right]}, \tag{4.91}$$

where

$$\mathbf{F}_{\alpha-1} = \mathbf{M}(\mathbf{R}^{(1)})\mathbf{M}(\mathbf{R}^{(2)})\ldots\mathbf{M}(\mathbf{R}^{(\alpha-1)}), \tag{4.92}$$

$$\mathbf{G}_{\alpha+1} = \mathbf{M}(\mathbf{R}^{(\alpha+1)})\mathbf{M}(\mathbf{R}^{(\alpha+2)})\ldots\mathbf{M}(\mathbf{R}^{(n)}), \tag{4.93}$$

and

$$\mathbf{D}_{\alpha}^{\xi} = \frac{\partial}{\partial\xi^{(\alpha)}}\mathbf{M}(\mathbf{R}^{(\alpha)}). \tag{4.94}$$

Using the cyclic property of the trace, the numerator of Eq. 4.91 can be expressed

$$\text{Tr}\left[\mathbf{F}_{\alpha-1}\mathbf{D}_{\alpha}^{\xi}\mathbf{G}_{\alpha+1}\right] = \text{Tr}\left[\mathbf{D}_{\alpha}^{\xi}\mathbf{H}_{\alpha}\right], \tag{4.95}$$

where $\mathbf{H}_{\alpha}$ is the 'hole' matrix that is given by

$$\mathbf{H}_{\alpha} = \mathbf{G}_{\alpha+1}\mathbf{F}_{\alpha-1} = \mathbf{M}(\mathbf{R}^{(\alpha+1)})\ldots\mathbf{M}(\mathbf{R}^{(n)})\mathbf{M}(\mathbf{R}^{(1)})\ldots\mathbf{M}(\mathbf{R}^{(\alpha-1)}). \tag{4.96}$$

Since the matrices $\mathbf{M}(\mathbf{R}^{(\alpha)})$ do not generally commute, a naive algorithm would individually determine the hole matrix for each ring-polymer bead, at a combined cost of that entails $\mathcal{O}(n^2)$ matrix

multiplications. Using the algorithm outlined below, however, only $\mathcal{O}(n)$ matrix multiplications are required.

4.B.4 The Bell algorithm

The gradients of $V_{\text{eff}}^{\text{KC}}(\{\mathbf{R}^{(\alpha)}\}, y)$ can be efficiently evaluated by taking advantage of the appearance of common terms in the hole matrices for different ring-polymer beads.[89] By calculating and storing portions of these matrices, the overall time for the calculation is greatly reduced. The algorithm is clearly outlined in Ref. 90 and proceeds as follows.

1. Set $\mathbf{F}_1 = \mathbf{M}(\mathbf{R}^{(1)})$ and compute $\mathbf{F}_\alpha$ for $\alpha = 2, \ldots, n-1$ recursively, noting that $\mathbf{F}_\alpha = \mathbf{F}_{\alpha-1}\mathbf{M}(\mathbf{R}^{(\alpha)})$. This step requires $n-2$ matrix multiplications.

2. Set $\mathbf{G}_n = \mathbf{M}(\mathbf{R}^{(n)})$ and compute $\mathbf{G}_\alpha$, $\alpha = n-1, n-2, \ldots, 2$ recursively, noting that $\mathbf{G}_\alpha = \mathbf{M}(\mathbf{R}^{(\alpha)})\mathbf{G}_{\alpha+1}$. This step requires $n-2$ matrix multiplications.

3. Compute $\mathbf{H}_\alpha$ for $\alpha = 1, \ldots, n$ using Eq. 4.96. This only requires $n-2$ matrix multiplications because $\mathbf{H}_1 = \mathbf{G}_2$ and $\mathbf{H}_n = \mathbf{F}_{n-1}$.

With this algorithm, all the $\mathbf{H}_\alpha$ matrices required for evaluation of the gradients of $V_{\text{eff}}^{\text{KC}}(\{\mathbf{R}^{(\alpha)}\}, y)$ are constructed in $3n-6$ matrix multiplications.

Appendix C Derivation of the mass of the auxiliary variable

In this appendix, we derive the mass of the auxiliary variable, m_y, which is chosen such that the KC-RPMD TST recovers the Landau-Zener (LZ) TST[91,92] in the limit of weak diabatic coupling. We first describe the case of a 1D redox system with classical nuclei and constant diabatic coupling, before outlining the general case of a multi-dimensional system with position-dependent diabatic coupling and quantized nuclei.

4.C.5 1D redox system with constant K and classical nuclei

The LZ TST rate for a non-adiabatic process in 1D is given by[93]

$$k_{\mathrm{TST}}^{\mathrm{LZ}} = \int_0^\infty d\dot{x}\dot{x}P(\dot{x}, x^\ddagger)P_{0\to1}(\dot{x}), \tag{4.97}$$

where $P(\dot{x}, x^\ddagger)$ denotes the probability of reaching the diabatic crossing $x = x^\ddagger$ with velocity $\dot{x}$ and $P_{0\to1}(\dot{x})$ indicates the non-adiabatic transition probability for a given $\dot{x}$. The probability of reaching the diabatic crossing is

$$P(\dot{x}, x^\ddagger) = \frac{1}{Q_R}\int_{-\infty}^\infty dx\delta(x - x^\ddagger)e^{-\beta\left[\frac{1}{2}m\dot{x}^2 + V_0(x)\right]}, \tag{4.98}$$

where Q_R is the reactant partition function, which takes the form

$$Q_R = \left(\frac{2\pi}{\beta m}\right)^{1/2}\int dx e^{-\beta V_0(x)}. \tag{4.99}$$

The probability of a non-adiabatic transition under the assumption of small, constant coupling K is[91,92]

$$P_{0\to1}(\dot{x}) = \left[\frac{2\pi|K|^2}{\hbar\dot{x}|V_0'(x) - V_1'(x)|}\right]_{x=x^\ddagger}. \tag{4.100}$$

Inserting Eqs. 4.98-4.100 into Eq. 4.97 and evaluating the velocity integral yields the LZ TST rate

$$k_{\mathrm{TST}}^{\mathrm{LZ}} = \frac{\pi}{\hbar}\frac{|K|^2}{|V_1'(x) - V_0'(x)|_{x=x^\ddagger}}\frac{e^{-\beta V_0(x^\ddagger)}}{\int dx e^{-\beta V_0(x)}}. \tag{4.101}$$

The KC-RPMD TST rate associated with the $y^\ddagger = 0$ dividing surface takes the form

$$k_{\mathrm{TST}}^{\mathrm{KC-RPMD}} = \sqrt{\frac{1}{2\pi\beta m_y}}\frac{e^{-\beta\Delta F(y^\ddagger)}}{\int_{-\infty}^{y^\ddagger} dy e^{-\beta\Delta F(y)}}, \tag{4.102}$$

which in the low-coupling limit can be expressed as

$$k_{\mathrm{TST}}^{\mathrm{KC-RPMD}} = |K|^2 \beta^2 \sqrt{\frac{1}{2\pi\beta m_y}} \frac{e^{-\beta V_0(x^\ddagger)}}{\int dx e^{-\beta V_0(x)}}. \tag{4.103}$$

Equating the rate expressions in Eqs. 4.101 and 4.103 and solving for the mass of the auxiliary variable yields

$$m_y = \frac{\beta^3 \hbar^2}{2\pi^3} \left| V_1'(x) - V_0'(x) \right|^2_{x=x^\ddagger}. \tag{4.104}$$

4.C.6 Multi-dimensional redox system with position-dependent $K(\mathbf{R})$

For a general multi-dimensional redox system, the auxiliary-variable mass m_y can be analogously derived. In this case, the diabatic coupling $K(\mathbf{R})$ can vary along the seam of crossing of the diabatic surfaces. Using the multi-dimensional analog of the LZ non-adiabatic transition probability,[71] Eq. 4.97 for the general case becomes

$$k_{\mathrm{TST}}^{\mathrm{LZ}} = \frac{\pi}{\hbar} \frac{\int d\mathbf{R} \delta(\xi(\mathbf{R})) |K(\mathbf{R})|^2 e^{-\beta V_0(\mathbf{R})}}{\int d\mathbf{R} e^{-\beta V_0(\mathbf{R})}}, \tag{4.105}$$

where $\xi(\mathbf{R}) = V_0(\mathbf{R}) - V_1(\mathbf{R})$. If we assume that the diabatic coupling is constant in the direction perpendicular to the crossing of the diabatic surfaces, such that

$$\nabla \left(K(\mathbf{R}) \right) \cdot \nabla \xi(\mathbf{R}) |_{\xi(\mathbf{R})=0} = 0, \tag{4.106}$$

then this result can be expressed as follows,

$$k_{\mathrm{TST}}^{\mathrm{LZ}} = \frac{\pi}{\hbar} \frac{\int d\mathbf{R} \delta(w(\mathbf{R})) |K(\mathbf{R})|^{-1} |K(\mathbf{R})|^2 e^{-\beta V_0(\mathbf{R})}}{\int d\mathbf{R} e^{-\beta V_0(\mathbf{R})}}. \tag{4.107}$$

In analogy to Eq. 4.103, the KC-RPMD TST rate associated with the $y^\ddagger = 0$ dividing surface can be expressed

$$k_{\mathrm{TST}}^{\mathrm{KC-RPMD}} = \sqrt{\frac{\beta^3}{2\pi m_y}} \langle |\nabla w(\mathbf{R})| \rangle_{\mathrm{c}} \frac{\int d\mathbf{R}\, \delta(w(\mathbf{R})) |K(\mathbf{R})|^2 e^{-\beta V_0(\mathbf{R})}}{\int d\mathbf{R} e^{-\beta V_0(\mathbf{R})}}. \tag{4.108}$$

Equating the rate expressions in Eqs. 4.107 and 4.108 and solving for m_y yields the final expression for a multi-dimensional system with classical nuclei,

$$m_y = \frac{\beta^3 \hbar^2}{2\pi^3} \left[\frac{\langle |\nabla w(\mathbf{R})| \rangle_{\mathrm{c}}}{\langle |K(\mathbf{R})|^{-1} \rangle_{\mathrm{c}}} \right]^2. \tag{4.109}$$

For the case of a multi-dimensional system with quantized nuclei, the resulting mass expression in Eq. 4.109 is unchanged if we make the approximations outlined in Section 4.A.3 (i.e., that the ring-polymer position is approximated by its centroid and that contributions from multi-kink-pair configurations are neglected) and if the LZ TST is expressed in terms of the ring-polymer centroid.

References

[1] P. Ehrenfest, Z. Phys **45**, 455 (1927).

[2] H. D. Meyer and W. H. Miller, J. Chem. Phys. **70**, 3214 (1979).

[3] D. A. Micha, J. Chem. Phys. **78**, 7138 (1983).

[4] J. C. Tully, *Classical and Quantum Dynamics in Condensed Phase Simulations: Proceedings of the International School of Physics Proceedings of the International School of Physics*, edited by B. B. J., C. G., and C. D. F. (World Scientific, 1998).

[5] M. Hack and D. G. Truhlar, J. Phys. Chem. A **104**, 7917 (2000).

[6] J. C. Tully and R. K. Preston, J. Chem. Phys. **55**, 562 (1971).

[7] J. C. Tully, J. Chem. Phys. **93**, 1061 (1990).

[8] P. J. Kuntz, J. Chem. Phys. **95**, 141 (1991).

[9] H. Wang, X. Sun, and W. H. Miller, J. Chem. Phys. **108**, 9726 (1998).

[10] X. Sun, H. Wang, and W. H. Miller, J. Chem. Phys. **109**, 7064 (1998).

[11] S. J. Cotton and W. H. Miller, J. Phys. Chem. A **117**, 7190 (2013).

[12] P. Huo, T. F. Miller, and D. F. Coker, J. Chem. Phys. **139**, 151103 (2013).

[13] I. R. Craig and D. E. Manolopoulos, J. Chem. Phys. **121**, 3368 (2004).

[14] S. Habershon, D. E. Manolopoulos, T. E. Markland, and T. F. Miller, Annu. Rev. Phys. Chem. **64**, 387 (2013).

[15] R. P. Feynman and A. R. Hibbs, *Quantum mechanics and path integrals* (McGraw-Hill, New York, New York, 1965).

[16] R. Collepardo-Guevara, Y. V. Suleimanov, and D. E. Manolopoulos, J. Chem. Phys. **130** (2009).

[17] R. Perez de Tudela, F. J. Aoiz, Y. V. Suleimanov, and D. E. Manolopoulos, J. Phys. Chem. Lett. **3**, 493 (2012).

[18] Y. V. Suleimanov, R. Collepardo-Guevara, and D. E. Manolopoulos, J. Chem. Phys. **134**, 044131 (2011).

[19] J. W. Allen, W. H. Green, Y. Li, H. Guo, and Y. V. Suleimanov, J. Chem. Phys. **138**, 221103 (2013).

[20] I. R. Craig and D. E. Manolopoulos, J. Chem. Phys. **122**, 084106 (2005).

[21] I. R. Craig and D. E. Manolopoulos, J. Chem. Phys. **123**, 034102 (2005).

[22] R. Collepardo-Guevara, I. R. Craig, and D. E. Manolopoulos, J. Chem. Phys. **128**, 144502 (2008).

[23] A. R. Menzeleev, N. Ananth, and T. F. Miller, J. Chem. Phys. **135**, 074106 (2011).

[24] J. S. Kretchmer and T. F. Miller, J. Chem. Phys. **138**, 134109 (2013).

[25] N. Boekelheide, R. Salomón-Ferrer, and T. F. Miller, Proc. Natl. Acad. Sci. U. S. A. **108**, 16159 (2011).

[26] T. F. Miller and D. E. Manolopoulos, J. Chem. Phys. **122**, 184503 (2005).

[27] T. F. Miller and D. E. Manolopoulos, J. Chem. Phys. **123**, 154504 (2005).

[28] T. F. Miller, J. Chem. Phys. **129**, 194502 (2008).

[29] S. Habershon, T. E. Markland, and D. E. Manolopoulos, J. Chem. Phys. **131**, 024501 (2009).

[30] S. Habershon and D. E. Manolopoulos, J. Chem. Phys. **131**, 244518 (2009).

[31] T. E. Markland, S. Habershon, and D. E. Manolopoulos, J. Chem. Phys. **128**, 194506 (2008).

[32] A. R. Menzeleev and T. F. Miller, J. Chem. Phys. **132**, 034106 (2010).

[33] T. E. Markland, J. A. Morrone, B. J. Berne, K. Miyazaki, E. Rabani, and D. R. Reichman, Nat. Phys. **7**, 134 (2011).

[34] T. E. Markland, J. A. Morrone, K. Miyazaki, B. J. Berne, D. R. Reichman, and E. Rabani, J. Chem. Phys. **136**, 074511 (2012).

[35] F. Calvo and D. Costa, J. Chem. Theory Comput. **6**, 508 (2010).

[36] Y. V. Suleimanov, J. Phys. Chem. C **116**, 11141 (2012).

[37] I. R. Craig and D. E. Manolopoulos, Chem. Phys. **322**, 236 (2006).

[38] S. Habershon, G. S. Fanourgakis, and D. E. Manolopoulos, J. Chem. Phys. **129** (2008).

[39] M. Shiga and A. Nakayama, Chem. Phys. Lett. **451**, 175 (2008).

[40] D. Chandler and P. G. Wolynes, J. Chem. Phys. **74**, 4078 (1981).

[41] M. Parrinello and A. Rahman, J. Chem. Phys. **80**, 860 (1984).

[42] B. De Raedt, M. Sprik, and M. L. Klein, J. Chem. Phys. **80**, 5719 (1984).

[43] P. Shushkov, R. Li, and J. C. Tully, J. Chem. Phys. **137**, 13 (2012).

[44] N. A. T. F. Miller and III, J. Chem. Phys. **133**, 234103 (2010).

[45] J. O. Richardson and M. Thoss, J. Chem. Phys. **139**, 031102 (2013).

[46] N. Ananth, J. Chem. Phys. **139**, 124102 (2013).

[47] G. Stock and M. Thoss, Phys. Rev. Lett. **78**, 578 (1997).

[48] D. Chandler, *Introduction to Modern Statistical Mechanics* (Oxford University Press, 1987).

[49] D. M. Ceperley, Rev. Mod. Phys. **67**, 279 (1995).

[50] M. Marchi and D. Chandler, J. Chem. Phys. **95**, 889 (1991).

[51] A. Kuki and P. G. Wolynes, Science **236**, 1647 (1987).

[52] A. O. Caldeira and A. J. Leggett, Ann. Phys. **149**, 374 (1983).

[53] B. V. A., M. D. E., and A. C. Wight, in *Adv. Chem. Phys.*, Vol. 88 (John Wiley & Sons, Inc., 1994).

[54] C. S., G. B. C., and M. W. H., J. Chem. Phys. **63**, 2710 (1975).

[55] C. G. Callan and S. Coleman, Phys. Rev. D. **16**, 1762 (1977).

[56] P. Hanggi and W. Hontscha, J. Chem. Phys. **88**, 4094 (1988).

[57] W. H. Miller, J. Chem. Phys. **62**, 1899 (1975).

[58] J. O. Richardson and S. C. Althorpe, J. Chem. Phys. **131**, 214106 (2009).

[59] S. C. Althorpe, J. Chem. Phys. **134**, 114104 (2011).

[60] J. O. Richardson and S. C. Althorpe, J. Chem. Phys. **134**, 054109 (2011).

[61] A. Liwo, S. Oldziej, M. R. Pincus, R. J. Wawak, S. Rackovsky, and H. A. Scheraga, J. Comput. Chem. **18**, 849 (1997).

[62] S. Izvekov and G. A. Voth, J. Phys. Chem. B **109**, 2469 (2005).

[63] W. G. Noid, J.-W. Chu, G. S. Ayton, V. Krishna, S. Izvekov, G. A. Voth, A. Das, and H. C. Andersen, J. Chem. Phys. **128**, 244114 (2008).

[64] T. F. Miller, E. Vanden-Eijnden, and D. Chandler, Proc. Natl. Acad. Sci. U. S. A. **104**, 14559 (2007).

[65] J. S. Cao and G. A. Voth, J. Chem. Phys. **100**, 5106 (1994).

[66] S. Jang and G. A. Voth, J. Chem. Phys. **111**, 2371 (1999).

[67] P. Shushkov, J. Chem. Phys. **138**, 224102 (2013).

[68] B. J. Braams and D. E. Manolopoulos, J. Chem. Phys. **125**, 124105 (2006).

[69] T. J. H. Hele and S. C. Althorpe, J. Chem. Phys. **138**, 084108 (2013).

[70] S. C. Althorpe and T. J. H. Hele, J. Chem. Phys. **139**, 084115 (2013).

[71] J. R. Stine and J. T. Muckerman, J. Chem. Phys. **65**, 3975 (1976).

[72] D. Frenkel and B. Smit, *Understanding molecular simulation : from algorithms to applications*, 2nd ed. (Academic Press, San Diego, 2002).

[73] D. Chandler, J. Chem. Phys. **68**, 2959 (1978).

[74] C. H. Bennett, in *Algorithms for Chemical Computations*, ACS Symposium Series, Vol. 46, edited by R. E. Christofferson (American Chemical Society, 1977) Chap. 4.

[75] E. A. Carter, G. Ciccotti, J. T. Hynes, and R. Kapral, Chem. Phys. Lett. **156**, 472 (1989).

[76] G. K. Schenter, B. C. Garrett, and D. G. Truhlar, J. Chem. Phys. **119**, 5828 (2003).

[77] J. B. Watney, A. V. Soudackov, K. F. Wong, and S. Hammes-Schiffer, Chem. Phys. Lett. **418**, 268 (2006).

[78] S. Kumar, D. Bouzida, R. H. Swendsen, P. A. Kollman, and J. M. Rosenberg, J. Comput. Chem. **13**, 1011 (1992).

[79] S. Kumar, J. M. Rosenberg, D. Bouzida, R. H. Swendsen, and P. A. Kollman, J. Comput. Chem. **16**, 1339 (1995).

[80] B. Roux, Comput. Phys. Commun. **91**, 275 (1995).

[81] H. C. Andersen, J. Comput. Phys. **52**, 24 (1983).

[82] D. E. Manolopoulos, J. Chem. Phys. **85**, 6425 (1986).

[83] B. R. Johnson, J. Chem. Phys. **13**, 445 (1973).

[84] N. S. Hush, Trans. Faraday Soc. **57**, 557 (1961).

[85] R. A. Marcus and N. Sutin, Biochim. Biophys. Acta **811**, 265 (1985).

[86] J. Ulstrup and J. Jortner, J. Chem. Phys. **63**, 4358 (1975).

[87] J. Ulstrup, *Charge Transfer Processes in Condensed Media* (Springer Verlag, Berlin, 1979).

[88] C. Stutz, Am. J. Phys. **36**, 826 (1968).

[89] M. T. Bell, (2005), unpublished contribution to an RPMD group meeting in Oxford.

[90] T. J. H. Hele, *An Electronically Non-Adiabatic Generalization of Ring Polymer Molecular Dynamics*, Master's thesis, Exeter College, Oxford University (2011).

[91] L. Landau, Phys. Z. Sowjet. **1**, 88 (1932).

[92] C. Zener, Proc. R. Soc. A **137**, 696 (1932).

[93] A. Nitzan, *Chemical Dynamics in Condensed Phases* (Oxford University Press, Oxford, 2006).

Appendix A

Deriving the mass of the continuous auxiliary variable in KC-RPMD

This appendix presents a didactically expanded version of the derivation of the mass associated with the continuous auxiliary variable in KC-RPMD. An abridged version can be found within Chapter 4.

In order to be able to run dynamics, a continuous auxiliary variable y has been introduced into the Hamiltonian. Its conjugate momentum p_y is introduced as Gaussian, with associated mass m_y. Since the y variable is fictitious, its mass cannot be determined *a priori*, and below we describe a derivations of this mass term.

A.1 Deriving the KC-RPMD mass from 1D Landau-Zener transition state theory

In a system with classical nuclei, we derive the mass from a transition state theory (TST) rate for a nonadiabatic process with nonadiabatic transitions described by Landau-Zener theory.

The Landau-Zener probability of a nonadiabatic transition between states a and b with constant coupling V_{ab} is given, in the low-coupling limit, by [1,2]

$$P_{a\to b}(\dot{x}) = \left[\frac{2\pi|V_{ab}|^2}{\hbar\dot{x}|V_a'(x) - V_b'(x)|}\right]_{x=x^\dagger} \tag{A.1}$$

where primes denote differentiation and the terms are evaluated at the point of state degeneracy(crossing of the diabats) $x = x^\dagger$. The TST rate is [3]

$$\begin{aligned} k_{\mathrm{TST}} =& \int_0^\infty d\dot{x}\dot{x}P(\dot{x}, x^\dagger)P_{b\to a}(\dot{x}) \\ =& \frac{1}{Q_R}\int_0^\infty d\dot{x}\int_{-\infty}^\infty d\dot{x}\dot{x}\delta(x - x^\dagger)e^{-\beta\left[\frac{1}{2}m\dot{x}^2 + V_a(x)\right]}\left[\frac{2\pi|V_{ab}|^2}{\hbar\dot{x}|V_b'(x) - V_a'(x)|}\right]_{x=x^\dagger} \\ =& \left[\frac{2\pi|V_{ab}|^2}{\hbar|V_b'(x) - V_a'(x)|}\right]_{x=x^\dagger} e^{-\beta V_a(x^\dagger)}\frac{1}{Q_R}\int_0^\infty d\dot{x}e^{-\beta\frac{1}{2}m\dot{x}^2}. \end{aligned} \tag{A.2}$$

The reactant partition function is

$$Q_R = \int dx \int d\dot{x} e^{-\beta\left[\frac{1}{2}m\dot{x}^2 + V_a(x)\right]} = \left(\frac{2\pi}{\beta m}\right)^{1/2} \int dx e^{-\beta V_a(x)}. \tag{A.3}$$

Inserting the partition function into Eq. A.2 and performing the velocity integrals yields

$$\begin{aligned} k_{\mathrm{TST}}^{\mathrm{LZ}} =& \frac{2\pi}{\hbar} \frac{|V_{ab}|^2}{|V_b'(x) - V_a'(x)|}_{x=x^\dagger} \frac{e^{-\beta V_a(x^\dagger)}}{\int dx e^{-\beta V_a(x)}} \frac{1}{2} \left(\frac{2\pi}{\beta m}\right)^{1/2} \left(\frac{\beta m}{2\pi}\right)^{1/2} \\ =& \frac{1}{2} \frac{2\pi}{\hbar} \frac{|V_{ab}|^2}{|V_b'(x) - V_a'(x)|}_{x=x^\dagger} \frac{e^{-\beta V_a(x^\dagger)}}{\int dx e^{-\beta V_a(x)}} \end{aligned} \tag{A.4}$$

The KC-RPMD rate equation, where the auxiliary variable is taken to be the reaction coordinate, is given by

$$k_{\mathrm{ET}} = \lim_{t\to\infty} k_{\mathrm{TST}}^{\mathrm{KC-RPMD}} \kappa(t) = (2\pi\beta m_y)^{-1/2} \frac{e^{-\beta\Delta F(y^\dagger)}}{\int_{-\infty}^{y^\dagger} dy e^{-\beta\Delta F(y)}} \lim_{t\to\infty} \kappa(t) \tag{A.5}$$

Assuming that y is a good reaction coordinate, the recrossing coefficient tends to unity, $\lim_{t\to\infty} \kappa(t) \approx 1$.

To solve for the m_y we require that in the low-coupling limit with classical nuclei, the KCPI TST rate equals the TST rate with nonadiabatic transitions described by LZ theory.

$$\begin{aligned} k_{\mathrm{TST}}^{\mathrm{LZ}} =& k_{\mathrm{TST}}^{\mathrm{KCPI}} \\ \frac{1}{2} \frac{2\pi}{\hbar} \frac{|V_{ab}|^2}{|V_b'(x) - V_a'(x)|}_{x=x^\dagger} \frac{e^{-\beta V_a(x^\dagger)}}{\int dx e^{-\beta V_a(x)}} =& (2\pi\beta m_y)^{-1/2} \frac{e^{-\beta\Delta F(y^\dagger)}}{\int_{-\infty}^{y^\dagger} dy e^{-\beta\Delta F(y)}}. \end{aligned} \tag{A.6}$$

In the KC-RPMD rate equation, the free energy terms can be evaluated as

$$\begin{aligned}
e^{-\beta F(y*)} &= \int dx \int dy \delta(y - y*) e^{-\beta_P V(x,y))} \\
&= \int dx \int dy \delta(y - y*) \left[\prod_{\alpha=1}^{P} M_{00}(x) f(y,-1) + \prod_{\alpha=1}^{P} M_{11}(x) f(y,+1) + \right. \\
&\quad + f(y,0) \, (\, C_2(c) \sum_{\{i_\alpha\}}{}^{2'} \prod_{\alpha=1}^{P} \widetilde{M}_{i_\alpha, i_{\alpha+1}}(x;c) + \\
&\quad + C_4(c) \sum_{\{i_\alpha\}}{}^{4'} \prod_{\alpha=1}^{P} \widetilde{M}_{i_\alpha, i_{\alpha+1}}(x;c) + \\
&\quad \left. + C_6(c) \sum_{\{i_\alpha\}}{}^{6'} \prod_{\alpha=1}^{P} \widetilde{M}_{i_\alpha, i_{\alpha+1}}(x;c) + ... \right) \Bigg] \\
&= \int dx \int dy \delta(y - y*) \left[\prod_{\alpha=1}^{P} M_{00}(x) f(y,-1) + \prod_{\alpha=1}^{P} M_{11}(x) f(y,+1) + \right. \\
&\quad \left. + f(y,0) \left(C_2(c) \sum_{\{i_\alpha\}}{}^{2'} \prod_{\alpha=1}^{P} \widetilde{M}_{i_\alpha, i_{\alpha+1}}(x;c) \right) \right] .
\end{aligned} \tag{A.7}$$

Here, we employ the notation from Chapter 4, and in the last line, low coupling is assumed in order to neglect terms with large numbers of kinks. Note that at the barrier

$$f(y*, 0) = 1, \tag{A.8}$$

$$f(y*, +1) = f(y*, -1) = 0 \tag{A.9}$$

and the integral in Eq. A.7 simplifies to

$$I = \int dx \left(C_2(c) \sum_{\{i_\alpha\}}{}^{2'} \prod_{\alpha=1}^{P} \widetilde{M}_{i_\alpha, i_{\alpha+1}}(x;c) \right) . \tag{A.10}$$

Inserting the values of the interaction matrix and the normalization constant C from Appendix A of Chapter 4, we obtain

$$I = (\beta\Delta)^2 e^{-\beta V_{11}(x^\dagger)} \tag{A.11}$$

The denominator of the LHS of Eq. A.6 can be similarly simplified. At low coupling the partition function is dominated by ring-polymer configurations associated with the reactant and product basins, such that

$$f(y^a, 1) = 1 \tag{A.12}$$

$$f(y^a, 0) = f(y^a, -1) = 0. \tag{A.13}$$

The denominator of Eq. A.7 is therefore

$$\int_{-\infty}^{y^\dagger} dy e^{-\beta \Delta F(y)} = \int_{-\infty}^{\infty} dx e^{-\beta V_{11}(x)} \tag{A.14}$$

Inserting all this into Eq. , and canceling terms, we obtain

$$\begin{aligned} k_{\mathrm{TST}}^{\mathrm{LZ}} =& k_{\mathrm{TST}}^{\mathrm{KC-RPMD}} \\ \frac{1}{2}\frac{2\pi}{\hbar}\frac{|V_{ab}|^2}{|V_b'(x) - V_a'(x)|_{x=x\dagger}}\frac{e^{-\beta V_a(x^\dagger)}}{\int dx e^{-\beta V_a(x)}} =& (2\pi\beta m_y)^{-1/2}\frac{(\beta\Delta)^2 e^{-\beta V_{11}(x^\dagger)}}{\int_{-\infty}^{\infty} dx e^{-\beta V_{11}(x)}} \\ \frac{\pi}{\hbar\beta^2}\frac{1}{|V_b'(x) - V_a'(x)|_{x=x\dagger}} =& (2\pi\beta m_y)^{-1/2}, \end{aligned} \tag{A.15}$$

where we have identified $V_a = V_{11}, V_b = V_{22}, V_{12} = \Delta$. Rearranging the last equation yields

$$m_y = \frac{\beta^3\hbar^2}{2\pi^3}|V_b'(x) - V_a'(x)|^2_{x=x\dagger} \tag{A.16}$$

Note that this equation has a useful property that the mass of the auxiliary variable is determined by the local characteristics of the diabatic surfaces.

A.2 Deriving a multidimensional LZ-TST

In this section, we derive the multidimensional expression for the LZ transition state theory. This expression is then used in the derivation of the KC-RPMD mass condition for a multidimensional system with classical nuclei, which appears in Chapter 4. Here, $\mathbf{x}$ denotes the multidimensional vector of classical coordinates (rather than the vector of ring polymer bead coordinates).

This section follows the approach and notation presented in Ref 4. Starting from multidimensional adiabatic energy surfaces $W_1(\mathbf{x})$ and $W_2(\mathbf{x})$, we perform a rotation into a specific diabatic representation:

$$H = \begin{pmatrix} H_{11}(\mathbf{x}) & H_{12} \\ H_{12} & H_{22}(\mathbf{x}) \end{pmatrix} \tag{A.17}$$

Where $H_{12} = \Delta$, and is independent of $\mathbf{x}$. This can always be done provided angle of rotation is given by

$$\theta(\mathbf{x}) = \frac{1}{2}\sin^{-1}\left(\frac{2\Delta}{W(\mathbf{x})}\right) \tag{A.18}$$

where $W(\mathbf{x}) = W_2(\mathbf{x}) - W_1(\mathbf{x})$. Note that this is not necessarily the diabatic representation that may be most natural for the problem. Alternatively, we start in this diabatic representation.

Define the $f-1$ dimensional intersection of the diabatic surfaces as $w(\mathbf{x}) = H_{22}(\mathbf{x}) - H_{11}(\mathbf{x}) = 0$. Define a Hessian matrix of W

$$\eta_{ij} = \left(\frac{\partial^2 W}{\partial x_i \partial x_j}\right)_0 = \frac{1}{2\Delta}\left[\left(\frac{\partial w}{\partial x_i}\right)\left(\frac{\partial w}{\partial x_j}\right)\right]_0 \tag{A.19}$$

The Hessian matrix has only 1 nonzero eigenvalue.

Take $\mathbf{R} = (\eta_{11}, \eta_{12}, \ldots, \eta_{1f})$ to be the direction in which the multidimensional intersection behaves like a one-dimensional curve crossing. Note that the vector normal to the surface of avoided intersection ($[\nabla w(\mathbf{x})]_0$) can be determined from Eq. A.19 as

$$[\nabla w(\mathbf{x})]_0 = \left(\frac{2\Delta}{\eta_{11}}\right)^{1/2} (\eta_{11}, \eta_{12}, \ldots, \eta_{1f}) \tag{A.20}$$

Now, once we have the direction along which the curve crossing is one-dimensional, the Landau-Zener transition probability can be derived as follows

$$P_{1\to 1}(\dot{w}) = P_{a\to b}(\dot{w}) = 1 - \exp\left(-\frac{2\pi\Gamma(\dot{w})}{\hbar}\right), \tag{A.21}$$

where

$$\Gamma(\dot{w}) = \frac{\Delta^2}{|(\partial w/\partial t)_0|}. \tag{A.22}$$

The velocity along the normal vector can be expressed in terms of $\dot{\mathbf{x}}$ as

$$\left(\frac{\partial w}{\partial t}\right)_0 = \sum_i^f \left(\frac{\partial w}{\partial x_i}\right)_0 (\dot{x}_i)_0 = (\nabla w \cdot \dot{\mathbf{x}})_0 \tag{A.23}$$

Where the subscript $_0$ denotes evaluation at the surface of the diabatic crossing. At low coupling ($\beta\Delta \ll 1$), this simplifies to

$$P_{a\to b}(\dot{\mathbf{x}}) = \frac{2\pi}{\hbar}\frac{\Delta^2}{(\nabla w \cdot \dot{\mathbf{x}})_0} \tag{A.24}$$

A TST using Multidimensional LZ The TST rate in f dimensions is given by the usual multidimensional TST expression;[3] however, the probability of performing the reaction at the dividing surface $\xi(\mathbf{x}) = \xi^\dagger$ is not unity but instead given by the LZ nonadiabatic transition probability $P_{a\to b}(\dot{\mathbf{x}})$.

$$k_{\mathrm{TST}}^{\mathrm{LZ}} = \frac{1}{Q_R}\int d\mathbf{x}\int d\mathbf{p}\delta(\xi(\mathbf{x}))\dot{\xi}(\mathbf{x},\mathbf{p})h(\dot{\xi}(\mathbf{x},\mathbf{p}))e^{-\beta H(\mathbf{x},\mathbf{p})}P_{a\to b}(\dot{\mathbf{x}}) \tag{A.25}$$

$$\dot{\xi}(\mathbf{x},\mathbf{p}) = \sum_i^f \left(\frac{\partial \xi}{\partial x_i}\right)(\dot{x}_i) = \nabla\xi\cdot\dot{\mathbf{x}} \tag{A.26}$$

$$\begin{aligned} k_{\mathrm{TST}}^{\mathrm{LZ}} &= \frac{1}{Q_R}\int d\mathbf{x}\int d\mathbf{p}\ \delta(\xi(\mathbf{x}))\dot{\xi}(\mathbf{x},\mathbf{p})h(\dot{\xi}(\mathbf{x},\mathbf{p}))e^{-\beta H(\mathbf{x},\mathbf{p})}P_{a\to b}(\dot{\mathbf{x}}) \\ &= \frac{1}{Q_R}\int d\mathbf{x}\int d\mathbf{p}\ \delta(\xi(\mathbf{x}))h(\dot{\xi}(\mathbf{x},\mathbf{p}))\,(\nabla\xi\cdot\dot{\mathbf{x}})\,e^{-\beta H(\mathbf{x},\mathbf{p})}\frac{2\pi}{\hbar}\frac{\Delta^2}{\nabla w\cdot\dot{\mathbf{x}}} \\ &= \frac{1}{Q_R}\frac{2\pi\Delta^2}{\hbar}\int d\mathbf{x}\int d\mathbf{p}\ \delta(\xi(\mathbf{x}))h(\dot{\xi}(\mathbf{x},\mathbf{p}))\frac{(\nabla\xi\cdot\dot{\mathbf{x}})}{\nabla w\cdot\dot{\mathbf{x}}}e^{-\beta H(\mathbf{x},\mathbf{p})} \end{aligned} \tag{A.27}$$

The LZ probability expression contains the assumption that nuclear motion proceeds perpendicular to the seam of diabatic intersection – that is, along the direction of w. Thus, the (as yet undefined) reaction coordinate $\xi(\mathbf{x})$ is identified the difference in diabatic energies $w(\mathbf{x})$. At first, it appears that the equation is poorly defined because we have not specified what the form of $H(\mathbf{x},\mathbf{p})$ (or rather $V(\mathbf{x},\mathbf{p})$) . However, because this is performed *at the crossing of the diabatic surfaces*, $V = V_{11}(\mathbf{x}) = V_{22}(\mathbf{x})$, and there is no ambiguity.

Rewriting Eq. A.27 with this information and canceling tems

$$\begin{aligned} k_{\mathrm{TST}}^{\mathrm{LZ}} &= \frac{1}{Q_R}\frac{2\pi\Delta^2}{\hbar}\int d\mathbf{x}\int d\mathbf{p}\ \delta(\xi(\mathbf{x}))\ h(\dot{\xi}(\mathbf{x},\mathbf{p}))\ e^{-\beta\left(\mathbf{p}^{-1}\mathbf{M}\mathbf{p}+V_{11}(\mathbf{x})\right)} \\ k_{\mathrm{TST}}^{\mathrm{LZ}} &= \frac{1}{2}\frac{2\pi\Delta^2}{\hbar}\frac{\int d\mathbf{x}\ \delta(w(\mathbf{x}))e^{-\beta V_{11}(\mathbf{x})}}{\int d\mathbf{x}\ h(-w(\mathbf{x}))e^{-\beta V_{11}(\mathbf{x})}} \\ &= \frac{1}{2}\frac{2\pi\Delta^2}{\hbar}\frac{\int d\mathbf{x}\ \delta(w(\mathbf{x}))e^{-\beta V_{11}(\mathbf{x})}}{\int d\mathbf{x}\ e^{-\beta V_{11}(\mathbf{x})}} \end{aligned} \tag{A.28}$$

Where we have performed the integrals over momentum to arrive to the second line, and used the assumption that $\int d\mathbf{x}\ h(-w(\mathbf{x}))e^{-\beta V_{11}(\mathbf{x})} = \int d\mathbf{x}\ e^{-\beta V_{11}(\mathbf{x})}$ (*i.e* that the $w(\mathbf{x}) \geq 0$ contribute negligibly to the integral) to arrive at the third.

Equation A.28 has the form of a TST with the reaction coordinate $\xi(\mathbf{x}) = w(\mathbf{x})$ (the crossing of the multidimensional diabatic surfaces with $\xi = 0$ defining the transition state) multiplied by constants describing the nonadiabatic behavior at the crossing of the diabats.

The mass of associated with the auxiliary variable in multidimensional KC-RPMD is derived in a straightforward fashion by equating this rate to the multidimensional KC-RPMD TST rate. This derivation is contained in Appendices to Chapter 4.

Reducing to a single dimension The multidimensional LZ-TST rate reduces to the 1D case as follows. Starting with

$$w(\mathbf{x}) = w(x) = V_{11}(x) - V_{22}(x) \tag{A.29}$$

the LZ-TST is

$$\begin{aligned} k_{\mathrm{TST}}^{\mathrm{LZ}} &= \frac{1}{2}\frac{2\pi\Delta^2}{\hbar}\frac{\int d\mathbf{x}\ \delta(w(\mathbf{x}))e^{-\beta V_{11}(\mathbf{x})}}{\int d\mathbf{x}\ e^{-\beta V_{11}(\mathbf{x})}} \\ &= \frac{1}{2}\frac{2\pi\Delta^2}{\hbar}\frac{\int dx\ \delta(w(x))e^{-\beta V_{11}(x)}}{\int dx\ e^{-\beta V_{11}(x)}} \\ &= \frac{1}{2}\frac{2\pi\Delta^2}{\hbar}\frac{\int dx\ \frac{\delta(x^\dagger)}{|V_{11}'(x)-V_{22}'(x)|}e^{-\beta V_{11}(x)}}{\int dx\ e^{-\beta V_{11}(x)}} \\ &= \frac{1}{2}\frac{2\pi\Delta^2}{\hbar}\frac{1}{|V_{11}'(x^\dagger)-V_{22}'(x^\dagger)|}\frac{e^{-\beta V_{11}(x^\dagger)}}{\int dx\ e^{-\beta V_{11}(x)}} \end{aligned} \tag{A.30}$$

where the last equation is the same as 1D LZ-TST, Eq. A.4

References

[1] L. Landau, Phys. Z. Sowjet. **1**, 88 (1932).

[2] C. Zener, Proc. R. Soc. A **137**, 696 (1932).

[3] A. Nitzan, *Chemical Dynamics in Condensed Phases* (Oxford University Press, Oxford, 2006).

[4] J. R. Stine and J. T. Muckerman, J. Chem. Phys. **65**, 3975 (1976).